Théorie du champ moyen dynamique de la supraconductivité, du pseudogap et de l'ordre de charge dans les cuprates

Dynamical mean field theory of superconductivity, pseudogap and charge-order in cuprates

par

Sidhartha Shankar Dash

Thèse présentée au département de physique
en vue de l'obtention du grade de docteur ès science (Ph.D.)
FACULTÉ des SCIENCES
Université de Sherbrooke

Sherbrooke, Québec, Canada, 4 octobre, 2021

Le 31 décembre 2021,

le jury a accepté la thèse de Monsieur Sidhartha Shankar Dash dans sa version finale.

Membres du jury

Professeur David Sénéchal
Directeur de recherche
Département de physique

Professeur Ion Garate
Membre interne
Département de physique

Professeur André-Marie Tremblay
Président rapporteur
Département de physique

Professeur Marcello Civelli
Membre externe
Laboratoire de Physique des Solides
Université Paris Saclay

Sommaire

Les cuprates supraconducteurs sont l'objet de recherche continuelle depuis la découverte de la supraconductivité dans le composé d'oxyde de cuivre $La_{2-\delta}Ba_{\delta}CuO_4$ il y a 35 ans. Le grand nombre de phases, comme la supraconductivité, obtenues par dopage des composés parents des cuprates supraconducteurs, rend difficile la construction d'une théorie unique qui les décrive tous. Cependant, des progrès importants ont été réalisés dans notre compréhension du diagramme de phase de dopage-température de ces matériaux. Des méthodes théoriques nouvelles faisant appel aux superordinateurs modernes ont été en mesure d'expliquer la plupart de ces phases. Il y a un consensus croissant au cours des dernières années que la supraconductivité dans les cuprates provient des interactions entre électrons, médiées par des fluctuations antiferromagnétiques à courte portée. C'est fondamentalement différent de la théorie BCS où l'attraction entre les électrons est médiée par les phonons. Dans cette thèse, nous étudions la supraconductivité, le pseudogap et les ondes de densité de charge dans les cuprates supraconducteurs en appliquant la théorie du champ moyen dynamique au modèle de Hubbard à température nulle. Nous démontrons que l'appariement est médié par des fluctuations antiferromagnétiques à courte portée dans le modèle de Hubbard à trois bandes; suite à cela, nous expliquons la corrélation observée entre la température critique T_c et la teneur en trous d'oxygène au dopage optimal, comme observé dans les expériences. De plus, on observe que l'apparition du pseudo-gap dans la phase supraconductrice est associée à une transition du premier ordre dans le modèle de Hubbard à trois bandes. Cela mène à un gap asymétrique au niveau de Fermi, tel qu'observé dans les expériences. En outre, nous étudions divers ordres de charge au sein du modèle Hubbard à une bande, à température nulle. Nous observons une compétition entre les ondes de densité de charge et la supraconductivité, comme on le voit dans de nombreuses expériences. Nous observons également la présence d'une onde de densité de paire lorsque les ondes de densité de charge et la supraconductivité coexistent.

Abstract

There has been an active, ongoing research on high-T_c cuprate superconductors for around 35 years since the discovery of superconductivity in the copper oxide compound $\mathrm{La}_{2-\delta}\mathrm{Ba}_{\delta}\mathrm{CuO}_4$. The large number of phases on doping the parent compounds of cuprate superconductors, which include superconductivity, makes it difficult to construct a single theory which describes all of them. However, there has been a significant progress in understanding the various phases in the temperature-doping phase diagram of these materials. Theoretical methods, with the use of modern computers, have been able to describe most of these phases. There has been a growing consensus, for the last few years, that superconductivity in cuprate superconductors originates from attractive interactions between electrons mediated by short-range antiferromagnetic fluctuations. This is fundamentally different from the BCS theory where the attraction between electrons is mediated by phonons. In this thesis, we study superconductivity, the pseudogap and charge-density-waves in cuprate superconductors using cluster dynamical mean field theory on the Hubbard model at zero temperature. We show that pairing is mediated by short-range antiferromagnetic fluctuations within the three-band Hubbard model; using this, we explain the correlation of the critical temperature T_c and the oxygen hole content at optimal doping, as observed in experiments. Furthermore, we observe that the onset of the pseudogap within the superconducting phase is associated with a first-order transition in the three-band Hubbard model; this leads to a large asymmetric gap at the Fermi level, as observed in experiments. Additionally, we also study various charge-density-wave orders within the one-band Hubbard model at zero temperature. We observe a competition between charge-density-waves and superconductivity, as seen in many experiments, and we also observe the presence of a pair-density-wave order when charge-density-waves and superconductivity coexist.

Acknowledgements

As I am standing at the final stages of my PhD, I would like to take this opportunity to thank everyone who has been an integral part of this journey. It's been a path full of moments of learning. There has been plenty of instances where I received extensive support from the people around me which helped me undertake the projects that led to this thesis.

First of all, I would like to express my gratitude to my supervisor, David Sénéchal, for his extended support and complete involvement in every aspect of my PhD. He was always eager to help and made himself available for the tiniest of my requirements. He provided an empathetic work environment, which led to ample scientific discussions that helped me remain motivated throughout the journey. I would like to thank you for the invaluable advice and suggestions which helped me grow immensely. Finally, I would like to acknowledge your vast contribution in making this journey smooth for me. I will always remember it as a great opportunity for having the pleasure and privilege to do my PhD with you.

I would like to express my heartfelt appreciation for André-Marie Tremblay, with whom I have interacted closely, especially for the last project of my PhD. I sincerely acknowledge the scientific temperament that he offers, conveying his passion for science which arose the enthusiasm in me. The interesting discussions, your guidance, and your support have definitely helped me grow.

I am also indebted to Ion Garate for his invaluable comments and suggestions during all the committee meetings.

I would also like to extend my gratitude to the members of my committee: Marcello Civelli, Ion Garate, André-Marie Tremblay and David Sénéchal for the careful reading of the thesis and the extremely helpful suggestions, which helped me tremendously to improve the quality of the thesis. Further, I deeply appreciate David for his continuous input on the thesis throughout the period of drafting until its completion.

Then, I would like to express my gratitude to Nicolas Kowalski, with whom I worked closely for the last part of my PhD. Thank you very much for all the discussions, for teaching me how to use Git effectively, and for your help in producing all the complicated figures.

Further, I would like to thank the members of the group: Alexandre Prémont-Foley, Mathieu Bélanger, Bahman Pahlevanzadeh Garjani and Sekou-Oumar Kaba, with whom I had great discussions on various topics including physics. I would also like to thank colleagues: Simon Verret, Yan Wang, Chloé-Aminata Gauvin-Ndiaye, Shaheen Acheche, Reza Nourafkan, Olivier Simard and Charles-David Hébert for the interesting discussions in the group meetings.

I have had many friends in the department, whom I would like to thank: Redha Rouane, Arghyadip Ghosh, Mohammad Abbasi Eskandari, Seyedeh Sara Ghotb, Arash Akbari Sharbaf, Simon Bertrand and Lucas Désoppi. Thank you for the numerous lunches together, and the very interesting discussions therein. Among others, I would like to thank Gunjan Dadhwal and Om Mattagajasingh for being my family away from home. I would always remember the memorable weekends that we spent together. I cannot forget my college friends: Siddharth Sourabh Sahu, Swapna Sindhu Mishra, Bikash Das Mohapatra, Hardik Routray, Biswajeet Nayak, Nilesh Vyas, Amit Nanda, Kaushal Gianchandani and Divyansh Srimali who have played a great role in what I am today. Thank you Swapna and Siddharth for your availability; the last few calls helped me boost my morale to keep going. I am also grateful to my family (mama, baba, Bibhu, jejema, nuama) for supporting me throughout and being with me in all my decisions. Thank you Bibhu for all your help in linux and computers in general. Thank you Lisa nani, Jyoti bhaina, badamaamu, badamaain, saanamaamu, saanamaain for making me feel at home, even from across the border. Thank you badamaamu-badamaain for coming all the way from Dallas to welcome me at the Montréal airport, on my first day in Canada, and to help me settle in Sherbrooke over the subsequent days. Finally, I would like to thank my wife Amruta Sahoo for always being there for me and supporting me in the worst of times. Thank you for being my best friend, and for all the discussions that helped me immensely in all aspects of life. I owe you everything.

Table of Contents

Sommaire i

Abstract iii

1 High-T_c superconductors: Cuprates 1

1.1 History of superconductivity . . . 1

1.2 Cuprates . . . 5

1.2.1 Structure . . . 5

1.2.2 Electronic structure . . . 6

1.2.3 Characteristics of the superconducting state in cuprates . . . 8

1.3 The pseudogap and its relation with superconductivity . . . 10

1.4 Charge-density-waves . . . 13

1.5 What controls the T_c? . . . 17

Summary . . . 20

2 Many body physics and the Hubbard model 21

2.1 The Green function . . . 23

2.1.1 The non-interacting Green function . . . 23

2.1.2 The many-body Green function at zero temperature . . . 26

2.1.3 The spectral representation . . . 27

2.1.4 Observables . . . 28

2.1.5 The spectral function . . . 30

2.1.6 The self energy 31
2.2 The Hubbard model 33
2.2.1 The one-band Hubbard model 34
2.2.2 The Mott insulator 36
2.2.3 The three band Hubbard model 38
2.2.4 The charge-transfer Insulator 39
2.3 The BCS theory of superconductivity 41
2.3.1 The superconducting order parameter 47
Summary 48

3 Methods **50**
3.1 The cluster approach 52
3.1.1 Tiling the lattice by clusters 53
3.1.2 Green functions 54
3.1.3 Cluster perturbation theory (CPT) 55
3.1.4 Reciprocal lattices and superlattices 56
3.1.5 Periodization of the CPT Green function 60
3.2 Exact Diagonalization 61
3.2.1 Lanczos algorithm for the ground state 62
3.2.2 Lanczos algorithm for the Green function 64
3.3 Cluster dynamical mean field theory (CDMFT) 68
3.3.1 The impurity model 69
3.3.2 Self-consistency 71
3.3.3 Bath hybridization for the case of a superconducting solution 75
Summary 76

4 Superconductivity in the three band Hubbard model 78
4.1 Parameters of the model 79
4.2 Doping the charge-transfer insulator 80
4.3 A first order transition within the superconducting phase 85
4.4 Correlation with oxygen hole content 93
4.5 Pairing 100
4.6 Dependence on various parameters 104
4.7 Details of the cluster-bath impurity model 107
4.8 Perspective 112
Summary 114

5 Charge density waves in the one-band Hubbard model 116
5.1 Parameters of the model 117
5.2 Definition of various density-wave order parameters 118
5.3 Density-wave orders in a doped Mott insulator 119
5.4 Competition between BDW and superconductivity 123
5.5 Details of the cluster-bath impurity model 131
    5.5.1 Are our density-wave orders artefacts of CDMFT? 135
5.6 Perspective 137
Summary 138

Conclusion 139

A Appendices 145
A.1 Fourier transformation of Green function 145
A.2 Inversion of a 2 × 2 block matrix 146
A.3 Path integral formulation of the impurity problem 147
A.4 Correlation between the maximum superconducting gap and the hole content in oxygen orbitals 148
A.5 Calculation of the superconducting order parameter 148

A.6 Projection of the lattice Green function on Cu orbitals in the three-band Hubbard model 152
A.7 Susceptibility at zero temperature 153

List of Figures

1.1 Discovery of superconductivity. 2
1.2 Structure of cuprate superconductors. 6
1.3 Temperature-hole doping phase diagram of cuprates. 8
1.4 Tunneling conductance spectra of superconductors measured by STM. The conductance is directly proportional to the the number of available states, at a given energy [1]. Thus, a dip in the conductance indicates a gap in the energy spectrum. 9
1.5 The d-wave superconducting gap $\Delta(\mathbf{k}) = \Delta_0 \big(\cos(k_x) - \cos(k_y)\big)$. 10
1.6 Spectral signatures of the pseudogap. 11
1.7 Spectral signatures of the competition between superconductivity and pseudogap. 12
1.8 Charge-density-wave (CDW) modulation. 14
1.9 Signatures of competition between superconductivity and charge-density-waves. 16
1.10 Relation between the charge-transfer gap and the superconducting critical temperature T_c. 17
1.11 Relation between the maximum superconducting T_c and the hole content on oxygen orbitals. 19

2.1 Contour in the complex frequency plane for calculating the averages of one-body operators. 29
2.2 Pictorial representation of the one-band Hubbard model. 35

2.3 Schematic picture of the density of states of a Mott insulator for large U. . . 37
2.4 The three-band Hubbard model and the charge-transfer insulator. 40
2.5 The BCS gap. 44

3.1 Tiling a lattice by clusters. 52
3.2 Relation between lattice and super-lattice vectors and the relation between the corresponding vectors in the reciprocal lattice and the reciprocal super-lattice. 57

4.1 Variation of density. 81
4.2 Order parameter as a function of the hole doping for various parameter-sets around the ionic case Eq. (4.1) with various values of U_d. 82
4.3 Order parameter as a function of the hole doping for various parameter-sets around the covalent case Eq. (4.2) with various values of U_d. 83
4.4 Density of states across the first-order transition. 84
4.5 Distinct behavior of the gap at the Fermi level (see Fig. 4.4) from that of the order parameter. 85
4.6 Momentum distribution of spectral weight at the Fermi level, in the first quadrant of the Brillouin zone, across the first-order transition. 88
4.7 Momentum distribution of spectral weight at the Fermi level, in the first quadrant of the Brillouin zone, across the first-order transition in the true normal phase. 90
4.8 Features of the normal self-energy before and after the first-order transition. 92
4.9 Order parameter as a function of the hole content on O orbitals for various parameter-sets around the ionic case Eq. (4.1) with various values of U_d. . . 94
4.10 Order parameter as a function of the hole content on O orbitals for various parameter-sets around the covalent case Eq. (4.2) with various values of U_d. 95
4.11 Relation between the maximum order parameter and the corresponding hole content on oxygen. 96

4.12 Order parameter and charge-transfer gap. 98
4.13 Oxygen hole content and charge-transfer gap. 99
4.14 Imaginary part of the spin susceptibility and the cumulative order parameter as functions of frequency. 102
4.15 Antiferromagnetic superexchange, charge-transfer gap and the order parameter. 104
4.16 Cartoon of the cluster-bath impurity model. 108
4.17 Cluster-bath hybridization. 109

5.1 Cartoon of density-wave (DW) modulations on the lattice. 119
5.2 Density-wave order in the normal phase. 120
5.3 Scaling of the maximum BDW order parameter with $1/U$. 122
5.4 Effect of the second-neighbor hopping t' on the BDW order. 124
5.5 The *normal*, *superconducting* and *coexistence* phases at $U = 14$. 125
5.6 The *normal*, *superconducting* and *coexistence* phases at $U = 16$. 126
5.7 Competition between the BDW order and superconductivity. 127
5.8 Order parameters in the coexistence phase for various values of U. 128
5.9 Superconductivity and the U-dependence of the BDW order. 130
5.10 Choice of the clusters for the impurity model. 132
5.11 Cluster-bath hybridization. 133
5.12 The period-2 DW order. 136
5.13 Choice of clusters for probing density-waves in the three-band Hubbard model. 137

A.1 Correlation between the maximum superconducting gap and the oxygen hole content. 149
A.2 Deformed version of the contour Fig. 2.1 to express the contour integral in Eqs. (A.24) as an integral over the real frequency. 150

List of Tables

4.1 Gradient of the maximum order parameter and the optimal charge-transfer gap. 106

5.1 Fit parameters of the polynomial functions used in Fig. 5.3. 122

List of Abbreviations

BCS	Bardeen-Cooper-Schrieffer
ARPES	Angle-resolved photoemission spectroscopy
STM	Scanning tunneling microscopy
CDW	Charge-density-wave
PDW	Pair-density-wave
BDW	Bond-density-wave
DW	Density-wave
ZSA	Zaanen-Sawatzky-Allen
CTI	Charge-transfer insulator
CTG	Charge-transfer gap
DMFT	Dynamical mean field theory
DCA	Dynamical cluster approximation
CDMFT	Cluster dynamical mean field theory
LHB	Lower Hubbard band
UHB	Upper Hubbard band
CTB	Charge-transfer band
DFT	Density functional theory
ED	Exact diagonalization
QMC	Quantum Monte Carlo
CTQMC	Continuous-time quantum Monte Carlo
CPT	Cluster perturbation theory
BSCO	$Bi_2Sr_2CaCu_2O_8$
YBCO	$YBa_2Cu_3O_7$

Chapter 1

High-T_c superconductors: Cuprates

In this chapter, we provide a very brief introduction to superconductors with a focus on cuprate superconductors, and discuss a few current problems in the area of superconductivity in cuprate superconductors, which set the direction of our work in this thesis. In section 1.1, we briefly discuss the discovery of superconductivity and further developments in this field. In section 1.2, we discuss various aspects of superconductivity in cuprate superconductors. In sections 1.3, 1.4, 1.5, we discuss three unresolved issues in this area and ask specific questions which we aim to answer in this thesis.

1.1 History of superconductivity

Superconductivity was discovered by Heike Kamerlingh Onnes on April 8, 1911 at Leiden University. He observed that the resistance of mercury dropped sharply to zero at 4.2K [2]. Access to such low temperatures were only possible after Kamerlingh Onnes was successful in liquefying Helium in 1908. Further, Kamerlingh Onnes and his team had also observed the superfluid transition of liquid Helium at 2.2K in the same experiment, without actually realizing it. Two years later, superconductivity was observed in

Lead below 7.2K [3], and then various other superconducting materials were discovered in the subsequent decades.

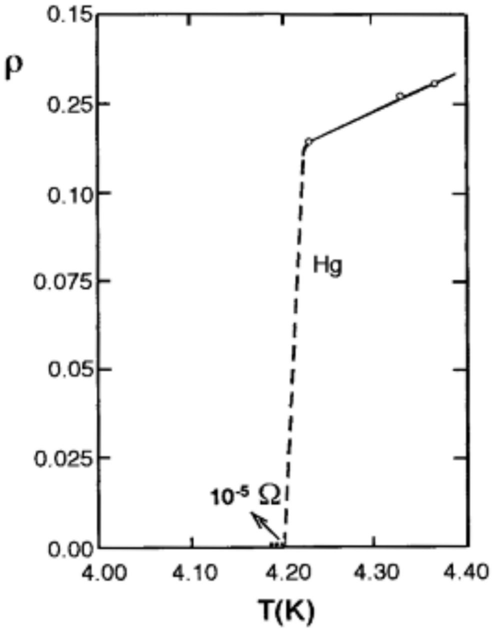

Figure 1.1: Discovery of superconductivity. Plot of resistance (Ohms) versus temperature (Kelvin) for mercury from the experiment on 26 October 1911 showing the transition to the superconducting state [4]. The resistance drops abruptly to almost zero at 4.20K.

In 1933, another important property of superconductors was discovered: materials were observed to spontaneously expel magnetic fields from within, as they became superconductors at temperatures below T_c, the superconducting critical temperature. This phenomenon is called the Meissner-Ochsenfeld effect, named after Walther Meissner and Robert Ochsenfeld, who discovered it in 1933 [5]. This causes superconductors to be perfect diamagnets, called Meissner states, in the presence of magnetic fields. However, superconducting states can be destroyed by a large enough magnetic field. Superconductors are classified as type-I and type-II based on their response to increasing magnetic fields. In type-I superconductors (mostly metallic superconductors), the superconducting state is destroyed (the material develops finite resistance) as the magnetic field is increased beyond a certain critical value (H_c) accompanied by a loss of diamagnetism. In type-II superconductors, there are two such critical values of the magnetic field (H_{c1} and H_{c2}). As the magnetic field increases beyond H_{c1}, magnetic flux penetrates into the superconductor, within vortices carrying a quantum of flux, but the resistance still remains zero [6]. The superconducting state is destroyed when the magnetic field is raised above H_{c2}.

Theoretical developments were a bit slow to come. A phenomenological explanation for the Meissner effect was given by Fritz and Heinz London in 1935, which asserts that the Meissner states minimize the electromagnetic free energy [7]. They introduced a parameter, the London penetration depth λ, denoting the penetration depth of magnetic fields in superconductors. In 1950, Vitaly Ginzburg and Lev Landau presented a very powerful phenomenological theory of the superconducting state [8]. The Ginzburg-Landau theory introduced yet another important parameter, the coherence length ξ, defined as the length over which the density of superconducting electrons decays at an interface with normal state electrons. The ratio $\kappa = \lambda/\xi$, of these two lengths, was used by Alexei Abrikosov in an article published in 1957 to predict whether a superconductor would behave as a type-I or a type-II superconductor [9]. The discovery of the Bardeen-Cooper-Schrieffer (BCS) theory in 1957 by John Bardeen, Leon Cooper and John Schrieffer came as a major breakthrough, providing a microscopic theory of superconductivity. The BCS theory describes the superconducting ground state as a condensate of pairs of electrons called Cooper pairs. These are formed due to an attractive interaction between the electrons mediated by phonons. The BCS theory relates the superconducting transition temperature T_c to the magnitude V of the electron-phonon coupling potential and the electronic density of states $N(0)$ at the Fermi level:

$$T_c \propto e^{-1/N(0)V}. \tag{1.1}$$

It could describe superconductivity in most metallic superconductors. This idea of an attractive interaction between electrons caused by phonons was formulated in a more rigorous manner, known as the Migdal-Eliashberg theory. This could explain superconductivity in metals with a strong electron-phonon coupling e.g. Lead (Pb) and Niobium (Nb), where the predictions of BCS theory differ significantly from experiments.

Until 1975, numerous superconductors had been discovered with T_c reaching as high as 23.9K with the discovery of Nb_3Ge in 1973 [3]. Theories using phonon-mediated pairing mechanisms were successful in explaining all superconductors discovered until then. In 1975 superconductivity was discovered in $BaPb_{1-\delta}Bi_\delta O$, where T_c was observed to change on varying the ratio of the concentration of Bi to that of Pb [10]. The carrier concentration in the oxide material was found to be smaller (by an order of magnitude or more) than in ordinary metallic superconductors and yet had a T_c as high as around 12K [11]. This led to a doubt whether the superconductivity in the Ba compound could be explained with phonon-mediated pairing mechanisms or whether it was a new kind of superconductivity. A major point in the history of superconductivity was when the compound $La_{2-\delta}Ba_\delta CuO_4$ with $T_c \approx 30-40$K, was discovered in 1986 by Bednorz and Müller [12]. This was followed by an explosion in the discovery of copper oxide superconductors, for instance $YBa_2Cu_3O_{7-\delta}$ with $T_c \approx 92$K and $HgBa_2Ca_2Cu_3O_{8+\delta}$ with $T_c \approx 135$K. Such large values of T_c would need an extremely strong electron phonon coupling to be explained by the conventional BCS theory. This led people to believe that the superconductivity in these materials might not be explained by phonon-mediated pairing mechanisms. Further, in 1980, superconductivity was first discovered, below 0.9K in the organic compound $(TMTSF)_2PF_6$ [13] where TMTSF is an organic molecule: tetra-methyl-tetra-selenium-fulvalene. It was followed by the discovery of superconductivity in C_{60} in 1991, and in Boron carbides in 1994 [14, 15]. In 2008, superconductivity was discovered in the iron-based compound $LaO_{1-x}F_xFeAs$ below 26K [16]. In 2018, superconductivity was discovered in bilayer Graphene twisted at an angle of approximately 1.1 degrees [17]. Although the T_c was small, superconductivity in such systems is considered to be unconventional because of their extremely low carrier density [17]. Such new kinds of superconductors were called "unconventional superconductors" or sometimes "high-T_c superconductors" since the BCS theory could not explain the superconductivity in these materials. However, in recent years, many conventional superconductors (those that could be described by the BCS theory) having large values of T_c under high pressures have been discovered. For instance H_2S (2014) has a $T_c \approx 80$K and H_3S (2015) has a $T_c \approx 200$K at pressures around 150GPa [18, 19]. In 2019, LaH_{10} was discovered, which is also a conventional superconductor, with a T_c of 250K under a pressure of 170GPa [20]. Recently, superconductivity has also been discovered in nickel oxide compounds, which are analogous to the copper oxide superconductors but have a much lower T_c [21]. Another interesting class of compounds, worth mentioning, are those based on iridium oxides. One of the most studied iridium oxide compound is Sr_2IrO_4: the physics in this material is very similar to that in the copper oxide superconductors, but superconductivity is not yet established in these materials [22, 23].

1.2 Cuprates

1.2.1 Structure

The cuprate superconductors have a layered structure. The layers can be classified into two parts on the basis of their function: i) CuO_2 planes and ii) blocking layers (see Fig. 1.2). The CuO_2 planes are responsible for superconductivity and the blocking layers supply charge carriers to the CuO_2 planes [24, 25]. These blocking layers also play a role in determining important physical quantities in the CuO_2 planes, which in turn affect the critical temperature T_c. However, it is strongly believed that the processes crucial for superconductivity occur mainly in the CuO_2 planes and that a good understanding of the physics of the CuO_2 plane is sufficient to understand the origin of superconductivity in these materials [26].

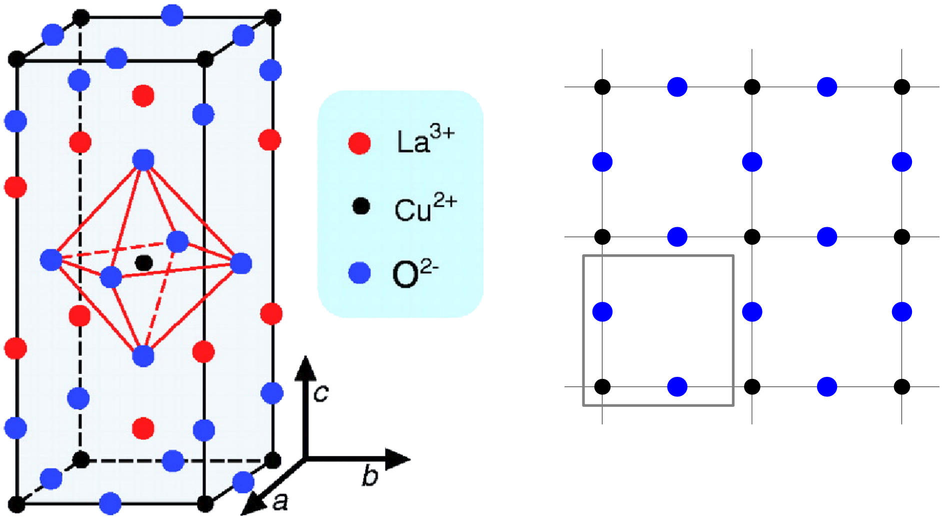

Figure 1.2: Structure of cuprate superconductors. *Left*: Crystal structure of La_2CuO_4, which is the parent compound for the high-T_c superconductor $La_{2-\delta}Sr_\delta CuO_4$ (Adapted from ref. [27]). Three CuO_2 planes are shown in the figure, which extend in the a-b plane. Superconductivity occurs in the CuO_2 planes in all cuprate high-T_c superconductors, although the crystal structures are slightly different across different families of cuprates. In this family, doping is achieved by replacing some of the La ions by Sr ions to form $La_{2-\delta}Sr_\delta CuO_4$. *Right*: CuO_2 plane. The unit cell of the lattice contains one Cu ion and two O ions.

1.2.2 Electronic structure

In the CuO_2 plane, one Cu^{2+} is surrounded by four O^{2-} (Fig. 1.2). Furthermore, the Copper ion is surrounded in the perpendicular direction by apical oxygen(s) or halogen(s). An important characteristic of such compounds is that they are insulators with an odd number of electrons in the unit cell of the CuO_2 lattice [28]. The regular band-theory describes these compounds to be metallic because of the partially filled valence band. For instance, in undoped $La_{2-\delta}Sr_\delta CuO_4$, which is an insulator, Cu^{2+} has a $3d^9$ electronic configuration and O^{2-} has a $2p^6$ configuration [26, 29]. The important fact to consider here is that the Coulomb repulsion between the electrons is high in the CuO_2 plane [30].

Let us consider a simplified model, known as the Hubbard model[1] (described in details in sec. 2.2), to understand the effect of such strong Coulomb repulsion in a two dimensional lattice. Here, we consider only the outer most orbital of the Cu atoms which has just one electron, and for simplicity we neglect the oxygen atoms. Let us say electrons repel each other only when they are at the same site on the lattice, the Coulomb repulsion energy being U. In this approximation, a large value of U would prohibit 2 electrons to occupy a site. And in a half-filled case, where all sites have one electron each, the motion of electrons would freeze and we would have an insulator referred to as a "Mott insulator" [31]. This broadly describes what happens in the CuO_2 planes of the cuprate materials. This simple picture considering just one orbital in the unit cell of the CuO_2 lattice holds because the hybridization between Cu and O leads to a local singlet, known as Zhang-Rice singlets [32], and this singlet plays an important role in the physics of the CuO_2 plane; this is why we can consider one effective orbital in the unit cell corresponding to these states, to describe the physics of the CuO_2 plane, instead of the outer most orbitals of all the Cu and O atoms.

---

[1] specifically, the one-band Hubbard model.

In a Mott insulator, the motion of charge is completely frozen. However the orientation of the spin of the electrons remains free. This allows the system to minimize the energy through the process of virtual hopping, respecting the Pauli exclusion principle, leading to an antiferromagnetic ground state at low temperatures. Adding or removing electrons (electron doping/hole doping) from the CuO_2 planes eventually suppresses the antiferromagnetic order. This is what happens for the cuprate superconductors (see Fig. 1.3). In this thesis, we will focus on the physics of hole doped cuprates. Figure 1.3 shows the various phases realized as holes are added to the CuO_2 planes. Superconductivity is observed beyond some critical value of hole doping. The superconducting transition temperature T_c increases with further doping and then decreases to zero at an upper critical value of doping. We have a metallic state at large values of the hole doping. Figure 1.3 shows the existence of some other phases which overlap with superconductivity: the pseudogap and the charge-density-wave phase. We discuss these phases in Sections 1.3 and 1.4.

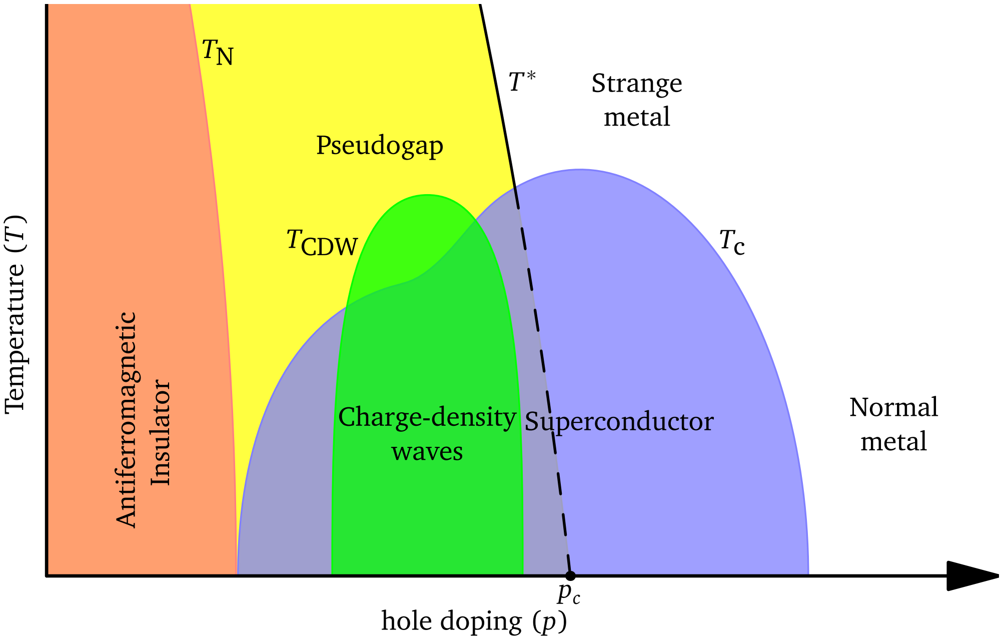

T_N
T^*
Strange metal
Pseudogap
T_{CDW}
T_c
Temperature (T)
Antiferromagnetic Insulator
Charge-density waves
Superconductor
Normal metal
p_c
hole doping (p)

Figure 1.3: Temperature-hole doping phase diagram of cuprates. The undoped cuprate materials are antiferromagnetic insulators at sufficiently low temperatures. On doping with holes, various phases, including superconductivity, are realized. Finally they become metallic at sufficiently high hole doping values.

1.2.3 Characteristics of the superconducting state in cuprates

The superconducting state is characterized by the formation of a gap in the spectrum, pinned to the Fermi level. The gap in the energy spectrum stabilizes the superconducting state. The zero temperature gap $\Delta(0)$, along with the T_c, gives an indication of the strength of the interaction that causes pairing; a relevant dimensionless ratio is $2\Delta(0)/k_B T_c$. For BCS superconductors, this ratio is 3.56 [4]. This ratio is much higher (2 to 3 times) in cuprates, suggesting a strong coupling mechanism for pairing [4].

Figure 1.4 shows examples of the superconducting gap, in the energy spectrum, for conventional and unconventional superconductors. The BCS gap is a full rectangular gap, i.e., there are absolutely no energy states between the two peaks. However, in cuprates, the superconducting gap is a partial gap. A feature that is common to both gaps is the presence of peaks, known as coherence peaks, on either side of the gap.

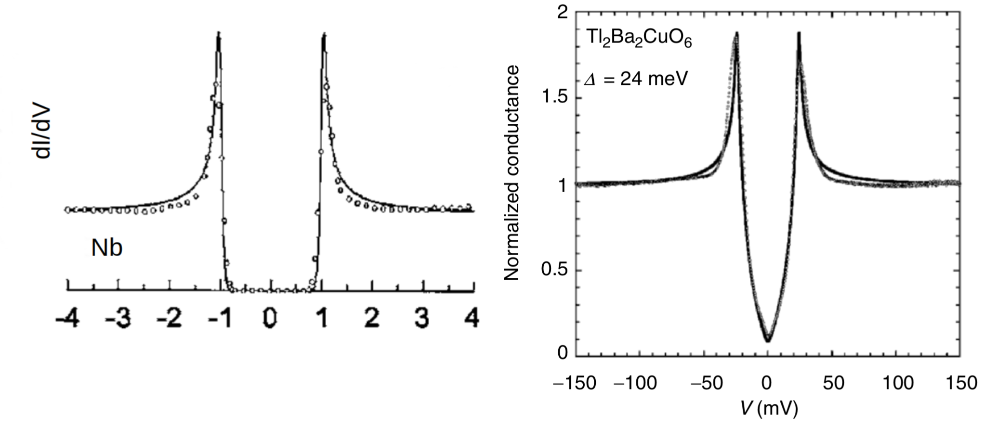

Figure 1.4: Tunneling conductance spectra of superconductors measured by STM. The conductance is directly proportional to the the number of available states, at a given energy [1]. Thus, a dip in the conductance indicates a gap in the energy spectrum. *Left:* Conductance of the conventional superconductor Nb at $T = 335$ mK is shown by open circles, along with a BCS fit with gap amplitude $\Delta_0 = 1.0$ meV (solid line) [1] . *Right:* Same for the cuprate superconductor $\mathrm{Tl_2Ba_2CuO_6}$ at $T = 4.2\ K$, along with a fit assuming a d-wave symmetry [33].

In conventional superconductors, the superconducting gap Δ does not depend on the momentum, i.e., it is isotropic in momentum space (s-wave symmetry). However, in cuprates, the gap is highly anisotropic. Its sign changes under a $\pi/2$ rotation in momentum space. It takes the form $\Delta(\mathbf{k}) = \Delta_0\big(\cos(k_x) - \cos(k_y)\big)$, where $\mathbf{k} = (k_x, k_y)$ belongs to the Brillouin zone [34–36]. Such a gap is said to have a d-wave symmetry. Figure 1.5 shows a d-wave superconducting gap. The left panel shows a polar plot of the gap for a constant $|\mathbf{k}|$. The magnitude of the gap attains its maximum value (anti-nodes) around $(\pi, 0)$, $(0, \pi)$, $(-\pi, 0)$ and $(0, -\pi)$, known as the anti-nodal regions. The gap vanishes (nodes) along (π, π), $(-\pi, \pi)$, $(-\pi, -\pi)$, $(\pi, -\pi)$, known as the nodal regions. This can be seen more clearly in Fig. 1.5 (right panel), where the gap vanishes at $\theta = 45^\circ$ (node) and attains its maximum value close to $\theta = 0^\circ$ (anti-node).

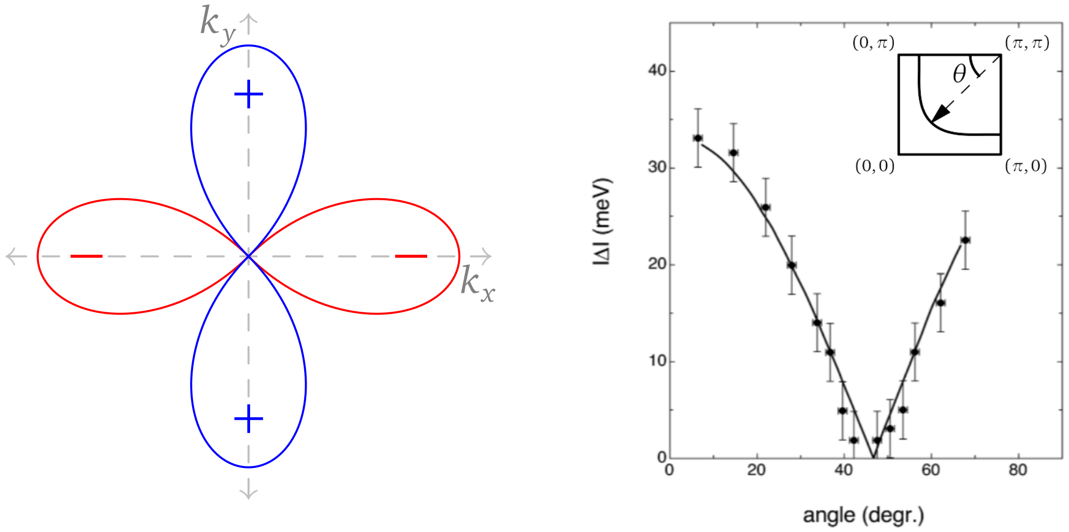

Figure 1.5: The d-wave superconducting gap $\Delta(\mathbf{k}) = \Delta_0\left(\cos(k_x) - \cos(k_y)\right)$. *Left:* Polar plot of Δ at a constant value of $|\mathbf{k}|$. The gap function changes its sign under a $\pi/2$ rotation and attains a zero in between. *Right:* Angle dependence of the superconducting gap of $Bi_2Sr_2CaCu_2O_8$, measured by ARPES (obtained from ref. [4]). The solid line is a fit based on the d-wave symmetry of the gap; the gap goes to zero at an angle close to $\pi/4$.

1.3 The pseudogap and its relation with superconductivity

As the name suggests, the pseudogap is a partial gap in the spectrum of a periodic crystal [37, 38]. In hole-doped cuprates, the pseudogap manifests itself as a gap in the antinodal region of the Brillouin zone [38–40]. It occurs below a certain value of hole doping [39, 41] below the onset temperature T^* [38, 41], as shown in the phase diagram in Fig. 1.3.

This effect can be seen in the momentum distribution of the electronic density of states around the Fermi energy, where there is a loss of the density of states near the antinodal region. This can be seen in *Angle-resolved photoemission spectroscopy* (ARPES) experiments which probe the density of states of electrons in a crystalline lattice, at a given energy and momenta. In the case of metals, the momentum distribution of the electronic density of states at the Fermi energy forms a closed curve, known as the Fermi surface. However, the pseudogap leads to a broken Fermi surface, with disconnected arcs (known as the Fermi arcs) near the nodal region [37,42]. Figure 1.6 (left panel) shows the Fermi surface for an overdoped (high value of hole doping: $p \gtrsim p_c$) sample and the Fermi arc for an underdoped (low value of hole doping: $p \lesssim p_c$) sample illustrating the effect of the pseudogap .

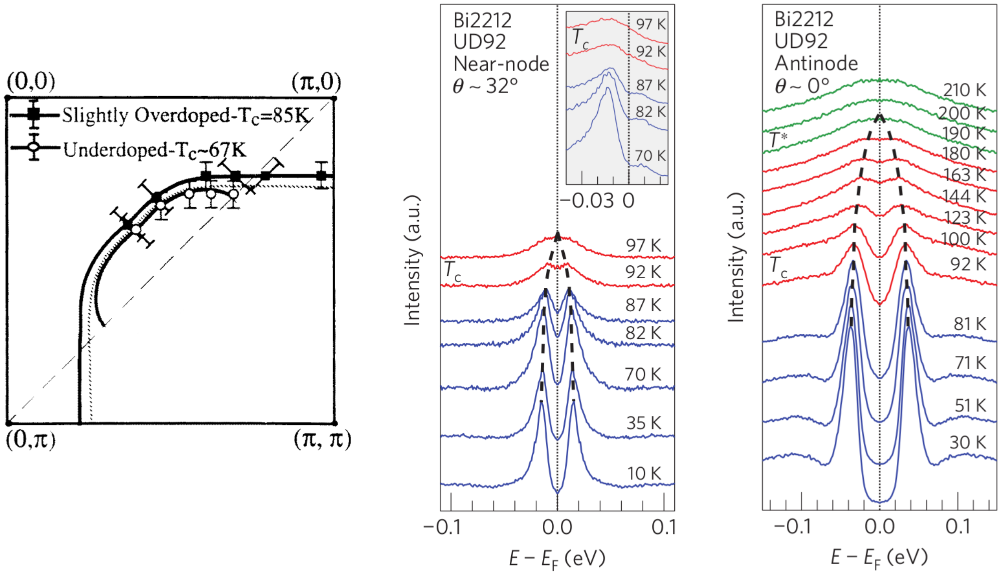

Figure 1.6: Spectral signatures of the pseudogap. *Left:* Fermi surface in underdoped and overdoped Bi2212 (adapted from ref. [39]). In the underdoped region, the Fermi surface is partially destroyed by the pseudogap, i.e., around the antinodal regions, leading to a disconnected arc around the nodal region known as a Fermi arc. *Right:* Spectral gap measured by ARPES near the nodal and antinodal regions (obtained from ref. [40]). The superconducting gap can be seen below the critical temperature T_c (blue curves) in both plots, i.e., in the nodal and antinodal regions. In the nodal region, the gap closes at T_c, however, in the antinodal region there is still a gap above T_c, which closes completely only at the temperature T^*. Hence, the pseudogap manifests itself at temperatures below the so called T^*.

Figure 1.6 (right panel) shows the symmetrized spectral gap measured by ARPES near the nodal and antinodal regions of the Brillouin zone. The gap near the nodal region closes above T_c, suggesting that it originates from superconductivity. On the other hand, the antinodal gap persists above T_c and closes at T^*, indicating the presence of the pseudogap in the antinodal region. This happens in the region where the pseudogap overlaps with the superconducting phase, i.e., the underdoped region of the phase diagram in Fig. 1.3. The effect of the pseudogap within the superconducting phase (below T_c) is not clear, since the density of states is already gapped in the antinodal region (due to superconductivity), and as a result the Fermi surface is reduced to just a node. Furthermore, there is no consensus on a broken symmetry order parameter which describes the pseudogap, which makes it very difficult to characterize. However, there are indications of a competition between superconductivity and the pseudogap when they coexist [43–45].

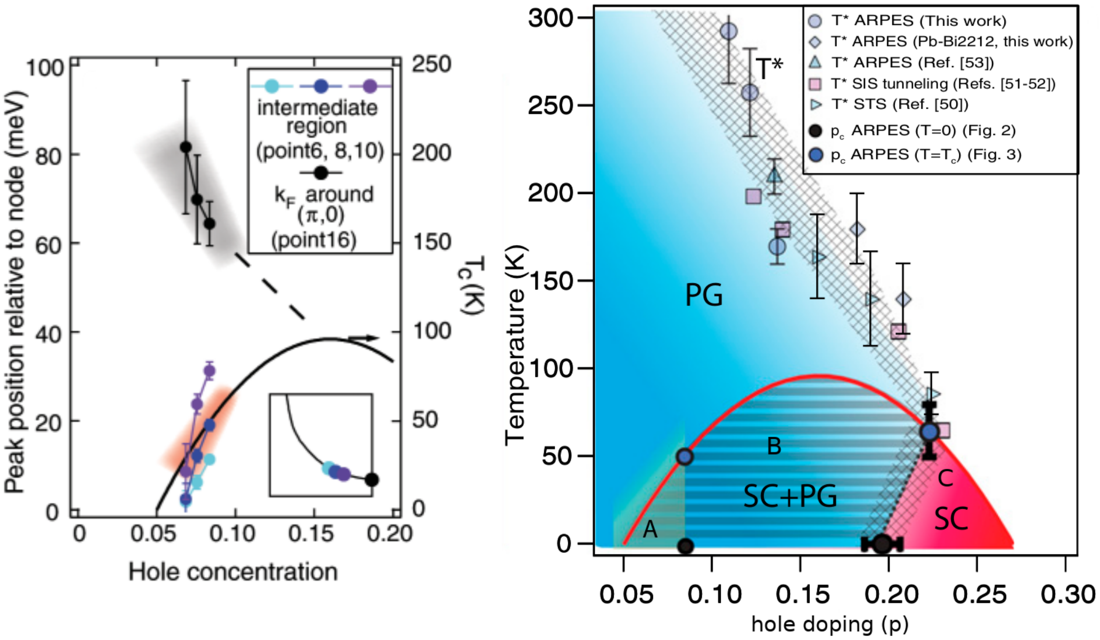

Figure 1.7: Spectral signatures of the competition between superconductivity and pseudogap. *Left:* ARPES spectral gap near the antinodal (black dots) and nodal (coloured dots) regions (obtained from ref. [43]). The gap near the antinodal region represents the pseudogap and increases as the hole concentration decreases (underdoping). The gap at various momentum values near the nodal region, which represents the strength of superconductivity (since it follows T_c), decreases with underdoping. *Right:* Observation of three different phases in the superconducting dome from ARPES data (figure obtained from ref. [46]): C → pure superconductivity, B → coexistence of superconductivity and pseudogap, A → nodeless (fully gapped) superconductivity. Ref. [46] reports a competition between superconductivity and pseudogap in the phase B. Further, the crossover between phases B and C is reported to be abrupt.

Figure 1.7 (left panel) shows the spectral gap measured by ARPES in the antinodal and the near-nodal regions along with T_c, as functions of hole doping. The antinodal gap, representing the pseudogap , increases with underdoping while the near-nodal gap decreases. The near-nodal gap, which is composed mainly of the superconducting gap, follows the T_c curve. This suggests that superconductivity is weakened with underdoping, as the strength of the pseudogap increases, indicating the possibility of competition between superconductivity and the pseudogap. Further, Fig. 1.7 (right panel) shows three distinct phases observed within the superconducting dome, identified by studying the angular and temperature dependence of the spectral gap measured in ARPES experiments [46]. These observations suggest that the pseudogap competes with superconductivity, when both phases coexist at low doping values (the underdoped region) below the critical temperature T_c, and that this coexistence phase is distinct from the pure superconducting phase at larger values of doping (the overdoped region). Theoretical studies using cluster dynamical mean field theory (described in sec. 3.3) on the one-band Hubbard model (described in sec. 2.2.1) observe such a crossover between a standard d-wave superconductivity, in the overdoped region, and an unconventional superconductivity in the underdoped region coexisting with the pseudogap [47, 48]. These studies also show that the nodal and antinodal gaps behave differently with doping, in the underdoped region, as seen in Fig. 1.7.

In this thesis (in chapter 4), we study the pseudogap within the superconducting phase in the three-band Hubbard model using cluster dynamical mean field theory at zero temperature. We focus on the following questions:

- Is the onset of the pseudogap within the superconducting phase a crossover or a first-order transition as also seen in the normal state [49–51]?
- What are the changes in the superconducting phase within the pseudogap?

1.4 Charge-density-waves

Charge-density modulations in underdoped samples have been observed in various families of cuprate superconductors [52–55]. These are commonly referred to as charge-density waves (CDWs). These density modulations are centered on the oxygen orbitals in the CuO_2 planes [54,56]. Figure 1.8 (left panel) shows the STM image of CDW of a period of 4 unit cells centred on O atoms. The CDWs are usually unidirectional [52, 54, 55] and have a d-wave form factor [54,56]. Fig. 1.8 (right panel) shows a cartoon, for clarity, of the d-wave CDW centred on O orbitals in the CuO_2 plane. A d-wave symmetry is realized in real space by a phase difference of π between the modulation along X and Y directions.

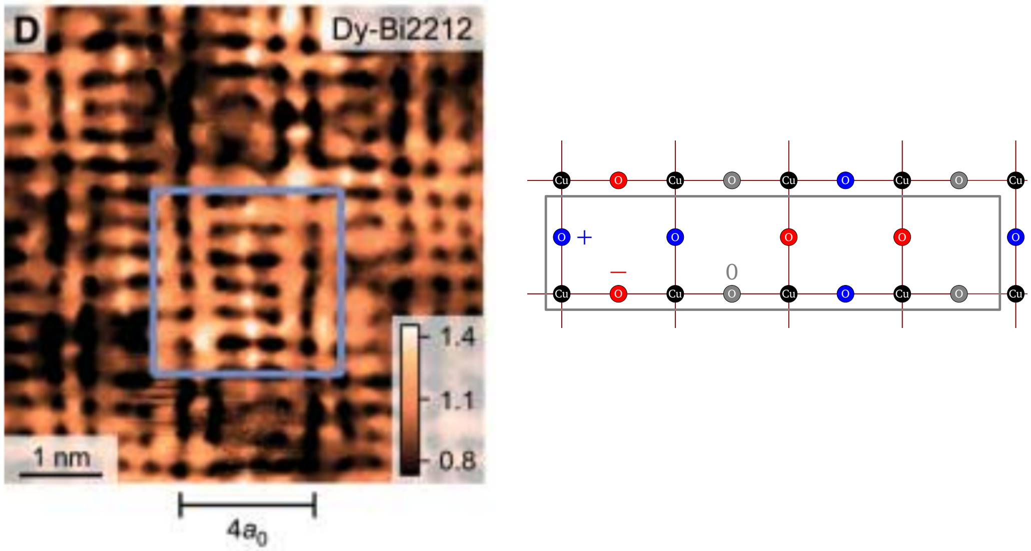

Figure 1.8: Charge-density-wave (CDW) modulation. *Left:* STM image of a CDW modulation, showing that the period of the modulation is 4 unit cells (obtained from ref. [52]). *Right:* Cartoon of a CDW modulation in the CuO_2 lattice. The charge modulation occurs on the O orbitals: red indicates the negative amplitude, blue indicates the positive amplitude and gray indicates zero.

The CDW order overlaps with superconductivity and pseudogap in the phase diagram of hole doped cuprates (Fig. 1.3). It is usually considered to be a normal state property of cuprates and is suppressed below T_c by the presence of superconductivity [53, 57–61]. Figure 1.9 shows that the CDW intensity increases below the onset temperature T_{CDW} upto T_c and then starts decreasing. It suggests that the superconducting order is detrimental to the CDW order. Further, when superconductivity is weakened by applying magnetic fields of increasing values, the CDW intensity grows, suggesting a competition between the two [58–60,62]. Various theoretical studies [63–68] have also observed strong indications of the competition between CDW order and superconductivity.

There have been quite conflicting opinions regarding the origin of the CDW order. Many theoretical studies with an effective Hamiltonian, explicitly containing antiferromagnetic interactions, e.g. the t-J model and various forms of it, have been able to obtain the CDW order [67, 69–75]. Further, spin-fermion models with short-range antiferromagnetic fluctuations have also been able to obtain the CDW order [65, 66, 68]. These observations suggest that antiferromagnetic correlations play a crucial role for the existence of the CDW order. Along this direction, refs. [74, 76] observe that large values of the second-neighbor hopping parameter t' suppresses the CDW order; an increased lattice frustration, which is detrimental for antiferromagnetism is also detrimental for the CDW order. However, ref. [70] observe that the CDW order is strengthened as the magnitude of t' increases up to a certain value, beyond which it starts to weaken. Besides, various studies have linked the CDW order with the pseudogap [55, 77, 78], suggesting that the CDW order might originate from the Fermi-surface instability of the pseudogap. However, other studies [79, 80] advocate against a direct relation between CDW order and the pseudogap. Hence, the origin of the CDW order is not clear.

Furthermore, cuprates have also been found to support the density modulation of Cooper pairs, known as pair density waves (PDWs), in the underdoped region. PDWs have been found to exist in two forms arising in different situations. A period-4[2] s'-wave PDW has been reported to exist due to the coexistence of d-wave CDW and d-wave superconductivity [81, 82]. However, a period-8 d-wave PDW has also been observed on the application of magnetic field on the superconducting state of cuprates [83, 84]. The latter kind is known as the Fulde-Ferrell-Larkin-Ovchinnikov phase [85]. In this work, we focus the former kind of PDW originating directly from the coexistence of CDWs and superconductivity.

---

[2] By period-n, we mean a period of n unit cells in the lattice.

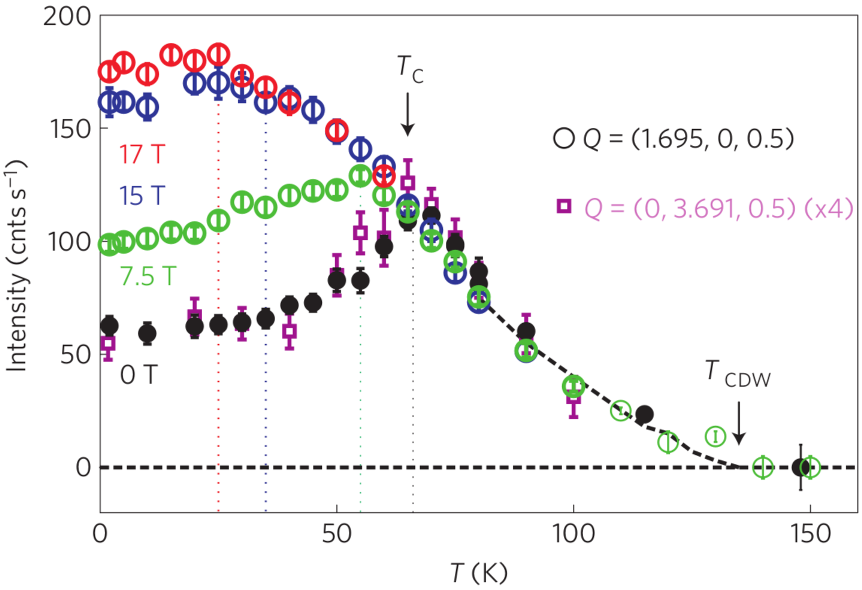

Figure 1.9: Signatures of competition between superconductivity and charge-density-waves. Temperature dependence of the peak intensity of the CDW modulation, using X-ray diffraction, at different values of the magnetic field (obtained from ref. [60]). The intensity starts increasing below the onset temperature for the CDW order, T_{CDW}, and increases as the temperature is lowered up to the superconducting critical temperature T_c, below which the intensity starts decreasing as the temperature decreases. This behavior below T_c occurs when the magnetic field is zero or has a small value. However, the intensity continues to increase with decrease in temperature at high values of magnetic fields. Note that the behavior above T_c is not affected by the presence of a magnetic field. This suggests that the suppression of the CDW intensity below T_c, at zero magnetic field, is due the presence of superconductivity; this suppression is cured at high values of magnetic field because the superconducting order is weakened by magnetic fields.

In this thesis (in chapter 5), we study charge-density-waves within the one-band Hubbard model using cluster dynamical mean field theory at zero temperature. We focus on the following questions:

- Are the local interaction effects captured by cluster dynamical mean field theory sufficient to describe the period-4 density-waves as observed in experiments [52,54] within the Hubbard model?
- What is the role of antiferromagnetic fluctuations in the existence of density-wave orders?

- Can density-waves and superconductivity coexist with each other and, if so, does the density-wave order compete with superconductivity as observed in experiments [60, 61]?
- Is there a pair-density-wave when CDW and superconductivity coexist, as seen in experiments [81]?

1.5 What controls the T_c?

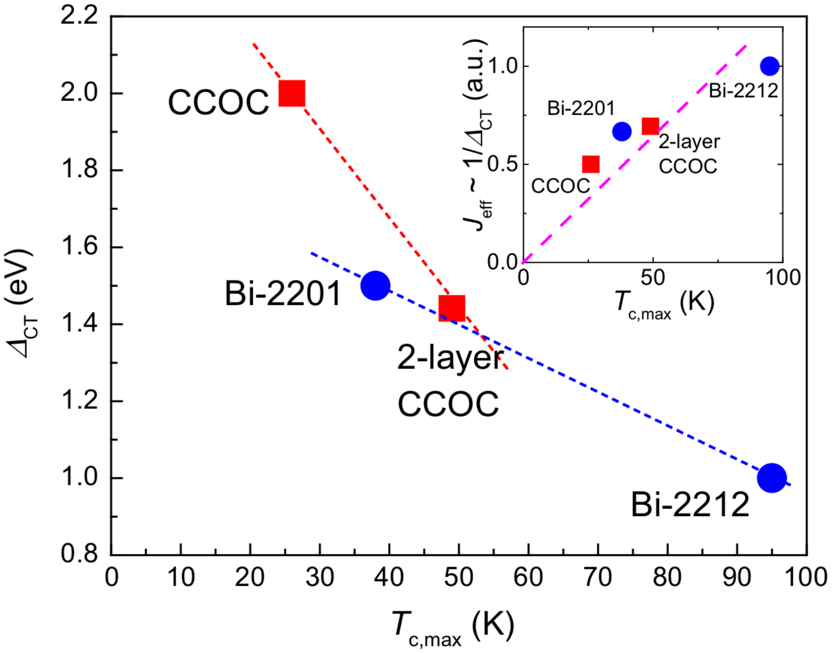

Figure 1.10: Relation between the charge-transfer gap and the superconducting critical temperature T_c. The charge-transfer gap (CTG) as a function of the maximum superconducting critical temperature $T_{c,max}$ (obtained from ref. [86]). There is roughly an inverse relation between the $T_{c,max}$ and the CTG. Further, the inset shows the effective antiferromagnetic superexchange J_{eff} as a function of $T_{c,max}$, showing an almost linear relation.

The simple picture of the Hubbard model with one orbital in the unit cell (known as the one-band Hubbard model), as discussed in page 6, describes very well the qualitative features of the phase diagram of cuprates including *d*-wave superconductivity [47, 48, 87–90], where the parent compounds of cuprates (i.e. at zero doping) are described as Mott insulators. However, the picture of a Mott insulator fails to describe the correct nature of the insulating gap in undoped cuprates: the excitations on a Mott insulator involve the transfer of an electron betwen two d-orbitals resulting in a d-d type gap, but the excitations in undoped cuprates involve the transfer of an electron from a p-orbital to a d-orbital leading to a p-d type gap [91–93]. Evidently, the undoped cuprates are classified more accurately as charge-transfer insulators (described in details in sec. 2.2.4) in the Zaanen-Sawatzky-Allen (ZSA) scheme [93–95], which classifies different kinds of insulators based on the nature of their gaps. The main differences between a charge-transfer insulator (CTI) and a Mott insulator are: 1) In the CTI picture, the O orbitals, along with the Cu orbitals, are considered in the unit cell of the lattice, 2) the insulating gap in this case, known as the charge-transfer gap (CTG), is formed between a Cu dominant band and an O dominant band (Fig. 2.4 (right panel)), 3) A CTI is realized theoretically within a three-band Hubbard model (section 2.2.3), rather than a one-band Hubbard model. This charge-transfer gap (CTG) has been observed to play an important role in determining the T_c [86]. Fig. 1.10 shows the plot of the CTG, denoted as Δ_{CT}, as a function of the maximum T_c for various cuprate superconductors. The $T_{\mathrm{c,max}}$ is observed to be roughly inversely proportional to the CTG. Furthermore, the inset shows the effective antiferromagnetic superexchange between Cu atoms, $J_{\mathrm{eff}} \approx 1/\Delta_{\mathrm{CT}}$, as a function of $T_{\mathrm{c,max}}$. The form for the antiferromagnetic superexchange is motivated from the case of a Mott insulator, where $J \propto 1/U$ [87, 96, 97], with U being the magnitude of the insulating gap, since the Mott insulator and the CTI behave similarly when the insulating gaps are large [93], which is true for cuprates. Note that the $T_{\mathrm{c,max}}$ is roughly correlated with the effective superexchange J_{eff}, suggesting that the maximum value of the critical temperature T_c might be controlled by the antiferromagnetic superexchange, for a doped CTI. This has been observed theoretically for the simpler case of a doped Mott insulator [87, 88, 96, 98]. Moreover, there are strong indications that pairing in a doped Mott insulator is mediated by short-range antiferromagnetic fluctuations [99, 100]. Experiments have also confirmed the role of antiferromagnetic superexchange in the formation of Cooper pairs in cuprates [101].

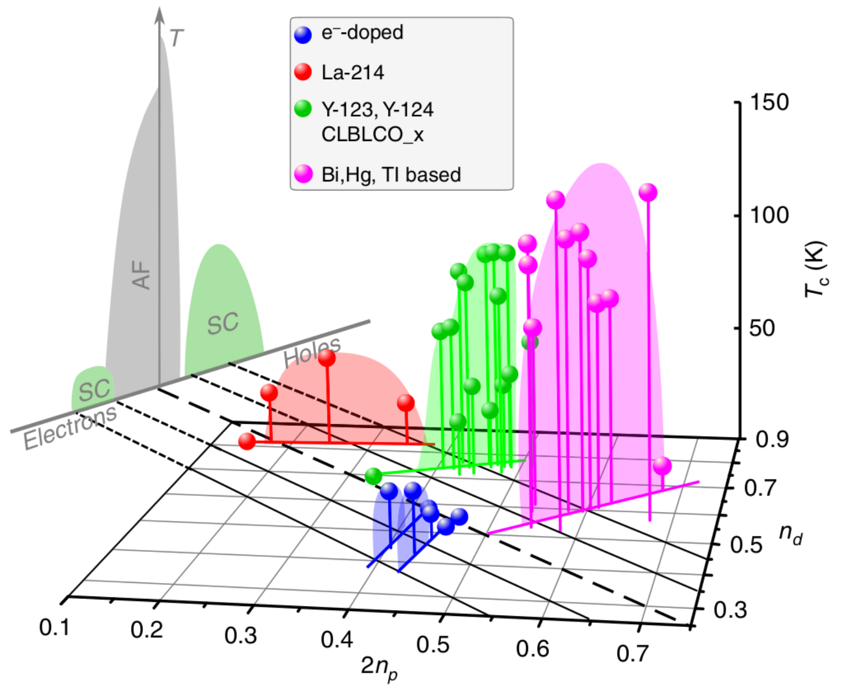

Figure 1.11: Relation between the maximum superconducting T_c and the hole content on oxygen orbitals. Superconducting T_c domes as functions of the copper (n_d) and oxygen ($2n_p$) hole contents for various families of cuprates (obtained from ref. [102]). For the hole doped cuprates, the height of the superconducting domes, i.e., the maximum T_c, monotonously increases with the corresponding value of the oxygen hole content.

Additionally, the maximum T_c is also observed to be correlated with the oxygen hole content, across various families of cuprates [102, 103]. Fig. 1.11 shows the superconducting domes for various families of cuprates in the plane of O and Cu hole contents, denoted as $2n_p$ and n_d respectively. The height of the domes, which gives the maximum value of T_c, increases monotonously with an increase in the corresponding O hole content, across various hole-doped cuprate families. This correlation between the O hole content and the maximum T_c cannot be described within the one-band Hubbard model, since it does not describe the O orbitals explicitly. A three-band Hubbard model could provide relevant information regarding the oxygen orbitals.

In this thesis (in chapter 4), we study the three-band Hubbard model (described in details in section 2.2.3), which describes a CTI in the limit of strong interactions at zero doping, to understand the correlation between the order parameter[3] and the oxygen hole content at optimal doping, as well as the relation between the order parameter and the effective superexchange. We focus on the following questions:

- Is pairing in the three-band Hubbard model mediated by antiferromagnetic fluctuations, as observed in the one-band Hubbard model [99, 100]?
- Is there a correlation of the optimal superconducting order parameter, taken as a proxy for the maximum T_c, with the oxygen hole content as seen in experiments [102] within the three-band Hubbard model?
- Is the correlation of the optimal superconducting order parameter with the oxygen hole content a coincidence or it is related fundamentally to the origin of superconductivity in cuprates?
- What do we learn from cuprates using the three-band Hubbard model that would allow us to design new high-T_c superconductors?

Summary

In this chapter, we first introduce the phenomena of superconductivity, and briefly discuss the major historical developments in this area. We introduce the so-called "high-T_c" cuprate superconductors, which turned out to be very different from the conventional superconductors and could not be described by the BCS theory. We then discuss these cuprate superconductors in some details, including the structure of these materials and the nature of the superconducting state realized in these materials. Lastly, we discuss the recent literature on a few aspects of these superconductors and enlist the questions which we try to answer in this thesis.

---

[3] We take the order parameter as a proxy for the critical temperature T_c

Chapter 2

Many body physics and the Hubbard model

The quantum mechanical description of a non-relativistic system of N electrons is governed by the Schrödinger equation[1]

$$\left[-\frac{\hbar^2}{2m}\sum_j \nabla_j^2 + \frac{1}{2}\sum_{i\neq j} V(\mathbf{r}_i - \mathbf{r}_j) + \sum_j V_{\text{ext}}(\mathbf{r}_j)\right]\Psi = i\hbar\frac{\partial \Psi}{\partial t}\ , \tag{2.1}$$

where $V(\mathbf{r})$ is the interaction potential and $V_{\text{ext}}(\mathbf{r})$ is the potential resulting from an external field including the potential from positive ions. Note that here we have used the Born-Oppenheimer approximation which amounts to assumming that the ions, which are much heavier than the electrons, are fixed in space and Eq. (2.1) corresponds to the electronic part of the Schrödinger equation (hence, phonons are neglected here).

The solution to the above equation is the many-particle wavefunction $\Psi(x_1, x_2, \cdots, x_N, t)$, from which we can know everything about the system. The arguments x_i denote the position and spin of electrons $x_i \equiv (\mathbf{r}_i, \sigma_i)$. However, solving the Schrödinger equation even for a small number of electrons is extremely difficult. Furthermore, the wavefunction at a given time depends on $3N$ space coordinates and N spin variables. The number of electrons N for a macroscopic system is of the order 10^{23}, which makes Eq. (2.1) impossible to solve. Moreover, even if we have the many-particle wavefunction Ψ for a system consisting of as small as 10 electrons, it would depend on 30 spatial variables and 10 spin variables; not only this is difficult to store in a computer, it is also very difficult to extract any useful information out of it. Hence, many-particle wavefunctions are not the most efficient quantities that can give us relevant information about a system.

---

[1] $\hbar = h/2\pi$, where $h = 6.62607015 \times 10^{-34} Js$ is Planck's constant.

In this chapter, we will discuss an alternative framework to describe a system of many electrons on a lattice using second-quantization operators. In this framework, we do not use the wavefunction of the many-electron system to get information about the system; rather, we use a special function called the *Green function* for most purposes. The Green function depends on at most $2N_d$ spatial coordinates (N_d is the spatial dimension), 2 time coordinates and 2 spin variables; this is much less than the number of variables required to describe a many-particle wavefunction for a macroscopic system. In the following sections, we will formulate the many-body problem in terms of the Green function.

In section 2.1, we introduce the Green function and discuss how to extract various observable quantities from the Green function. We also introduce a quantity known as the self-energy, which forms an important part of the Green function for interacting systems. In section 2.2, we discuss the one-band and the three-band Hubbard models, and the physical description they provide, which was mentioned briefly in chapter 1. In section 2.3, we discuss the BCS theory of superconductivity. We also define the superconducting order parameter in this section, which is a quantity that describes the strength of superconductivity in a superconductor, and we also discuss how to measure this order parameter from the Green function.

2.1 The Green function

Green functions have been used in many different areas of physics where they have different physical interpretations. Conventionally, Green functions have been used as mathematical tools to solve inhomogeneous differential equations of the form $L_x \phi(x) = f(x)$, where L_x is a linear differential operator with respect to x. In this context, the Green function G is defined as $L_x G(x, x') = \delta(x - x')$, i.e., it is a function which, when acted upon by L_x produces the delta function. The function $\phi(x)$ can then be obtained as $\phi(x) = \int dx' \; G(x, x') f(x')$. The Green function, in this context, can be interpreted as a potential originating from a point source.

In many-body physics, the Green function takes the form of a propagator, i.e., it gives the propagation amplitude of an electron or hole excitation in an equillibrium state of a many-body system. It is mostly used for two main purposes: 1) to calculate thermal expectation values of operators of the form $c^\dagger_\alpha c_\beta$, which includes many observables like the kinetic energy, electron density and so on; 2) to obtain the energy momentum distribution of electronic states, i.e., the spectral function, which, in principle, is measured in ARPES experiments.

2.1.1 The non-interacting Green function

The time evolution of a single particle state [104] is given by

$$|\Psi(t)\rangle = e^{-iH(t-t')} |\Psi(t')\rangle \; , \tag{2.2}$$

where the states are expressed in the Schrödinger picture. Projecting the equation in the position basis, we have

$$\Psi(\mathbf{r},t)\theta(t-t') = \int d^3\mathbf{r}'\ \langle\mathbf{r}|e^{-iH(t-t')}|\mathbf{r}'\rangle\Psi(\mathbf{r}',t')\theta(t-t')\,, \tag{2.3}$$

where we have used a complete set of states. The heaviside step function θ^2 is included to restrict ourselves to the case where $t > t'$. In this context, we define the retarded Green function by

$$\Psi(\mathbf{r},t)\theta(t-t') = i\int d^3\mathbf{r}'\ G^R(\mathbf{r},\mathbf{r}',t,t')\Psi(\mathbf{r}',t')\,, \tag{2.4}$$

where the retarded Green function takes the following form in the position basis:

$$\boxed{G^R(\mathbf{r},\mathbf{r}',t,t') = -i\langle\mathbf{r}|e^{-iH(t-t')}|\mathbf{r}'\rangle\theta(t-t')}\,. \tag{2.5}$$

Note that the superscript in G^R denotes that the Green function is *retarded*, which means that it propagates the wavefunction from an earlier time t' to a later time $t > t'$; this is ensured by the heaviside step function.

Although the Green function, as introduced (Eq. (2.5)) is in the retarded form and is explicitly written in the position basis, it is useful to note the generic form of the Green function operator

$$G(t-t') = -ie^{-iH(t-t')}\,, \tag{2.6}$$

which can be used as a starting point to express the Green function in any basis (position or momentum). Also, starting from Eq. (2.6), we can express the Green function operator

---

[2] $\theta(x) = \begin{cases} 1; & x > 0 \\ 1/2; & x = 0 \\ 0; & x < 0 \end{cases}$

in terms of energy by doing a Fourier transform

$$G(\omega) = \int_0^\infty d(t-t')G(t-t')e^{i\omega(t-t')} \tag{2.7}$$

$$\Rightarrow G(\omega) = \frac{1}{\omega\mathbb{1} - H} \,. \tag{2.8}$$

Then, the *retarded* Green function operator becomes

$$G^R(\omega) = \frac{1}{(\omega + i\eta)\mathbb{1} - H} \,, \tag{2.9}$$

where $\eta \rightarrow 0^+$ is a small positive number which ensures that the Green function goes to zero as $t \rightarrow \infty$[3]. The Green function operator in this form (Eq. (2.9)) is also called the *resolvent* operator.

Although we define the non-interacting Green function in this section starting from the single particle wavefunction, the definition Eq. (2.8, 2.9) still holds for the case of a non-interacting many-particle system. Consequently, the Green function defined here is also known as the *one-body* Green function: In many-body physics, the phrase *one-body* is associated to a quantity (operator) which does not describe interaction between particles. While, for an interacting many-particle system, the Green function is called the *many-body* Green function which includes the effect of interaction between particles, and is defined in the section 2.1.2. Moreover, it is often useful to define the non-interacting Green function (the *one-body* Green function) even for an interacting many-particle system; this is done by excluding the interaction terms of the Hamiltonian in the expression for the Green function, i.e., by using the non-interacting part (or *one-body* part) of the Hamiltonian in Eq. (2.8). This is useful to define a quantity called the self-energy (see section 2.1.6) for an interacting system which separately includes all effects of interaction in the system, and is used in the perturbation expansion of the many-body Green function.

---

[3] Doing a Fourier transform of $G^R(\omega)$ leaves us with an additional factor $e^{-\eta t}$ with the Green function in the time domain.

2.1.2 The many-body Green function at zero temperature

At zero temperature, all information about an interacting many electron system is contained in the ground state $|\Omega\rangle$. Although we can extract any physical information from the ground state $|\Omega\rangle$, it is usually very cumbersome to perform computations with it. On the other hand, the task becomes easy once we compute and store the corresponding Green function for the system, and the Green function is further used to calculate various physical quantities for the system.

We can directly extend the Green function for the single particle system (Eq. (2.5)) to write the Green function for a many-body system in terms of the creation/annihilation operators

$$G^R(\mathbf{r},\mathbf{r}',t,t') = -i\langle\Omega|c_{\mathbf{r}}\, e^{-iH(t-t')}\, c^\dagger_{\mathbf{r}'}|\Omega\rangle\theta(t-t')\,, \tag{2.10}$$

where $|\Omega\rangle$ is the ground state for the many-body system, which is equivalent to the vacuum for a single particle system. Here $c^\dagger_{\mathbf{r}}$ creates an electron at point $\mathbf{r}$ and $c_{\mathbf{r}}$ annihilates an electron at point $\mathbf{r}$.

A more natural way to express the Green function, starting from Eq. (2.10), is

$$G^R(\mathbf{r},\mathbf{r}',t,t') = -i\langle\Omega|c_{\mathbf{r}}(t)c^\dagger_{\mathbf{r}'}(t')|\Omega\rangle\theta(t-t')\,, \tag{2.11}$$

using the operators in their Heisenberg representations. This amounts to adding a constant term E_0 to the energy variable ω in the Fourier transform of Eq. (2.10) (see Eq. (A.7)), where E_0 is the energy of the many-body ground state; $H|\Omega\rangle = E_0|\Omega\rangle$. This expression Eq. (2.11) allows us to interpret that the Green function gives the amplitude that an electron inserted in the state $|\Omega\rangle$ at position $\mathbf{r}'$ at time t' propagates to the position $\mathbf{r}$ at a later time t. This requires, as an initial condition, that the Green function for $t = t'$ becomes a delta function $\delta(\mathbf{r}-\mathbf{r}')$. The Green function for the single particle system Eq. (2.5) satisfies this condition, however Eq. (2.11) does not in general become a delta function for $t = t'$. Using the anticommutation relation for fermionic operators[4] to fix this, the many-body Green function, at zero temperature, is defined as

$$\boxed{G^R(\mathbf{r},\mathbf{r}',t,t') = -i\left[\langle\Omega|c_{\mathbf{r}}(t)c^{\dagger}_{\mathbf{r}'}(t')|\Omega\rangle + \langle\Omega|c^{\dagger}_{\mathbf{r}'}(t')c_{\mathbf{r}}(t)|\Omega\rangle\right]\theta(t-t')}\,, \tag{2.12}$$

which indeed becomes a delta function $\delta(\mathbf{r}-\mathbf{r}')$ at $t = t'$. The second term in Eq. (2.12) describes the propagation of holes in the system. Hence, the many-body Green function gives the combined propagation amplitude of an additional electron and hole in the ground state $|\Omega\rangle$. The Green function of this kind, which gives the propagation amplitude of a single particle excitation, is known as the single-particle Green function or the one-particle Green function[5].

2.1.3 The spectral representation

It is the frequency-dependent Green function that is directly relevant for experiments. After a Fourier transform (see section A.1), Eq. (2.12) becomes

$$G^R(\mathbf{r},\mathbf{r}',\omega) = \langle\Omega|c_{\mathbf{r}}\frac{1}{\omega+i\eta-H+E_0}c^{\dagger}_{\mathbf{r}'}|\Omega\rangle + \langle\Omega|c^{\dagger}_{\mathbf{r}'}\frac{1}{\omega+i\eta+H-E_0}c_{\mathbf{r}}|\Omega\rangle\,. \tag{2.13}$$

Now, let us label the complete eigenbasis $\{|n\rangle\}$ which spans the subspace with one particle more than in the ground state $|\Omega\rangle$ by a positive integer n. We introduce this complete set of states in the numerator of the first term in Eq. (2.13). Similarly, we introduce a complete eigenbasis $\{|n\rangle\}$ $(n < 0)$, which spans the subspace with one particle less than in the ground state $|\Omega\rangle$, in the numerator of the second term in Eq. (2.13). Then, we have

---

[4] $\{c_{\mathbf{r}}(t), c^{\dagger}_{\mathbf{r}'}(t)\} = c_{\mathbf{r}}(t)c^{\dagger}_{\mathbf{r}'}(t) + c^{\dagger}_{\mathbf{r}'}(t)c_{\mathbf{r}}(t) = \delta(\mathbf{r}-\mathbf{r}')$

[5] This is true for all Green functions in this thesis. It is not to be confused with the *one-body* Green function which refers to the non-interacting Green function.

$$\boxed{G^R(\mathbf{r},\mathbf{r}',\omega) = \sum_{n>0} \frac{\langle\Omega|c_{\mathbf{r}}|n\rangle\langle n|c^\dagger_{\mathbf{r}'}|\Omega\rangle}{\omega + i\eta - (E_n - E_0)} + \sum_{n<0} \frac{\langle\Omega|c^\dagger_{\mathbf{r}'}|n\rangle\langle n|c_{\mathbf{r}}|\Omega\rangle}{\omega + i\eta + (E_n - E_0)}} \quad E_n - E_0 > 0 \;\forall\; n\,, \tag{2.14}$$

which is known as the spectral representation (also known as the Lehmann representation) of the many-body Green function. Note that, had we included a complete basis set which spans the full Hilbert space, all terms except those included in Eq. (2.14) would vanish.

The Green function includes terms corresponding to one particle (hole) excitations on the ground state $|\Omega\rangle$, hence contains information about the photoemission as well as the inverse photoemission spectra.

2.1.4 Observables

The averages of one-body operators of the form

$$O = \sum_{\alpha,\beta} s_{\alpha\beta} c^\dagger_\alpha c_\beta \tag{2.15}$$

can be easily computed using the Green function Eq. (2.14). These include many observables such as the kinetic energy, density of various kinds (total, spin resolved, spatial resolved, momentum resolved) and so on. Note that we use abstract indices in this section to remain general. In this notation Eq. (2.14) becomes

$$G_{\alpha\beta}(z) = \sum_{n>0} \frac{\langle\Omega|c_\alpha|n\rangle\langle n|c^\dagger_\beta|\Omega\rangle}{z - (E_n - E_0)} + \sum_{n<0} \frac{\langle\Omega|c^\dagger_\beta|n\rangle\langle n|c_\alpha|\Omega\rangle}{z + (E_n - E_0)}\,, \tag{2.16}$$

where we have expressed the Green function in terms of the complex frequency z. The first term in Eq. (2.16) has poles on the positive real axis and the second term has poles on the negative real axis in the complex frequency plane.

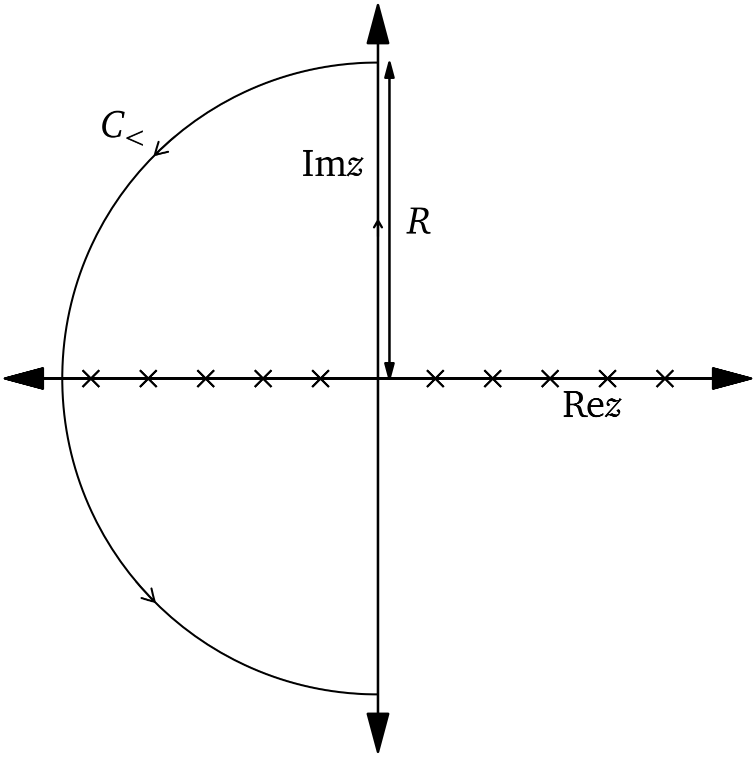

Figure 2.1: Contour in the complex frequency plane for calculating the averages of one-body operators. We perform the contour integral in the limit $R \to \infty$.

We notice that the integration of $G_{\alpha\beta}(z)$ over a contour around the negative real axis, as shown in Fig 2.1, gives

$$\oint_{C_<} \frac{dz}{2\pi i} G_{\alpha\beta}(z) = \langle c_\beta^\dagger c_\alpha \rangle \ . \tag{2.17}$$

Hence, the average of a general one-body operator O (Eq. (2.15)) can be computed as

$$\langle O \rangle = \frac{1}{N} \sum_{\alpha,\beta} s_{\alpha\beta} \oint_{C_<} \frac{dz}{2\pi i} G_{\beta\alpha}(z) = \frac{1}{N} \oint_{C_<} \frac{dz}{2\pi i} \mathrm{tr}\left[\mathbf{sG}\right] \ , \tag{2.18}$$

where N is the number of sites in the lattice.

2.1.5 The spectral function

Although until now we have used the Green function in the position basis, it can also be expressed in the momentum basis. Since we will be dealing with translationally invariant lattices, the Green function expressed in the momentum basis will always be diagonal. The Green function expressed in terms of momentum is relevant for interpreting ARPES experiments. These experiments measure a quantity known as the spectral function $A(\mathbf{k}, \omega)$, which is defined by

$$G^R(\mathbf{k}, \omega) = \frac{1}{2\pi} \int_{-\infty}^{\infty} d\omega' \, \frac{A(\mathbf{k}, \omega')}{\omega - \omega' + i\eta} \, . \tag{2.19}$$

It follows from Eq. (2.19) that

$$A(\mathbf{k}, \omega) = -2\mathrm{Im}G^R(\mathbf{k}, \omega) \, , \tag{2.20}$$

on using the identity

$$\lim_{\eta \to 0} \frac{\eta/\pi}{(\omega - \omega')^2 + \eta^2} = \delta(\omega - \omega') \, . \tag{2.21}$$

We can write the full spectral function by substituting the spectral representation of the Green function Eq. (2.14) in terms of momentum into Eq. (2.20), which gives

$$\boxed{A(\mathbf{k}, \omega) = 2\pi \left[\sum_{n>0} |\langle \Omega | c_{\mathbf{k}} | n \rangle|^2 \, \delta(\omega - (E_n - E_0)) + \sum_{n<0} |\langle n | c_{\mathbf{k}} | \Omega \rangle|^2 \, \delta(\omega - (E_0 - E_n)) \right]} \, , \tag{2.22}$$

where we have used the identity Eq. (2.21). Hence, the spectral function is basically a sum of many delta functions centred at the poles of the Green function Eq. (2.14). Thus, the spectral function has discrete delta function peaks for a finite system, and becomes a continuous function in the thermodynamic limit. However, while working with the spectral function for a finite system, it is a standard procedure to use the identity Eq. (2.21) to express the delta functions as lorentzian functions with an appropriately small value of η which broadens the delta peaks (computers cannot plot delta functions[6]), so that we have a continuous function without loosing important spectral features.

On inspection, we find that $\frac{1}{2\pi}\int d\omega\, A(\mathbf{k},\omega) = 1$. This is an important consequence for the spectral function, suggesting that it is a probability density. This is also evident from Eq. (2.22), where we can interpret $A(\mathbf{k},\omega)$ as the probability density for an electron that is added or removed from the system with momentum $\mathbf{k}$ to have an energy ω.

Another related quantity, the density of states $\rho(\omega)$ is defined as

$$\rho(\omega) = \frac{1}{N}\sum_{\mathbf{k}} A(\mathbf{k},\omega)\,, \tag{2.23}$$

where N is the number of sites in the lattice. Eq. (2.23) is the probability density that an electron which is added or removed from the system has an energy ω. This gives a measure of the fraction of one-electron states available at energy ω in the system.

2.1.6 The self energy

The self energy is an important concept and tool in describing the physics of interacting many-particle systems. Mathematically, it is a function with the same analytic properties as the Green function, which contains all the effects of interactions in the system. It is usually defined from the perturbation expansion of the many-body Green function $\mathbf{G}$ [7], where $\mathbf{G}$ is expanded in terms of the non-interacting (one-body) Green function for the system $\mathbf{G}_0$ and the self-energy $\mathbf{\Sigma}$. Here, we introduce the self energy as the difference between the inverse of the one-body Green function $\mathbf{G}_0$ and the many-body Green function

---

[6] It is also not very useful to look at the density of states as a bunch of delta function peaks, as it makes it hard to identify important spectral features.

[7] $\mathbf{G}$ (in bold) denotes the matrix representation of the many-body Green function operator G in the one particle basis $\{c_\alpha\}$.

G:

$$\mathbf{G}^{-1} = \mathbf{G}_0^{-1} - \boldsymbol{\Sigma}\,. \tag{2.24}$$

Eq. (2.24) is known as the Dyson equation. From the generic definition of the non-interacting (one-body) Green function in terms of frequency Eq. (2.8), we can write the one-body Green function matrix for a many-body system $\mathbf{G}_0$ as

$$\mathbf{G}_0(\omega) = \frac{1}{\omega - \mathbf{h}_0}\,, \tag{2.25}$$

where $\mathbf{h}_0$ is the matrix representation of the non-interacting part of the full many-body Hamiltonian H, in the one-particle basis $\{c_\alpha\}$. Hence, the many-body Green function can be expressed in terms of the self energy as

$$\boxed{\mathbf{G}(\omega) = \frac{1}{\omega - \mathbf{h}_0 - \boldsymbol{\Sigma}(\omega)}}\,. \tag{2.26}$$

The form Eq. (2.26) for the many-body Green function looks much simpler than the spectral representation of the many-body Green function in Eq. (2.14). However, the applicability of Eq. (2.26) relies on the fact that we are accurately able to extract the self-energy for an interacting system. This is a quite difficult task and becomes increasingly daunting as the system size increases. For small systems, exact diagonalization at zero temperature gives the exact ground state $|\Omega\rangle$ and hence the self-energy, whereas at finite temperatures, Monte Carlo methods [105–107] provide a very good approximation for the self-energy [108–110]. However, these methods cannot be used directly for large systems[8].

There are various approximate methods to incorporate long-range effects in the finite system, which involve self-consistent embedding of a finite interacting system into a dynamical mean field. Some of these methods are Dynamical mean field theory (DMFT) and its extensions such as the Dynamical cluster approximation (DCA) and the Cluster dynamical mean field theory (CDMFT). We will be using CDMFT in this work, which we will discuss in chapter 3.

---

[8] There are some diagrammatic Monte Carlo methods that can be used in the thermodynamic limit [111, 112], however they describe only upto a finite order in the perturbation series.

For more details on the Green function and the self-energy, one can refer to standard textbooks on many-body physics [113–115].

2.2 The Hubbard model

The Hubbard model is a very simplified model to study the motion of electrons under the influence of strong Coulomb interactions on a lattice. It was proposed in the 1960's by Hubbard [116], Kanamori [117] and Gutzwiller [118]. It was developed specifically to describe electrons in $3d$ transition metals where, because of the small radial extent of the $3d$ orbitals and occupation of these orbitals by several electrons, the average electrostatic energy is large. The Hubbard model could successfully describe the insulating properties of many transition metal monoxides (such as FeO, NiO, CoO) which were earlier predicted to be metallic due to their half-filled conduction bands. Such insulators came to be known as correlated insulators. Also, after the discovery of the high-T_c superconducting cuprates in 1987, there was a renewed interest in the Hubbard model, since it was able to describe the strong correlation effects on the CuO_2 planes which are crucial for the unconventional superconductivity seen in these materials.

The Hubbard model is defined on a lattice with originally one orbital per site, typically known as the one-band Hubbard model (described in section 2.2.1). This orbital is carefully choosen looking at the electronic structure of the material, such that it corresponds to an isolated band near the Fermi level which participates in the low energy physics of the material. Thereby, it excludes all the other electrons in orbitals corresponding to bands away from the Fermi level. This is a huge simplification, yet the Hubbard model describes many non-trivial properties of solid state systems. One immediate improvement to the one-band Hubbard model for describing the CuO_2 planes is to include 3 orbitals in the unit cell of the lattice; 1 Cu 3*d* orbital and 2 O 2*p* orbitals, known as the three-band Hubbard model (described in section 2.2.3).

2.2.1 The one-band Hubbard model

It was demonstrated by Zhang and Rice [32] that the Hubbard model with one orbital per site is sufficient to describe the physics of CuO_2 planes. This rests on the idea that there are singlets formed between the electrons residing on the Cu and the O orbitals, and that the low energy physics of the CuO_2 planes can be described by the motion of these singlets [32, 119]. This singlet band around the Fermi energy is considered in the one-band Hubbard model. Indeed, the one-band Hubbard model describes most of the qualitative features of the phase diagram (Fig. 1.3) of cuprates; superconductivity [87–89, 120–124], antiferromagnetism [87,89,122], the pseudogap [44,51,123–125], charge-density waves [64] and stripes [76].

The model includes two main ingredients; the kinetic energy of electrons in the lattice and the Coulomb potential energy between electrons on the same site. The kinetic energy is described by the hopping of electrons from one site to another; this corresponds to the Bloch states. The orbitals on different sites, which are localized Wannier orbitals, are orthogonal, but the matrix element $t_{\mathbf{r}\mathbf{r}'}$ of the Hamiltonian between the orbitals at $\mathbf{r}$ and $\mathbf{r}'$ is finite when $\mathbf{r}$ and $\mathbf{r}'$ are close and vanishes when they are far from each other[9]. The Coulomb repulsion between electrons is neglected when they are in orbitals on different sites, but when two electrons (with opposite spins[10]) occupy the same orbital, the energy of the system increases by an amount U. The screening effects in the lattice suppress the long-range Coulomb interaction between electrons, hence the short-range Coulomb interaction plays an important role. Thus the assumption of the local (on-site) nature of the Coulomb interaction is a good approximation to incorporate the short-range Coulomb interaction effects. The Hamiltonian can be written as

---

[9] Note that here we use (also for the rest of the thesis) $\mathbf{r}$ to denote the position vector of the sites on a crystal lattice, as opposed to its earlier usage as a continuous position vector.

$$H = \overbrace{-\sum_{\mathbf{r}\neq\mathbf{r}',\sigma} t_{\mathbf{r}\mathbf{r}'} c^{\dagger}_{\mathbf{r}\sigma} c_{\mathbf{r}'\sigma}}^{\text{kinetic energy}} + \overbrace{U\sum_{\mathbf{r}} n_{\mathbf{r}\uparrow} n_{\mathbf{r}\downarrow}}^{\text{potential energy}} - \mu \sum_{\mathbf{r}} (n_{\mathbf{r}\uparrow} + n_{\mathbf{r}\downarrow})\,, \tag{2.27}$$

where $c^{\dagger}_{\mathbf{r}\sigma}$ creates an electron with spin σ at the site $\mathbf{r}$ in the lattice, $n_{\mathbf{r}\sigma} = c^{\dagger}_{\mathbf{r}\sigma} c_{\mathbf{r}\sigma}$ counts the number of electrons with spin σ at site $\mathbf{r}$ and μ is the chemical potential which controls the number of electrons in the system. We limit ourselves to the case where electrons in a given orbital hop only to the orbitals in their first, second and third neighbouring sites with amplitudes t, t' and t'' respectively. The one-band Hubbard model is illustrated in Fig. 2.2.

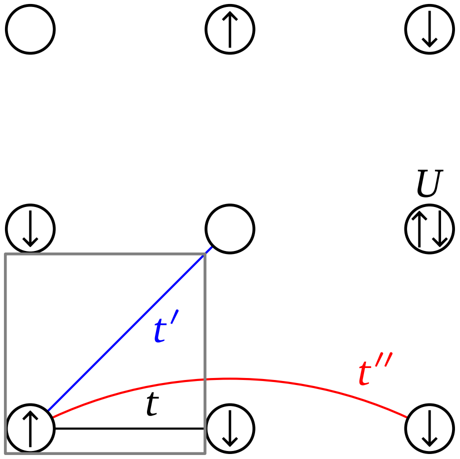

Figure 2.2: Pictorial representation of the one-band Hubbard model. t, t' and t'' are the amplitudes for hopping to the first, second and third neighbors respectively. U is the Coulomb potential energy when two electrons occupy a single site. The gray box marks the unit cell.

---

[10] because of the Pauli principle.

2.2.2 The Mott insulator

The physics of the Hubbard model is governed by the competition between the kinetic energy term, which tends to delocalize electrons on the lattice, and the potential energy term, which penalizes a double occupation at a site. When the kinetic energy dominates, the ground state is a Bloch state, whereas when the potential energy dominates, the electrons are localized in their respective Wannier orbitals. The ground state becomes highly non-trivial when both kinetic and potential energy terms are comparable; this is the case for cuprate superconductors. When the potential energy term is large, i.e., when $U > W$ (difference in energy between the highest and lowest energy Bloch states) and when the lattice is half-filled (one electron at each site), the ground state is an insulator known as the *Mott insulator*. In this state, all the sites are occupied by an electron and since double occupation on any site costs a large energy U, there is almost no hopping, hence we have an insulator. Such a state additionally becomes antiferromagnetic when there is no frustration in the lattice. For instance, for $t' = 0,\ t'' = 0$, doing a second order degenerate perturbation theory in t, one can obtain an antiferromagnetic interaction $J\mathbf{S}_{\mathbf{r}} \cdot \mathbf{S}_{\mathbf{r}'}$ with $J = 4t^2/U$ [126, 127] and $\mathbf{S}_{\mathbf{r}}$ being the spin operator at the site $\mathbf{r}$. This leads to a lowering of energy for antiparallel spins on neighbouring sites $\mathbf{r}$ and $\mathbf{r}'$, hence favoring an antiferromagnetic order.

In a Mott insulator, the density of states (Fig. 2.3(a)) vanishes at the Fermi level and there are two bands separated roughly by the energy U; the band below the Fermi level is known as the lower Hubbard band (LHB) and the band above the Fermi level is known as the upper Hubbard band (UHB). The LHB corresponds to the filled electronic states in the lattice; there are N such states (singly occupied orbitals) where N is the number of sites in the lattice. The UHB corresponds to states that can be obtained by single electron excitations above the Fermi level; there are N such states since we can doubly occupy all the singly occupied N sites. Since double occupation at each site costs an energy U, the UHB is separated from the LHB by the energy U.

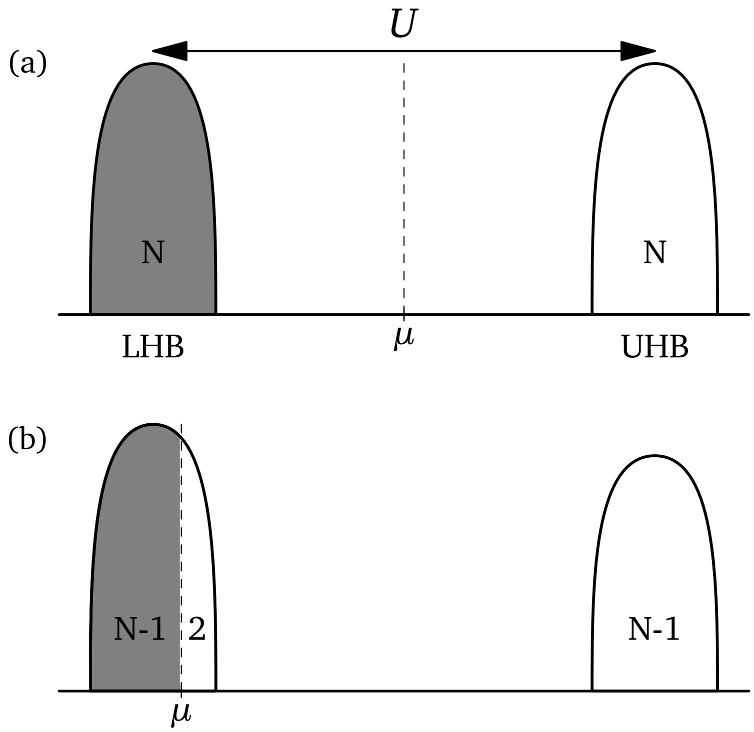

Figure 2.3: Schematic picture of the density of states of a Mott insulator for large U. Density of states for (a) a Mott insulator and (b) a doped Mott insulator. The shaded area denotes filled electronic states, i.e., states below the Fermi level. In the half-filled case (a), where we have one electron per site (with a total of N sites), the lower Hubbard band (LHB) contains N electronic states corresponding to the singly occupied orbitals in all of the N sites. The upper Hubbard band (UHB) contains all possible double occupation states achievable by adding one electron in the half-filled system; there are exactly N such states. In the doped case (b), where there are $N-1$ electrons on the lattice, the UHB in turn is reduced in size to contain the $N-1$ possible double occupation states. The remaining two states, out of a total of $2N$ states, exist in the unoccupied part of the LHB, increasing its size to contain a total of $N+1$ electronic states.

The parent (undoped) cuprate superconductors are described well by antiferromagnetic Mott insulators. On doping the Mott insulator, we get various interesting physics including unconventional superconductivity. The study of doped Mott insulators hence becomes important to understand unconventional superconductivity in cuprates. Let's try to understand the density of states on doping the Mott insulator (Fig. 2.3(b)). Let's say we dope the system with holes, such that there are $N-1$ electrons on the lattice. This has an effect on the UHB: Since the number of possible doubly-occupied states now decreases to $N-1$, the UHB now contains $N-1$ electronic states and is smaller. This leaves us with 2 unoccupied states out of a total of $2N$ states on the lattice; these two states correspond to the possibility of filling the empty site by a spin up or a spin down electron. These two states are included in the LHB and hence the size of the LHB increases to contain a total of $N + 1$ electronic states. Similarly, on further doping the system with holes, the UHB gradually decreases in size and the LHB increases in size. Also, the empty sites provide an opportunity for electrons to move around without doubly occupying any site; this leads the system to gradually become metallic as we dope the system with holes. This transition from the insulating regime to the metallic regime, on doping the system with holes, is accompanied by the growth of a peak (associated to the so called quasiparticles) at the Fermi energy, which is a signature of the metallic phase[11].

2.2.3 The three band Hubbard model

Although the one-band Hubbard model explains well the qualitative features of the phase diagram of cuprates, it does not give information explicitly about the role of copper or oxygen orbitals in the CuO_2 plane. This becomes important since experiments have shown that the hole content in oxygen orbitals on the CuO_2 plane is correlated with the superconducting critical temperature T_c across various families of cuprates [102, 103]. Hence, it is important to study a more realistic model for the CuO_2 planes which explicitly includes copper and oxygen orbitals, such as the three-band Hubbard model, also known as the Emery-VSA model [94, 95]. This model includes three orbitals in the unit cell: one Cu $3d_{x^2-y^2}$ orbital, one O $2p_x$ orbital for oxygen bonding with copper along the x-direction and one O $2p_y$ orbital for oxygen bonding with copper along the y-direction. This is illustrated in Fig. 2.4. The full Hamiltonian can be written as

---

[11] This is described within the Fermi liquid theory [128–130].

$$
\begin{aligned}
H = &-\sum_{\mathbf{r},\mathbf{s},\sigma} t_{\mathbf{r},\mathbf{s}} \left(p^\dagger_{\mathbf{s}\sigma} d_{\mathbf{r}\sigma} + d^\dagger_{\mathbf{r}\sigma} p_{\mathbf{s}\sigma}\right) - \sum_{\mathbf{s}\neq\mathbf{s}',\sigma} t_{\mathbf{s}\mathbf{s}'} p^\dagger_{\mathbf{s}\sigma} p_{\mathbf{s}'\sigma} + (\epsilon_d - \mu) \sum_{\mathbf{r},\sigma} n^d_{\mathbf{r}\sigma} \\
&+ \left(\epsilon_p - \mu\right) \sum_{\mathbf{s},\sigma} n^p_{\mathbf{s}\sigma} + U_d \sum_{\mathbf{r}} n^d_{\mathbf{r}\uparrow} n^d_{\mathbf{r}\downarrow} + U_p \sum_{\mathbf{s}} n^p_{\mathbf{s}\uparrow} n^p_{\mathbf{s}\downarrow} \\
&+ U_{pd} \sum_{\langle \mathbf{r},\mathbf{s}\rangle} \left(\sum_{\sigma} n^d_{\mathbf{r}\sigma}\right)\left(\sum_{\sigma} n^p_{\mathbf{s}\sigma}\right),
\end{aligned}
\tag{2.28}
$$

where $\mathbf{r}$ gives the position of the copper sites, $\mathbf{s}$ gives the position of the oxygen sites, $p^\dagger_{\mathbf{s}\sigma}$ creates an electron in the p orbital at the site $\mathbf{s}$, $d^\dagger_{\mathbf{r}\sigma}$ creates an electron in the d orbital at the site $\mathbf{r}$, $n^d_{\mathbf{r}\sigma}$ counts the number of electrons with spin σ in the d orbital at site $\mathbf{r}$, $n^p_{\mathbf{s}\sigma}$ counts the number of electrons with spin σ in the p orbital at site $\mathbf{s}$, U_d is the Coulomb repulsion energy when two electrons occupy the same d orbital, U_p is the Coulomb repulsion energy when two electrons occupy the same p orbital and U_{pd} is the Coulomb repulsion energy between neighboring d and p orbitals. We limit ourselves to the hopping amplitudes shown in Fig. 2.4. We neglect U_p and U_{pd}, i.e., we take $U_p = 0$ and $U_{pd} = 0$ in our model, since DFT+U calculations have shown that these energies are much smaller than U_d [131, 132].

2.2.4 The charge-transfer Insulator

The three-band Hubbard model also describes a correlated insulator at large values of U_d at a particular filling of the lattice. From DFT calculations of the band structure of cuprates, we have $\epsilon_p > \epsilon_d$[12] [133,134]; in this regime, an insulator is formed and is known as a charge-transfer insulator (CTI) [93] at a filling of 5 electrons per unit cell. The cartoon of the density of states of a CTI is shown in the right panel of Fig. 2.4. Such an insulator is realized as U_d increases and splits the Cu band into lower and upper Hubbard bands, such that the upper Hubbard band crosses the band (of mostly oxygen character) around

---

[12] After subtracting the double counting contribution from ϵ_d [133].

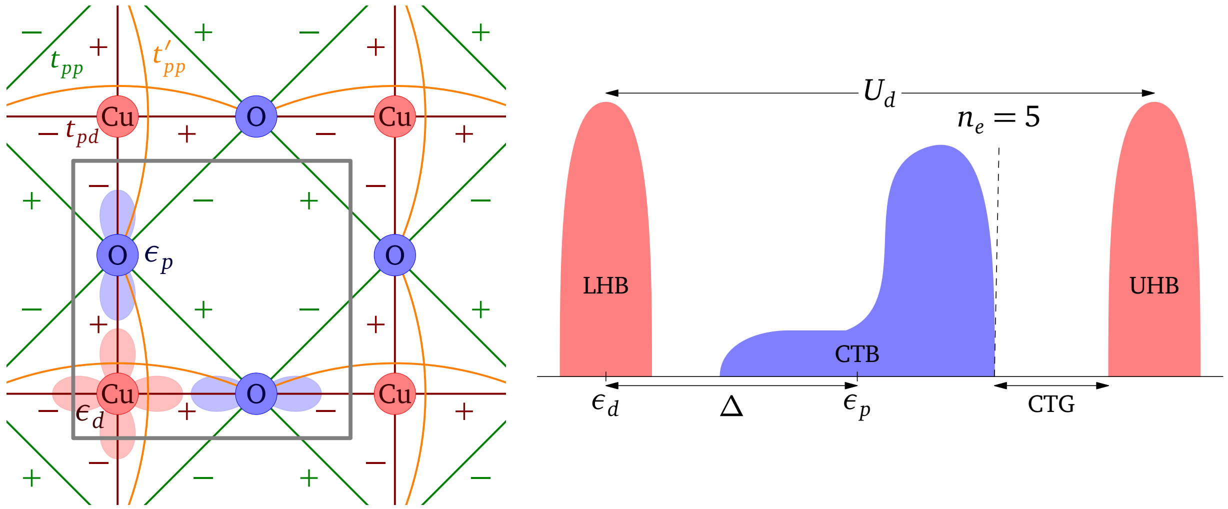

Figure 2.4: The three-band Hubbard model and the charge-transfer insulator. *Left*: Pictorial representation of the non-interacting part of the three-band Hubbard model on the CuO_2 plane. The unit cell is demarkated by a gray box and contains 3 orbitals: Cu $3d_{x^2-y^2}$ orbital, O $2p_x$ and O $2p_y$ orbitals. Various hopping amplitudes are shown: t_{pd} between Cu d orbital and O p orbital (brown bonds), t_{pp} between nearest neighbor O p orbitals (green bonds), t'_{pp} between two oxygen p orbitals separated by a Cu d orbital (orange bonds). The sign on the bonds gives the combined phase of the orbitals participating in bonding. ϵ_d is the orbital energy of the Cu d orbital and ϵ_p is the orbital energy of the O p orbitals. *Right*: Cartoon of the density of states of a charge-transfer insulator (CTI). This is valid for the number of electrons in the unit cell $n_e = 5$. LHB stands for lower Hubbard band, UHB for upper Hubbard band, CTB for charge-transfer band and CTG for charge-transfer gap. A charge-transfer insulator (CTI) is realized at a filling of 5 electrons in the unit cell when U_d is sufficiently large. The color codes for the LHB, UHB and CTB are in line with the figure on the left panel; UHB and LHB are mostly of Cu character, CTB is mostly of O character. CTG is the equivalent of the Mott gap in the three-band Hubbard model with $\epsilon_p > \epsilon_d$.

ϵ_p. This happens at a filling of 5 electrons in the unit cell, with one electron in the Cu d orbital and 2 electrons in both of the O p orbitals; this freezes the motion of electrons due to a large value of U_d on the Cu d orbital hence leading to an insulating state. The oxygen dominant band around ϵ_p is also known as the charge-transfer band (CTB). The insulating gap in this case, known as the charge-transfer gap (CTG), is formed between the upper Hubbard band (UHB) and the CTB. This is different from the case of a Mott insulator where the insulating gap ($\approx U$) is formed between the lower and upper Hubbard bands. Hence, the effective interaction in the three-band Hubbard model is controlled by both U_d and the difference between the Cu and O orbital energies $\epsilon_p - \epsilon_d$. On doping the CTI, the holes primarily go into the O orbitals since they are close to the Fermi level; this is also seen in experiments [135–137]. Doped charge-transfer insulators have been able to describe various aspects of the phase diagram of cuprates along with a more realistic description of the distribution of doped holes in the CuO_2 plane [133,138].

2.3 The BCS theory of superconductivity

The BCS theory is the first microscopic theory of superconductivity, put forward by John Bardeen, Leon Cooper and John Schrieffer in 1957. It could explain all superconductors known at that time. BCS theory describes Cooper pairs as bound states formed due to attractive interaction between electrons near the Fermi level, mediated by phonons. However, around 1980s new kinds of superconductors were discovered which could not be described completely by phonon-mediated mechanisms. These came to be known as unconventional superconductors. The superconducting phase in these unconventional cuprate superconductors was always found in proximity to a metal-insulator transition caused by strong Coulomb interaction in these materials. This suggested that the strong Coulomb interactions between electrons might play a role in unconventional superconductivity. We study the unconventional superconductivity in cuprates within both one-band and three-band Hubbard model in chapters 4, 5 using numerical techniques discussed in chapter 3.

There are certain fundamental aspects of superconductivity which are the same for both conventional and cuprate superconductors: A gap develops at the Fermi level in the superconducting state for both cases, we have Cooper pairs as charge carriers for both cases and also the spin part of the pair wave function is a singlet for both conventional and cuprate superconductors. In this section, we briefly discuss important results of the BCS theory of superconductivity to develop an intuition for the universal characteristic properties of the superconducting state. For full details on the theory, one should look at text books on the BCS theory [139–142].

The BCS Hamiltonian is given by

$$H_{\mathrm{BCS}} = \sum_{\mathbf{k},\sigma} (\zeta(\mathbf{k}) - \mu)\, c^{\dagger}_{\mathbf{k}\sigma} c_{\mathbf{k}\sigma} - V_{\mathrm{eff}} \sum_{\mathbf{k},\mathbf{k}'}^{|\zeta - E_F| < \hbar\omega_D} c^{\dagger}_{\mathbf{k}\uparrow} c^{\dagger}_{-\mathbf{k}\downarrow} c_{-\mathbf{k}'\downarrow} c_{\mathbf{k}'\uparrow} \,, \tag{2.29}$$

where μ is the chemical potential. The first term is the kinetic energy term expressed in terms of the momentum $\mathbf{k}$; it is diagonal in momentum because of the translational invariance of the lattice. The second term describes the attractive interaction ($V_{\mathrm{eff}} > 0$) between electrons with opposite momentum and spin to form Cooper pairs. This attractive interaction is known to come from phonons only between the Bloch states with energy close to the Fermi level; this is incorporated as a restricted sum over momenta such that the energy lies within an window $\hbar\omega_D$ (the Deby energy) around the Fermi level E_F[13] [139]. In the BCS theory this attractive interaction is taken as granted and the interaction potential is taken to be a constant V_{eff}.

The Hamiltonian Eq. (2.29) is an interacting Hamiltonian and is hard to solve exactly [14]. A standard way to deal with a term with many operators is to divide the term into two factors and replace one factor with its average value, for instance, here we replace $c_{-\mathbf{k}'\downarrow} c_{\mathbf{k}'\uparrow}$ by its average value $\langle c_{-\mathbf{k}'\downarrow} c_{\mathbf{k}'\uparrow} \rangle$. This is known as a *mean-field* approximation. Then, on making the Hamiltonian hermitian, we have

$$H^{\mathrm{MF}}_{\mathrm{BCS}} = \sum_{\mathbf{k},\sigma} (\zeta(\mathbf{k}) - \mu)\, c^{\dagger}_{\mathbf{k}\sigma} c_{\mathbf{k}\sigma} + \sum_{\mathbf{k}} \left(c^{\dagger}_{\mathbf{k}\uparrow} c^{\dagger}_{-\mathbf{k}\downarrow} \Delta + \Delta^{*} c_{-\mathbf{k}\downarrow} c_{\mathbf{k}\uparrow} \right) \,, \tag{2.30}$$

where

$$\Delta = -\frac{1}{N} V_{\mathrm{eff}} \sum_{\mathbf{k}'} \langle c_{-\mathbf{k}'\downarrow} c_{\mathbf{k}'\uparrow} \rangle \,. \tag{2.31}$$

---

[13] The Fermi energy E_F is essentially the same as the chemical potential μ for a metal, since a change in μ directly changes the occupation number in a metal. However, in a gapped state, μ and E_F can be different from each other: μ can be anywhere within the gap to lead to the same occupation in the system, but E_F is the highest occupied energy, i.e. the left edge of the gap (for example, see Figs. 2.3, 2.5).

[14] The exact solution of this Hamiltonian was given by Richardson in 1963 [143–145], however we use the mean-field approximation to solve this, which is more relevant in the context of this thesis.

Then the Hamiltonian Eq. (2.30) can be readily expressed in terms of matrices in a basis of single particle operators $\{c_{\mathbf{k}\uparrow}, c^{\dagger}_{-\mathbf{k}\downarrow}\}$:[15]

$$\mathbf{H}^{\mathrm{MF}}_{\mathrm{BCS}}(\mathbf{k}) = \begin{bmatrix} \zeta(\mathbf{k}) - \mu & \Delta \\ \Delta^{*} & -(\zeta(\mathbf{k}) - \mu) \end{bmatrix}, \tag{2.32}$$

and the energy eigenvalues, for each $\mathbf{k}$, can be calculated as

$$\omega = \pm E_{\mathbf{k}} = \pm\sqrt{(\zeta(\mathbf{k}) - \mu)^2 + |\Delta|^2}\,. \tag{2.33}$$

Note that the use of the basis $\{c_{\mathbf{k}\uparrow}, c^{\dagger}_{-\mathbf{k}\downarrow}\}$, known as the Nambu basis, makes it easy to deal with the pairing terms in the mean-field BCS Hamiltonian Eq. (2.30), which in turn appear as off-diagonal terms in the matrix form of the Hamiltonian. Equation (2.33) gives the allowed energy values in the spectrum. Note that the energy cannot be arbitrarily close to zero and there is a gap of magnitude 2Δ in the spectrum; this is the superconducting gap. This is illustrated in Fig. 2.5 where the right panel shows energy eigenvalues of the mean-field BCS Hamiltonian Eq. (2.30) along with the eigenvalues for the normal state (no superconductivity: $\Delta = 0$) solution. The left panel of the Fig. (2.5) shows the density of states for the normal state and the superconducting state in the model Eq. (2.30) with only nearest neighbour hopping on a 2D square lattice. There are no states with energy within the window Δ around the Fermi level in the superconducting solution, resulting in the formation of the superconducting gap.

The basis in which the mean-field BCS Hamiltonian Eq. (2.30) is diagonal is related to the Nambu basis by the Bogoliubov-Valentin transformation

$$\begin{bmatrix} b_{\mathbf{k}\uparrow} \\ b^{\dagger}_{-\mathbf{k}\downarrow} \end{bmatrix} = \begin{bmatrix} u^{*}_{\mathbf{k}} & v_{\mathbf{k}} \\ -v^{*}_{\mathbf{k}} & u_{\mathbf{k}} \end{bmatrix} \begin{bmatrix} c_{\mathbf{k}\uparrow} \\ c^{\dagger}_{-\mathbf{k}\downarrow} \end{bmatrix}, \tag{2.34}$$

---

[15] $H^{\mathrm{MF}}_{\mathrm{BCS}} = \sum_{\mathbf{k}} \begin{bmatrix} c^{\dagger}_{\mathbf{k}\uparrow} & c_{-\mathbf{k}\downarrow} \end{bmatrix} \mathbf{H}^{\mathrm{MF}}_{\mathrm{BCS}}(\mathbf{k}) \begin{bmatrix} c_{\mathbf{k}\uparrow} \\ c^{\dagger}_{-\mathbf{k}\downarrow} \end{bmatrix} + \text{constant}$

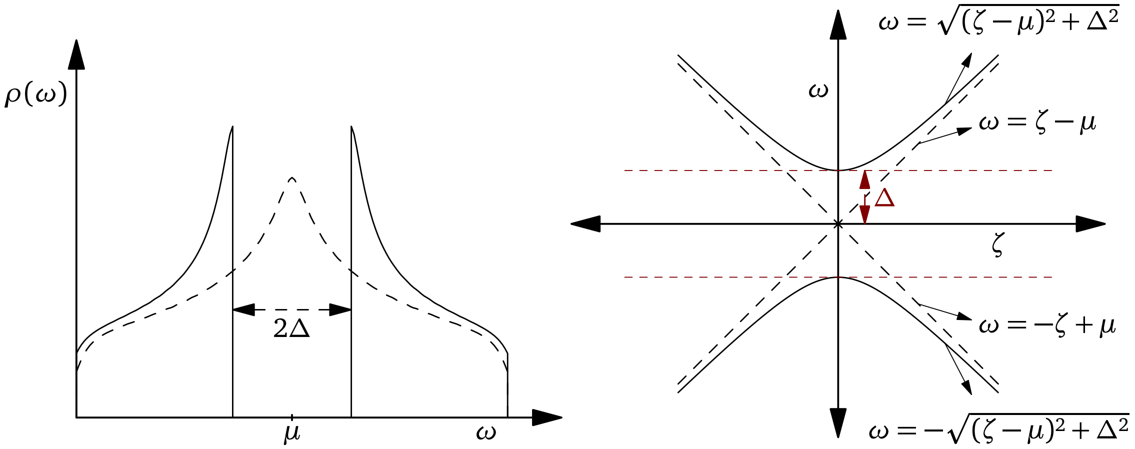

Figure 2.5: The BCS gap. *Left*: Density of states for the superconducting solution (solid line) along with that for the non-superconducting solution (dashed line) for the Hamiltonian Eq. (2.30) with $\zeta(\mathbf{k}) = -2t(\cos(k_x)+\cos(k_y))$, $t = 1$. The superconducting density of states shows a gap of magnitude 2Δ around the Fermi level. *Right*: Energy eigenvalues of the Hamiltonian Eq. (2.30) as a function of the dispersion ζ for the superconducting state (solid line) along with that for the non-superconducting state ($\Delta = 0$) (dashed line).

with

$$u_{\mathbf{k}} = \frac{1}{\sqrt{2}}\sqrt{1+\frac{\zeta(\mathbf{k})-\mu}{E_{\mathbf{k}}}}\,e^{-i\phi_{1\mathbf{k}}}\,, \tag{2.35}$$

$$v_{\mathbf{k}} = \frac{1}{\sqrt{2}}\sqrt{1-\frac{\zeta(\mathbf{k})-\mu}{E_{\mathbf{k}}}}\,e^{-i\phi_{2\mathbf{k}}}\,. \tag{2.36}$$

Note that $|u_{\mathbf{k}}|^2+|v_{\mathbf{k}}|^2 = 1$, so that the transformation is unitary and the new set of operators satisfy the usual fermionic anti-commutation relations and hence correspond to the new fermionic particles known as the Bogoliubov quasiparticles. The two peaks surrounding the superconducting gap in Fig. 2.5 correspond to the dispersion relation Eq. (2.33) which are the exact energies of the so called Bogoliubov quasiparticles; the peaks are known as the coherence peaks. In this basis, the ground state of the Hamiltonian Eq. (2.30), let's call it $|\mathrm{BCS}\rangle$, is the vacuum

$$b_{\mathbf{k}\sigma}|\mathrm{BCS}\rangle = 0\,. \tag{2.37}$$

On inspection, one can write the ground state at zero temperature as

$$|\mathrm{BCS}\rangle = \prod_{\mathbf{k}} \left(1 + \frac{v_{\mathbf{k}}}{u^*_{\mathbf{k}}} c^\dagger_{-\mathbf{k}\downarrow} c^\dagger_{\mathbf{k}\uparrow} \right) |0\rangle \ . \tag{2.38}$$

The ground state $|\mathrm{BCS}\rangle$ is a linear combination of states with different number of Cooper pairs, hence does not contain a definite number of particles.

Note that the equation for the gap Δ (Eq. (2.31)) is a self-consistent equation; the Hamiltonian Eq. (2.30) depends on Δ, which in turn depends on the Hamiltonian through $\langle c_{-\mathbf{k}\downarrow} c_{\mathbf{k}\uparrow} \rangle$. Using the inverse Bogoliubov-Valentin transformation to compute $\langle c_{-\mathbf{k}\downarrow} c_{\mathbf{k}\uparrow} \rangle$ in Eq. (2.31), one can express the gap Δ as

$$\Delta = \frac{1}{2} \Delta \frac{V_{\mathrm{eff}}}{N} \sum_{\mathbf{k}} \frac{1 - 2n_F(E_{\mathbf{k}})}{E_{\mathbf{k}}} \ , \tag{2.39}$$

where $E_{\mathbf{k}}$ depends explicitly on Δ. This is known as the *BCS gap equation*. Here $n_F(E) = 1/(e^{\beta E} + 1)$ is the Fermi-Dirac distribution function with $\beta = 1/k_B T$. Eq. (2.39) can be further simplified as[16]

$$1 = \frac{V_{\mathrm{eff}}}{2N} \sum_k \frac{\tanh(E_k/2k_B T)}{E_k} \tag{2.40}$$

$$\Rightarrow 1 = \frac{V_{\mathrm{eff}}}{2} \int d^3k \frac{\tanh(E_k/2k_B T)}{E_k} \tag{2.41}$$

$$\Rightarrow 1 = \frac{V_{\mathrm{eff}}}{2} \int d\epsilon \, N(\epsilon) \frac{\tanh(E/2k_B T)}{E} \ , \tag{2.42}$$

where we have converted the sum over momentum $\mathbf{k}$ to an integral over the energy ϵ, with $E = \sqrt{\epsilon^2 + \Delta^2}$ and $N(\epsilon)$ being the density of states. Taking $N(\epsilon)$ to be a constant with the value at the Fermi level $N(0)$ and doing the integral in Eq. (2.42) close to the Fermi level in the interval $-\hbar\omega_D \leq \epsilon \leq \hbar\omega_D$, in the limit $\Delta \to 0$ (i.e. $T \to T_c$), we obtain the BCS equation for the critical temperature T_c

---

[16] $1 - 2n_F(E) = (e^{\beta E} - 1)/(e^{\beta E} + 1) = \tanh(\beta E/2)$.
$\sum_k = \frac{V}{(2\pi)^3} \int d^3k = N \int d^3k$, where V is the volume and N is the total number of momentum states.

$$\boxed{k_B T_c = 1.13\hbar\omega_D\, e^{-1/V_{\text{eff}}N(0)}}\,. \tag{2.43}$$

Similarly, doing the integral in Eq. (2.42) at $T = 0$ gives the the BCS gap at zero temperature

$$\boxed{2\Delta(0) = 3.56 k_B T_c}\,. \tag{2.44}$$

Thus, the gap at zero temperature gives the measure of the critical temperature T_c. Eq. (2.44) is observed to hold accurately for many conventional superconductors.

As we saw, the basic assumption of the BCS theory is to take a momentum independent attractive interaction within a shell around the Fermi level in order to mimic the retarded attractive interaction between electrons mediated by phonons. This is valid only when the coupling between electrons and phonons is weak. For instance, Eq. (2.44) is not valid when the coupling between electrons and phonons is strong. A complete treatment of the interaction mediated by phonons would include the phonon spectrum as well the electron-phonon coupling matrix. This is done in the Migdal-Eliashberg theory of superconductivity [146, 147] which is an extension of the BCS theory of superconductivity to systems with a strong electron-phonon coupling such as Pb and Nb.

The s-wave symmetry for conventional superconductors comes from the momentum independent attractive interaction which leads to a momentum independent gap. However for cuprate superconductors, the gap is highly anisotropic and has a d-wave symmetry. It is now known that the pairing in cuprate superconductors mainly comes from the strong Coulomb repulsion effects, specifically from antiferromagnetic fluctuations in a correlated insulator [88, 99–101]. This cannot be solved using a static mean-field approach[17], as implemented here, since a static mean-field theory cannot describe a correlated insulator to start with.

2.3.1 The superconducting order parameter

The superconducting phase is characterized by an order parameter which is defined as the expectation value of the operator $\hat{\Psi}$

$$\hat{\Psi} = \frac{1}{2N} \sum_{\mathbf{r},\mathbf{r}'} g_{\mathbf{r},\mathbf{r}'} \left[c_{\mathbf{r}\uparrow} c_{\mathbf{r}'\downarrow} - c_{\mathbf{r}\downarrow} c_{\mathbf{r}'\uparrow} \right] , \tag{2.45}$$

which creates a superposition of N Cooper pair states on the lattice. Here $g_{\mathbf{r},\mathbf{r}'}$ is the pairing amplitude and depends only on the relative position $\mathbf{r}-\mathbf{r}'$. Note that we restrict ourselves to spin-singlet superconductivity as seen for the case of BCS superconductors and that of cuprate superconductors. In momentum space, the operator $\hat{\Psi}$ can be written as

$$\hat{\Psi} = \frac{1}{2N} \sum_{\mathbf{k}} g_{\mathbf{k}} \left[c_{\mathbf{k}\uparrow} c_{-\mathbf{k}\downarrow} - c_{\mathbf{k}\downarrow} c_{-\mathbf{k}\uparrow} \right] \qquad g_{\mathbf{k}} = \sum_{\mathbf{r}} g_{\mathbf{r},0} e^{-i\mathbf{k}\cdot\mathbf{r}} \tag{2.46}$$

after Fourier transformation of the annihilation operators in Eq. (2.45). Note that the operator $\hat{\Psi}$ breaks the $U(1)$ gauge symmetry and hence does not conserve particle number. In the superconducting phase, we have a finite value of the anomalous Green function, also known as the Gorkov function, defined as

$$F_{\mathbf{r}\mathbf{r}'}(z) = \langle \Omega | c_{\mathbf{r}\uparrow} \frac{1}{z - H + E_0} c_{\mathbf{r}'\downarrow} | \Omega \rangle + \langle \Omega | c_{\mathbf{r}'\downarrow} \frac{1}{z + H - E_0} c_{\mathbf{r}\uparrow} | \Omega \rangle \ . \tag{2.47}$$

The Gorkov function is naturally integrated into the definition of Green function in the Nambu formalism. In the Nambu formalism, we define operators $d_{\mathbf{r}\sigma} = (c_{\mathbf{r}\uparrow}, c^{\dagger}_{\mathbf{r}\downarrow})$, where a particle-hole transformation is performed in the spin down sector. We work in the basis

---

[17] The term *static* signifies that the mean field parameter is a constant, as seen in Eq. (2.30).

$\{\{c_{\mathbf{r}\uparrow}\}, \{c^\dagger_{\mathbf{r}'\downarrow}\}\}$ with respect to which the Green function is expressed as a 2×2 block matrix

$$\mathbf{G}(z) = \begin{bmatrix} \mathbf{G}_\uparrow(z) & \mathbf{F}(z) \\ \mathbf{F}^\dagger(z) & -\mathbf{G}^*_\downarrow(-z^*) \end{bmatrix} , \tag{2.48}$$

where $\mathbf{G}_\uparrow(z)$ and $\mathbf{G}_\downarrow(z)$ are the Green function matrices corresponding to up spin and down spin sectors respectively. Similar to the derivation of Eq. (2.18) (see sec. A.5), we can obtain the average of the operator $\hat{\Psi}$ Eq. (2.45), $\langle\hat{\Psi}\rangle$, which is the definition of the superconducting order parameter, as

$$\langle\hat{\Psi}\rangle = -\frac{1}{N} \oint_{C_<} \frac{dz}{2\pi i} \operatorname{tr}\left[\mathbf{gF}\right] . \tag{2.49}$$

The pairing amplitude g can have a definite symmetry property. For conventional (BCS) superconductors, g has a s-wave symmetry, i.e., $g_{\mathbf{r},\mathbf{r}'}$ depends only on $|\mathbf{r}-\mathbf{r}'|$. For cuprate superconductors, g has a d-wave symmetry, i.e., it changes its sign under a rotation of 90^0: $g(\hat{\mathbf{x}}) = -g(\hat{\mathbf{y}})$.

Summary

In this chapter, we start by motivating the usage of Green function to study a macroscopic system. We define the Green function as the propagator, starting with an example of a single particle state, and then motivate the form of the Green function for an interacting many-particle system at zero temperature. We then discuss how to measure observables using the Green function and define the spectral function and the density of states. Next, we introduce the concept of self-energy and discuss its importance for various methods used to solve strongly interacting systems. We then discuss the Hubbard model, the one-band and the three-band models, and describe the physical picture they provide in the limit of a strong interaction, i.e. a Mott insulator within the one-band Hubbard model and a charge-transfer insulator within the three-band Hubbard model. Finally, we briefly discuss the BCS theory of superconductivity and introduce the definition of the superconducting order parameter.

Chapter 3

Methods

Superconductivity in the BCS theory originates from a metallic state at low temperature. As we saw in the last chapter, this can be explained in the framework of mean field theory. However, superconductivity in cuprates originates from a doped correlated insulator which cannot be explained in this way. Indeed, applying mean field theory on the Hubbard model, which is the simplest model that describes a correlated insulator, gives a frequency-independent self-energy and hence cannot describe a Mott insulator [1]. Hence, we need methods that incorporate the physics of strongly correlated systems. Numercial methods like exact diagonalization (ED) and quantum Monte Carlo (QMC) methods [90,105–110] have been used extensively in this direction, and provide exact solutions for small systems. ED is used mostly at zero temperature and has severe size limitations. QMC methods work at finite temperature; however they are limited by the fermion sign problem. Both of these methods cannot be extended to arbitrarily large systems[2]. Dynamical mean field theory (DMFT) [148] provides approximate solutions in the thermodynamic limit for the Hubbard model with moderate to strong Coulomb repulsion. It takes into account the correlation effects limited to a single site. This describes a Mott insulator, but does not explain superconductivity in a doped Mott insulator.

---

[1] Since the frequency dependence of the self-energy is essential to describe the spectral weight transfer between the upper and the lower Hubbard bands as seen in Fig. 2.3.

[2] There are some diagrammatic Monte Carlo methods that can be used in the thermodynamic limit [111, 112], however they describe only upto a finite order in the perturbation series.

Superconductivity in cuprates originates from the strong Coulomb repulsion between electrons, where a local s-wave pairing (as seen in BCS) is unfavorable and the Cooper-pair wavefunction is extended in space and has a d-wave symmetry. This amounts to pair formation between nearest neighbor sites in the lattice. Hence, we need to incorporate non-local interactions beyond a single site to be able to explain d-wave superconductivity in cuprates. Cluster extensions of DMFT such as Cluster dynamical mean field theory (CDMFT) [149–151] and the Dynamical cluster approximation (DCA) [152, 153], which take into account the non-local correlations within a small unit of the lattice (a cluster), have been used extensively to study superconductivity and various other phases in cuprates and other unconventional superconductors.

A practical way to incorporate the non-local correlation effects in a lattice is to solve the Hamiltonian exactly for a smaller system (a cluster), representative of the lattice, and then to somehow extend the solution to the thermodynamic limit. The methods used to solve the cluster problem are known as impurity solvers. Continuous-time quantum Monte Carlo [109, 154] (CTQMC) is one of the most commonly used impurity solvers at finite temperature. Exact diagonalization (ED) methods based on the Lanczos algorithm [26] are commonly used as impurity solvers at zero temperature. Then, the connection of the solution of the cluster problem to that of the infinite lattice is made by embedding the cluster within the infinite medium. The simplest embedding procedure is known as cluster perturbation theory (CPT), which we describe in details in section 3.1.3. The embedding procedure can also be optimized, i.e., we have a self-consistent bath connected to the cluster as in DMFT (single site is used instead of a cluster), CDMFT and DCA. In this work, we study superconductivity and charge-density waves in cuprates at zero temperature using cluster dynamical mean field theory (CDMFT) with exact diagonalization (ED) as the impurity solver.

In section 3.1, we discuss the general approach to express a model Hamiltonian and the Green function in forms that explicitly contain information regarding the way clusters are defined on a lattice. We also discuss the CPT approximation in this section, which provides the simplest solution to an interacting problem with a given definition of clusters on the lattice. In section 3.2, we discuss the ED method to obtain the ground state and the ground state energy of an interacting many-particle system. In section 3.3, we discuss the CDMFT with the detailed steps suited to be used with the ED impurity solver.

3.1 The cluster approach

Methods using clusters to solve interacting quantum systems are commonly known as quantum cluster methods [153]. In this section, we discuss the basic preliminaries behind all quantum cluster methods, along with cluster perturbation theory (CPT) which is the simplest of all of them.

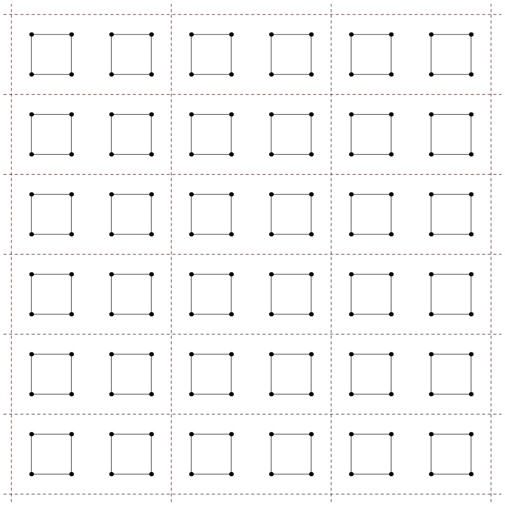

Figure 3.1: Tiling a lattice by clusters. The original square lattice $\mathscr{L}$ is tiled by 2 × 2 clusters. The super-cell, which becomes the repeated unit of the lattice, is marked by dashed lines and contains two 2 × 2 clusters.

3.1.1 Tiling the lattice by clusters

Let us take the lattice to be tiled by small units, known as clusters, which are disconnected from each other. The repeated unit of the lattice, which might contain one or more clusters, is known as the *super-cell*. For instance, Fig. 3.1 shows a lattice with a super-cell containing two identical 2 × 2 clusters. Note that the clusters within a super-cell may or may not be identical in shape.

Let us consider the case of the one-band Hubbard model Eq. (2.27), which we can express as $H = H_0 + H_1$, where H_0 is the non-interacting part of the Hamiltonian which includes all the hopping terms and H_1 includes the local Coulomb interactions at each site. We do not include the chemical potential term for now. In the cluster representation, the non-interacting part of the Hamiltonian H_0 can be written as

$$H_0 = H_0' + V \,, \tag{3.1}$$

where H_0' includes all hopping terms between sites belonging to the same cluster and V includes all hopping terms between sites belonging to different clusters. We can express H_0' as

$$H_0' = \sum_j \sum_{\alpha\alpha'} \left(t_c^{(j)}\right)_{\alpha\alpha'} c_\alpha^\dagger c_{\alpha'} = \sum_{\mu\neq\nu} t'_{\mu\nu} c_\mu^\dagger c_\nu \,, \tag{3.2}$$

where $\left(t_c^{(j)}\right)_{\alpha\alpha'}$ is an element of the matrix $\mathbf{t}_c^{(j)}$ which is the hopping matrix for hopping within the cluster j and $t'_{\mu\nu}$ is an element of the matrix $\mathbf{t}' = \bigoplus_j \mathbf{t}_c^{(j)}$ which is the hopping matrix containing only intra-cluster hopping amplitudes. We can express V as

$$V = \sum_{\alpha,\beta} (t_{\mathrm{ic}})_{\alpha\beta}\, c_\alpha^\dagger c_\beta \,, \tag{3.3}$$

where $(t_{\rm ic})_{\alpha\beta}$ is an element of the matrix $\mathbf{t}_{\rm ic}$ which is the hopping matrix containing hopping amplitudes between sites belonging to different clusters.

Since the interaction part includes only on-site Coulomb repulsion terms, it can be trivially written as

$$H_1 = \sum_j H_1^{(j)} \,, \tag{3.4}$$

where $H_1^{(j)}$ is the restriction of H_1 on the cluster j.

3.1.2 Green functions

The one-body Green function (2.8) for the lattice $\mathbf{G}_0$ can be written as[3]

$$\mathbf{G}_0 = \frac{1}{\omega - \mathbf{t}' - \mathbf{t}_{\rm ic}} \,, \tag{3.5}$$
$$\mathbf{G}_0 = \frac{1}{\mathbf{G}_0'^{-1} - \mathbf{t}_{\rm ic}} \,, \tag{3.6}$$

where $\mathbf{G}_0' = [\omega - \mathbf{t}']^{-1}$ is the one-body Green function restricted to the clusters. Note that the relation between $\mathbf{G}_0$ and $\mathbf{G}_0'$ Eq. (3.6) follows naturally by the definition of one-body Green functions.

The interacting Green function for the lattice can be written using the Dyson equation Eq. (2.24) as

$$\mathbf{G} = \frac{1}{\mathbf{G}_0^{-1} - \mathbf{\Sigma}} = \frac{1}{\omega - \mathbf{t}' - \mathbf{t}_{\rm ic} - \mathbf{\Sigma}(\omega)} \,, \tag{3.7}$$

---

[3] Bold faced symbols for Green functions indicate matrix representations.

where $\mathbf{\Sigma}$ is the self energy of the lattice and can be written in the cluster representation as

$$\mathbf{\Sigma}(\omega) = \mathbf{\Sigma}'(\omega) + \mathbf{\Sigma}^{\mathrm{ic}}(\omega)\,, \tag{3.8}$$

$$\mathbf{\Sigma}'(\omega) = \bigoplus_{j} \mathbf{\Sigma}_c^{(j)}(\omega)\,, \tag{3.9}$$

where $\mathbf{\Sigma}_c^{(j)}$ is the self-energy for the cluster j and $\mathbf{\Sigma}^{\mathrm{ic}}$ is the off-diagonal part of the self-energy (inter-cluster self-energy).

3.1.3 Cluster perturbation theory (CPT)

Note that no approximation has been made until now and all the expressions are exact. The cluster perturbation theory (CPT) [155,156] is the simplest scheme to extend the solution for a finite-size interacting system to a periodic lattice. The approximation in CPT is to neglect the off-diagonal self-energy between the clusters $\mathbf{\Sigma}^{\mathrm{ic}}$. As a result, the interacting Green function takes the form

$$\mathbf{G}_{\mathrm{cpt}} = \frac{1}{\omega - \mathbf{t}' - \mathbf{t}_{\mathrm{ic}} - \mathbf{\Sigma}'}\,, \tag{3.10}$$

$$\mathbf{G}_{\mathrm{cpt}} = \frac{1}{\mathbf{G}'^{-1} - \mathbf{t}_{\mathrm{ic}}}\,, \tag{3.11}$$

where $\mathbf{G}' = \left[\omega - \mathbf{t}' - \mathbf{\Sigma}'\right]^{-1}$ is the interacting Green function restricted to the clusters, which can also be expressed as

$$\mathbf{G}'^{-1} = \bigoplus_{j} \left[\mathbf{G}_c^{(j)}\right]^{-1}\,, \tag{3.12}$$

$$\mathbf{G}_c^{(j)} = \frac{1}{\omega - \mathbf{t}_c^{(j)} - \mathbf{\Sigma}_c^{(j)}}\,. \tag{3.13}$$

The approximation of neglecting the off-diagonal self-energy $\mathbf{\Sigma}^{\mathrm{ic}}$ can, in principle, be derived by treating V as a perturbation; at lowest order in V, the interacting Green function indeed becomes Eq. (3.11) [157]. CPT becomes exact in the $U \to \infty$ (strong coupling) limit. It is also exact in the $U \to 0$ limit, since the self-energy vanishes in this case. Although CPT takes into account the effects of strong interactions as well as of non-local interactions within the cluster, it does not describe broken symmetry states such as superconductivity, charge-density waves and so on. In CPT, one just has to solve exactly for the clusters within the super-cell, which can be done using an impurity solver. Then the CPT Green function for the lattice Eq. (3.11) can be obtained by using equations (3.12, 3.13); although this does not seem practical because we have a direct sum of infinite number of matrices in Eq. (3.12), this becomes very convenient when expressed as a partial Fourier transform as seen in the next section 3.1.4.

3.1.4 Reciprocal lattices and superlattices

As we saw, the super-cell is defined to be the repeated unit of the lattice which contains one or more clusters. The super-cell can be considered to be the unit cell of yet another lattice known as the super-lattice. Let us denote the set of points in the original lattice by $\mathscr{L}$ and the set of points in the super-lattice by $\mathscr{S}$. Then, clearly $\mathscr{S}$ is a subset of $\mathscr{L}$. The left panel of Fig. 3.2 shows the super-lattice $\mathscr{S}$ with sites at positions labelled by the vector $\tilde{\mathbf{r}}$. Each site of the super-lattice represents a super-cell containing two 2×2 clusters in the original lattice $\mathscr{L}$. The position of sites inside a super-cell can be measured with respect to the corresponding site in the super-lattice and is denoted by vector $\mathbf{R}$. Hence, the position of any site $\mathbf{r}$ in the original lattice can be expressed uniquely as $\mathbf{r} = \tilde{\mathbf{r}} + \mathbf{R}$.

Let us say the super-cell contains L sites, then the Brillouin zone of the original lattice $\mathrm{BZ}_{\mathscr{L}}$ contains L points belonging to the reciprocal space of the super-lattice and the Brillouin zone of the super-lattice $\mathrm{BZ}_{\mathscr{S}}$ has an area $1/L$ times the area of $\mathrm{BZ}_{\mathscr{L}}$. Any vector in $\mathrm{BZ}_{\mathscr{L}}$, $\mathbf{k}$ (conjugate to $\mathbf{r}$) can be uniquely written as $\mathbf{k} = \mathbf{K} + \tilde{\mathbf{k}}$, where $\tilde{\mathbf{k}}$ (conjugate to $\tilde{\mathbf{r}}$) is a

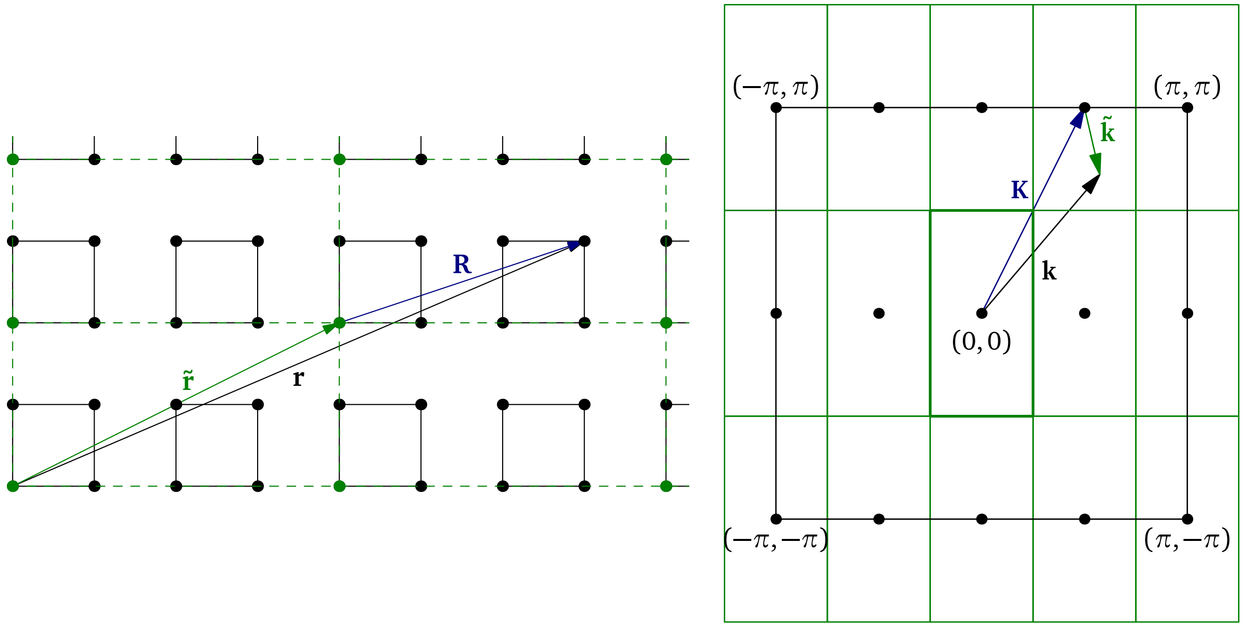

Figure 3.2: Relation between lattice and super-lattice vectors and the relation between the corresponding vectors in the reciprocal lattice and the reciprocal super-lattice. *Left*:The sites belonging to the super-lattice $\mathscr{S}$ are shown on the original lattice $\mathscr{L}$ in green. Each site of the super-lattice is associated with a super-cell (marked by dashed lines) containing two 2×2 clusters. A general lattice vector $\mathbf{r}$ is shown along with the corresponding super-lattice vector $\tilde{\mathbf{r}}$ and the position vector within the respective super-cell $\mathbf{R}$. *Right*: The Brillouin zone of the original lattice $\mathrm{BZ}_{\mathscr{L}}$ is shown along with the Brillouin zone (in green) of the super-lattice $\mathrm{BZ}_{\mathscr{S}}$. The area of the $\mathrm{BZ}_{\mathscr{S}}$ is $1/L$ times the area of $\mathrm{BZ}_{\mathscr{L}}$. A general wave vector $\mathbf{k}$ in $\mathrm{BZ}_{\mathscr{L}}$ is shown along with the associated vectors in the corresponding $\mathrm{BZ}_{\mathscr{S}}$ $\tilde{\mathbf{k}}$ and in the reciprocal space of the super-lattice $\mathbf{K}$.

vector in $\mathrm{BZ}_{\mathscr{S}}$ and $\mathbf{K}$ (conjugate to $\mathbf{R}$) is a vector in $\mathrm{BZ}_{\mathscr{L}}$ and in the reciprocal space of the superlattice (Fig. 3.2 (right)).

We can go back and forth between the real space and the reciprocal (momentum) space via Fourier transforms

$$f'(\mathbf{k}) = \sum_{\mathbf{r}} U^{\mathscr{L}}_{\mathbf{k},\mathbf{r}} f_{\mathbf{r}} \,, \qquad f'(\tilde{\mathbf{k}}) = \sum_{\tilde{\mathbf{r}}} U^{\mathscr{S}}_{\tilde{\mathbf{k}},\tilde{\mathbf{r}}} f_{\tilde{\mathbf{r}}} \,, \qquad f'_{\mathbf{K}} = \sum_{\mathbf{R}} U^{\mathrm{sc}}_{\mathbf{K},\mathbf{R}} f_{\mathbf{R}} \,, \tag{3.14}$$

$$f_{\mathbf{r}} = \sum_{\mathbf{k}} (U^{\mathscr{L}}_{\mathbf{k},\mathbf{r}})^* f'(\mathbf{k}) \,, \qquad f_{\tilde{\mathbf{r}}} = \sum_{\tilde{\mathbf{k}}} (U^{\mathscr{S}}_{\tilde{\mathbf{k}},\tilde{\mathbf{r}}})^* f'(\tilde{\mathbf{k}}) \,, \qquad f_{\mathbf{R}} = \sum_{\mathbf{K}} (U^{\mathrm{sc}}_{\mathbf{K},\mathbf{R}})^* f'_{\mathbf{K}} \,, \tag{3.15}$$

where f is a single-index quantity dependent on the position and f' is the Fourier transform of f. The unitary transformation matrices $\mathbf{U}^{\mathscr{L}}$, $\mathbf{U}^{\mathscr{S}}$, $\mathbf{U}^{\text{sc}}$ are given by

$$U^{\mathscr{L}}_{\mathbf{k},\mathbf{r}} = \frac{1}{\sqrt{N}} e^{-i\mathbf{k}\cdot\mathbf{r}},\;\; U^{\mathscr{S}}_{\tilde{\mathbf{k}},\tilde{\mathbf{r}}} = \sqrt{\frac{L}{N}} e^{-i\tilde{\mathbf{k}}\cdot\tilde{\mathbf{r}}},\;\; U^{\text{sc}}_{\mathbf{K},\mathbf{R}} = \frac{1}{\sqrt{L}} e^{-i\mathbf{K}\cdot\mathbf{R}}\,, \tag{3.16}$$

where N is the number of sites in the lattice $\mathscr{L}$. Note that although we want to describe an infinite lattice, we take the number of sites in the lattice to be denoted by N to be able to express the Fourier transformation matrices explicitly. Hence, $\mathbf{U}^{\mathscr{L}}$ is a $N \times N$ matrix, $\mathbf{U}^{\mathscr{S}}$ is a $N/L \times N/L$ matrix and $\mathbf{U}^{\text{sc}}$ is a $L \times L$ matrix. Note that applying the transformation matrix $\mathbf{U}^{\mathscr{L}}$ is not equivalent to applying both $\mathbf{U}^{\mathscr{S}}$ and $\mathbf{U}^{\text{sc}}$, i.e., $\mathbf{U}^{\mathscr{S}} \otimes \mathbf{U}^{\text{sc}} \neq \mathbf{U}^{\mathscr{L}}$. This can be seen by expanding $e^{-i\mathbf{k}\cdot\mathbf{r}}$ as

$$e^{-i\mathbf{k}\cdot\mathbf{r}} = e^{-i(\tilde{\mathbf{k}}+\mathbf{K})\cdot(\tilde{\mathbf{r}}+\mathbf{R})} = e^{-i\tilde{\mathbf{k}}\cdot\tilde{\mathbf{r}}} e^{-i\mathbf{K}\cdot\mathbf{R}} e^{-i\tilde{\mathbf{k}}\cdot\mathbf{R}} e^{-i\mathbf{K}\cdot\tilde{\mathbf{r}}}\,. \tag{3.17}$$

The last term $e^{-i\mathbf{K}\cdot\tilde{\mathbf{r}}} = 1$ because $\tilde{\mathbf{r}}$ and $\mathbf{K}$ belong to the direct and reciprocal spaces respectively of the super-lattice. Hence, $e^{-i\mathbf{k}\cdot\mathbf{r}}$ has an additional factor $e^{-i\tilde{\mathbf{k}}\mathbf{R}}$ other than $e^{-i\tilde{\mathbf{k}}\cdot\tilde{\mathbf{r}}} e^{-i\mathbf{K}\cdot\mathbf{R}}$.

The annihilation operator $c_{\mathbf{r}} = c_{\tilde{\mathbf{r}}+\mathbf{R}}$ can be represented in various forms using Eqs. (3.14,3.15):

$$c_{\mathbf{k}} = \sum_{\mathbf{r}} U^{\mathscr{L}}_{\mathbf{k},\mathbf{r}} c_{\mathbf{r}}\;\;,\;\; c_{\tilde{\mathbf{r}},\mathbf{K}} = \sum_{\mathbf{R}} U^{\text{sc}}_{\mathbf{K},\mathbf{R}} c_{\tilde{\mathbf{r}}+\mathbf{R}}\;\;,\;\; c_{\mathbf{R}}(\tilde{\mathbf{k}}) = \sum_{\tilde{\mathbf{r}}} U^{\mathscr{S}}_{\tilde{\mathbf{k}},\tilde{\mathbf{r}}} c_{\tilde{\mathbf{r}}+\mathbf{R}}\;\;,\;\; c_{\mathbf{K}}(\tilde{\mathbf{k}}) = \sum_{\tilde{\mathbf{r}},\mathbf{R}} U^{\mathscr{S}}_{\tilde{\mathbf{k}},\tilde{\mathbf{r}}} U^{\text{sc}}_{\mathbf{K},\mathbf{R}} c_{\tilde{\mathbf{r}}+\mathbf{R}}\,. \tag{3.18}$$

Similarly, various forms for the creation operator $c^{\dagger}_{\mathbf{r}} = c^{\dagger}_{\tilde{\mathbf{r}}+\mathbf{R}}$ can be written, which would be the adjoint of the equations Eq. (3.18). For a two-index quantity such as the hopping matrix $t_{\mathbf{r}\mathbf{r}'}$ or the Green function $G_{\mathbf{r}\mathbf{r}'}$, the first index $\mathbf{r}$ transforms like $c_{\mathbf{r}}$ and the second index $\mathbf{r}'$ transforms like $c^{\dagger}_{\mathbf{r}'}$, for example

$$t_{\mathbf{RR}'}(\tilde{\mathbf{k}},\tilde{\mathbf{k}}') = \sum_{\tilde{\mathbf{r}}\tilde{\mathbf{r}}'} U^{\mathscr{S}}_{\tilde{\mathbf{k}},\tilde{\mathbf{r}}} (U^{\mathscr{S}}_{\tilde{\mathbf{k}}',\tilde{\mathbf{r}}'})^{*} t_{\mathbf{rr}'} \,, \tag{3.19}$$

where $\mathbf{r} = \tilde{\mathbf{r}} + \mathbf{R}$ and $\mathbf{r}' = \tilde{\mathbf{r}}' + \mathbf{R}'$. However, in Eq. (3.19) $t_{\mathbf{RR}'}(\tilde{\mathbf{k}},\tilde{\mathbf{k}}') = 0$ when $\tilde{\mathbf{k}} \neq \tilde{\mathbf{k}}'$ since we have translational invariance on the super-lattice. Hence, we can rewrite Eq. (3.19) as

$$t_{\mathbf{RR}'}(\tilde{\mathbf{k}}) = \sum_{\tilde{\mathbf{r}}} e^{-i\tilde{\mathbf{k}}\cdot\tilde{\mathbf{r}}} t_{\mathbf{rr}'} \,, \tag{3.20}$$

where we have redefined $\tilde{\mathbf{r}} - \tilde{\mathbf{r}}'$ as $\tilde{\mathbf{r}}$ which amounts to fixing the origin at $\tilde{\mathbf{r}}'$; this leads to an additional factor N/L and the summation is just over $\tilde{\mathbf{r}}$.

The representation of quantities in the mixed basis $\big(\mathbf{R},\tilde{\mathbf{k}}\big)$ as shown for the hopping matrix in Eq. (3.20) is especially useful for practical purposes while dealing with clusters. In this representation, we can express quantities such as the hopping matrix, the Green function and the self-energy for the infinite lattice as small $dL \times dL$ matrices with a functional dependence on $\tilde{\mathbf{k}}$ ($d \rightarrow$ total number of spin and orbital degrees of freedom). For instance, the CPT Green function Eq. (3.10) can be written as

$$\boxed{\mathbf{G}^{-1}_{\mathrm{cpt}}(\tilde{\mathbf{k}},\omega) = [\mathbf{G}^{\mathrm{sc}}(\omega)]^{-1} - \mathbf{t}_{\mathrm{ic}}(\tilde{\mathbf{k}})} \,, \tag{3.21}$$

where $\mathbf{t}_{\mathrm{ic}}$ is the inter-cluster hopping matrix ($dL \times dL$) in the $(\mathbf{R},\tilde{\mathbf{k}})$ representation. The inter-cluster hopping matrix could be written in this form because of the translation invariance on the super-lattice. Further, $\mathbf{G}^{\mathrm{sc}}$ is the interacting Green function restricted to clusters within a super-cell:

$$[\mathbf{G}^{\mathrm{sc}}(\omega)]^{-1} = \bigoplus_{j}^{j\in\text{ super-cell}} [\mathbf{G}^{(j)}_{c}(\omega)]^{-1} \,, \tag{3.22}$$

where $\mathbf{G}_c^{(j)}$ is the interacting cluster Green function Eq. (3.13) for the jth cluster within the super-cell.

3.1.5 Periodization of the CPT Green function

The CPT Green function Eq. (3.21) is diagonal in $\tilde{\mathbf{k}}$ because of translational invariance on the super-lattice $\mathscr{S}$. However, $\mathbf{G}_{\text{cpt}}$ is not translationally invariant on the original lattice $\mathscr{L}$, i.e., $G_{\text{cpt}}(\mathbf{k},\mathbf{k}') \neq 0$ for $\mathbf{k} \neq \mathbf{k}'$. This can be seen from the following transformation of the CPT Green function:

$$G(\mathbf{k},\mathbf{k}',\omega) = G_{\mathbf{K}\mathbf{K}'}(\tilde{\mathbf{k}},\omega) = \frac{1}{L}\sum_{\mathbf{R}}\sum_{\mathbf{R}'} e^{-i(\mathbf{K}\cdot\mathbf{R}-\mathbf{K}'\cdot\mathbf{R}')}G_{\mathbf{R}\mathbf{R}'}(\tilde{\mathbf{k}},\omega)\,, \tag{3.23}$$

which suggests that the CPT Green function is diagonal in $\tilde{\mathbf{k}}$ but has off-diagonal terms with respect to $\mathbf{K}$, $\mathbf{K}'$, hence it also has off-diagonal terms with respect to $\mathbf{k}$, $\mathbf{k}'$. This happens because the hopping terms within the clusters and those in between the clusters are treated separately.

One way to obtain a fully translationally invariant Green function is to periodize the Green function Eq. (3.21) as follows [156]:

$$G_{\text{periodized}}(\mathbf{k},\omega) = \frac{1}{L}\sum_{\mathbf{R},\mathbf{R}'} e^{-i\mathbf{k}\cdot(\mathbf{R}-\mathbf{R}')}G_{\mathbf{R}\mathbf{R}'}(\tilde{\mathbf{k}},\omega)\,. \tag{3.24}$$

This amounts to including only the diagonal part, i.e., $\mathbf{K}=\mathbf{K}'$ (or $\mathbf{k}=\mathbf{k}'$) terms in $G_{\mathbf{K}\mathbf{K}'}(\tilde{\mathbf{k}})$, and neglecting the off-diagonal part. Periodization is required to obtain a translationally invariant lattice Green function. Although periodization provides only an approximation to $G(\mathbf{k},\omega)$, it is often useful to compare with ARPES experiments. This periodization scheme is known as the Green function periodization [157]. There are various other periodization schemes [48,158,159] that can also be used.

However, observables can be computed directly using the unperiodized CPT Green function $\mathbf{G}_{\text{cpt}}(\tilde{\mathbf{k}}, \omega)$. To do this, the operators are expressed in the $(\mathbf{R}, \tilde{\mathbf{k}})$ representation and Eq. (2.18) becomes

$$\langle O \rangle = \frac{1}{N} \sum_{\tilde{\mathbf{k}}} \oint_{C_<} \frac{dz}{2\pi i} \mathrm{tr}\left[\mathbf{s}(\tilde{\mathbf{k}}) \mathbf{G}_{\text{cpt}}(\tilde{\mathbf{k}}, z) \right] , \tag{3.25}$$

where $\mathbf{s}$ is a $dL \times dL$ matrix and is diagonal in $\tilde{\mathbf{k}}$ because of the translational invariance on the super-lattice.

3.2 Exact Diagonalization

Exact diagonalization is one of the most commonly used methods to solve a model Hamiltonian for a system of interacting particles on a finite-size lattice. However, it is limited to small-size systems since the order of the Hamiltonian matrix increases exponentially with the size of the lattice. In this work, we use exact diagonalization based on the Lanczos algorithm as the impurity solver, i.e., to obtain the ground states and the Green functions for the clusters within a super-cell, at zero temperature.

In the exact diagonalization method, the first step is to specify the basis for the many-body Hilbert space, with respect to which the Hamiltonian matrix would be represented. A general basis state can be written in terms of creation operators as

$$|n_{1\uparrow} n_{2\uparrow} \cdots n_{M\uparrow} n_{1\downarrow} n_{2\downarrow} \cdots n_{M\downarrow}\rangle = (c^\dagger_{1\uparrow})^{n_{1\uparrow}} (c^\dagger_{2\uparrow})^{n_{2\uparrow}} \cdots (c^\dagger_{M\uparrow})^{n_{M\uparrow}} (c^\dagger_{1\downarrow})^{n_{1\downarrow}} (c^\dagger_{2\downarrow})^{n_{2\downarrow}} \cdots (c^\dagger_{M\downarrow})^{n_{M\downarrow}} |0\rangle , \tag{3.26}$$

where the occupation number $n_{i\sigma}$ $(= 0$ or $1)$ is the number of electrons with spin σ at the orbital i, and there are a total of M orbitals in the impurity model which is to be solved. From Eq. (3.26), we can see that there are 2^{2M} states in the basis. Hence, the full Hamiltonian matrix would be of order 2^{2M}. However, if the spin of electrons or the number of electrons or both are conserved, the Hamiltonian becomes a block-diagonal matrix. Then exact diagonalization can be done on a particular subspace of the Hilbert space, for example, if the ground state can be predicted to have a given number of electrons of each spin ($N_\uparrow$, $N_\downarrow$), we can restrict ourselves to a subspace of dimension $d = d_\uparrow d_\downarrow$ with

$$d_\sigma = \frac{M!}{N_\sigma!(M-N_\sigma)!} \ .$$

For instance, for the half-filled case where the ground state has an equal number of up and down spin electrons ($N_\uparrow = N_\downarrow = M/2$), the order of the Hamiltonian matrix is $\left(M!/(M/2)!^2\right)^2$; for a 2 × 2 cluster ($M = 4$), this is 36, whereas the full Hamiltonian matrix is of order 256. Although using conserved quantities leads to a reduction in the dimension of the problem, it still increases exponentially with the system size. An optimal size of the system for implementing exact diagonalization would be around 12 orbitals, considering the multiple iterations needed for achieving self-consistency in CDMFT.

3.2.1 Lanczos algorithm for the ground state

The Lanczos method [26, 160] is used for calculating the extreme eigenvalues and eigenvectors of a Hermitian matrix. It is based on the idea that the Hamiltonian H can be represented as a tridiagonal matrix when projected onto a special subspace of the Hilbert space, known as the Krylov subspace. The Krylov subspace $\mathscr{K}$ is spanned by vectors produced by the repeated application of H on a vector $|\phi_0\rangle$:

$$\mathscr{K} = \text{span}\{|\phi_0\rangle, H|\phi_0\rangle, H^2|\phi_0\rangle, \cdots, H^K|\phi_0\rangle\} \ , \tag{3.27}$$

where $|\phi_0\rangle$ is randomly selected from the relevant subspace of the Hilbert space. It is essential for the algorithm that $|\phi_0\rangle$ has a finite overlap with the ground state. The Hamiltonian matrix has a tridiagonal representation when expressed in terms of an orthogonal basis for the Krylov subspace as shown below.

Starting with $|\phi_0\rangle$, we define a new vector $|\phi_1\rangle$ to be created by the application of H on $|\phi_0\rangle$ such that $|\phi_1\rangle$ is orthogonal to $|\phi_0\rangle$:

$$|\phi_1\rangle = H|\phi_0\rangle - \frac{\langle\phi_0|H|\phi_0\rangle}{\langle\phi_0|\phi_0\rangle}|\phi_0\rangle \, , \tag{3.28}$$

where the orthogonality is ensured by the subtraction of the projection of $H|\phi_0\rangle$ over $|\phi_0\rangle$. Similarly, we can define another vector $|\phi_2\rangle$ obtained by the application of H on $|\phi_1\rangle$ orthogonal to both $|\phi_0\rangle$ and $|\phi_1\rangle$:

$$|\phi_2\rangle = H|\phi_1\rangle - \frac{\langle\phi_1|H|\phi_1\rangle}{\langle\phi_1|\phi_1\rangle}|\phi_1\rangle - \frac{\langle\phi_1|\phi_1\rangle}{\langle\phi_0|\phi_0\rangle}|\phi_0\rangle \, . \tag{3.29}$$

We can generalize this by the following recursion relation:

$$|\phi_{n+1}\rangle = H|\phi_n\rangle - a_n|\phi_n\rangle - b_n^2|\phi_{n-1}\rangle \, , \tag{3.30}$$

where

$$a_n = \frac{\langle\phi_n|H|\phi_n\rangle}{\langle\phi_n|\phi_n\rangle} \, , \quad b_n^2 = \frac{\langle\phi_n|\phi_n\rangle}{\langle\phi_{n-1}|\phi_{n-1}\rangle} \tag{3.31}$$

with $b_0 = 0$ and $|\phi_{-1}\rangle = 0$. Note from Eq. (3.30) that $H|\phi_n\rangle$ can be expressed in terms of only $|\phi_{n+1}\rangle$, $|\phi_n\rangle$ and $|\phi_{n-1}\rangle$; this leads to the tridiagonal form for the Hamiltonian matrix with respect to the basis $\{|\phi_n\rangle\}$. In terms of the normalized basis $\{|\overline{\phi}_n\rangle\}$ $\left(|\overline{\phi}_n\rangle = |\phi_n\rangle/\sqrt{\langle\phi_n|\phi_n\rangle}\right)$, the Hamiltonian matrix takes the form

$$\mathbf{H} = \begin{bmatrix} a_0 & b_1 & 0 & 0 & \cdots & 0 \\ b_1 & a_1 & b_2 & 0 & \cdots & 0 \\ 0 & b_2 & a_2 & b_3 & \cdots & 0 \\ \vdots & \vdots & \vdots & \vdots & \ddots & \vdots \\ 0 & 0 & 0 & 0 & \cdots & a_K \end{bmatrix} . \tag{3.32}$$

The Hamiltonian matrix in the tridiagonal form Eq. (3.32) can be easily diagonalized using fast algorithms specific for tridiagonal matrices. The lowest eigenvalue of the tridiagonal matrix Eq. (3.32), after it has converged (takes in the order of 100 iterations for 12 orbitals), is a very good approximation for the ground state energy of the Hamiltonian H[4]. Then, the ground state $|\Omega\rangle$ would be given by the eigenvector corresponding to the lowest eigenvalue. However, we would only have the ground state $|\Omega\rangle$ in terms of the basis $\{|\overline{\phi}_n\rangle\}$; this can be converted into the original basis with the knowledge of $\langle\phi_n|\Omega\rangle$ which can be extracted by running the Lanczos iterations again.

3.2.2 Lanczos algorithm for the Green function

The zero temperature Green function Eq. (2.13) can be obtained easily using the ground state $|\Omega\rangle$ with the Lanczos algorithm. For convenience, let us express the Green function Eq. (2.13) as

$$G_{\mu\nu}(z) = G^e_{\mu\nu}(z) + G^h_{\mu\nu}(z) \,, \tag{3.33}$$

$$G^e_{\mu\nu}(z) = \langle\Omega|c_\mu \frac{1}{(z+E_0)-H} c^\dagger_\nu|\Omega\rangle \,, \tag{3.34}$$

$$G^h_{\mu\nu}(z) = \langle\Omega|c^\dagger_\nu \frac{1}{(z-E_0)+H} c_\mu|\Omega\rangle \,, \tag{3.35}$$

---

[4] The Krylov subspace is a subspace of the Hilbert space, which grows with each iteration of the Lanczos procedure. Once it includes the ground state, the lowest eigenvalue does not change anymore with the Lanczos iterations, indicating that the lowest eigenvalue is indeed the ground state energy.

where z is the complex valued frequency. Let us first consider the case of $G^e_{\mu\mu}$

$$G^e_{\mu\mu} = \langle\phi_\mu|\frac{1}{z_e - H}|\phi_\mu\rangle \ , \tag{3.36}$$

where $|\phi_\mu\rangle = c^\dagger_\mu|\Omega\rangle$[5] and $z_e = z + E_0$. For obtaining $G^e_{\mu\mu}$, we would need to obtain the action of $\frac{1}{z_e - H}$ on $|\phi_\mu\rangle$. To do this, we first build a tridiagonal matrix representation of H in the Krylov subspace $\mathscr{K} = \text{span}\{|\phi_\mu\rangle, H|\phi_\mu\rangle, H^2|\phi_\mu\rangle, \cdots, H^K|\phi_\mu\rangle\}$. This is done by running the Lanczos iterations Eqs. (3.30, 3.31) starting with $|\phi_0\rangle = |\phi_\mu\rangle$. We stop when b_n takes a value close to zero and then represent H in terms of the normalized vectors, which then takes the tridiagonal form Eq. (3.32). Then we need to obtain the (0, 0) element of the matrix representation of $(z_e - H)^{-1}$ which would give us $G^e_{\mu\mu}/\langle\phi_\mu|\phi_\mu\rangle$.

The matrix representation of $(z_e - H)$, which we denote as $\mathbf{D}$, becomes

$$\mathbf{D} = \begin{bmatrix} z_e - a_0 & -b_1 & 0 & 0 & \cdots & 0 \\ -b_1 & z_e - a_1 & -b_2 & 0 & \cdots & 0 \\ 0 & -b_2 & z_e - a_2 & -b_3 & \cdots & 0 \\ \vdots & \vdots & \vdots & \vdots & \ddots & \vdots \\ 0 & 0 & 0 & 0 & \cdots & z_e - a_K \end{bmatrix} . \tag{3.37}$$

It is convenient to use the 2 × 2 block matrix form for $\mathbf{D}$

$$\mathbf{D} = \begin{bmatrix} z_e - a_0 & \mathbf{B}_1^T \\ \mathbf{B}_1 & \mathbf{D}_1 \end{bmatrix} , \tag{3.38}$$

where $\mathbf{B}_1$ is a $K \times 1$ column matrix which contains the first column of $\mathbf{D}$ (Eq. (3.37)) except the first term and $\mathbf{D}_1$ is the matrix obtained by excluding the first row and column of the matrix $\mathbf{D}$ (Eq. (3.37)). Then the (0, 0) element of the inverse of $\mathbf{D}$, which gives the Green function $G^e_{\mu\mu}$, can be expressed using Eq. (A.16) as

---

[5] We first obtain the ground state $|\Omega\rangle$ using the Lanczos procedure described in section 3.2.1.

$$\frac{G^e_{\mu\mu}}{\langle\phi_\mu|\phi_\mu\rangle} = (\mathbf{D}^{-1})_{00} = \frac{1}{z_e - a_0 - \mathbf{B}_1^T\mathbf{D}_1^{-1}\mathbf{B}_1} = \frac{1}{z_e - a_0 - b_1^2(\mathbf{D}_1^{-1})_{00}} \,. \tag{3.39}$$

Further, $\mathbf{D}_1$ can also be written as a 2 × 2 block matrix

$$\mathbf{D}_1 = \begin{bmatrix} z_e - a_1 & \mathbf{B}_2^T \\ \mathbf{B}_2 & \mathbf{D}_2 \end{bmatrix} , \tag{3.40}$$

and $(\mathbf{D}_1^{-1})_{00}$ can be written using Eq. (A.16) as

$$(\mathbf{D}_1^{-1})_{00} = \frac{1}{z_e - a_1 - \mathbf{B}_2^T\mathbf{D}_2^{-1}\mathbf{B}_2} = \frac{1}{z_e - a_1 - b_2^2(\mathbf{D}_2^{-1})_{00}} \,. \tag{3.41}$$

Using Eq. (3.41) in Eq. (3.39), we have

$$\frac{G^e_{\mu\mu}}{\langle\phi_\mu|\phi_\mu\rangle} = (\mathbf{D}^{-1})_{00} = \cfrac{1}{z_e - a_0 - \cfrac{b_1^2}{z_e - a_1 - b_2^2(\mathbf{D}_2^{-1})_{00}}} \,. \tag{3.42}$$

Going along this direction by successively inverting the matrices $\mathbf{D}_i$, we can express the Green function $G^e_{\mu\mu}$ as a continued fraction:

$$G^e_{\mu\mu}(z) = \cfrac{\langle\phi_\mu|\phi_\mu\rangle}{z_e - a_0 - \cfrac{b_1^2}{z_e - a_1 - \cfrac{b_2^2}{z_e - a_2 - \cdots}}} , \tag{3.43}$$

which terminates with $-b_K^2/(z_e - a_K)$. Hence, the Green function $G^e_{\mu\mu}$ can be obtained by evaluating the continued fraction.

Note that the above procedure works only for the diagonal elements of the Green function $G^e_{\mu\mu}$. For the case of $G^e_{\mu\nu}$, when $\mu \neq \nu$, we consider the following Green function:

$$G^{e+}_{\mu\nu}(z) = \langle\Omega|(c_\mu + c_\nu)\frac{1}{z_e - H}(c_\mu + c_\nu)^\dagger|\Omega\rangle \ . \tag{3.44}$$

Then, we have

$$G^e_{\mu\nu}(z) = \frac{1}{2}\left(G^{e+}_{\mu\nu}(z) - G^e_{\mu\mu}(z) - G^e_{\nu\nu}(z)\right) , \tag{3.45}$$

where we have used the symmetry $G^e_{\mu\nu} = G^e_{\nu\mu}$. We can compute $G^{e+}_{\mu\nu}$ in Eq. (3.45) in a similar way as we did for the case of $G^e_{\mu\mu}$.

For the case of $G^h_{\mu\mu}$, we can proceed similarly as in the case of $G^e_{\mu\mu}$ and we obtain

$$G^h_{\mu\mu}(z) = \cfrac{\langle\phi'_\mu|\phi'_\mu\rangle}{z_h + a_0 - \cfrac{b_1^2}{z_h + a_1 - \cfrac{b_2^2}{z_h + a_2 - \cdots}}} , \tag{3.46}$$

where $|\phi'_\mu\rangle = c_\mu|\Omega\rangle$, $z_h = z - E_0$ and the coefficients $\{a_n\}$ and $\{b_n\}$ are from the Lanczos iterations Eqs. (3.30, 3.31) starting with $|\phi_0\rangle = |\phi'_\mu\rangle$. $G^h_{\mu\nu}$, when $\mu \neq \nu$, is obtained by proceeding similarly as we did for $G^e_{\mu\nu}$.

The Green function here is expressed in terms of composite indices which include all degrees of freedom including the spin of electrons. However, in the basic Hubbard model, spin is conserved and hence the Green function for the up spin sector and the down spin sector is exactly same. Therefore we would need to compute the Green function just for the up (or down) spin sector.

An alternative approach for calculating Green functions is the *band Lanczos* method which directly gives the Lehmann representation for the Green function Eq. (2.14). It involves performing Lanczos iterations simultaneously with many states, and the matrix representation of the Hamiltonian in the Krylov subspace takes a band form (many diagonals around the central diagonal unlike just one in the case of a tridiagonal matrix). This requires more memory compared to the standard Lanczos method, however it is much faster than the latter. We do not discuss the details of the band Lanczos algorithm in this thesis; for more details one can take a look at the refs. [161, 162].

3.3 Cluster dynamical mean field theory (CDMFT)

Cluster dynamical mean field theory (CDMFT) [149, 163], also known as *Cellular dynamical mean field theory*, is the cluster extension of the Dynamical mean field theory (DMFT) formulated in real space. As discussed briefly in page 51, an efficient way to include the non-local correlation physics of a lattice, in our solutions, is to embed a small system (a cluster) in an effective medium, where we first solve the cluster and then extend the solution to the lattice through the embedding procedure. This embedding procedure can also be optimized for a higher accuracy; by demanding that two approximate solutions for the Green function must be consistent with each other, a procedure known as self consistency. DMFT is the simplest example of such a self-consistent embedding where the cluster contains just one correlated site. In DMFT, the single site is hybridized to a non-interacting bath (the effective medium), which forms the Anderson impurity model; this is solved self-consistently with respect to the parameters of the bath, by requiring that the solution of the Anderson impurity model is consistent with the solution obtained using the Dyson's equation (2.24) with the self-energy of the single site. Hence, DMFT assumes that the strong correlation effects are local (limited to a single site); this is exact in the limit of infinite dimensions where the self-energy is only dependent on frequency [164]. In finite dimensions, DMFT neglects the momentum dependence of the self-energy. However, it successfully describes the Mott insulator. Despite of this success, it turns out that

DMFT cannot describe superconductivity within the two dimensional Hubbard model because non-local correlations are essential for pairing in the Hubbard model. To tackle this problem, CDMFT involves a small collection of sites (instead of a single site), known as a cluster, connected to a non-interacting bath which is optimized self-consistently. The idea is to treat the degrees of freedom within the cluster exactly so that the non-local correlation effects within the cluster are taken into account, which are crucial for the d-wave superconductivity.

3.3.1 The impurity model

In CDMFT, each cluster within the super-cell is connected to a set of non-interacting bath orbitals to form a cluster-bath impurity model. The Hamiltonian for a general impurity model is given by

$$H_{\text{imp}} = \overbrace{-\sum_{i\neq j,\sigma} t_{c,ij} c^{\dagger}_{i\sigma} c_{j\sigma} + \sum_{i} U n_{i\uparrow} n_{i\downarrow}}^{H_{\text{cluster}}} + \overbrace{\sum_{m=1,\sigma}^{N_b} \epsilon_{m\sigma} a^{\dagger}_{m\sigma} a_{m\sigma}}^{H_{\text{bath}}} + \overbrace{\sum_{i,m,\sigma} \left(\theta_{im} c^{\dagger}_{i\sigma} a_{m\sigma} + \text{H.c.}\right)}^{H_{\text{hybridization}}}, \tag{3.47}$$

where $c^{\dagger}_{i\sigma}$ creates an electron with spin σ at the site labelled i in the cluster, $t_{c,ij}$ is the matrix element of the cluster hopping matrix $\mathbf{t}_c$, $n_{i\sigma}$ counts the electrons with spin σ at the site i, U is the on-site Coulomb repulsion energy in the cluster, $a^{\dagger}_{m\sigma}$ creates an electron with spin σ in the bath orbital m, θ_{im} is the hopping amplitude from the bath orbital m to the cluster site i, ϵ_m is the energy of the bath orbital m and N_b is the number of bath orbitals. To summarize the impurity model, it consists of a cluster coupled to a set of N_b non-interacting bath orbitals. Note that the bath orbitals have no hopping between them, which we can assume without a loss of generality; this is because we can always diagonalize the bath Hamiltonian by an unitary transformation.

In CDMFT, the Green function for the cluster contains the effect of the bath orbitals through a quantity known as the *bath hybridization* function $\mathbf{\Gamma}(\omega)$, which is obtained in a self-consistent manner. The bath hybridization function appears in the non-interacting cluster Green function as we show below. The non-interacting Green function for the impurity model is given by the 2 × 2 block matrix:

$$\mathbf{G}_0^{\text{imp}}(z) = \begin{bmatrix} z - \mathbf{t}_c & -\boldsymbol{\theta} \\ -\boldsymbol{\theta}^\dagger & z - \boldsymbol{\epsilon} \end{bmatrix}^{-1} , \tag{3.48}$$

where z is the complex frequency, $\mathbf{t}_c$ is the $M \times M$ ($M \rightarrow$ no. of orbitals in the cluster) hopping matrix for the cluster, $\boldsymbol{\theta}$ is the $M \times N_b$ hybridization matrix between the cluster and the bath, $\boldsymbol{\epsilon}$ is the $N_b \times N_b$ diagonal bath Hamiltonian matrix. The non-interacting cluster Green function $\mathbf{G}_{0c}$ is the $(0,0)$ block of $\mathbf{G}_0^{\text{imp}}$ (see Eq. (A.16) for the inverse of a 2 × 2 block matrix):

$$\mathbf{G}_{0c}(z) = \frac{1}{z - \mathbf{t}_c - \boldsymbol{\Gamma}(z)} \ , \ \boldsymbol{\Gamma}(z) = \boldsymbol{\theta} \frac{1}{z - \boldsymbol{\epsilon}} \boldsymbol{\theta}^\dagger \ , \tag{3.49}$$

where the contribution of the bath is included in the bath hybridization function $\boldsymbol{\Gamma}$, as we discussed earlier.

The interacting cluster Green function $\mathbf{G}_c$ is then given by

$$\mathbf{G}_c(z) = \frac{1}{z - \mathbf{t}_c - \boldsymbol{\Gamma}(z) - \boldsymbol{\Sigma}_c(z)} \ , \tag{3.50}$$

where $\boldsymbol{\Sigma}_c$ is the self-energy of the cluster. The methods used for obtaining the cluster Green function are commonly known as impurity solvers. In this work, we use exact diagonalization solvers, specifically Lanczos and band Lanczos methods for obtaining the cluster Green function at zero temperature. In exact diagonalization, we are limited by the number of bath orbitals that we can have. An optimal number of orbital degrees of freedom that we can have in the impurity model is around 12, so that the computation times are reasonable even with the many steps of the impurity solver required for the CDMFT self-consistency.

The term *Dynamical mean field* in CDMFT and DMFT comes from the path integral formulation of the impurity problem, where $\mathbf{G}_{0c}$ is introduced, without an a priori knowledge of the bath Hamiltonian, as the dynamical mean field which takes into account the non-interacting part of the cluster along with the effective hybridization of the cluster orbitals with the rest of the lattice (see section A.3).

3.3.2 Self-consistency

The goal is to optimize the bath hybridization function $\mathbf{\Gamma}(z)$ so that it corresponds as closely as possible to the actual environment of the cluster. This is done by a self-consistent procedure as we describe below.

In cluster approaches, the best approximation for the lattice Green function is the CPT Green function Eq. (3.21) which can be written as

$$\mathbf{G}(\tilde{\mathbf{k}}, z) = \frac{1}{z - \mathbf{t}(\tilde{\mathbf{k}}) - \mathbf{\Sigma}(z)}\,, \tag{3.51}$$

where $\mathbf{t}(\tilde{\mathbf{k}})$ is the full dispersion of the lattice expressed as a matrix with respect to the super-cell indices along with a dependence on $\tilde{\mathbf{k}}$ in the Brillouin zone of the super-lattice (i.e., in the $(\mathbf{R}, \tilde{\mathbf{k}})$ representation). The self-energy is a direct sum:

$$\mathbf{\Sigma}(z) = \bigoplus_{j}^{j \in \text{super-cell}} \mathbf{\Sigma}_c^{(j)}(z)\,, \tag{3.52}$$

where $\mathbf{\Sigma}_c^{(j)}$ is the self-energy of the jth cluster within the super-cell. It is obtained as

$$\mathbf{\Sigma}_c^{(j)}(z) = z - \mathbf{t}_c^{(j)} - \mathbf{\Gamma}^{(j)}(z) - \left[\mathbf{G}_c^{(j)}\right]^{-1}(z)\,, \tag{3.53}$$

where $\mathbf{t}_c^{(j)}$ is the hopping matrix for the jth cluster, $\mathbf{\Gamma}^{(j)}$ is the known bath hybridization function for the jth cluster and $\mathbf{G}_c^{(j)}$ is the Green function for the jth cluster obtained from the ED impurity solver.

Let us first consider the case where the super-cell contains just one cluster, for simplicity. In this case, the self-consistency condition is that the cluster Green function $\mathbf{G}_c(z)$ is equal to the projection of the lattice Green function (3.51) on the $\tilde{\mathbf{r}} = 0$ cluster, i.e.,

$$\mathbf{G}_c(z) = \bar{\mathbf{G}}(z) , \tag{3.54}$$

where

$$\bar{\mathbf{G}}(z) = \frac{L}{N} \sum_{\tilde{\mathbf{k}}} \mathbf{G}(\tilde{\mathbf{k}}, z) = \frac{L}{N} \sum_{\tilde{\mathbf{k}}} \left[z - \mathbf{t}(\tilde{\mathbf{k}}) - \mathbf{\Sigma}_c(z) \right]^{-1} . \tag{3.55}$$

An important approximation in the CDMFT self-consistency Eq. (3.54) is that the lattice Green function $\mathbf{G}(\tilde{\mathbf{k}}, z)$ neglects the inter-cluster self-energy, hence CDMFT does not include the non-local correlation effects beyond a cluster.

Furthermore, the self-consistency Eq. (3.54) cannot be implemented as such in the case where ED is used as the impurity solver; this is because the number of bath parameters in ED is finite. As a result, the self-consistency condition (3.54) cannot be satisfied exactly for all frequencies. Therefore, we use an approximate method for achieving self-consistency, which involves minimizing the distance d between $\mathbf{G}_c^{-1}$ and $\bar{\mathbf{G}}^{-1}$,

$$d(\boldsymbol{\theta}, \boldsymbol{\epsilon}) = \sum_n W(i\omega_n) \operatorname{tr} \left| \mathbf{G}_c^{-1}(i\omega_n) - \bar{\mathbf{G}}^{-1}(i\omega_n) \right|^2 , \tag{3.56}$$

with respect to the bath parameters $\boldsymbol{\theta}$ and $\boldsymbol{\epsilon}$. Here $\omega_n = (2n+1)\pi/\beta$ with n being an integer, is the fermionic Matsubara frequency associated with a fictious temperature $T = 1/\beta$ and $W(z)$ is the weight of the contribution to the distance d from the frequency z. Note that we use the ED impurity solver strictly at zero temperature and the fictious temperature $T = 1/\beta$ plays the role of temperature just for sampling the frequency points in the imaginary axis. We choose the weight function

$$W(i\omega_n) = \begin{cases} 1 & 0 \leq \omega_n \leq \omega_c \\ 0 & \text{otherwise} \end{cases} \tag{3.57}$$

in the distance function Eq. (3.56) following the analysis in ref. [165]. The exact values of β and ω_c are specific to the model and are mentioned in sections 4.7, 5.5 for the respective computations.

Now, let us consider the case where we have more than one cluster in the super-cell. This situation arises when the desired super-cell contains more orbitals (along with an adequate number of bath orbitals) than what we can handle with the impurity solver; we then divide the super-cell into more than one identical or non-identical clusters. The choice of the super-cell (and clusters within it) is made so as to accommodate a specific density-wave that we want to probe. In this case, we can write Eq. (3.51) explicitly as a $n \times n$ block matrix (for n clusters within the super-cell):

$$G(\tilde{\mathbf{k}}, z) = \begin{bmatrix} z - \mathbf{t}^{(11)}(\tilde{\mathbf{k}}) - \boldsymbol{\Sigma}_c^{(1)}(z) & -\mathbf{t}^{(12)}(\tilde{\mathbf{k}}) & \cdots & -\mathbf{t}^{(1n)}(\tilde{\mathbf{k}}) \\ -\mathbf{t}^{(21)}(\tilde{\mathbf{k}}) & z - \mathbf{t}^{(22)}(\tilde{\mathbf{k}}) - \boldsymbol{\Sigma}_c^{(2)}(z) & \cdots & -\mathbf{t}^{(2n)}(\tilde{\mathbf{k}}) \\ \vdots & \vdots & \ddots & \vdots \\ -\mathbf{t}^{(n1)}(\tilde{\mathbf{k}}) & -\mathbf{t}^{(n2)}(\tilde{\mathbf{k}}) & \cdots & z - \mathbf{t}^{(nn)}(\tilde{\mathbf{k}}) - \boldsymbol{\Sigma}_c^{(n)}(z) \end{bmatrix}^{-1}, \tag{3.58}$$

where $\mathbf{t}^{(ii)}(\tilde{\mathbf{k}})$ is the projection of the full hopping matrix $\mathbf{t}(\tilde{\mathbf{k}})$ on the ith cluster, $\mathbf{t}^{(ij)}$ for $i \neq j$ is intercluster hopping matrix between the ith and the jth cluster and $\boldsymbol{\Sigma}_c^{(j)}$ is the self-energy of the jth cluster which is obtained as in Eq. (3.53). Then, the projection of $\mathbf{G}(\tilde{\mathbf{k}}, z)$ on the super-cell at the origin ($\tilde{\mathbf{r}} = 0$), $\bar{\mathbf{G}}(z) = \sum_{\tilde{\mathbf{k}}} \mathbf{G}(\tilde{\mathbf{k}}, z)$. The distance function now takes the following form:

$$d(\boldsymbol{\theta}^{(1)},\cdots,\boldsymbol{\theta}^{(n)},\boldsymbol{\epsilon}^{(1)},\cdots,\boldsymbol{\epsilon}^{(n)})=\sum_{n,j}W(i\omega_n)\,\mathrm{tr}\left|\left[\mathbf{G}_c^{(j)}\right]^{-1}(i\omega_n)-\left[\bar{\mathbf{G}}^{-1}\right]^{(jj)}(i\omega_n)\right|^2\,, \tag{3.59}$$

where $\boldsymbol{\theta}^{(i)}$ is the hybridization matrix between the ith cluster and the bath corresponding to it, $\boldsymbol{\epsilon}^{(i)}$ is the Hamiltonian matrix for the bath corresponding to the ith cluster, $\left[\mathbf{G}_c^{(i)}\right]^{-1}=z-\mathbf{t}_c^{(i)}-\boldsymbol{\Sigma}_c^{(i)}-\boldsymbol{\Gamma}^{(i)}$ is the inverse of the Green function for the ith cluster and $\left[\bar{\mathbf{G}}^{-1}\right]^{(ii)}$ is the projection of the matrix $\bar{\mathbf{G}}^{-1}$ on the ith cluster within the super-cell. The distance function Eq. (3.59) is to be minimized with respect to all the $\boldsymbol{\theta}^{(i)}$'s and $\boldsymbol{\epsilon}^{(i)}$'s.

We summarize the CDMFT procedure for a general case, with n clusters within the super-cell, below:

1. We start with trial values for the bath parameters $\boldsymbol{\theta}^{(i)}$, $\boldsymbol{\epsilon}^{(i)}$ and then we obtain the bath hybridization function $\boldsymbol{\Gamma}^{(i)}=\boldsymbol{\theta}^{(i)}[z-\boldsymbol{\epsilon}^{(i)}]^{-1}(\boldsymbol{\theta}^{(i)})^{\dagger}$ for each cluster i within the super-cell.

2. We use the ED impurity solver for the cluster-bath impurity models to obtain the Green function $\mathbf{G}_c^{(i)}$ for each cluster i. The self-energy for the ith cluster $\boldsymbol{\Sigma}_c^{(i)}$ is then obtained using Eq. (3.53).

3. We obtain the CPT Green function Eq. (3.51); here we use the self-energy $\boldsymbol{\Sigma}$ which is the direct sum Eq. (3.52) of the cluster self-energies obtained in step 2. We then obtain the projection of the CPT Green function on the $\tilde{\mathbf{r}}=0$ super-cell $\bar{\mathbf{G}}$.

4. We minimize the distance function Eq. (3.59) and obtain a new set of bath parameters $(\boldsymbol{\theta}^{(i)},\boldsymbol{\epsilon}^{(i)})$ for each cluster i. This gives us a new set of bath hybridization functions $\{\boldsymbol{\Gamma}^{(i)}\}$.

5. We go back to step 2 and repeat the steps until all bath hybridization functions $\boldsymbol{\Gamma}^{(i)}$ converge.

Let us now summarize the similarities and differences between CDMFT and CPT for clarity. The inter-cluster self-energy is neglected in CDMFT as is also the case for CPT, since CDMFT uses CPT to obtain the lattice Green function in each step of the self-consistency. However, CDMFT provides a much better approximation for the self-energy of the cluster which is achieved through the self-consistency procedure. Though, CPT can still describe a correlated insulator. But CPT cannot capture the spontaneous symmetry breaking leading to a broken symmetric phase like superconductivity or density-wave orders. CDMFT incorporates this through the bath in the impurity model, as discussed in sections 3.3.3, 4.7, 5.5.

3.3.3 Bath hybridization for the case of a superconducting solution

In CDMFT, a broken symmetry state originates in the bath of the impurity model. In the superconducting phase, the $U(1)$ gauge symmetry is broken. As a result the particle number is not conserved in the system. This is incorporated in CDMFT by including additional anomalous hybridization terms in the cluster-bath impurity model Eq. (3.47)

$$H_{\text{imp}} = H_{\text{cluster}} + \sum_{i=1,\sigma}^{N_b} \epsilon_{i\sigma} a_{i\sigma}^{\dagger} a_{i\sigma} + \sum_{p,i,\sigma} \left(\theta_{pi} c_{p\sigma}^{\dagger} a_{i\sigma} + \text{H.c.} \right) + \sum_{p,i} \left[\Delta_{ip} \left(c_{p\uparrow} a_{i\downarrow} - c_{p\downarrow} a_{i\uparrow} \right) + \text{H.c.} \right] , \tag{3.60}$$

where H_{cluster} is the Hamiltonian for the cluster (defined in Eq. (3.47)) and Δ_{ip} is the pairing amplitude for a singlet formed between site p in the cluster and bath orbital i. The bath hybridization function $\mathbf{\Gamma}$ in this case is modified to include the pairing terms as we show below.

The non-interacting part of the full impurity Hamiltonian can be conveniently represented as a matrix in the Nambu formalism, i.e., in the basis $\{C_{\uparrow}, C_{\downarrow}^{\dagger}, A_{\uparrow}, A_{\downarrow}^{\dagger}\}$, where

$C_\sigma = (c_{1\sigma}, \cdots, c_{M\sigma})$ and $A_\sigma = (a_{1\sigma}, \cdots, a_{N_b\sigma})$

$$H_0^{\text{imp}} = \begin{pmatrix} C_\uparrow^\dagger & C_\downarrow & A_\uparrow^\dagger & A_\downarrow \end{pmatrix} \begin{pmatrix} \mathbf{T} & \mathbf{\Theta} \\ \mathbf{\Theta}^\dagger & \mathbf{E} \end{pmatrix} \begin{pmatrix} C_\uparrow \\ C_\downarrow^\dagger \\ A_\uparrow \\ A_\downarrow^\dagger \end{pmatrix} , \tag{3.61}$$

where

$$\mathbf{T} = \begin{pmatrix} \mathbf{t}_c & \mathbf{0} \\ \mathbf{0} & -\mathbf{t}_c \end{pmatrix}, \mathbf{\Theta} = \begin{pmatrix} \boldsymbol{\theta} & -\mathbf{\Delta}^\dagger \\ -\mathbf{\Delta}^T & -\boldsymbol{\theta}^* \end{pmatrix}, \mathbf{E} = \begin{pmatrix} \boldsymbol{\epsilon} & \mathbf{0} \\ \mathbf{0} & -\boldsymbol{\epsilon} \end{pmatrix} , \tag{3.62}$$

$\mathbf{t}_c$ is the $M \times M$ hopping matrix on the cluster, $\boldsymbol{\theta}$ is the $M \times N_b$ cluster-bath hybridization matrix, $\mathbf{\Delta}$ is the $N_b \times M$ anomalous hybridization matrix between the cluster and the bath, and $\boldsymbol{\epsilon}$ is the $N_b \times N_b$ diagonal bath matrix. Hence, the non-interacting Green function for the impurity model $\mathbf{G}_0^{\text{imp}}$ in the Nambu basis becomes

$$\mathbf{G}_0^{\text{imp}} = \begin{bmatrix} z - \mathbf{T} & -\mathbf{\Theta} \\ -\mathbf{\Theta}^\dagger & z - \mathbf{E} \end{bmatrix}^{-1} . \tag{3.63}$$

The non-interacting cluster Green function $\mathbf{G}_{0c}$ is then obtained as the $(0,0)$ block of $\mathbf{G}_0^{\text{imp}}$ (see Eq. (A.16) for the $(0,0)$ block of the inverse of a 2×2 block matrix)

$$\mathbf{G}_{0c} = \frac{1}{z - \mathbf{T} - \mathbf{\Gamma}(z)} \ , \ \ \mathbf{\Gamma} = \mathbf{\Theta} \, (z - \mathbf{E})^{-1} \, \mathbf{\Theta}^\dagger \, . \tag{3.64}$$

The exact forms of $\boldsymbol{\theta}$ and $\mathbf{\Delta}$ are specific to the cluster-bath impurity model. It is also possible to exploit the symmetries of the problem (i.e., the symmetry of the ground state which we want to probe) [89,166], to reduce the number of independent elements of matrices $\boldsymbol{\theta}$ and $\mathbf{\Delta}$, which in turn reduces the number of parameters with respect to which we have to minimize the distance function (3.59). This significantly reduces the computation times in most cases.

Summary

In this chapter, we start by motivating the use of cluster methods to probe superconductivity in correlated insulators. We introduce the approach taken in all cluster methods, i.e., to write the Hamiltonian explicitly as a sum of intra-cluster and inter-cluster terms. We do the same for the Green function and the self-energy. We then discuss the simplest of all cluster methods, the Cluster perturbation theory (CPT), which amounts to solve for the Green function of the lattice after neglecting the inter-cluster self-energy. We discuss the relation between the lattice and the superlattice vectors, and between the vectors belonging to the respective reciprocal lattices. We define various Fourier transformation relations between the direct and the reciprocal lattices, and show that doing partial Fourier transformations always leads to partially broken translational symmetry. Then we discuss the exact diagonalization method based on the Lanczos algorithm, to obtain the ground state and the ground state energy. Finally, we discuss the cluster dynamical mean field theory (CDMFT) formulated using an Anderson-like impurity model, i.e., with the impurity as a cluster rather than a single site. We define the bath hybridization function and describe the self-consistency procedure to optimize the bath, which involves multiple usages of CPT, both for a normal ground state and a superconducting ground state.

Chapter 4

Superconductivity in the three band Hubbard model

In this chapter, we study various aspects of the superconducting phase that arises on doping the charge-transfer insulator, within cluster dynamical mean field theory (CDMFT) with an exact diagonalization (ED) impurity solver at zero temperature. We perform calculations for various parameter-sets in the vicinity of two limiting cases. We study the onset of the pseudogap within the superconducting phase, and the factors controlling the superconducting strength in cuprates, within the three-band Hubbard model. We answer the questions that we ask in pages 13, 20. To summarize the main outcomes:

1. We observe the onset of the pseudogap within the superconducting phase, which appears as a first-order transition, below a certain critical value of hole doping.
2. We observe a correlation between the maximum value of the superconducting order parameter and the corresponding oxygen hole content, both of which are influenced by the charge-transfer gap.

3. We observe that the antiferromagnetic spin fluctuations are responsible for pairing in the context of the three-band Hubbard model, which explains the correlation between the maximum order parameter and the corresponding oxygen hole content.
4. We observe that the model parameters which correspond to more covalent bonding between Cu and O orbitals lead to a higher superconducting order parameter.

In section 4.1, we discuss the two parameter-sets for the three-band Hubbard model, which we take as starting points for our computations. In section 4.2, we present the results of our CDMFT computations on doping the CTI; here we observe a finite value of the d-wave superconducting order parameter. In section 4.3, we investigate the presence of a discontinuous transition in our CDMFT solutions within the superconducting phase. In section 4.4, we observe a correlation between the maximum value of the order parameter and the hole content on oxygen orbitals and try to understand this correlation by looking at the CTG. In section 4.5, we explore the question whether superconductivity is mediated by short-range antiferromagnetic fluctuations within the three-band Hubbard model. In section 4.6, we discuss the dependence of the order parameter and the CTG on the different parameters that we vary in our computations. In section 4.7, we discuss the exact cluster-bath impurity model that we use for our CDMFT computations. In section 4.8, we provide a brief perspective on our results.

4.1 Parameters of the model

We study the three-band Hubbard model (see section 2.2.3) with the following two sets of parameters, and variations around them:

$$\epsilon_p = 7.0, \quad \epsilon_d = 0, \quad t_{pd} = 1.5, \quad t_{pp} = 1.0, \quad t'_{pp} = 1\,, \tag{4.1}$$

$$\epsilon_p = 2.3, \quad \epsilon_d = 0, \quad t_{pd} = 2.1, \quad t_{pp} = 1.0, \quad t'_{pp} = 0.2\,, \tag{4.2}$$

where the parameters (described in Fig. 2.4) are expressed in units of $t_{pp} \approx 0.65eV$ [133]. Note that we measure the O $2p$ orbital energy ϵ_p with respect to the Cu $3d$ orbital energy ϵ_d $(= 0)$. The parameter-set Eq. (4.1) is taken from ref. [138], which has a large separation between the Cu and O orbital energies to avoid sign problems within a Quantum Monte-Carlo solver, and hence describes a toy model for cuprates with a very low mixing between Cu and O orbitals. The parameter-set Eq. (4.2), taken from the ref. [133], describes a more realistic model for cuprates where the lower Hubbard band (LHB) is mixed with the charge-transfer band (CTB). We refer to the parameter-set Eq. (4.1) as the ionic case, because of the large difference in energy ϵ_p $(\epsilon_d = 0)$ between the O and Cu orbitals, and to the parameter-set Eq. (4.2) as the covalent case because the small energy difference ϵ_p leads to a higher covalency.

4.2 Doping the charge-transfer insulator

As discussed in section 2.2.4, a charge-transfer insulator is realized within the three-band Hubbard model at a filling of 5 electrons per unit cell. Figure 4.1(a) shows the density in the unit cell as a function of the chemical potential μ; the plateau in the curve at $n = 5$ (5 electrons per unit cell) denotes the charge-transfer insulator. At this filling the Cu orbital is slightly more than half-filled and the oxygen orbitals are slightly less than fully filled (Fig. 4.1(b)). This is different from a Mott insulator, i.e., in the one-band Hubbard model, where all orbitals are exactly occuppied by one electron when the lattice is half-filled [88, 89]. This suggests that, in the three-band Hubbard model, despite of the large Coulomb interaction U on the Cu orbitals, the presence of the uncorrelated O orbitals lowers the effective interaction on the Cu orbitals leading to more than half-filled Cu orbitals in the insulating phase.

We obtain superconductivity on doping the charge-transfer insulator [120, 138]. We measure the strength of superconductivity by an order parameter, which is defined as the

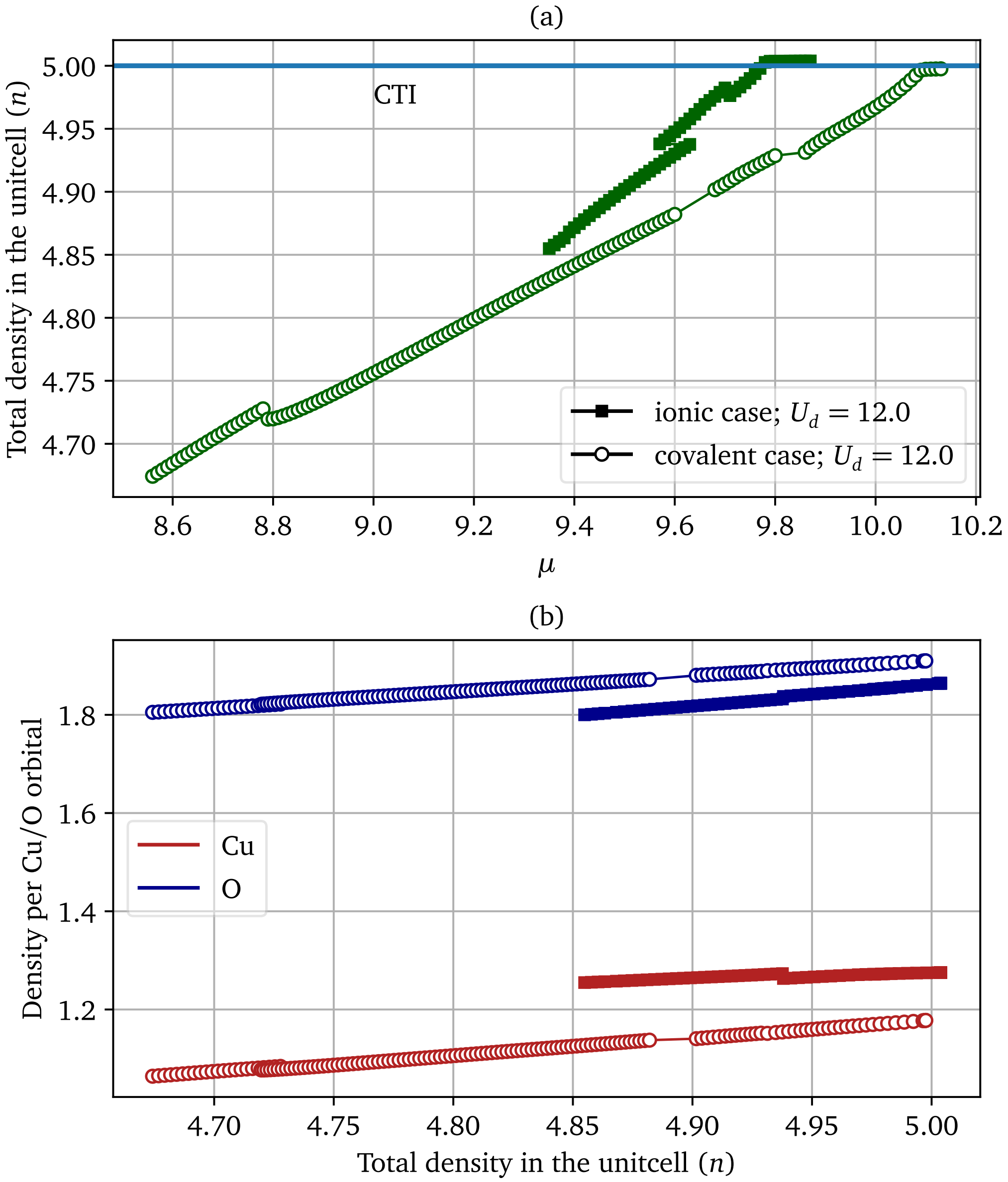

Figure 4.1: Variation of density. (a) Total density as a function of the chemical potential for the ionic Eq. (4.1) (filled symbols) and covalent Eq. (4.2) (open symbols) cases at $U_d = 12$. The plateau at $n = 5$ for both cases indicates the charge-transfer insulator (CTI). Note that the plateau for the ionic case is at a slightly higher electron density in the unit cell than the $n = 5$ line; this is due to a small numerical error in calculating the lattice average of the density Eq. (2.18). (b) Average density on the Cu (red) and O (blue) orbitals as a function of the total density n for the ionic Eq. (4.1) and covalent Eq. (4.2) cases at $U_d = 12$. Note that we have a charge-transfer insulator at an integer filling, $n = 5$, in the unit cell; however, the density on the Cu orbital is more than 1.0. This is due to the presence of the uncorrelated O orbitals, which decrease the effect of the Coulomb interaction felt on the Cu orbitals.

average of the d-wave pairing operator between nearest-neighbor Cu orbitals

$$\hat{\Psi} = \frac{1}{2}\left[\sum_{\langle ij\rangle_x}\left(d_{i\uparrow}d_{j\downarrow} - d_{i\downarrow}d_{j\uparrow}\right) - \sum_{\langle ij\rangle_y}\left(d_{i\uparrow}d_{j\downarrow} - d_{i\downarrow}d_{j\uparrow}\right) + \text{H.c.}\right], \tag{4.3}$$

where $d_{i\sigma}$ annihilates an electron in the Cu orbital located in the ith unit cell, and $\langle ij\rangle_{x(y)}$ denotes the sum over nearest neighbor unit cells along the $\hat{x}(\hat{y})$ direction. The order parameter $\langle\hat{\Psi}\rangle$ is then calculated using the Gorkov function (Eq. (2.49)) after the CDMFT iterations have converged (see sec. 3.3). Figures 4.2, 4.3 show the order parameter as a function of hole doping for various parameter-sets around the ionic case Eq. (4.1) and the covalent case Eq. (4.2) respectively for a few values of U_d.

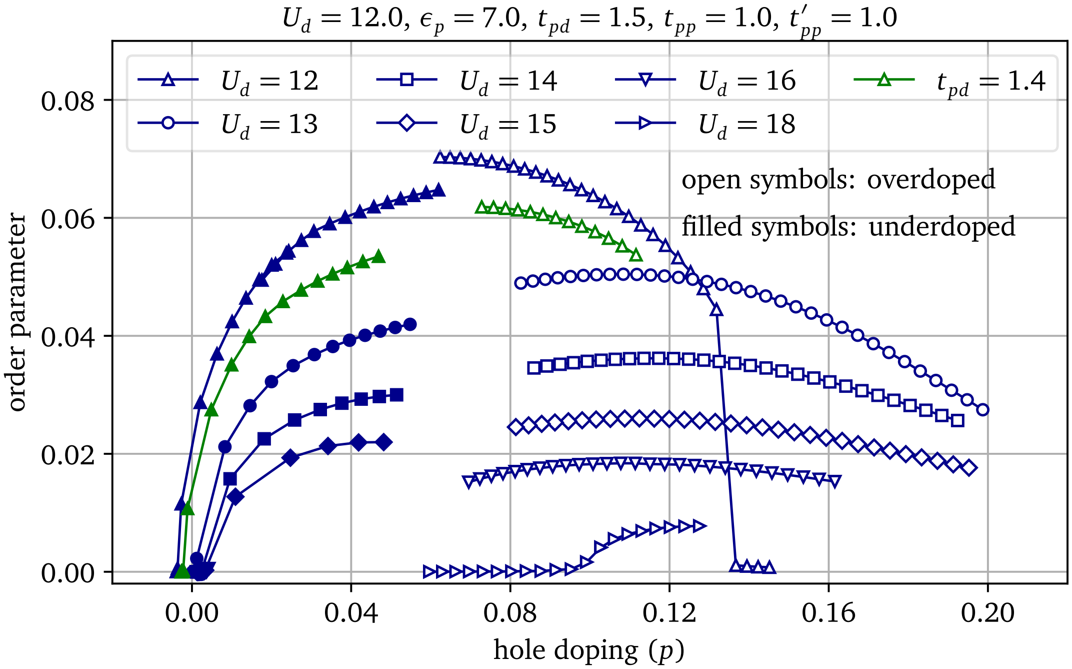

Figure 4.2: Order parameter as a function of the hole doping for various parameter-sets around the ionic case Eq. (4.1) with various values of U_d. The order parameter takes a dome-like structure as a function of hole doping as also seen for the case of the one-band Hubbard model [87, 89]; this is consistent with the fact that the superconducting critical temperature T_c, from experiments, takes the shape of a dome when plotted as a function of hole doping. However, we observe that each dome splits into two parts separated by a discontinuous transition; a hysteresis for the case of $U_d = 12$ suggests an underlying first order transition separating the underdoped (filled symbols) and the overdoped (open symbols) solutions.

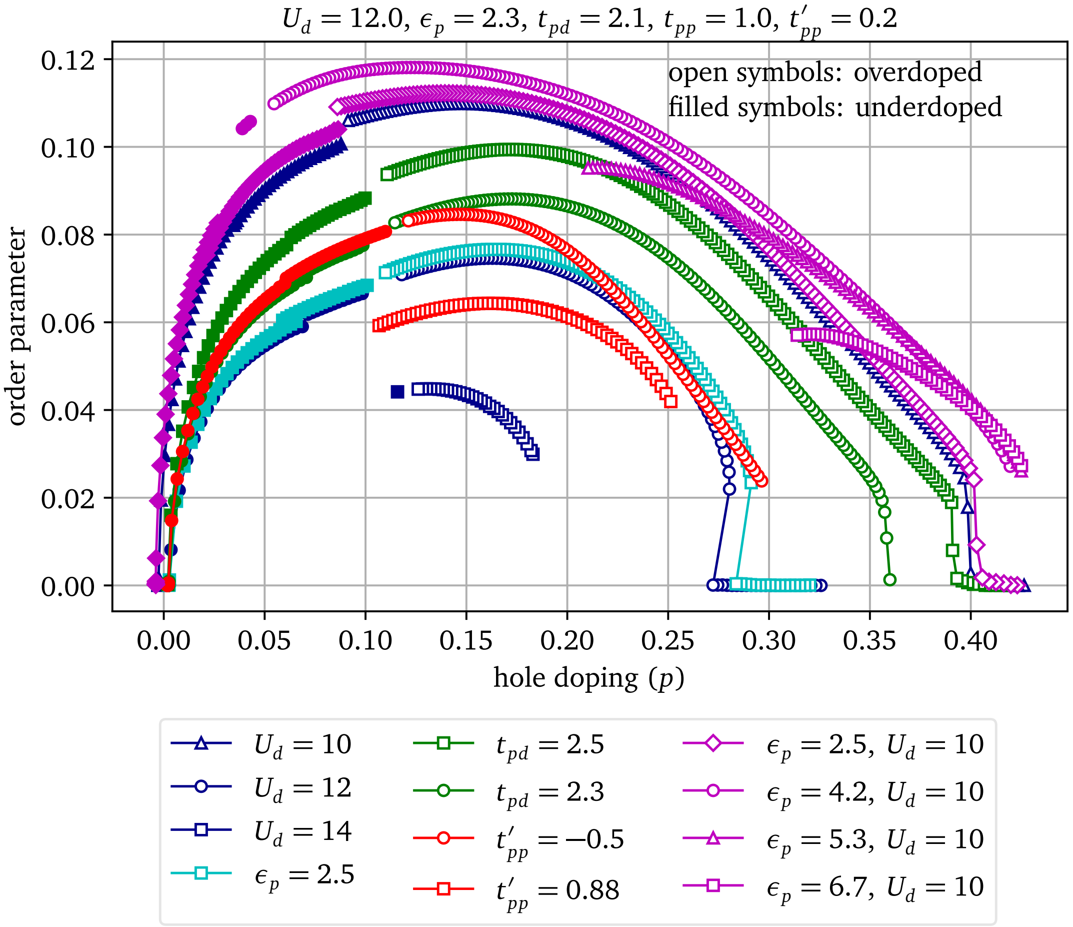

Figure 4.3: Order parameter as a function of the hole doping for various parameter-sets around the covalent case Eq. (4.2) with various values of U_d. We also observe a discontinuity in this case separating the order parameter domes into underdoped and overdoped solutions for most parameter-sets.

We obtain a finite order parameter as soon as we dope the charge-transfer insulator and the order parameter curve roughly takes the shape of a dome as also seen in previous CDMFT calculations [87–89, 138] similar to the critical temperature T_c as seen in experiments [167]. In real materials, superconductivity originates above a certain critical value of doping below which the antiferromagnetic order dominates the phase diagram (Fig. 1.3). This is also observed in CDMFT calculations within the one-band Hubbard model [89]. However, in the framework of our calculations, we use a parameterization of the bath which amounts to ignoring the possibility of antiferromagnetism (see section 4.7).

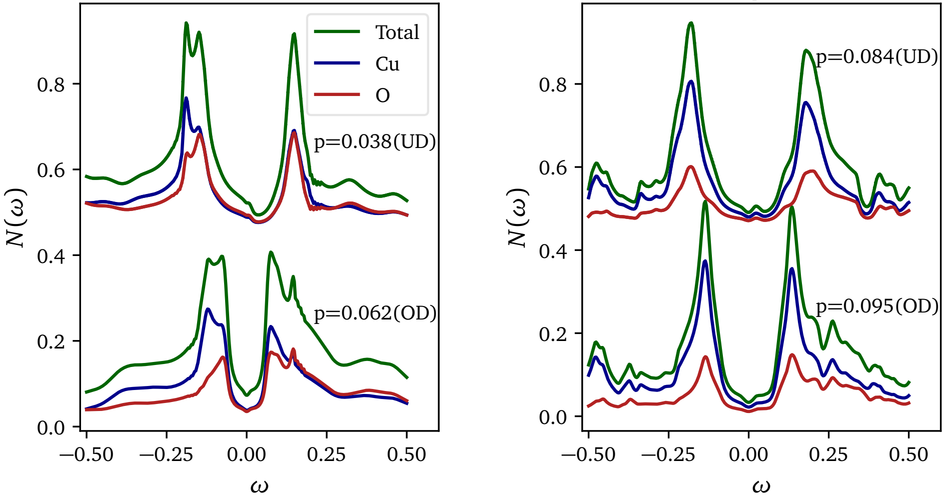
(a) ionic; $U_d = 12$

(b) covalent; $\epsilon_p = 2.5$, $U_d = 10$

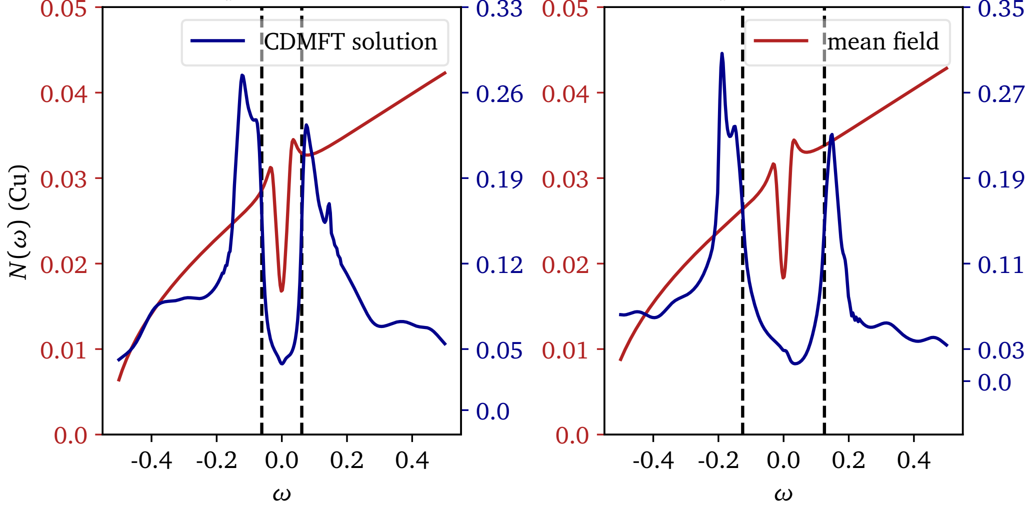
(c) ionic; $U_d = 12$, p = 0.062(OD)

(d) ionic; $U_d = 12$, p = 0.038(UD)

Figure 4.4: Density of states across the first-order transition. (a), (b) Density of states for hole doping values across the discontinuity for the ionic case Eq. (4.1) with $U_d = 12$ and for the covalent case Eq. (4.2) with $\epsilon_p = 2.5$ and $U_d = 10$ respectively. The superconducting gap can be seen for both Cu (blue) and O (red) components, hence in the total (green) density of states. The superconducting gap for the overdoped solution (OD) is symmetric around the Fermi level ($\omega = 0$), while that for the underdoped solution (UD) is asymmetric, for both ionic and covalent cases. (c), (d) Cu component of the density of states (blue) is shown for the overdoped and underdoped solutions respectively across the discontinuity, along with the density of states (red) for the mean-field Hamiltonian Eq. (4.4) with the corresponding values of density and the order parameter. Clearly, the gap in the density of states for the CDMFT solution increases across the transition while the that in the mean-field case decreases to give the same value of the order parameter as the CDMFT solution. The black dashed lines show how the gap is measured for the CDMFT solutions (used in Fig. 4.5); each dashed line marks a point of inflection ($d^2N(\omega)/d\omega^2 = 0$) in the density of states, and the gap is measured to be the distance between them.

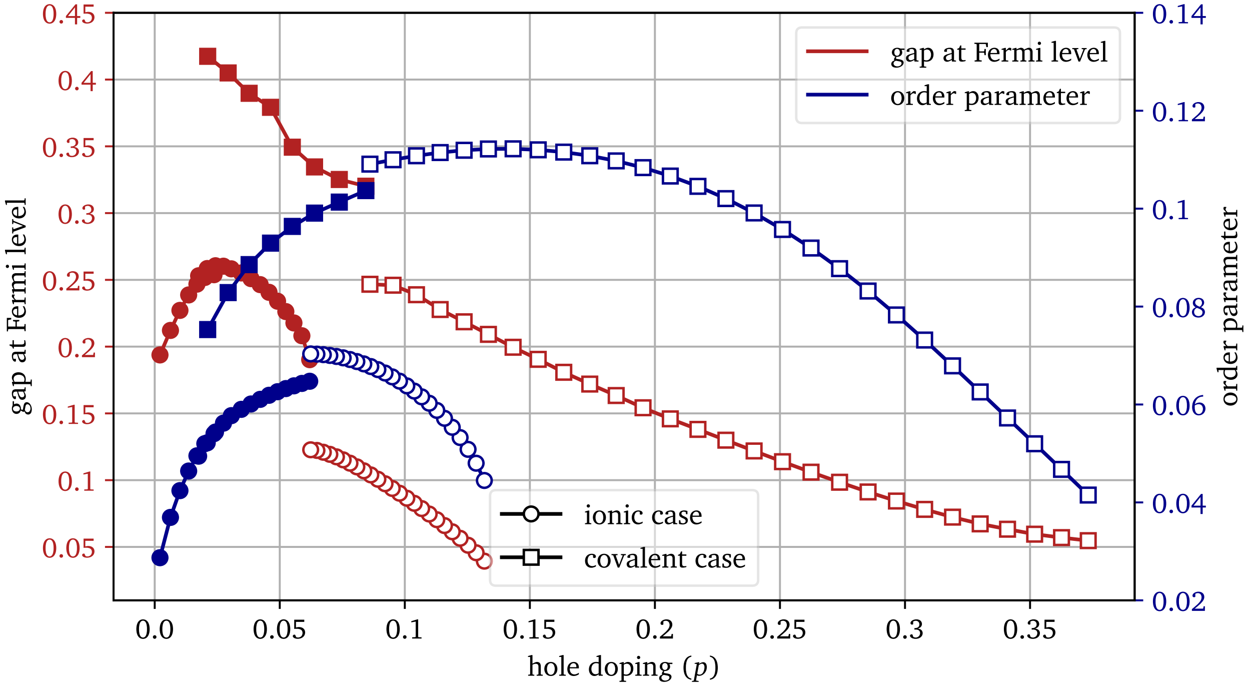

Figure 4.5: Distinct behavior of the gap at the Fermi level (see Fig. 4.4) from that of the order parameter. The gap at the Fermi level and the order parameter as functions of hole doping for the ionic case Eq. (4.1) with $U_d = 12$ (circles) and for the covalent case Eq. (4.2) with $\epsilon_p = 2.5$ and $U_d = 10$ (squares). Filled symbols mark the underdoped solution and open symbols mark the overdoped solution. The gap is measured as shown in Fig. 4.4. The order parameter (blue) decreases with the transition from the overdoped to the underdoped solution and continues to decrease with underdoping, while the gap (red) increases with the transition and continues to increase with underdoping close to the transition. In a conventional superconductor (Fig. 2.5), the gap at the Fermi level is a direct measure of the superconducting strength or the order parameter.

4.3 A first order transition within the superconducting phase

We observe a discontinuous transition for most parameter-sets, which separates the order parameter dome (Figs. 4.2, 4.3) into two parts. We refer to the part of the dome towards low doping as the underdoped solution (filled symbols) and to the part of the dome towards higher doping as the overdoped solution (open symbols). In particular, we observe a hysteresis for the ionic case with $U_d = 12$ and for the covalent case with $\epsilon_p = 2.5$ and $U_d = 10$, indicating a first order transition that separates the underdoped and overdoped solutions. For other cases, the underdoped and overdoped solutions are separated by a region where CDMFT does not converge, indicating an unstable region that could not be probed within our discrete bath framework (section 4.7). We assume that this is a remnant of the first order transition observed in the former two cases, as all curves share the same physics across the discontinuity as we discuss later.

Figure 4.4(a,b) shows the density of states close to the Fermi level before and after the first-order transitions for the ionic case at $U_d = 12$ and the covalent case at $\epsilon_p = 2.5$, $U_d = 10$. The superconducting gap can be seen in the density of states plots close to the Fermi level surrounded by the quasiparticle peaks for all the cases. The superconducting gap appears in both Cu and O components, and hence in the total density of states. Note the difference between the overdoped (marked by OD) and the underdoped (marked by UD) curves for both ionic and covalent cases. The gap, which is almost symmetric in the overdoped solution, becomes large and asymmetric across the transition in the underdoped solution. However, the order parameter decreases from the overdoped to the underdoped solution across the transition (see Figs. 4.2,4.3). To get more insights on this, we plot the density of states of the superconducting phase within mean-field theory corresponding to the CDMFT solutions before and after the transition. The mean-field Hamiltonian can be written as

$$\mathscr{H}^{\mathrm{MF}} = H_0 + \Delta\hat{\Psi} \ , \tag{4.4}$$

where H_0 is the non-interacting part of the Hamiltonian Eq. (2.28) and Δ is the mean-field parameter. In Fig. 4.4 we have compared the density of states for the ionic case at $U_d = 12$ with the density of states obtained using the mean-field Hamiltonian $\mathscr{H}^{MF}$, where the value of the mean field Δ is chosen so that the order parameter $\langle\hat{\Psi}\rangle$ is the same as that for the corresponding CDMFT solutions. Note that here we focus on the Cu component of the density of states since we want to compare the gap with the order parameter and the order parameter is measured as the average of $\hat{\Psi}$ which is a pairing operator between the nearest neighbor Cu orbitals. The comparison of the DOS from the CDMFT calculations with that from mean-field theory helps us identify the deviations of the superconducting gap in the

CDMFT solutions from the perfect d-wave gap in the mean-field case. For instance, in the overdoped case (Fig. 4.4(c)), the superconduting gap in the CDMFT solution is similar in shape to that of the mean-field solution, although we have a larger gap in the CDMFT solution compared to the mean-field solution with the same order parameter which suggests the presence of correlation effects in the CDMFT solution. Note, however that the superconducting gap for the CDMFT solution has additional structures at the end of the gap which are not seen in the mean-field solution. These subgap structures are the artefacts of the broken translational invariance in CDMFT leading to artificial charge-density waves [168]. In the underdoped case (Fig. 4.4(d)), although the order parameter is smaller (see Fig. 4.2), the gap in the CDMFT solution is larger and highly asymmetric. In this case the corresponding mean-field superconducting gap, which is directly proportional to the order parameter, is smaller than in Fig. 4.4(c). This suggests that superconducting gap in the CDMFT solution has an additional component in the underdoped solution which leads to the asymmetry and the large gap. Although we show the variation of the DOS across the transition for only two cases in Fig. 4.4, the same phenomena is observed across the discontinuity in all parameter-sets for both ionic and covalent cases.

To understand the variation of the gap at the Fermi level with hole doping, we have shown the magnitude of the gap (measured from the DOS as shown in Fig. 4.4(b,c)) as well as the order parameter in Fig. 4.5 as functions of hole doping for the ionic case Eq. (4.1) at $U_d = 12$ and the covalent case Eq. (4.2) at $\epsilon_p = 2.5$, $U_d = 10$. The underdoped and overdoped solutions are labelled by closed and open symbols respectively. The order parameter and the gap both increase with a decrease in hole doping for most part of the overdoped solution, however for the underdoped solution, the order parameter decreases while the gap increases close to the discontinuity. This suggests that the gap, as measured from the DOS, has a component other than superconductivity which leads to an increase in the gap (along with an asymmetry) after the transition even when the order parameter is decreasing. This leads to the suspicion that the discontinuous transition that we observe between the underdoped and the overdoped solution might indicate the onset of the pseudogap, and is the remnant of the finite-doping Mott transition transition as has been observed in the normal phase [50, 51, 88, 138].

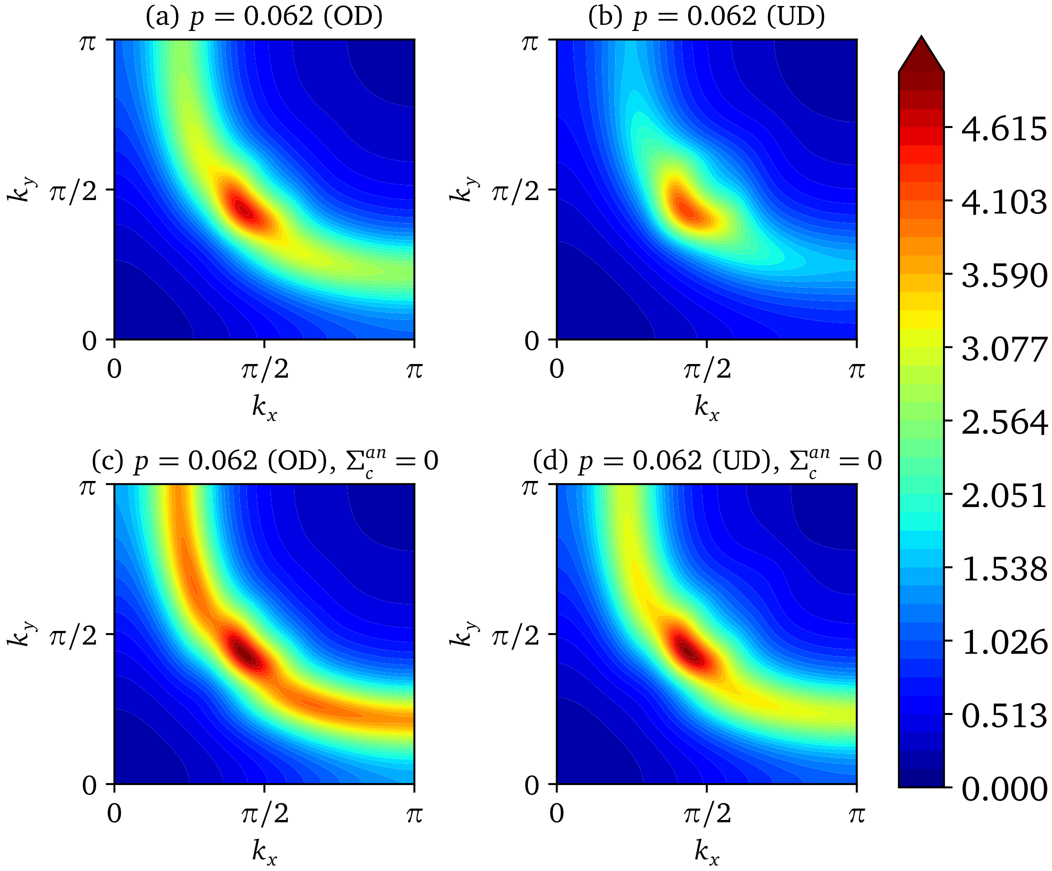

Figure 4.6: Momentum distribution of spectral weight at the Fermi level, in the first quadrant of the Brillouin zone, across the first-order transition. Fermi surfaces of the overdoped (OD) and underdoped (UD) solutions before (left) and after (right) the first-order transition (a,b) in the superconducting phase and (c,d) in the normal phase for the ionic case Eq. (4.1) with $U_d = 12$. The normal phase is obtained by setting the anomalous self-energy of the cluster $\Sigma_c^{an} = 0$. The spectral weight decreases significantly around the node in the superconducting phase from the overdoped (a) to the underdoped (b) solution. In the overdoped solution for the normal phase (c), a Fermi surface appears as expected in a metal. There is a loss of spectral weight at the antinodal regions in the underdoped solution (d), which can be interpreted as a transition from a full Fermi surface to a Fermi arc, suggesting the onset of the pseudogap.

To investigate further whether the transition is related to the pseudogap, we have shown the momentum distribution curves at the Fermi level in the first quadrant of the Brillouin zone in Fig. 4.6 for the last overdoped and the first underdoped solutions for the ionic case Eq. (4.1) at $U_d = 12$. Generically, the momentum distribution curves show closed surfaces, known as Fermi surfaces, in the metallic phase. The Fermi surface turns into disconnected arcs, known as Fermi arcs (Fig. 1.6) in the presence of the pseudogap, due to the loss of spectral weight in the antinodal regions. Furthermore, in the superconducting phase, the momentum distribution curve shows the presence of a node along the (π, π) direction associated to the opening of the d-wave superconducting gap. In Fig. 4.6(a,b), we indeed see the nodes due to the superconducting gap. The spectral weight of the nodes can be seen to decrease from the overdoped to the underdoped solution existing at the same value of hole doping. In Fig. 4.6(c,d) we show the corresponding momentum distribution curves in the underlying normal phase; we probe this by setting the anomalous part of the self-energy[1] $\Sigma^{an} = 0$ [47]. This is justified by looking at the Green function in the Nambu basis (see page 48),

$$\mathbf{G}(\mathbf{k}, z) = \begin{bmatrix} z - \epsilon(\mathbf{k}) - \Sigma^{nor}(\mathbf{k}, z) & -\Sigma^{an}(\mathbf{k}, z) \\ -\Sigma^{an}(\mathbf{k}, z)^* & z + \epsilon^*(\mathbf{k}) + \Sigma^{nor}(\mathbf{k}, -z)^* \end{bmatrix}^{-1}, \tag{4.5}$$

where the off-diagonal self-energy Σ^{an} includes the correlation effects leading to pair formation. Setting this to zero leaves us with the underlying normal phase. We indeed see a signature of the onset of the pseudogap while going from the overdoped to the underdoped solution in this underlying normal phase (Fig. 4.6(c,d)); the spectral weight decreases close to the antinodal regions, while the spectral weight near the node remains almost constant. This is also seen for all other parameter-sets both for the ionic and covalent cases.

Note that the normal phase obtained by setting the anomalous self-energy $\Sigma^{an} = 0$ is a very good approximation for the actual normal phase, however it is not exactly the same as the actual normal phase obtained within CDMFT. The latter can be obtained within CDMFT starting with no anomalous self-energy, i.e., by imposing the particle number conservation in the impurity model. This is different from the former case because there

---

[1] The anomalous part of the self-energy Σ^{an} is the off-diagonal block (upper) of the self-energy when expressed in the Nambu basis. The first diagonal block is known as the normal self-energy Σ^{nor}.

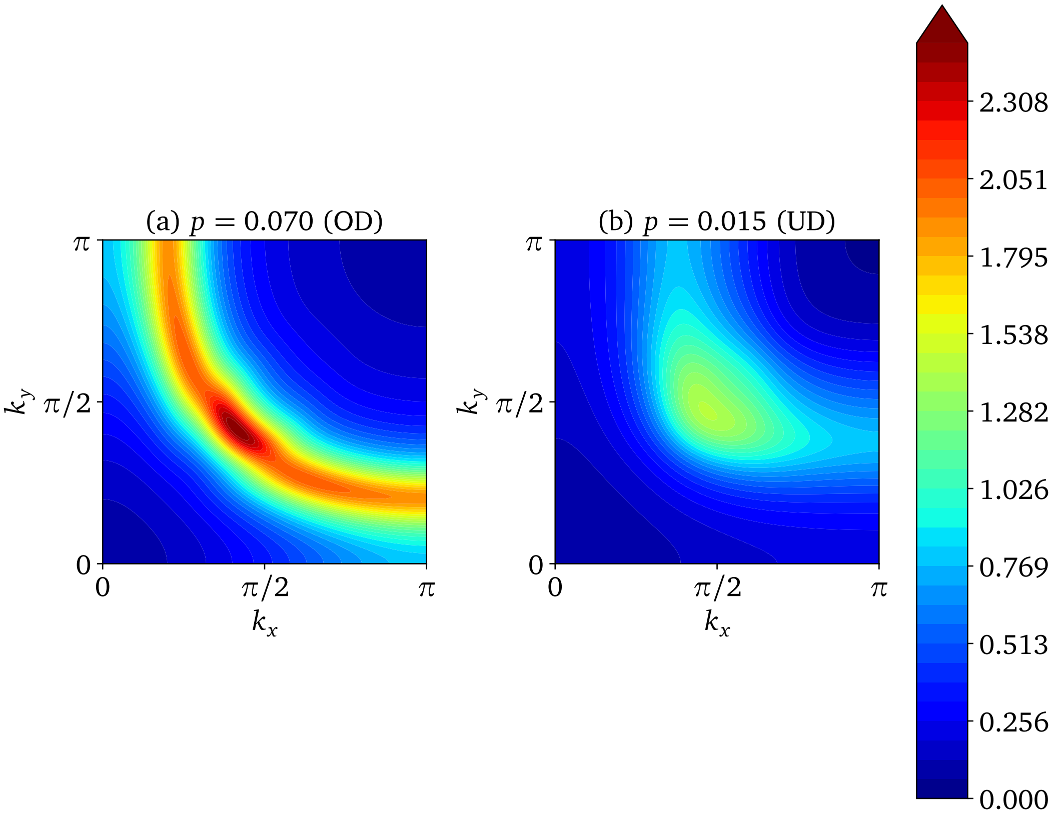

Figure 4.7: Momentum distribution of spectral weight at the Fermi level, in the first quadrant of the Brillouin zone, across the first-order transition in the true normal phase. Fermi surfaces of the overdoped (OD) and underdoped (UD) solutions before (left) and after (right) the first-order transition for the ionic case Eq. (4.1) with $U_d = 12$. The normal phase, in this figure, is obtained by separate CDMFT computations ($U(1)$ gauge symmetry is not broken in the impurity model, i.e., $\mathbf{\Delta} = \mathbf{0}$ in Eq. (3.62), (4.20)), and not by setting the anomalous self-energy to zero for the superconducting solutions as done in Fig. 4.6. Hence, the doping values at which we see the transition are different compared to the superconducting solutions. A clear transition can be seen from a full Fermi surface in the overdoped solution (a) to a disconnected Fermi surface (or a Fermi arc), with no spectral weight in the antinodal regions, in the underdoped solution (b), suggesting the onset of the pseudogap across this transition in the normal phase [49–51]. However, in our solutions, this pseudogap transition is also accompanied by a change in the occupation number of the impurity model, which is an artefact of the finite-sized bath (see section 4.7) that we use.

the effect of the anomalous self-energy feeds into the CDMFT self-consistency, as a result affecting the normal self-energy Σ^{nor} as well, and we just strip off the anomalous self-energy Σ^{an} at the end of the self-consistency to look only at the effects of the normal self-energy Σ^{nor} in the converged solution. Hence, it is an approximate way to obtain the normal phase. It would be ideal to look at the true normal phase, which is obtained without allowing for pairing within CDMFT. Fig. 4.7 shows Fermi surface plots in this normal phase; we also observe a first-order transition in the true normal phase, which is accompanied by a loss of spectral weight, in the antinodal regions, in the underdoped regime. Thus, this first-order transition in the normal phase is associated with the onset of the pseudogap as seen in refs. [49–51, 138]. Although the doping values at which the transition occurs in the normal phase is different than that in the superconducting phase, it strongly suggests that the first-order transition that we observe in the superconducting phase also describes the onset of the pseudogap. However, the transition in the normal phase is accompanied by another transition associated to a change in the total number of particles in the impurity model. The latter transition appears as an artefact of a finite bath system, and it occurs in the normal phase due to the conserved particle number in the impurity model. This makes it hard to distinguish the effect of the pseudogap transition from this artefact in the true normal phase.

Nevertheless, the signatures of the pseudogap can also be seen directly in the normal component of the self energy; the pseudogap is associated with a pole in the self-energy [90, 158, 169] and originates from Mott physics [49, 170]. We see both of these signatures in the normal component of the cluster self-energy shown in Fig. 4.8(a),(b) for the ionic case Eq. (4.1) at $U_d = 12$ and the covalent case Eq. (4.2) at U_d=10 respectively. The normal component of the cluster self-energy at the cluster momentum $\mathbf{K} = (\pi, 0)$ is plotted as a function of frequency for various values of hole doping for the underdoped and overdoped cases as well as at half filling for both cases. We observe the growth of a prominent pole near the Fermi level in the underdoped solutions (vertical dotted lines), which was absent in the overdoped solutions. Furthermore, this pole in the underdoped cases, evolves to become the dominant pole at half-filling, leading to the insulating phase[2]. We also show, in the inset, the position of the pole in the underdoped solution which falls rapidly towards zero near half-filling, suggesting that the pole in the underdoped solu-

---

[2] A pole in the self-energy at a given frequency results in the vanishing of the spectral function at that frequency, since the self-energy is in the denominator of the Green function; this leads to an insulator when it happens close to the Fermi level.

(a) ionic case; $U_d = 12.0$

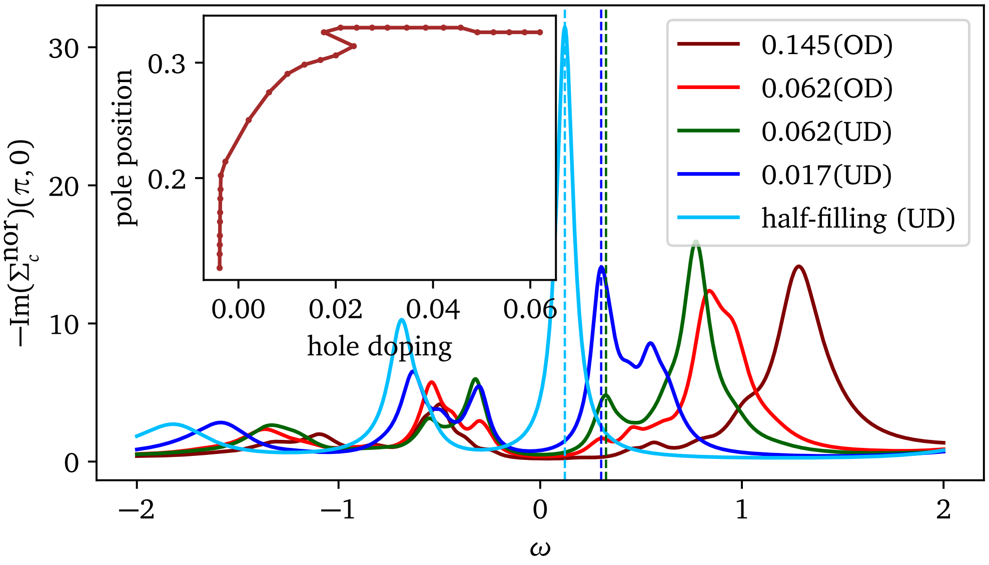

(b) covalent case; $U_d = 10.0$

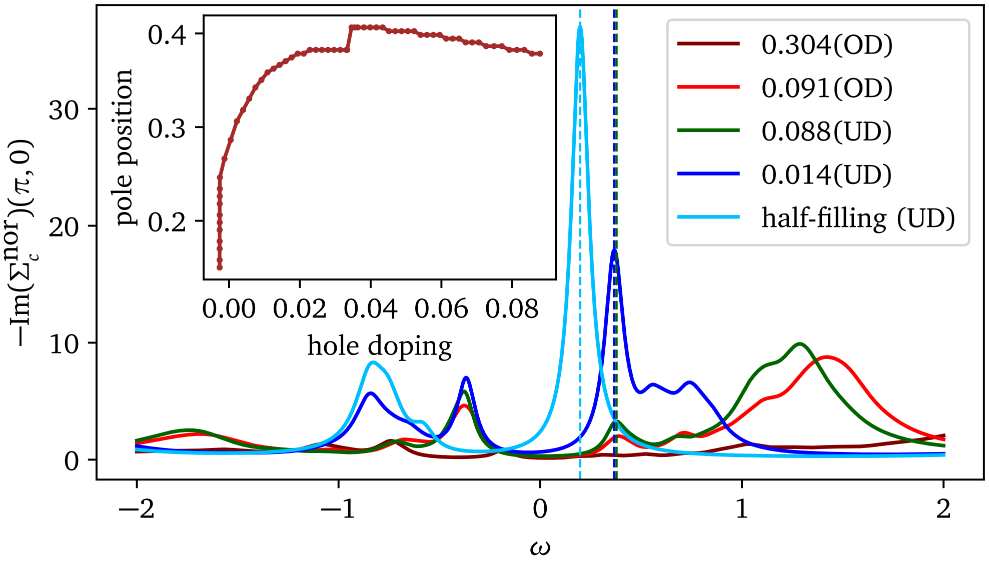

Figure 4.8: Features of the normal self-energy before and after the first-order transition. Imaginary part of the normal self-energy at the antinodal region as a function of ω for (a) the ionic case Eq. (4.1) with $U_d = 12$ and (b) the covalent case Eq. (4.2) with $U_d = 10$ for various values of hole doping. There is a growth of a pole (marked by dashed lines) near the Fermi surface in the underdoped (UD) solution after the first-order transition (green curve), for both cases, which becomes the pole leading to the charge-transfer insulator at half-filling ($n = 5$) (blue curve). The position of this pole is plotted as a function of hole doping in the inset; it falls rapidly to zero as we approach half-filling.

tion is indeed connected to the pole leading to the charge-transfer insulator at half-filling. Hence, we conclude that the transition from the overdoped to the underdoped solutions indeed mark the onset of the pseudogap and that the pseudogap is linked to the strong correlation effects leading to the formation of a charge-transfer insulator at half-filling.

4.4 Correlation with oxygen hole content

Another important observation that we made is that the hole content on the oxygen orbitals, at optimal doping, is monotonously related to the maximum value of the order parameter, across various parameter-sets (Figs. 4.9, 4.10). Considering the order parameter at zero temperature as a proxy for the critical temperature T_c[3], this is analogous to the correlation between the maximum superconducting T_c and the oxygen hole content measured in NMR experiments [102], as seen in Fig. 1.11. We observe this relation between the order parameter and the oxygen hole content at optimal doping, by varying various model parameters in the vicinity of the ionic Eq. (4.1) (Fig. 4.9) and the covalent Eq. (4.2) (Fig. 4.10) cases at different values of U_d. The height of the order parameter domes, i.e., the maximum order parameter, increases as the domes move towards a higher oxygen hole content for both cases. This relation does not hold for superconducting domes with higher values of ϵ_p (= 5.3, 6.7) where the maximum order parameter decreases as the oxygen hole content increases; this corresponds to the regime where the insulating gap (the CTG) is close to zero and the strong coupling limit does not hold (we discuss this in more details in the context of Fig. 4.12). Note that this limit is not encountered in cuprates, which instead have a finite charge-transfer gap; hence the monotonous relation holds in the relevant regime corresponding to the cuprates.

---

[3] We also observe this correlation between the maximum superconducting gap and the oxygen hole content as discussed in section A.4.

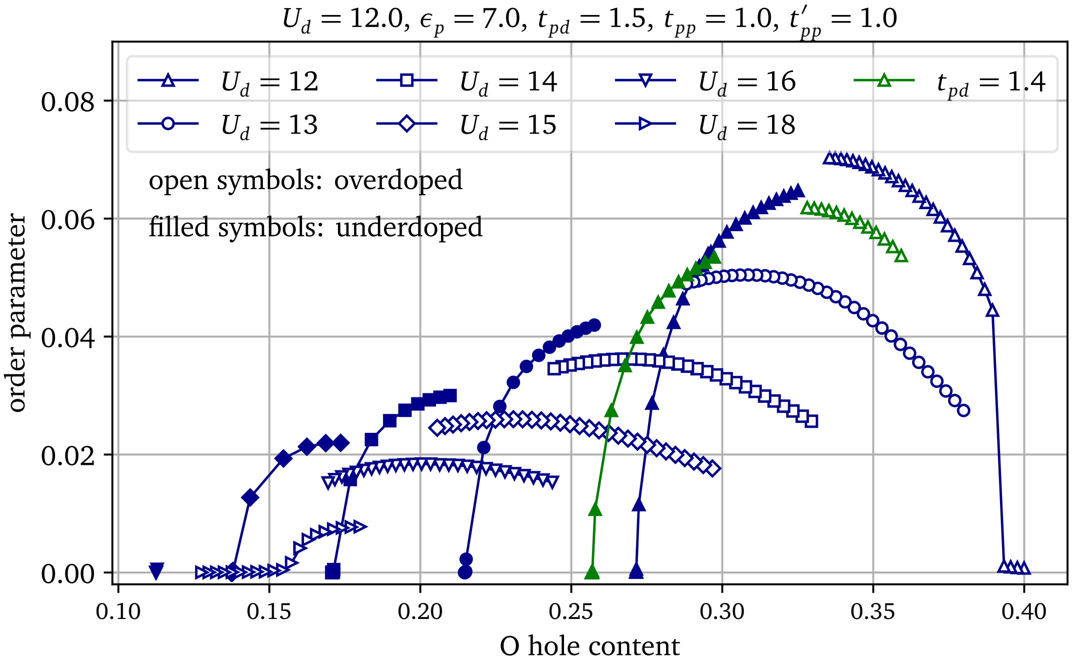

Figure 4.9: Order parameter as a function of the hole content on O orbitals for various parameter-sets around the ionic case Eq. (4.1) with various values of U_d. The height of the order parameter domes increase as we move towards higher hole content on oxygen orbitals.

To summarize these observations, we have shown a plot (Fig. 4.11) of the maximum value of the order parameter for each dome (along with the superconducting domes, in faint colors) as a function of the optimal oxygen hole content, for all the parameter sets. This clearly shows that the maximum value of the order parameter is monotonously related to the oxygen hole content at optimal doping for variations from both ionic Eq. (4.1) and covalent Eq. (4.2) cases, except in the regime where the charge-transfer gap is very close to zero. In contrast, we observe in the inset of Fig. 4.11 that the maximum value of the order parameter does not have any correlation with the total hole doping. This indicates that the oxygen hole content indeed plays a special role in the superconductivity of cuprates. However, the correlation between the maximum order parameter and the oxygen hole content is not perfect; although the curves corresponding to the variations of different parameters for a particular case (ionic or covalent) almost lie on top of each other, the curves for the variation of parameters from the ionic and the covalent cases are

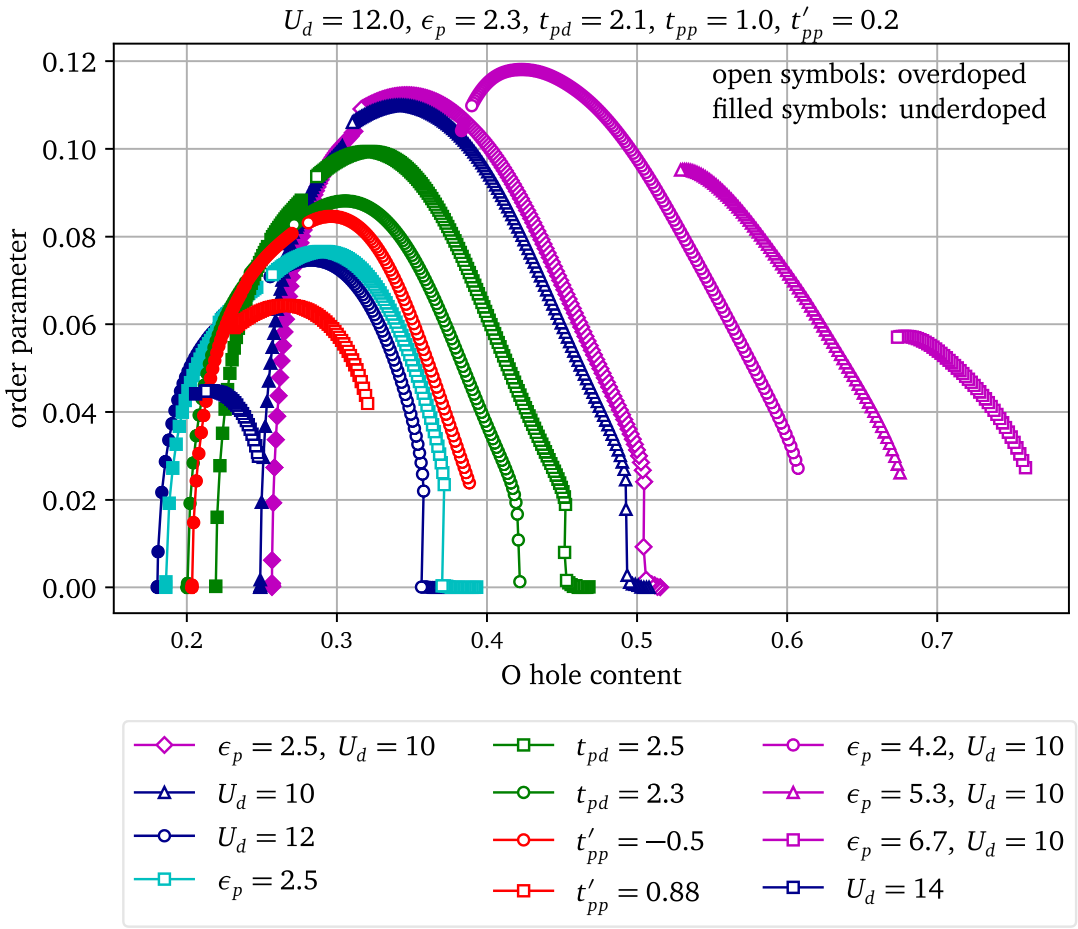

Figure 4.10: Order parameter as a function of the hole content on O orbitals for various parameter-sets around the covalent case Eq. (4.2) with various values of U_d. The height of the order parameter domes increase as we move towards higher hole content on oxygen orbitals except for parameter-sets with higher values of $\epsilon_p = 5.3, 6.7$. These two parameter-sets have a negligible charge-transfer gap (CTG) (see Fig. 4.12) and hence do not lie in the insulating regime and do not correspond to cuprates.

separated from each other. This suggests that the oxygen hole content cannot be the only factor for determining the superconducting strength of a cuprate superconductor.

It is known from both theoretical [133] and experimental studies [86] that the charge-transfer gap (CTG) is crucial for superconductivity in cuprates; the maximum T_c is inversely proportional to the charge-transfer gap (Fig. 1.10). This is usually understood in terms of an effective superexchange which mediates pairing, $J_{\text{eff}} = 4t_{\text{eff}}^2/\Delta_{\text{CT}}$, where Δ_{CT} is the magnitude of the CTG and t_{eff} is the effective hopping amplitude between the near-

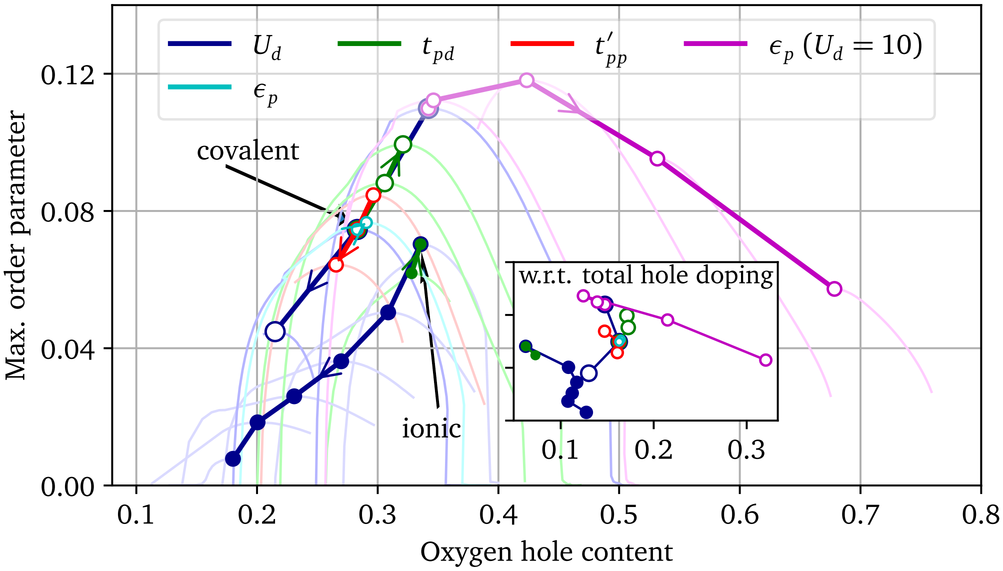

Figure 4.11: Relation between the maximum order parameter and the corresponding hole content on oxygen. Maximum value of the order parameter (top of each dome in Figs. 4.9, 4.10, shown in faint colors here) as a function of the hole content on O orbitals at optimal doping, for all parameter-sets around the ionic case Eq. (4.1) (filled symbols) and the covalent case Eq. (4.2) (open symbols), with various values of U_d. Each color denotes the parameter-sets explored by changing a single parameter (mentioned in the legend) starting from Eqs. (4.1), (4.2) with $U_d = 12$ for filled and open symbols respectively. $U_d \in \{12, 13, 14, 15, 16, 18\}$, $t_{pd} \in \{1.4, 1.5\}$ for filled symbols. $U_d \in \{10, 12, 14\}$, $t_{pd} \in \{2.1, 2.3, 2.5\}$, $t'_{pp} \in \{-0.5, 0.2, 0.88\}$, $\epsilon_p \in \{2.3, 2.5\}$, ϵ_p(with $U_d = 10) \in \{2.3, 2.5, 4.2, 5.3, 6.7\}$ for open symbols. The arrows point in the direction of increase in the respective parameters. The maximum value of the order parameter is monotonously related with the O hole content at optimal doping, except for parameter-sets with $\epsilon_p = 5.3, 6.7$, which do not correspond to cuprates. The inset shows the plot of the maximum order parameter as a function of the total hole doping; clearly there is no correlation between the maximum order parameter and the total hole doping.

est neighbor copper orbitals [86]. Note that the CTG is the equivalent of the Mott gap in the one-band Hubbard model; a similar relation is also seen between the maximum T_c and the Mott gap [88], i.e., the on-site Coulomb repulsion in the one-band Hubbard model. In order to understand the relation between the maximum order parameter and the oxygen hole content, we plot the maximum value of the order parameter as a function of the CTG in Fig. 4.12(a) and the oxygen hole content at optimal doping as a function of the CTG in Fig. 4.13(a). We observe in Fig. 4.12(a) that the maximum value of the order parameter indeed decreases as the CTG increases, except when the magnitude of CTG is very small, in which case the order parameter falls rapidly as the CTG goes to zero, as also seen in ref. [171]. The CTG is measured from the density of states as shown in Fig. 4.12(b). Note that we normalize the CTG with the bandwidth BW to be able to compare across all parameter-sets. Ideally, superconductivity can still occur when the CTG is zero, where it would be mediated by long wavelength spin fluctuations [172–174]. But, in our case, we use a 2×2 cluster for doing CDMFT, which only includes the short-range fluctuations, that are more relevant in the strong correlation regime. Hence, we just focus on the strong correlation regime which is suitable for cuprates. However, note that in the one-band Hubbard model with CDMFT, superconductivity still exists below the Mott transition point [88].

Further, we observe from Fig. 4.13(a) that the hole content on oxygen orbitals at optimal doping is very well correlated with the magnitude of the charge-transfer gap. Hence, the charge-transfer gap directly controls the hole content on the oxygen orbitals. This results in the monotonous relation between the order parameter and the oxygen hole content; an increase in the charge transfer gap leads to a decrease in the maximum order parameter as well as the oxygen hole content. Further, the relation between the CTG and the oxygen hole content can be understood by looking at the oxygen component of the density of states for the variation in a given parameter. Fig. 4.13(b) shows the oxygen component of the density of states for the ionic case Eq. (4.1), for different values of U_d. Note that the area occupied by the DOS curve above the Fermi level decreases as the CTG increases with U_d, leading to a drop in the oxygen hole content while the CTG increases. This is directly seen for the variation in U_d, since U_d directly affects the CTG without affecting the rest of the density of states (below the Fermi level) significantly. However, this phenomenon is true for the variation in all parameters where the area of the oxygen DOS above the Fermi level decreases with an increase in the CTG. This is natural since the overlap of the oxygen spectrum with the upper Hubbard band is suppressed as the CTG increases.

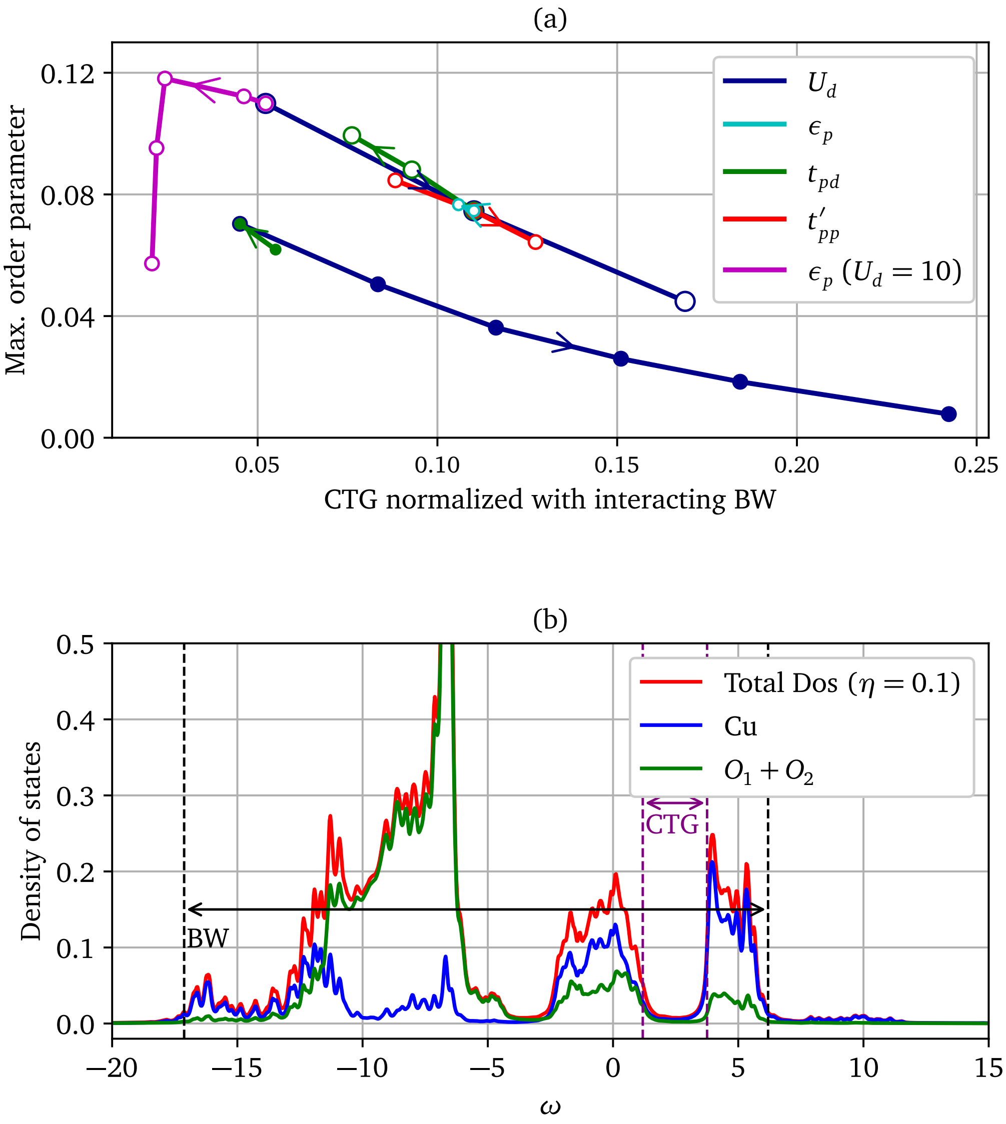

Figure 4.12: Order parameter and charge-transfer gap. (a) Maximum order parameter as a function of the charge-transfer gap (CTG), normalized with the total bandwidth, at optimal doping. Each curve denotes the variation of a single parameter starting from the ionic case Eq. (4.1) and the covalent case Eq. (4.2) with $U_d = 12$ marked by the filled and open symbols respectively. See Fig. 4.11 for the values of the parameters. The arrow indicates the direction of increase in the respective parameters. The maximum order parameter decreases with an increase in the CTG for all cases except for the two parameter-sets with higher values of ϵ_p $(= 5.3, 6.7)$, where the CTG is close to zero and hence they no longer lie in the insulating regime; hence, these last two parameter-sets do not correspond to cuprates which always have a finite CTG. (b) Density of states for the covalent case Eq. (4.2) with $U_d = 12$, showing the estimate of the charge-transfer gap (CTG) and the total bandwidth (BW).

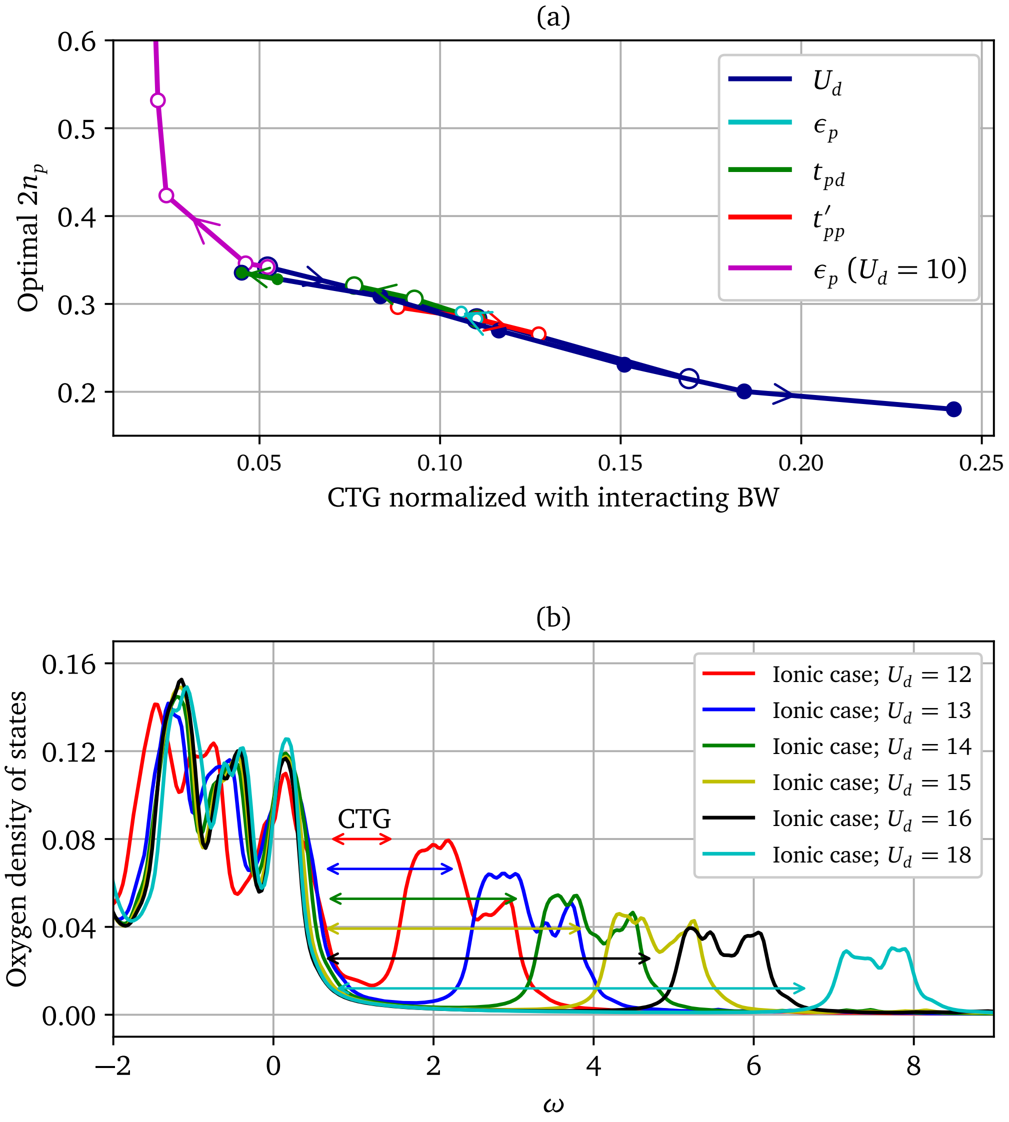

Figure 4.13: Oxygen hole content and charge-transfer gap. (a) Oxygen hole content, $2n_p$, at optimal doping, as a function of the charge-transfer gap normalized to the total bandwidth. Similar to Figs. 4.11, 4.12, each curve denotes the variation of a single parameter starting from the ionic case Eq. (4.1) and the covalent case Eq. (4.2) with $U_d = 12$ marked by the filled and open symbols respectively. The O hole content at optimal doping is very well correlated with the normalized CTG across all parameter-sets and decreases with increase in the CTG. (b) Oxygen component of the density of states are shown for the variation in the parameter U_d in the ionic case Eq. (4.1) . The area of the O DOS above the Fermi level gives the hole content on O orbitals, which clearly decreases as the CTG increases with U_d.

4.5 Pairing

There is a strong evidence from various studies with the one-band Hubbard model [87–89,123,124] that pairing in cuprate superconductors is mediated by short range antiferromagnetic fluctuations [87,99,100]. This is also supported by the observation that the critical temperature T_c scales as the superexchange J, which takes the form $4t^2/U$ [87,88,96,98] in the one-band Hubbard model. Recent experiments [101] have also confirmed the relation of antiferromagnetic paramagnons with pairing in cuprates. The charge-transfer gap (CTG) in the three-band Hubbard model is the equivalent of the Mott gap U in the one-band Hubbard model. That the order parameter decreases as the CTG increases also hints that an effective superexchange $J = 4t_{\text{eff}}^2/\Delta_{\text{CT}}$ controls superconductivity in the three-band Hubbard model, where Δ_{CT} is the magnitude of the CTG. To investigate further regarding the antiferromagnetic origin of superconductivity in the three-band Hubbard model, we plot various components of the spin susceptibility (see section A.7) along with the cumulative value of the order parameter, following ref. [99], in Fig. 4.14. The cumulative value of the order parameter $I_F(\omega)$ is given by[4]

$$I_F(\omega) = -\frac{1}{N}\int_0^{\omega} \frac{d\omega'}{\pi} \text{Im}\left[\text{tr}[\mathbf{g}\mathbf{F}^R(\omega')]\right] , \tag{4.6}$$

where

$$F_{ij}^R(\omega) = \langle\Omega|c_{i\uparrow}\frac{1}{\omega+i\eta-H+E_0}c_{j\downarrow}|\Omega\rangle + \langle\Omega|c_{j\downarrow}\frac{1}{\omega+i\eta+H-E_0}c_{i\uparrow}|\Omega\rangle \tag{4.7}$$

---

[4] This form is different than that for the order parameter (2.49). We discuss in section A.5 how to express the order parameter (2.49) as an integral over the real frequency (between Eq. (A.25) and Eq. (A.32)). $I_F(\omega)$ is the partially integrated order parameter (Eq. (A.32)).

is the retarded Gorkov function (Eq. (2.47)), i and j are nearest neighbors and $\mathbf{g}$ is the d-wave form factor matrix:

$$g_{ij} = \begin{cases} 1 & \text{when } i, j \text{ are first-neighbors along } x \text{ direction} \\ -1 & \text{when } i, j \text{ are first-neighbors along } y \text{ direction} \\ 0 & \text{otherwise} \end{cases} \cdot \tag{4.8}$$

$I_F(\omega)$ includes the contribution to the order parameter of frequencies up to ω, hence the plot of $I_F(\omega) \sim \omega$ (black curve) gives information about the growth of the order parameter with ω; in the limit of infinite frequency $\lim_{\omega\to\infty} I_F(\omega)$ gives the order parameter (A.32). The cumulative value of the order parameter grows mostly at low frequencies and stabilizes after decreasing to around 60% of its maximum value. The (π, π) component of the imaginary part of the spin susceptibility $\chi''(\pi, \pi)$ is dominant in the low frequency limit where the cumulative order parameter $I_F(\omega)$ grows the most. Specifically, the frequency at which $\chi''(\pi, \pi)$ attains its maximum value is close to the frequency where $I_F(\omega)$ attains half of its asymptotic value ($\omega \sim 0.1$). This is true for all the parameter-sets. Hence, this suggests that the pairing is also driven by antiferromagnetic spin fluctuations in the three-band Hubbard model.

In cluster methods, the superexchange J can be estimated by the pole of the imaginary part of the (π, π) spin susceptibility in the normal phase (no superconductivity or antiferromagnetism) at half filling [97]. Ref. [97] shows that this quantity scales very well with J obtained using the degenerate second order perturbation theory and the estimate improves as the on-site Coulomb repulsion U increases, within the one-band Hubbard model. This is justified, since on a small cluster there are no long wavelength spin fluctuations; hence $\chi''(\pi, \pi)$ peaks around the energy required to break the singlets between neighboring Cu orbitals. Thus, we use the peak of $\chi''(\pi, \pi)$, in our calculations, at zero doping in the respective normal phases (no superconductivity or antiferromagnetism) as an estimate of J. Figure 4.15 shows the plot of J, obtained this way, as a function of the

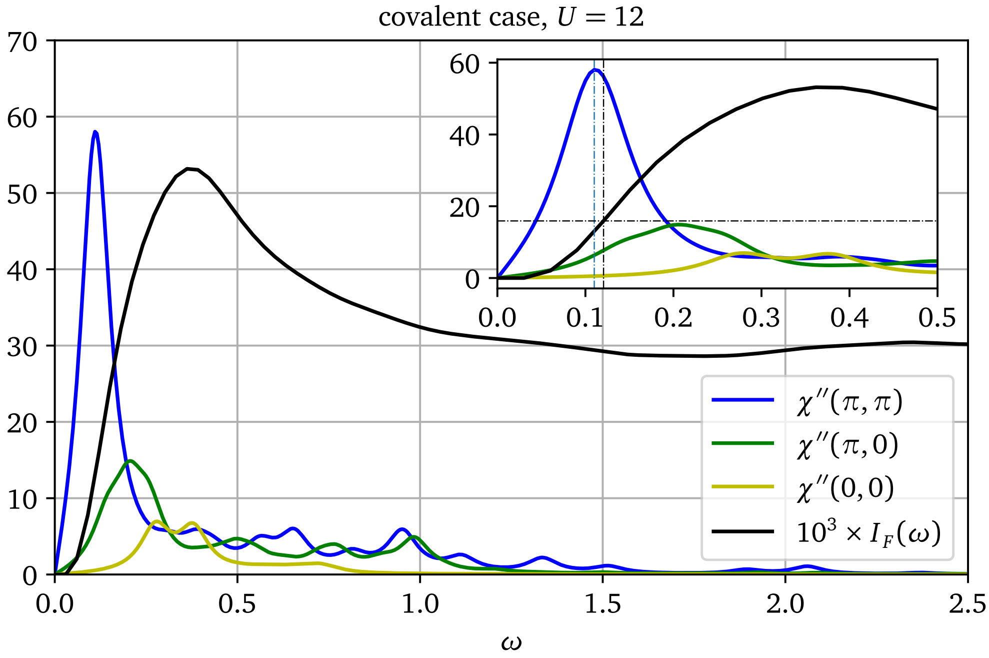

Figure 4.14: Imaginary part of the spin susceptibility and the cumulative order parameter as functions of frequency. The cumulative value of the order parameter $I_F(\omega)$ Eq. (4.6) grows mostly at low frequencies and becomes stationary as soon as $\omega \approx 1$ after decreasing to around 60% of its maximum value. The (π,π) component of the imaginary part of the spin susceptibility is seen to dominate at lower frequencies where $I_F(\omega)$ grows the most. The inset shows the plot at very small frequencies, where we can see that the peak of $\chi''((\pi,\pi),\omega)$ (blue dotted line) is very close to the frequency where (black dotted line) $I_F(\omega)$ attains half of its stationary value $1/2\lim_{\omega\to\infty} I_F(\omega)$. $\chi''(\mathbf{q},\omega)$ is the imaginary part of the retarded spin susceptibility $\chi^R_{\text{spin}}(\mathbf{q},\omega)$ (A.43).

CTG at optimal doping values for all parameter-sets except those with large values of ϵ_p. Note that we do not use the expression of J from perturbation theory since the energy scales of the hopping terms and that of the CTG are comparable. The value of J decreases with an increase in CTG, suggesting an approximately inverse relation; we can understand this by an effective $J = 4t_{\text{eff}}^2/\Delta_{\text{CT}}$ between the nearest neighbor Cu orbitals in the three-band Hubbard model, where Δ_{CT} is the magnitude of the CTG. The value of J is higher for the parameter-sets obtained by varying various parameters in the covalent case Eq. (4.2), than for the ionic case at a given value of the CTG, suggesting that the effective hopping t_{eff} between the nearest neighbor Cu orbitals is higher in the vicinity of the covalent case than for the ionic case.

Moreover, the behavior of the maximum value of the order parameter is fully captured by J: 1) In Fig. 4.12(a), we observe that the maximum order parameter is higher in the vicinity of the covalent case (open symbols) than for the ionic case (closed symbols) at a given value of the CTG, which can be attributed to a higher J for the covalent case (see Fig. 4.15), 2) In Fig. 4.12(a), we also observe that the maximum order parameter, in each case, decreases with increase in the CTG, which can be attributed to the fact that J decreases with an increase in the CTG (see Fig. 4.15). The dependence of the order parameter with the oxygen hole content is also justified in this light since the oxygen hole content is completely controlled by the CTG (Fig. 4.13(a)). Further, the inset of Fig. 4.15 directly shows the maximum order parameter as a function of J; as expected, there is a very good correlation across all the parameter sets in the vicinity of the ionic case Eq. (4.1) and the covalent case Eq. (4.2). This suggests that the order parameter at optimal doping indeed depends completely on J. Thus, the dependence of the maximum order parameter with all other quantities (oxygen hole content, charge-transfer gap) can be ultimately understood in terms of J.

Another very important conclusion is that the parameter-sets that correspond to a more covalent nature of bonding between Cu and O orbitals (i.e., a lower difference between the Cu and O orbital energies), i.e., in the vicinity of Eq. (4.2), have a higher value of the effective superexchange J (see Fig. 4.15) between the Cu orbitals, and hence a higher value of the maximum order parameter, for a given value of the CTG. This is also the reason, that among many transition metal oxides, cuprate superconductors have the highest T_c, because in reality, the Cu-O bond is the most covalent in nature among all transition metal oxides. The extent to which the bond between a metal and oxygen is covalent depends on how close the ionization energy of the metal and the electron affinity of oxygen are [95, 175]. For example, Ni-O bond is more ionic in nature, hence Nickelates have a lower T_c [21]. Thus, covalency is an important criteria for searching for new high temperature superconductors.

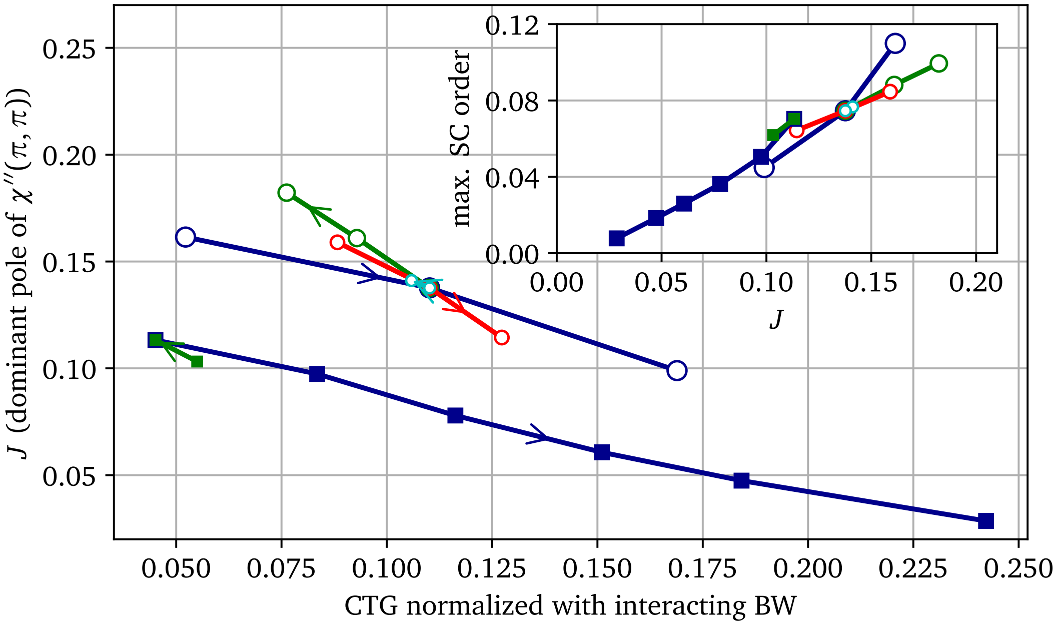

Figure 4.15: Antiferromagnetic superexchange, charge-transfer gap and the order parameter. Antiferromagnetic superexchange J, measured as the dominant pole of $\chi''(\pi,\pi)$ at zero doping in the respective normal phases (no superconductivity, no antiferromagnetism), as a function of the charge-transfer gap. J decreases with an increase in the charge-transfer gap (CTG) for most parameter-sets as expected from the effective form $J = 4t_{\text{eff}}^2/\Delta_{\text{CT}}$, where Δ_{CT} is the magnitude of the CTG. For a given value of the CTG, J is higher for variations from the covalent case Eq. (4.2) (open symbols) than that of the ionic case Eq. (4.1) (filled symbols), suggesting that the effective hopping t_{eff} is higher in the vicinity of the covalent case than in the ionic case. The inset shows the maximum order parameter as a function of J; the value of the maximum order parameter is quite well correlated with J, suggesting that J is indeed the single parameter that controls the maximum order parameter.

4.6 Dependence on various parameters

In this section[5], we compute the various components of the gradient of the optimal order parameter $\langle\Psi\rangle_{\max}(t_{pp}, \epsilon_p, t_{pd}, t'_{pp}, U_d)$ along the various parameters. The partial derivative of a quantity y, taking discrete values, with respect to a variable x, also taking discrete values, is approximated as the average slope of y with respect to x:

---

[5] In this section, we use the notation $\bar{x}$ for a parameter x defined in units of t_{pp} ($\bar{x} = x/t_{pp}$) and when used without the bar, it would mean the absolute value of x in eV. This is different for the rest of the chapter, where we denote a parameter x to be in units of t_{pp}.

$$\frac{\partial y}{\partial x} = \frac{y_N - y_1}{x_N - x_1}\,, \tag{4.9}$$

where N is the number of points, y denotes the maximum order parameter and x denotes one of the parameters that we vary. We calculate Eq. (4.9) in the regime where the variation of the maximum value of the order parameter with a given model parameter can be approximated to be linear; this is the case for the variation of all parameters (see caption of Fig. 4.11), except for the variation of ϵ_p at $U_d = 10$, for which we exclude the values $\epsilon_p = 5.3,\ 6.7$. Further, the component of the gradient along the parameter t_{pp} is computed via chain rule, since all other parameters are defined in units of t_{pp} and t_{pp} is not varied directly:

$$\frac{\partial \langle\Psi\rangle_{\max}}{\partial t_{pp}} = \frac{\partial \langle\Psi\rangle_{\max}}{\partial \bar{t}_{pd}}\frac{\partial \bar{t}_{pd}}{\partial t_{pp}} + \frac{\partial \langle\Psi\rangle_{\max}}{\partial \bar{\epsilon}_{p}}\frac{\partial \bar{\epsilon}_{p}}{\partial t_{pp}} + \frac{\partial \langle\Psi\rangle_{\max}}{\partial \bar{t}'_{pp}}\frac{\partial \bar{t}'_{pp}}{\partial t_{pp}} + \frac{\partial \langle\Psi\rangle_{\max}}{\partial \bar{U}_{d}}\frac{\partial \bar{U}_{d}}{\partial t_{pp}} \tag{4.10}$$

$$\Rightarrow \frac{\partial \langle\Psi\rangle_{\max}}{\partial t_{pp}} = -\frac{1}{t_{pp}}\left[\frac{\partial \langle\Psi\rangle_{\max}}{\partial \bar{t}_{pd}}\bar{t}_{pd} + \frac{\partial \langle\Psi\rangle_{\max}}{\partial \bar{\epsilon}_{p}}\bar{\epsilon}_{p} + \frac{\partial \langle\Psi\rangle_{\max}}{\partial \bar{t}'_{pp}}\bar{t}'_{pp} + \frac{\partial \langle\Psi\rangle_{\max}}{\partial \bar{U}_{d}}\bar{U}_{d}\right], \tag{4.11}$$

where the values of the parameters $\bar{x}$ is taken from Eq. (4.2) with $\bar{U}_d = 12$ for the variation of parameters starting with the covalent case Eq. (4.2). Note that Eq. (4.9) for calculation of the partial derivatives amounts to assuming a linear relation between y and x, which might not always be appropriate. However, this approximation is good enough to classify which parameters are more crucial for superconductivity than others. The components of the gradient of the optimal order parameter $\langle\Psi\rangle_{\max}$ are shown in tab. 4.1 along with the components of the gradient of the CTG for variations from the covalent case Eq. (4.2) and the ionic case Eq. (4.1). The optimal value of the order parameter $\langle\Psi\rangle_{\max}$ changes the most on changing the parameter t_{pd}, the hopping parameter between a Cu orbital and the nearest neighbor oxygen orbitals, for both ionic and covalent cases.

Table 4.1: Gradient of the maximum order parameter and the optimal charge-transfer gap. The components of the gradient of the order parameter at optimal doping $\langle\Psi\rangle_{\text{max}}$ with respect to various parameters are shown along with the components of the gradient of the charge-transfer gap at optimal doping. Ionic case: $U_d \in \{12, 13, 14, 15, 16, 18\}$, $t_{pd} \in \{1.4, 1.5\}$. Covalent case: $U_d \in \{10, 12, 14\}$, $t_{pd} \in \{2.1, 2.3, 2.5\}$, $t'_{pp} \in \{-0.5, 0.2, 0.88\}$, $\epsilon_p \in \{2.3, 2.5\}$, ϵ_p(with $U_d = 10$) $\in \{2.3, 2.5, 4.2\}$.

Model:	covalent (Eq. (4.2))		ionic (Eq. (4.1))	
Parameter (x)	$\frac{\partial\langle\Psi\rangle_{\text{max}}}{\partial x}(eV^{-1})$	$\frac{\partial\Delta_{\text{CT}}}{\partial x}(eV^{-1})$	$\frac{\partial\langle\Psi\rangle_{\text{max}}}{\partial x}(eV^{-1})$	$\frac{\partial\Delta_{\text{CT}}}{\partial x}(eV^{-1})$
t_{pp}	0.069	-7.524	-	-
t_{pd}	0.096	-2.449	0.131	-2.578
ϵ_p	0.016	-0.773	-	-
ϵ_p ($U_d = 10$)	0.007	-0.488	-	-
t'_{pp}	-0.023	1.083	-	-
U_d	-0.025	1.186	-0.016	1.315

We saw in the last section that the optimal order parameter is controlled by the antiferromagnetic superexchange $J = 4t_{\text{eff}}^2/\Delta_{\text{CT}}$, and hence, is suppressed as the magnitude of the CTG Δ_{CT} increases. This is also evident from table 4.1, where we have shown the various components of the gradient of the CTG at optimal doping: Each component of the gradient of the CTG has the opposite sign to that of the corresponding component of the gradient of the optimal order parameter $\langle\Psi\rangle_{\text{max}}$, as can also be concluded from Fig. 4.12. The charge-transfer gap is most sensitive to the nearest neighbor hopping parameter between the oxygen orbitals t_{pp}. If we consider only the parameters that we vary directly (i.e., leaving t_{pp}, which is a constant), then the magnitudes of the various components of the gradient follow the same order for both CTG and the optimal order parameter $\langle\Psi\rangle_{\text{max}}$. This reinforces the fact that the CTG is indeed an important quantity that controls the superconducting strength.

4.7 Details of the cluster-bath impurity model

In this work, we use a cluster of four sites (Fig. 4.16(b)), corresponding to four (correlated) Cu orbitals, connected to eight uncorrelated bath orbitals, to form the cluster-bath impurity model. A cluster of 4 sites is chosen so as to be able to include the short range antiferromagnetic correlations between the sites, which are crucial for d-wave superconductivity in cuprates [87,88,99,100]. We do not include O orbitals in the correlated cluster, since otherwise the impurity model would be much larger for the exact diagonalization solver. The effect of the O orbitals is taken into account as an additional hybridization term $\mathbf{\Gamma}_{\mathrm{O}}$ (which is a constant and depends on the parameters of the model, as discussed in section A.6) in the lattice Green function for the Cu orbitals:

$$\mathbf{G}_{\mathrm{Cu}}(\tilde{\mathbf{k}},\omega)^{-1} = \omega - \mathbf{t}_{\mathrm{Cu}}(\tilde{\mathbf{k}}) - \mathbf{\Gamma}_{\mathrm{O}}(\tilde{\mathbf{k}},\omega) - \mathbf{\Sigma}(\omega)\,, \tag{4.12}$$

where $\tilde{\mathbf{k}}$ is a vector in the Brillouin zone of the super-lattice (the unit cell of the super-lattice is marked by the gray box in Fig. 4.16(a)), $\mathbf{t}_{\mathrm{Cu}}(\tilde{\mathbf{k}})$ is the hopping matrix for the Cu orbitals; this vanishes here since we do not have any hopping between two Cu orbitals (Fig. 2.4). Since the oxygen orbitals are uncorrelated, this turns out to be a very good approximation [138]. Moreover, the effect of oxygen orbitals goes into the CDMFT procedure through the minimization of the distance function Eq. (3.56). This process of including the oxygen orbitals into the model is equivalent to taking an additional cluster for the O orbitals (blue box in Fig. 4.16(a)), which is not connected to any bath (as is done in section A.6). Then, the lattice Green function automatically takes the form Eq. (4.12) when projected on the Cu orbitals (see sec. A.6).

The self-energy $\mathbf{\Sigma}(\omega)$, in Eq. (4.12), is the self-energy for the Cu cluster to begin with. It eventually includes the effect of the oxygen orbitals (as well as the rest of the lattice) as

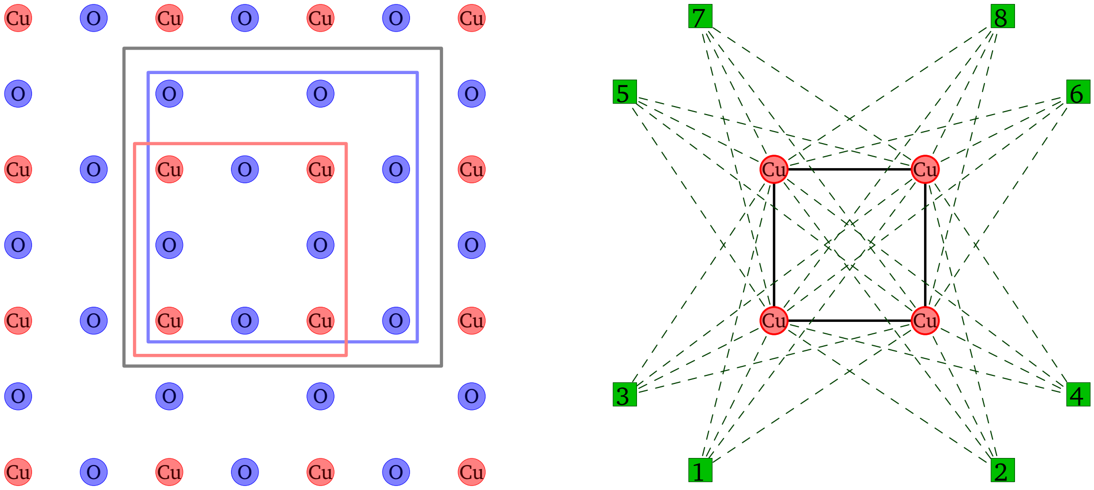

(a) (b)

Figure 4.16: Cartoon of the cluster-bath impurity model. (a) The $\mathrm{CuO_2}$ lattice is shown along with the super-cell (gray box). The super-cell contains 4 correlated Cu orbitals (red) and 8 uncorrelated O orbitals (blue). (b) The four correlated Cu orbitals in the super-cell are chosen to form the cluster in the impurity model for CDMFT. O orbitals are not included in the cluster since they are uncorrelated; they are taken into account in the CDMFT self-consistency through a constant hybridization function $\mathbf{\Gamma}_{\mathrm{O}}$ in the lattice Green function Eq. (4.12). Each site in the cluster is attached to 8 uncorrelated bath orbitals to form the cluster-bath impurity model.

we minimize the distance function Eq. (3.56) with

$$\bar{\mathbf{G}}(z) = \frac{4}{N} \sum_{\tilde{\mathbf{k}}} \mathbf{G}_{\mathrm{Cu}}(\tilde{\mathbf{k}}, z)\,, \tag{4.13}$$

with respect to the bath parameters. We use the weight function $W(i\omega_n)$ as defined in Eq. (3.57) with $\beta = 50/t_{pp}$ and $\omega_c = 2t_{pp}$. We made our choice based on ref. [165] after trying a few other values.

The bath hybridization function is given by (see section 3.3.3)

$$\mathbf{\Gamma} = \mathbf{\Theta}\,(z - \mathbf{E})^{-1}\,\mathbf{\Theta}^{\dagger}\,, \tag{4.14}$$

where

$$\mathbf{\Theta} = \begin{pmatrix} \boldsymbol{\theta} & -\mathbf{\Delta}^{\dagger} \\ -\mathbf{\Delta}^{T} & -\boldsymbol{\theta}^{*} \end{pmatrix}, \mathbf{E} = \begin{pmatrix} \boldsymbol{\epsilon} & \mathbf{0} \\ \mathbf{0} & -\boldsymbol{\epsilon} \end{pmatrix}. \tag{4.15}$$

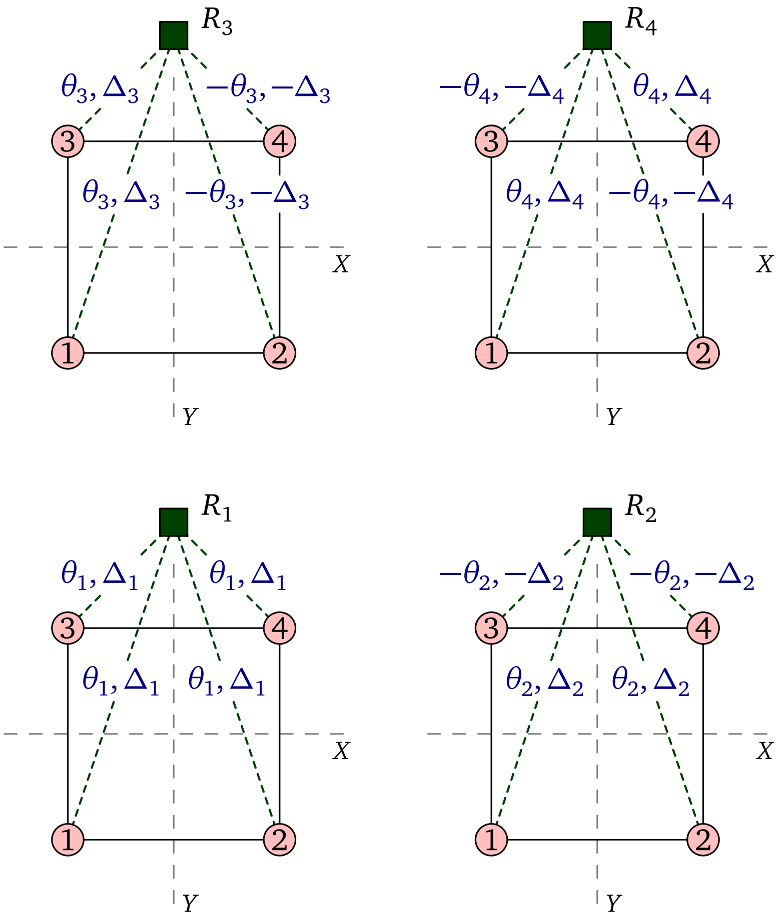

R_3
θ_3, Δ_3
$-\theta_3, -\Delta_3$
3
4
θ_3, Δ_3
$-\theta_3, -\Delta_3$
X
1
2
Y
R_4
$-\theta_4, -\Delta_4$
θ_4, Δ_4
3
4
θ_4, Δ_4
$-\theta_4, -\Delta_4$
X
1
2
Y
R_1
θ_1, Δ_1
θ_1, Δ_1
3
4
θ_1, Δ_1
θ_1, Δ_1
X
1
2
Y
R_2
$-\theta_2, -\Delta_2$
$-\theta_2, -\Delta_2$
3
4
θ_2, Δ_2
θ_2, Δ_2
X
1
2
Y

Figure 4.17: Cluster-bath hybridization. Cluster-bath hybridization terms corresponding to the 4 irreducible representations (labelled as R_i) of the point group C_{2v}. The elements of $\boldsymbol{\theta}$ are labelled as $\pm\theta_i$; for instance, if $\pm\theta_1$ appears on the bond between the cluster site 1 and a bath orbital, say k, then the matrix element (see Eq. (3.60)) $\theta_{1k} = \pm\theta_1$. Similarly, the elements of $\boldsymbol{\Delta}$ are labelled as $\pm\Delta_i$. Note that we have 8 bath orbitals in total; we take the hybridization of the cluster with 2 bath orbitals corresponding to each irreducible representation R_i.

Here $\boldsymbol{\theta}$ is the 4×8 cluster-bath hybridization matrix, $\boldsymbol{\Delta}$ is the 8×4 anomalous hybridization matrix between the cluster and the bath, and $\boldsymbol{\epsilon}$ is the 8×8 bath Hamiltonian matrix. Without loss of generality, we can take the bath Hamiltonian matrix $\boldsymbol{\epsilon}$ to be a diagonal matrix containing the energies of the eight bath orbitals as the diagonal elements, since we can always choose the basis with respect to which the bath Hamiltonian is diagonal. Hence, the total number of bath parameters with respect to which the distance function Eq. (3.56) is to be minimized is $32 + 32 + 8 = 72$.

As mentioned briefly in sec. 3.3.3, it is possible to reduce the number of independent bath parameters, by using various point group symmetries of the cluster [89, 166]. In this work, we follow Foley *et al.* [89] to parametrize the bath based on the irreducible representations of the point group $C_{2v} = \{e, \sigma_{yz}, \sigma_{xz}, C_2\}$, where e is the identity operation, σ_{yz} is the reflection across the YZ plane, σ_{xz} is the reflection across the XZ plane and C_2 is the two-fold rotation (by 180°) about the Z-axis.

The simplest basis for describing a single-particle state on the cluster is given by the set of localized Wannier states on the four cluster sites

$$\mathbb{B} = \{|1\rangle, |2\rangle, |3\rangle, |4\rangle\} \,, \tag{4.16}$$

where the state $|i\rangle$ corresponds to the Wannier state localized on the cluster site i (Fig. 4.17). The basis states transform under C_{2v} as follows:

$$\begin{pmatrix} |1\rangle \\ |2\rangle \\ |3\rangle \\ |4\rangle \end{pmatrix} \xrightarrow{e} \begin{pmatrix} |1\rangle \\ |2\rangle \\ |3\rangle \\ |4\rangle \end{pmatrix} \,, \quad \begin{pmatrix} |1\rangle \\ |2\rangle \\ |3\rangle \\ |4\rangle \end{pmatrix} \xrightarrow{\sigma_{yz}} \begin{pmatrix} |2\rangle \\ |1\rangle \\ |4\rangle \\ |3\rangle \end{pmatrix} \,, \quad \begin{pmatrix} |1\rangle \\ |2\rangle \\ |3\rangle \\ |4\rangle \end{pmatrix} \xrightarrow{\sigma_{xz}} \begin{pmatrix} |3\rangle \\ |4\rangle \\ |1\rangle \\ |2\rangle \end{pmatrix} \,, \quad \begin{pmatrix} |1\rangle \\ |2\rangle \\ |3\rangle \\ |4\rangle \end{pmatrix} \xrightarrow{C_2} \begin{pmatrix} |4\rangle \\ |3\rangle \\ |2\rangle \\ |1\rangle \end{pmatrix} \,. \tag{4.17}$$

If we use the basis

$$\begin{aligned} \mathbb{B}_{\text{ir}} &= \{|00\rangle, |01\rangle, |10\rangle, |11\rangle\} \,, \qquad (4.18) \\ |00\rangle &= \frac{1}{2}\left(|1\rangle + |2\rangle + |3\rangle + |4\rangle\right) \,, \\ |01\rangle &= \frac{1}{2}\left(|1\rangle + |2\rangle - |3\rangle - |4\rangle\right) \,, \\ |10\rangle &= \frac{1}{2}\left(|1\rangle - |2\rangle + |3\rangle - |4\rangle\right) \,, \\ |11\rangle &= \frac{1}{2}\left(|1\rangle - |2\rangle - |3\rangle + |4\rangle\right) \,, \end{aligned}$$

we can express all the symmetry transformations in the group C_{2v} as diagonal matrices with elements equal to ±1. $\mathbb{B}_{\text{ir}}$ is the basis in which the matrix representations of the elements of the group C_{2v} are not further reducible, i.e., it is not possible to lower the mixing further between basis elements (also there is no mixing at all in this case) for all symmetry transformations by doing a basis change. Hence, the basis $\mathbb{B}_{\text{ir}}$ corresponds to the irreducible representations of C_{2v}. It is useful to parameterize the cluster-bath hybridization in terms of the irreducible representations, since this uses the least number of parameters to do so. Fig. 4.17 shows the cluster-bath hybridization terms (both normal and anomalous) corresponding to the irreducible representations of C_{2v}, where R_i corresponds to the ith element of the basis $\mathbb{B}_{\text{ir}}$. We parametrize the hybridization terms for the bath orbitals i and $i+4$ using the irreducible representation R_i, where $i = 1, 2, 3, 4$. Hence, the bath hybridization matrices $\boldsymbol{\theta}$ and $\boldsymbol{\Delta}$ become

$$\boldsymbol{\theta} = \begin{pmatrix} \theta_1 & \theta_2 & \theta_3 & \theta_4 & \theta_5 & \theta_6 & \theta_7 & \theta_8 \\ \theta_1 & \theta_2 & -\theta_3 & -\theta_4 & \theta_5 & \theta_6 & -\theta_7 & -\theta_8 \\ \theta_1 & -\theta_2 & \theta_3 & -\theta_4 & \theta_5 & -\theta_6 & \theta_7 & -\theta_8 \\ \theta_1 & -\theta_2 & -\theta_3 & \theta_4 & \theta_5 & -\theta_6 & -\theta_7 & \theta_8 \end{pmatrix}, \tag{4.19}$$

$$\boldsymbol{\Delta} = \begin{pmatrix} \Delta_1 & \Delta_2 & \Delta_3 & \Delta_4 & \Delta_5 & \Delta_6 & \Delta_7 & \Delta_8 \\ \Delta_1 & \Delta_2 & -\Delta_3 & -\Delta_4 & \Delta_5 & \Delta_6 & -\Delta_7 & -\Delta_8 \\ \Delta_1 & -\Delta_2 & \Delta_3 & -\Delta_4 & \Delta_5 & -\Delta_6 & \Delta_7 & -\Delta_8 \\ \Delta_1 & -\Delta_2 & -\Delta_3 & \Delta_4 & \Delta_5 & -\Delta_6 & -\Delta_7 & \Delta_8 \end{pmatrix}. \tag{4.20}$$

Note that we now have a total of 2×8 (from $\boldsymbol{\theta}$ and $\boldsymbol{\Delta}$) $+\ 8$ (from $\boldsymbol{\epsilon}$) $= 24$ bath parameters with respect to which we have to minimize the distance function Eq. (3.56) in each CDMFT iteration. We consider the CDMFT iterations to have converged when the bath hybridization function $\boldsymbol{\Gamma}(\omega)$ converges. The criteria for the convergence of the bath hybridization function $\mathbf{\Gamma}(\omega)$ is defined as when $\delta\mathbf{\Gamma} \leq 10^{-5}$, where

$$\delta\mathbf{\Gamma} = \left[\frac{1}{N}\sum_{n=1}^{N} W(i\omega_n)||\mathbf{\Gamma}_j(i\omega_n) - \mathbf{\Gamma}_{j-1}(i\omega_n)||^2\right]^{1/2}, \tag{4.21}$$

$\mathbf{\Gamma}_j(i\omega_n)$ is the bath hybridization function at the jth iteration and $||\mathbf{A}|| = \sqrt{\sum_{i,j}|A_{ij}|^2}$ is the norm of a matrix $\mathbf{A}$.

For obtaining the normal phase, we do not break the $U(1)$ gauge symmetry in the impurity model, i.e., $\mathbf{\Delta} = \mathbf{0}$ in Eq. (4.15), (4.20).

4.8 Perspective

The one-band Hubbard model also captures some of the qualitative features indicating the presence of the pseudogap within the superconducting phase at low doping values [47, 48], where the onset of the pseudogap only appears as a smooth crossover. For instance, Ref. [47] observes that the superconducting gap near the nodal region behaves differently than the total superconducting gap (integrated over momentum) as a function of doping at low doping values, while both these gaps are equal at high values of hole doping; the nodal gap diverges from the total gap below the critical doping $p_c \approx 0.08$ and starts decreasing, while the total gap continues to increase until very low doping values. This behavior is similar to what we observe in Fig. 4.5, where we plot the superconducting order parameter and the magnitude of the gap as a function of hole doping, except for a first-order transition at the critical doping in our case. The nodal gap in ref. [47] is a measure of the superconducting strength which is given by our order parameter in Fig. 4.5. Thus, the increasing total superconducting gap until very low values of hole doping strongly suggests the presence of a pseudogap along with superconductivity in both the one-band and three-band Hubbard models. In our calculations, the critical doping p_c is around $0.05 - 0.08$ for parameter-sets around the ionic case Eq. (4.1) and around $0.08 - 0.12$ for parameter-sets around the covalent case Eq. (4.2).

Although there have been no reports of a first-order transition within the superconducting phase in previous studies of the Hubbard model with CDMFT, it is known that the onset of the pseudogap appears as a first-order transition in the normal phase, which we refer to as the *Sordi* transition [49–51, 88, 138]. This transition is observed below a certain critical temperature, close to the critical value of U (above the critical value U_c) for the metal-insulator transition, with a region of hysteresis (along the chemical potential for a given U and vice versa) where two metallic solutions might coexist. This becomes a crossover at higher temperatures (the crossover line is known as the Widom line) [88,138]. Moreover, the hysteresis region is connected to the hysteresis in U at half-filling [49, 50], suggesting that the first-order transition corresponding to the pseudogap is connected to the Mott transition. The first-order transition in our case is also connected to the physics of the metal-insulator transition at zero doping ($n = 5$), as seen in Fig. 4.8. Thus, there are strong indications that the first-order transition in our case is the remnant of the Sordi transition within the superconducting phase.

Note that everything that we observe here in the doped insulator are only the effects of the short-range correlations, i.e., within the 2×2 cluster. The fact that our observation of the first-order transition and the correlation between the order parameter and oxygen hole content are consistent qualitatively with experiments strongly implies that the short-range correlations are the dominant players in cuprate superconductivity. However, our results do not predict all the quantitative details correctly. For instance, the onset of the pseudogap within the superconducting phase of $Bi_2Sr_2CaCu_2O_{8+\delta}$ occurs at a critical doping $p_c \approx 0.19$ [46], 0.22 [176]. This corresponds to the parameter-set (4.2) in our calculations, where the first-order transition occurs around the critical value $p_c \approx$ 0.08-0.12 which is much lower than the experimental values. Thus, it seems that although the long-range correlations do not play an important role, they might be essential for describing the correct critical doping p_c.

One of the straightforward future directions would be to track the first-order transition that we associate with the onset of the pseudogap within the superconducting phase, in the three-band Hubbard model, as a function of temperature, to see whether the critical temperature T_p at which the transition ends is below or above or equal to the superconducting critical temperature T_c. It would also be useful to compare the T_p with that for the Sordi transition (i.e. in the normal phase) within the three-band Hubbard model [138], to see if they have the same end points. This would require a finite-T impurity solver. For instance, recently a first-order transition was observed within the superconducting phase in the same model (three-band Hubbard model with the ionic parameter-set (4.1)) at finite temperatures using CDMFT with a CTQMC solver [177].

Summary

In this chapter, we studied the three-band Hubbard model using cluster dynamical mean field theory with an exact diagonalization impurity solver at zero temperature, for various parameter-sets. We observed a discontinuous transition within the superconducting phase, which we associate with the onset of the pseudogap based on various signatures consistent with the literature. In addition, we observed that the maximum order parameter scales with the antiferromagnetic superexchange J across all parameter-sets (including parameter-sets corresponding to various cuprate families), which implies that pairing within this model is caused by the short-range antiferromagnetic fluctuations. Furthermore, we observed a correlation between the maximum order parameter and the hole content on oxygen orbitals, as observed in experiments, which followed from the correlation of the maximum order parameter with J. The main results regarding the onset of the pseudogap within the superconducting phase are published in *"S. S. Dash and D. Sénéchal. Pseudogap transition within the superconducting phase in the three-band Hubbard model.* Physical Review B*, 100(21):214509, 2019. URL:* `https://journals.aps.org/prb/abstract/10.1103/PhysRevB.100.214509`*"*, and the results regarding the antiferromagnetic origin of superconductivity in the three-band Hubbard model are published in *"N Kowalski, SS Dash, P Sémon, D Sénéchal, and AMS Tremblay. Oxygen hole content, charge-transfer gap, covalency, and cuprate superconductivity.* Proceedings of the National Academy of Sciences*, 118(40), 2021. URL:* `https://www.pnas.org/content/118/40/e2106476118`*"*.

Chapter 5

Charge density waves in the one-band Hubbard model

In this chapter, we study various density-wave (charge-density, bond-density and pair-density) orders within the one-band Hubbard model, using cluster dynamical mean field theory (CDMFT) with an exact diagonalization (ED) impurity solver at zero temperature. We perform CDMFT computations on the one-band Hubbard model with parameter sets corresponding to cuprate superconductors. We investigate various density-wave orders within CDMFT, and study the relation between the dominant density-wave order and superconductivity. We answer the questions that we ask in page 16. Let us summarize the main outcomes:

1. We obtain various density-wave orders: d-wave bond-density-wave, s'-wave bond-density-wave and s-wave charge-density-wave orders above a certain critical hole doping and all of them are weakened on increasing U in the normal state (no superconductivity).

2. We observe that the d-wave bond-density-wave (BDW) order is the dominant density-wave (DW) order in the one-band Hubbard model, as also seen in experiments on cuprates.
3. We observe that the d-wave BDW order is in competition with superconductivity when both orders coexist.
4. We observe that the coexistence of the BDW order and superconductivity leads to a s'-wave pair-density-wave (PDW) order which is weaker than both BDW order and superconductivity.
5. We observe that the d-wave BDW order grows on increasing the frustration on the lattice (by increasing the magnitude of the second nearest neighbor hopping t').

In section 5.1, we set the parameters of the one-band Hubbard model. In section 5.2, we define various DW operators which we probe in this work. In section 5.3, we present the results of our CDMFT computations on doping the Mott insulator, where we observe finite values of various DW order parameters both in the normal phase and in coexistence with superconductivity. In section 5.4, we observe and study the competition between d-wave BDW order and superconductivity. In section 5.5, we discuss the exact cluster-bath impurity model used in our CDMFT computations. In section 5.6, we provide a brief perspective on our results.

5.1 Parameters of the model

We study the one-band Hubbard model (Eq. (2.27)) by limiting ourselves to the first, second and third nearest neighbor hopping terms given by t, t' and t'' respectively, where

$$t = 1.0, t' = -0.3, t'' = 0.2 \tag{5.1}$$

unless otherwise stated. The parameter set Eq. (5.1) corresponds to $Bi_2Sr_2CaCu_2O_8$ (BSCO) [180] and also, to some extent, to $YBa_2Cu_3O_7$ (YBCO) [134]. All energies (including U and μ) are measured in units of t.

5.2 Definition of various density-wave order parameters

In real (cuprate) materials, charge density modulation occurs at the sites of O orbitals in the CuO_2 planes [52, 54]. In the one-band Hubbard model, since we do not explicitly include O orbitals in the lattice, the best way to incorporate the charge-density modulations on O orbitals is to include them as bond-density modulations on the first-neighbor bonds (Fig. 5.1(a), (b)) [64]. This is justified, since the actual position of O orbitals are at the centre of the first-neighbor bonds in the one-band Hubbard model. We define the bond-density-wave (BDW) operator as follows

$$\hat{\Psi}_{\text{BDW}} = \sum_{\mathbf{r}\sigma,\mathbf{a}} t_{\mathbf{q},\mathbf{a}} c^{\dagger}_{\mathbf{r},\sigma} c_{\mathbf{r}+\mathbf{a},\sigma} e^{i\mathbf{q}\cdot(\mathbf{r}+\mathbf{a}/2)} + \text{H.c.}\,, \tag{5.2}$$

where $\mathbf{a} = \pm\hat{\mathbf{x}},\ \pm\hat{\mathbf{y}}$. $t_{\mathbf{q},\mathbf{a}}$ decides the symmetry of the BDW modulation; $t_{\mathbf{q},\hat{\mathbf{x}}} = -t_{\mathbf{q},\hat{\mathbf{y}}} = 1$ leads to a d-wave BDW (Fig. 5.1(a)) and $t_{\mathbf{q},\hat{\mathbf{x}}} = t_{\mathbf{q},\hat{\mathbf{y}}} = 1$ leads to a s'-wave (extended s-wave) BDW (Fig. 5.1(b)).

We also study charge-density-waves centered on the lattice sites (Fig. 5.1(c)), given by the operator

$$\hat{\Psi}_{\text{CDW}} = \sum_{\mathbf{r}\sigma} c^{\dagger}_{\mathbf{r},\sigma} c_{\mathbf{r},\sigma} e^{i\mathbf{q}\cdot\mathbf{r}} + \text{H.c.}\,. \tag{5.3}$$

Finally, the pair-density-wave (PDW) operator is given by

$$\hat{\Psi}_{\text{PDW}} = \sum_{\mathbf{r},\mathbf{a}} u_{\mathbf{q},\mathbf{a}} \left(c_{\mathbf{r},\uparrow} c_{\mathbf{r}+\mathbf{a},\downarrow} - c_{\mathbf{r},\downarrow} c_{\mathbf{r}+\mathbf{a},\uparrow} \right) e^{i\mathbf{q}\cdot(\mathbf{r}+\mathbf{a}/2)} + \text{H.c.}\,, \tag{5.4}$$

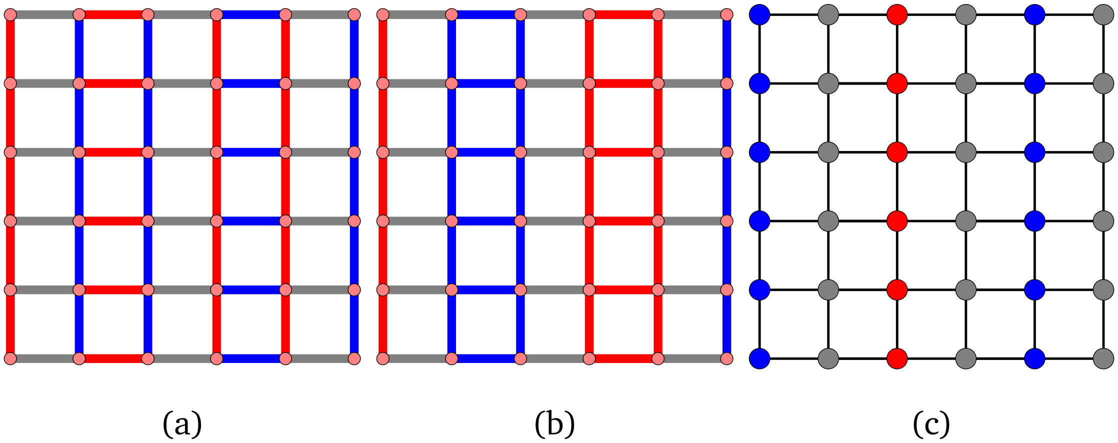
(a) (b) (c)

Figure 5.1: Cartoon of density-wave (DW) modulations on the lattice. Red indicates the negative amplitude, blue indicates the positive amplitude and gray indicates zero. (a) d-wave bond/pair-density-wave (BDW/PDW) modulation, (b) s'-wave BDW/PDW modulation, (c) s-wave charge-density-wave (CDW) modulation.

where $\mathbf{a} = \pm\hat{\mathbf{x}},\ \hat{\mathbf{y}}$. We focus on a s'-wave PDW, expected from the coexistence of the dominant d-wave BDW and d-wave superconductivity as seen in experiments [81], so we take $u_{\mathbf{q},\hat{\mathbf{x}}} = u_{\mathbf{q},\hat{\mathbf{y}}} = 1$. The order parameters corresponding to the density-wave operators Eqs. (5.2), (5.3), (5.4) are obtained by calculating the averages of the respective quantities as given by Eq. (2.18). We focus only on unidirectional period-4 density modulations as mostly seen in experiments [52, 54, 81], i.e., $\mathbf{q} = 2\pi/4\hat{\mathbf{x}}$ in Eqs. (5.2), (5.3), (5.4). Note that the different DW orders (s-wave CDW, s'-wave BDW and d-wave BDW) are the manifestations of the same broken translational symmetry and are not competing orders. The PDW order is caused by a broken translational symmetry as well by the broken $U(1)$-gauge symmetry.

5.3 Density-wave orders in a doped Mott insulator

We obtain finite values of various kinds of density-wave (DW) order parameters on hole doping the Mott insulator, only beyond a certain critical value of hole doping. Fig. 5.2 shows the d-wave BDW, s'-wave BDW and s-wave CDW order parameters for the parameter-set (5.1) with various values of the on-site Coulomb repulsion U. The d-wave BDW order is observed to be the dominant DW order; the s'-wave BDW order and the s-wave CDW order are weaker and have a magnitude which is always less than half of that of the d-wave BDW order at any given doping and U. This is consistent with the experiments on cuprates [54, 56], where it is observed that the d-wave CDW centered on O orbitals is the dominant DW order, with weaker s'-wave CDW centered on O orbitals and s-wave CDW centered on Cu orbitals. Note again that the BDW modulation in our model corresponds, in experiments, to a CDW modulation centered on the O orbitals and the CDW modulation in our model corresponds to CDW modulations centered on Cu orbitals. We focus on the d-wave BDW order for the rest of this chapter.

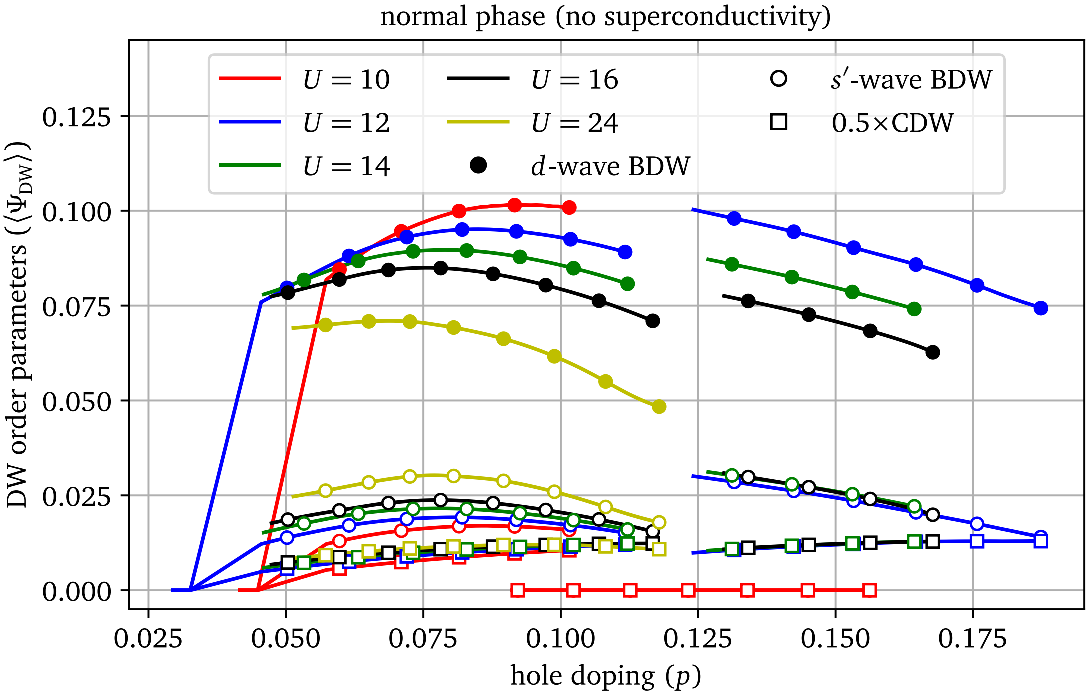

Figure 5.2: Density-wave order in the normal phase. Various density-wave (DW) order parameters as functions of hole doping in the normal phase (no superconductivity or antiferromagnetism) with parameter-set (5.1) for various values of U. The d-wave BDW order (filled circles) is the dominant DW order, as also seen in experiments [54]. The s'-wave BDW (open circles) and the CDW (open squares) orders are much weaker. Note that we have shown only 1/10th of the total number of points that we have, for clarity. The d-wave BDW order parameter decreases with U monotonously close to the optimal doping values (where $\partial \langle \Psi_{\mathrm{BDW}} \rangle / \partial p = 0$)

Note that there is a discontinuous transition in most of the order parameter curves; around $p = 0.1$ for $U = 10$ and around $p = 0.12$ for $U = 12,\ 14,\ 16$. This is an artefact of CDMFT with a finite bath and is realized when the particle number is conserved [1], i.e., in the normal phase (no superconductivity). In this case, when the (integer) number of electrons in the cluster-bath impurity model changes due to a sufficient change in the chemical potential, it is accompanied by a discontinuous transition which also appears as a hysteresis in some cases (for $U = 10$). Note, however, that the transition, which leads to the density-wave ordered state on the low doping side (we see it at around $p = 0.04$ for $U = 12$ and around $p = 0.055$ for $U = 10$), is not accompanied by any change in the total occupation of the cluster-bath impurity model.

We observe that the strength of the d-wave BDW order decreases on increasing U for most of the hole doping range where we obtain a solution. In particular, the optimal value of the d-wave BDW order parameter, i.e., the value of the order parameter where $\partial \langle \Psi_{\text{BDW}} \rangle / \partial p = 0$, clearly decreases with increase in U. This behavior could offer significant insights on the origin of the d-wave BDW order. For instance, the fact that the optimal superconducting order parameter (or T_c) is suppressed on increasing U within the one-band Hubbard model [87–89] is an indication that pairing within the model is mediated by short-range antiferromagnetic fluctuations [99,100] (also seen in the last chapter for the three-band Hubbard model) since the antiferromagnetic superexchange $J \propto 1/U$. This is also reinforced by the fact that the maximum superconducting T_c scales as J [88]. Hence, the suppression of the optimal d-wave BDW order with U could point towards a possible antiferromagnetic origin. Various theoretical studies using many variations of the t-J model have obtained the BDW order [67, 69–75], suggesting that the antiferromagnetic fluctuations are crucial for the BDW order. Fig. 5.3 shows the optimal d-wave BDW order parameter as a function of $1/U$ along with fits for the curve with polynomial functions of degrees 1 to 4. The coefficients for the polynomials are tabulated in Tab. 5.1. Note from

---

[1] This is not the case with the discontinuous transition seen in chapter 4, where the particle number is not conserved because of the broken $U(1)$ gauge symmetry in the superconducting phase.

Fig. 5.3 that the linear fit has a finite y-intercept. However, the y-intercepts of the fits (coefficient a_0 in Tab. 5.1) decreases as the fits become better by increasing the degree of the fitted polynomial. This suggests that the optimal d-wave BDW order parameter tends to go to zero as $U \to \infty$. At first sight, this favors the case of an antiferromagnetic origin for the d-wave BDW order.

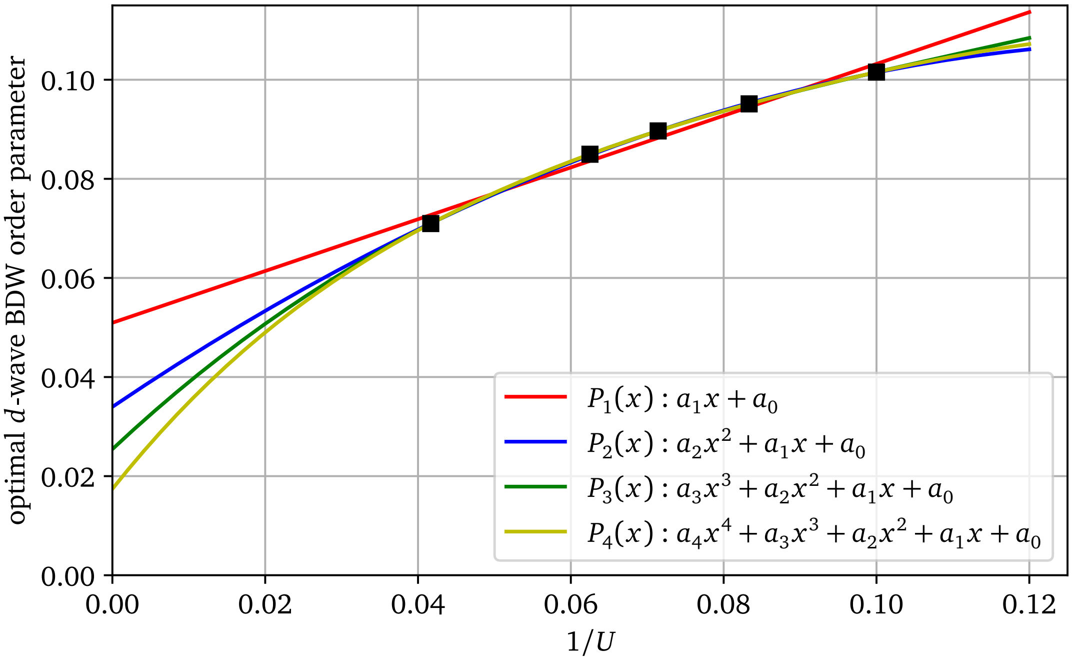

Figure 5.3: Scaling of the maximum BDW order parameter with $1/U$. Optimal value of the d-wave BDW order parameter (i.e., at doping p, where $\partial \langle \Psi_{\text{BDW}} \rangle / \partial p = 0$, in Fig. 5.2), in the normal phase, as a function of $1/U$, fitted with polynomial functions of various degrees. The coefficients of the polynomial functions are tabulated in table. 5.1. Note that the y-intercept of the fits decreases with the degree of the fitted polynomial, which suggests that the order parameter goes to zero as U becomes very large.

Table 5.1: Fit parameters of the polynomial functions used in Fig. 5.3.

	$P_1(x)$	$P_2(x)$	$P_3(x)$	$P_4(x)$
a_0	0.051 ± 0.0031	0.034 ± 0.0012	0.025 ± 0.00077	0.017
a_1	0.52 ± 0.042	1.043 ± 0.034	1.45 ± 0.036	1.94
a_2		-3.68 ± 0.24	-9.71 ± 0.54	-20.73
a_3			28.35 ± 2.52	133.67
a_4				-366.26

It is known that frustration on the lattice is detrimental to the antiferromagnetic fluctuations; in the one-band Hubbard model, the lattice frustration can be increased by increasing the magnitude of the second-neighbor hopping parameter t'. To investigate further the role of antiferromagnetic fluctuations on the BDW order, we vary the parameter t' in Eq. 5.1 while keeping other parameters constant at $U = 12$. Fig. 5.4 shows the d-wave BDW order parameter as a function of doping for various values of t' at $U = 12$. Note that we also observe the discontinuous transition here related to the change in the occupation number of the impurity model for the curves at $t' = -0.15$, -0.3, -0.4. The optimal value of the d-wave BDW order parameter increases when increasing the magnitude of t'. This suggests that lattice frustration actually favours the d-wave BDW order. Contrary to our conclusions from Fig. 5.3, this means that the suppression of antiferromagnetic fluctuations favours the d-wave BDW order; this suggests a competititve relationship between the two.

Further, to make sure that the growth of the d-wave BDW order parameter with $|t'|$ is not due to a change in the effective U, i.e., U/bandwidth, we checked that the non-interacting bandwidth remains at a constant value of 8 while t' changes from 0 to -0.4. This suggests that the growth of the d-wave BDW order as t' varies from 0 to -0.4 can be entirely ascribed to lattice frustration; this strengthens the argument that the antiferromagnetic fluctuations are detrimental for the d-wave BDW order. On the other hand, the superconducting order parameter is weakened, in the hole doped side, with an increase in $|t'|$ in the one-band Hubbard model [87], which is consistent with the fact that pairing is mediated by antiferromagnetic fluctuations [99].

5.4 Competition between BDW and superconductivity

We also study the d-wave BDW order in the presence of superconductivity; we achieve this by probing the coexistence phase where both superconductivity and DW orders are

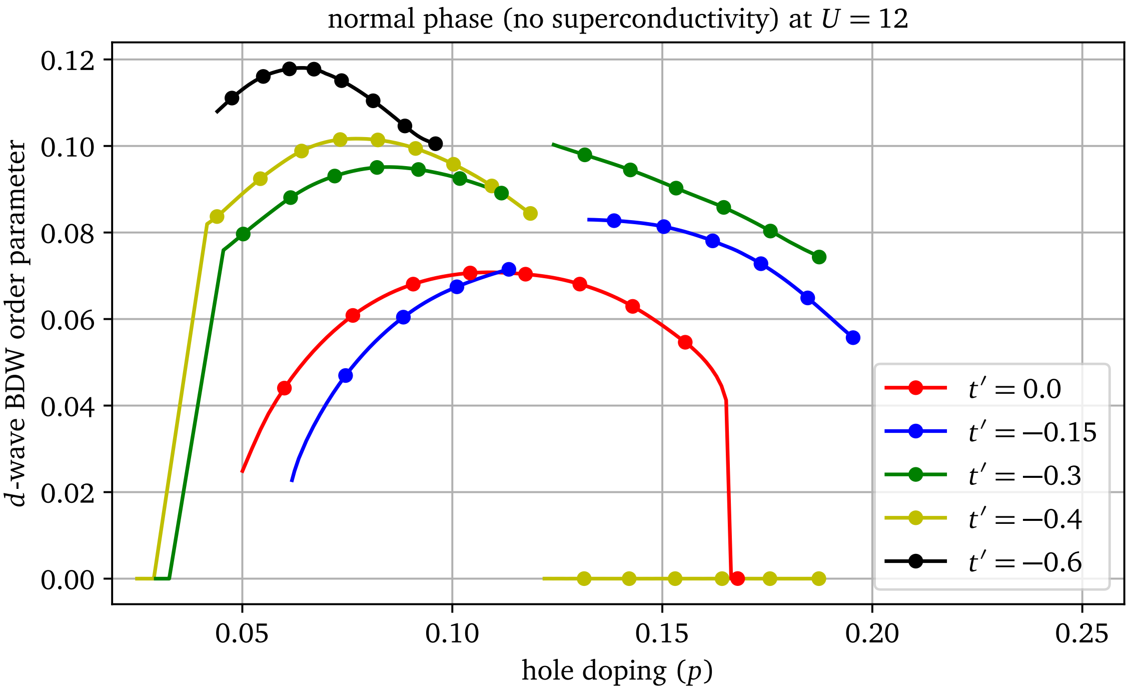

Figure 5.4: Effect of the second-neighbor hopping t' on the BDW order. d-wave BDW order parameter as a function of hole doping with the parameter-set (5.1), with various values of t', for $U = 12$. The optimal value of the order parameter increases with the magnitude of t', suggesting that the BDW order is favoured by lattice frustration. We have shown only 1/10th of the total number of points that we have, for clarity.

allowed in the impurity model (see sec. 5.5 for details on the impurity model). Figs. 5.5, 5.6 show the d-wave BDW order parameter, the d-wave superconducting order parameter and the s'-wave PDW order parameter as funtions of hole doping at $U = 14,\ 16$ respectively in the coexistence phase. Along with these, we also show the pure BDW order parameter (in the normal phase: no superconductivity) and the pure superconducting order parameter (in the superconducting phase: no DW) in Figs. 5.5, 5.6 at $U = 14$ and 16, respectively. The BDW order in the coexistence phase (filled red circles) is observed to be weaker than in the normal phase (open red circles). Moreover, the BDW order parameter in the coexistence phase starts taking non-zero values only above $p \approx 0.14$, in contrast to the normal phase where it has non-zero values as soon as $p \approx 0.05$. Furthermore, the superconducting order in the coexistence phase (filled blue circles) is also weaker than in the superconducting phase (open blue circles). Note that the superconducting order

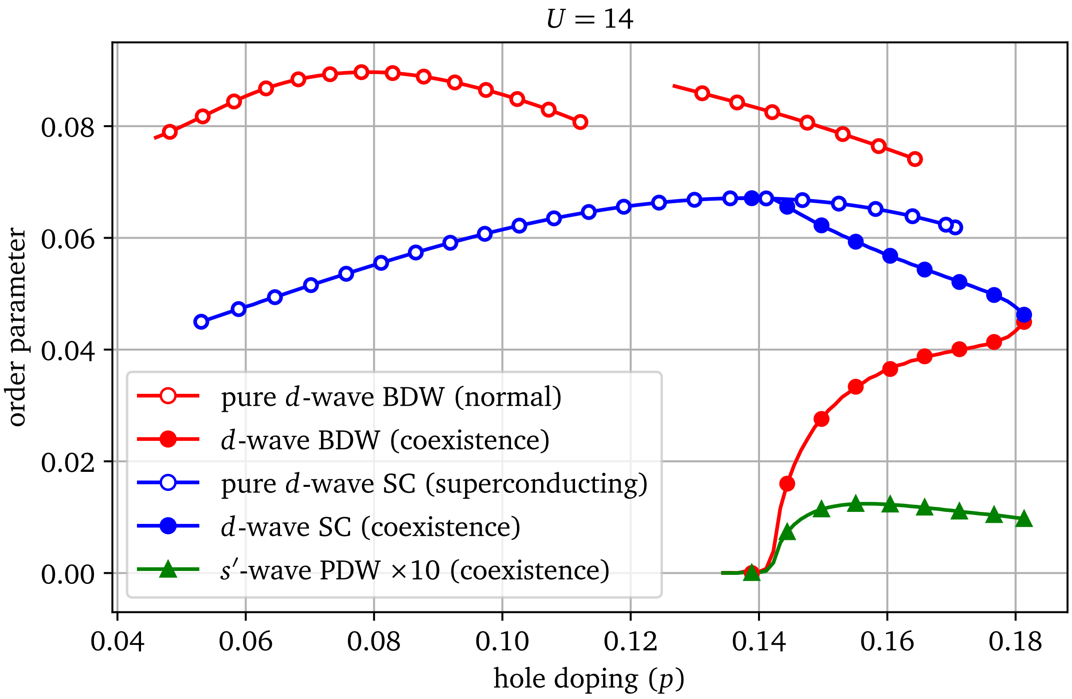

Figure 5.5: The *normal*, *superconducting* and *coexistence* phases at $U = 14$. Order parameters in the coexistence phase compared with those in the normal and the superconducting phases, with parameter-set (5.1) at $U = 14$. The d-wave BDW order parameter in the coexistence phase (filled red symbols) is much weaker than that in the normal phase (open red symbols), and only takes non-zero values above $p \sim 0.14$. Moreover, the BDW order parameter in the coexistence phase increases with doping as the superconducting order parameter decreases; this suggests that the BDW order is suppressed by superconductivity. The superconducting order parameter in the coexistence phase (filled blue symbols) is also weaker than that in the superconducting phase (open blue symbols). Further, the superconducting order parameter in the coexistence phase becomes equal to that in the superconducting phase as the BDW order goes to zero in the coexistence phase; this suggests that superconductivity is also suppressed by the BDW order. A very weak s'-wave pair-density-wave (PDW) order parameter is observed when the BDW order and superconductivity coexist. Note that we have shown only 1/5th of the total number of data points that we have, for clarity.

parameter in the coexistence phase becomes equal to that in the superconducting phase when the BDW order parameter vanishes. Hence, we observe that the d-wave BDW order and the superconducting order suppress each other when they coexist.

The amount by which the BDW (superconducting) order is weakened in the coexistence phase compared to when it is present alone, at a given value of doping, depends on the strength of the superconducting (BDW) order in the coexistence phase. This can be

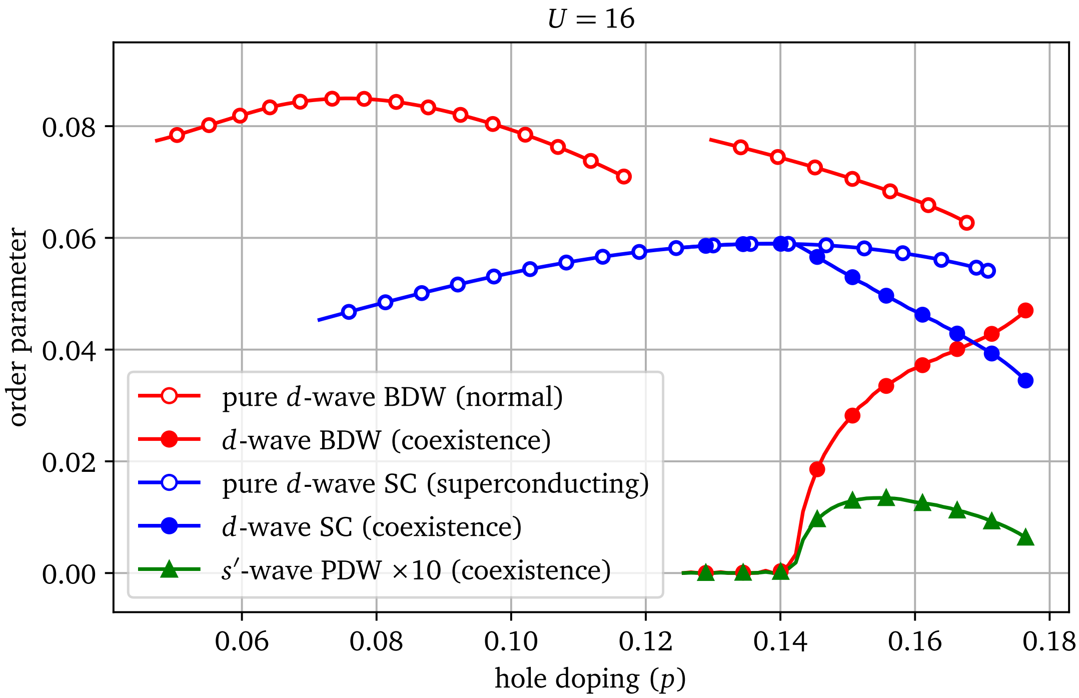

Figure 5.6: The *normal*, *superconducting* and *coexistence* phases at $U = 16$. Order parameters in the coexistence phase compared with those in the normal and the superconducting phases with parameter-set (5.1) at $U = 16$. The d-wave BDW order and superconductivity suppress each other in the coexistence phase as also seen for $U = 14$ (Fig. 5.5). We also observe a very weak PDW order parameter when both BDW and superconducting order parameters take non-zero values. We have shown only 1/5th of the total number of data points that we have, for clarity.

seen clearly in Fig. 5.7. In Fig. 5.7(a), the ratio of the d-wave BDW order parameter in the coexistence phase to that in the normal phase is plotted as a function of the superconducting order parameter in the coexistence phase for $U = 14,\ 16$. We observe that this ratio decreases monotonously as the superconducting order parameter increases in the coexistence phase, for both values of U. Similarly, in Fig. 5.7(b), the ratio of the superconducting order parameter in the coexistence phase to that in the (pure) superconducting phase is plotted as a function of the d-wave BDW order parameter in the coexistence phase. This ratio is equal to 1, when the d-wave BDW order parameter is zero, and decreases as the strength of the BDW order increases; this is an important observation which tells us that the only reason why the superconducting order is weaker in the coexistence phase is the presence of the BDW order. This clearly suggests that the d-wave BDW order and the

d-wave superconducting order compete with each other. Note, however, that the amount by which a given magnitude of the BDW order (superconducting order) weakens the superconducting order (BDW order) is higher for $U = 16$ than for $U = 14$.

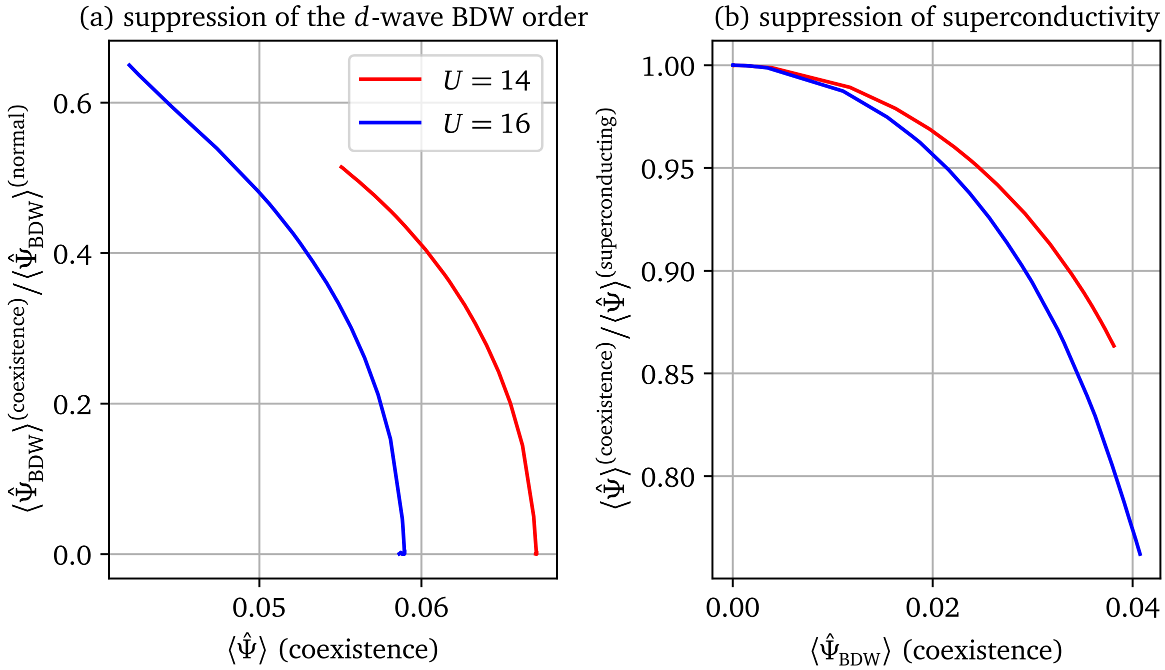
(a) suppression of the d-wave BDW order

(b) suppression of superconductivity

Figure 5.7: Competition between the BDW order and superconductivity. A more systematic way to show the competition between the BDW order and superconductivity using the data from Figs. 5.5, 5.6: the amount of suppression of an order in the coexistence phase (ratio of the order parameter in the coexistence phase to that in the pure phase) is plotted as a function of the magnitude of the other order parameter. We use interpolation of the data in Figs. 5.5, 5.6 to obtain a particular order parameter at a given doping in different phases. (a) Ratio of the BDW order parameter in the coexistence phase to that in the normal phase as a function of the superconducting order parameter in the coexistence phase for $U = 14,\ 16$. This ratio decreases as the magnitude of the superconducting order parameter increases in the coexistence phase for both values of U, suggesting that a higher value of the superconducting order parameter suppresses more the BDW order. (b) Ratio of the superconducting order parameter in the coexistence phase to that in the superconducting phase as a function of the BDW order parameter in the coexistence phase. This ratio also decreases as the magnitude of the BDW order parameter increases in the coexistence phase, hence a stronger BDW order also suppresses superconductivity more. This confirms the mutual suppression and hence a competition between the BDW order and superconductivity.

Furthermore, we observe a s'-wave PDW order (Figs. 5.5, 5.6) when both d-wave BDW order and d-wave superconductivity coexist, as also seen in experiments [81, 82]. It is consistent with Ginzburg Landau theory [181, 182] that a coexistence of d-wave BDW order and d-wave superconductivity leads to a s'-wave PDW order [81]. In other words, the s'-wave PDW order is a secondary order that is induced by the coexistence of the d-wave BDW order and d-wave superconductivity. Note that the PDW order is much weaker compared to both BDW order and superconductivity. We observe that the PDW order parameter vanishes when the BDW order parameter vanishes around $p = 0.14$ and it also decreases around $p = 0.18$, where the superconducting order parameter decreases; this suggests that both BDW order and superconductivity are crucial for the PDW order, justifying that it is indeed a secondary order.

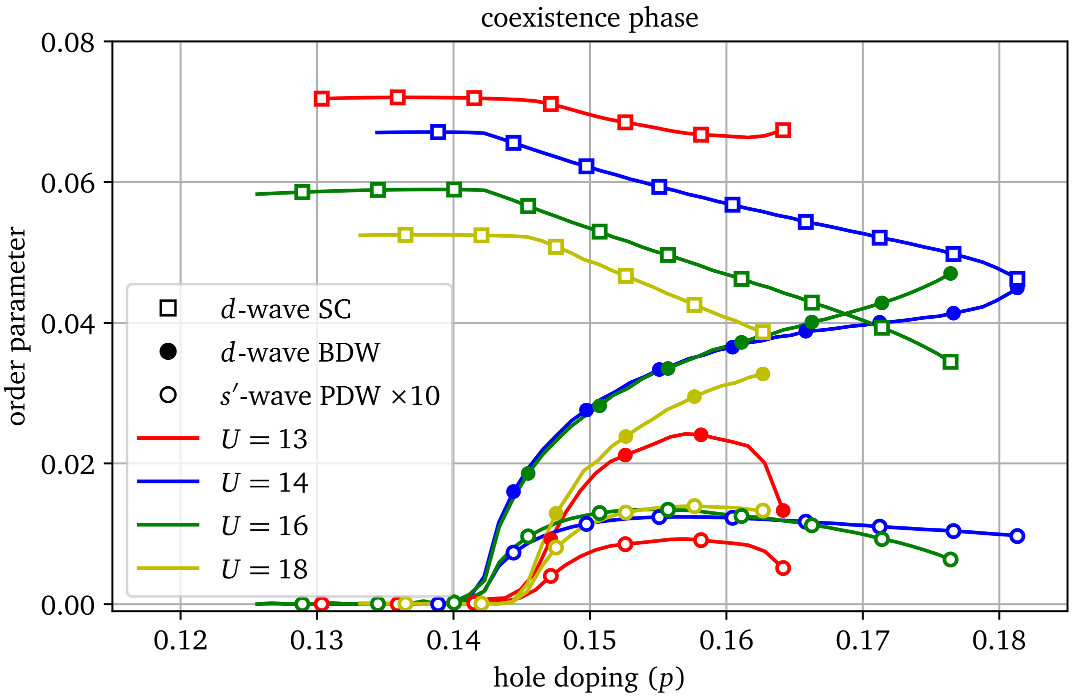

Figure 5.8: Order parameters in the coexistence phase for various values of U. The superconducting order parameter (open squares) decreases as U increases. The BDW order parameter (filled circles) increases from $U = 13$ to $U = 14$, remains almost the same for $U = 16$, and then decreases for $U = 18$. Note that this is different from the behavior of the BDW order parameter in the normal phase, where it decreases monotonously with U for most of the doping range. The PDW order parameter (open circles), which is very weak compared to both BDW and superconductivity, increases from $U = 13$ to $U = 14$ and then remains almost the same upto $U = 18$. We have shown only 1/5th of the total number of data points that we have, for clarity.

The competition between BDW order and superconductivity can also be deduced from the behavior of the BDW order parameter with U in the coexistence phase. In

Fig. 5.8, we have plotted all the order parameters in the coexistence phase as functions of doping for various values of U. We observe that the variation of the BDW order parameter with U, in the coexistence phase, is not monotonous; the BDW order parameter increases with U from $U = 13$ to $U = 14$, remains almost constant for $U = 16$, and then decreases for $U = 18$. This is different from the normal phase where the BDW order parameter at optimal doping (as well as for most doping values) decreases monotonously with U. The BDW order parameter in the coexistence phase depends on both U and the magnitude of the superconducting order parameter. Hence, we can understand its behavior in the coexistence phase based on these two factors. The effect of U, as can be exclusively observed in the normal phase Fig. 5.2, is to suppress the BDW order. Then regarding superconductivity, we saw from Figs. 5.5, 5.6, 5.7 that superconductivity competes with the BDW order; a higher value of the superconducting order parameter supresses more the BDW order. This is also seen clearly in Fig. 5.9, where the BDW order is suppressed in the coexistence phase (compared to normal phase) more at $U = 14$ than at $U = 16$ due to a larger value of the superconducting order parameter at $U = 14$. Hence, a larger value of the superconducting order in the coexistence phase leads to a larger suppression of the BDW order compared to the normal phase. Thus, the variation of the BDW order with U in the coexistence phase depends on which of the two factors (U or superconductivity) dominate.

When the value of U is lower, the superconducting order is strong (Fig. 5.8), hence the effect of superconductivity on the BDW order dominates in this regime; an increase in U leads to a decrease in the superconducting order and consequently to an increase in the strength of the BDW order (the suppression of the BDW order with U is less significant). On the other hand, when U is large, the superconducting order is weak (Fig. 5.8), as a result the effect of U on the BDW order dominates, i.e., the BDW order is suppressed with U in this regime (the increase in the strength of the BDW order due to the weakening of superconductivity in this regime is less significant). Naturally, there is a crossover between the superconductivity-dominant regime and the U-dominant regime which occurs

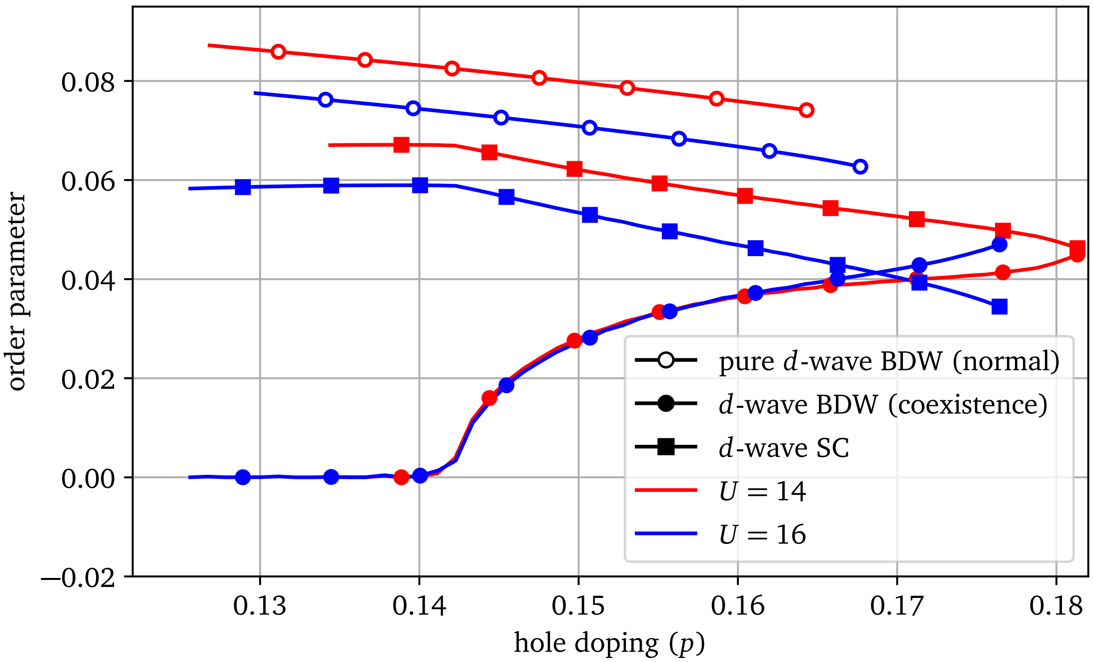

Figure 5.9: Superconductivity and the U-dependence of the BDW order. The effect of U on the suppression of the BDW order parameter in the coexistence phase (from its value in the normal phase) can be understood in terms of superconductivity. We have shown the data from Figs. 5.5, 5.6: the superconducting order parameter in the coexistence phase (filled squares) and the BDW order parameter in the coexistence (filled circles) and the normal (open circles) phases, for $U = 14,\ 16$. At any given doping, the BDW order in the coexistence phase is suppressed (from its value in the normal phase) more at $U = 14$ than at $U = 16$. This can be understood from the variation of the superconducting order parameter from $U = 14$ to $U = 16$: a higher value of the superconducting order parameter at $U = 14$ (than at $U = 16$) is responsible for a higher suppression of the BDW order at $U = 14$ (than at $U = 16$). We have shown only 1/5th of the total number of data points that we have, for clarity.

around $U = 14,\ 16$ where the BDW order parameter remains almost constant. Hence, the non-monotonic behavior of the BDW order parameter with U, in the coexistence phase, is a direct result of the competition between the BDW order and superconductivity.

However, note that the variation of the superconducting order parameter with U in the coexistence phase (Fig. 5.8) is the same as it is expected for pure superconductivity, i.e., it decreases monotonously as U increases [87–89]. Although the superconducting order is also suppressed by the BDW order, we can see from Fig. 5.7(b) that the amount by which the superconducting order is weakened by the BDW order is very small compared to the amount by which the BDW order is weakened, at least in the range of doping that we have explored. Hence, the effect of U on superconductivity remains as the dominant effect even in presence of the BDW order, in the coexistence phase. Furthermore, the PDW order parameter does not vary much with U (Fig. 5.8); it increases from $U = 13$ to $U = 14$ and remains almost constant upto $U = 18$.

5.5 Details of the cluster-bath impurity model

In this work, we probe three phases (three kinds of groundstates) using CDMFT on the one-band Hubbard model at zero temperature: 1) *the normal phase*, where we allow for charge/bond-density-wave (CDW/BDW) orders to exist, 2) *the coexistence phase*, where we allow density-wave orders as well as superconductivity to coexist, 3) *the superconducting phase*, where we allow only superconductivity to exist. We use three different cluster-bath impurity models for the three cases, since we need to break a different symmetry in the impurity model for each case.

For the *superconducting* phase, we use exactly the same cluster-bath impurity model as discussed in sec. 4.7. The steps in the CDMFT procedure are also the same except just one change; since we focus here on the one-band Hubbard model, the lattice Green function takes the form Eq. (3.51) (instead of Eq. (4.12)), where $t(\tilde{\mathbf{k}})$ is the hopping matrix on the lattice.

We will describe the cluster-bath impurity model for the *coexistence* phase in details, and as we shall see, the impurity model for the *normal* phase would just be a special case of this. The goal is to be able to probe a ground state where the translational symmetry is reduced or partially broken (because of the density-wave (DW) with period 4), and the $U(1)$ gauge symmetry is broken (due to superconductivity). Hence, we need to allow for these symmetries to break in the impurity model. As we discussed in sec. 4.7, we can allow for a broken $U(1)$ gauge symmetry in the impurity model by introducing anomalous hybridization terms between the cluster and the bath which are variationally optimized in the CDMFT procedure. Then, to allow for a period-4 unidirectional DW in the impurity model, ideally we have to at least take a cluster of size 4×2, i.e., containing 8 sites; note that we cannot take a perfectly unidirectional cluster (4×1), since we need to incorporate the local correlation effects, essential to describe the phase diagram of cuprates [87–89], for which the smallest possible cluster is a 2×2 cluster [183]. For a 8-site cluster, we would need a bath of 16 orbitals, since typically two bath orbitals per site on the cluster is required to capture the dynamical correlation effects [165,184]. However, this would make the impurity model really large and is not possible with the present state of the exact diagonalization solver that we use. Hence, instead of choosing a 8-site cluster, we choose two 2×2 clusters along the $\hat{\mathbf{x}}$ direction to form the 4×2 super-cell. Fig. 5.10 shows the choice of the two clusters within the super-cell along with a four-period density modulation. Further, each cluster is connected to a separate bath containing 8 orbitals (as also shown in Fig. 4.16(b)). The idea is that the bath parameters for the two cluster-bath systems are allowed to evolve independently through the CDMFT procedure and could finally lead to different densities on the two clusters creating a density-wave in the super-cell.

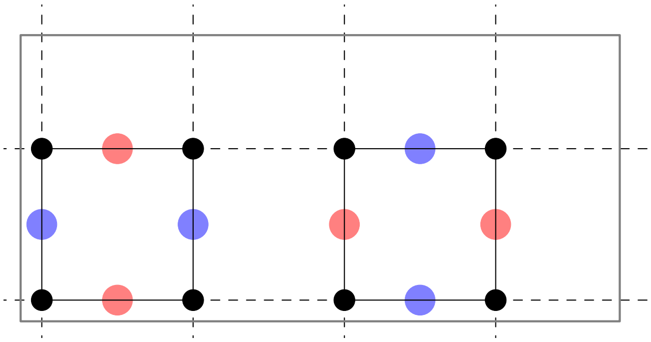

Figure 5.10: Choice of the clusters for the impurity model. We choose two 2×2 clusters within a 4×2 super-cell (gray box), to accomodate period-4 density-waves (DW) (we show a d-wave density modulation on the first-neighbor bonds within the clusters, where red indicates the negative amplitude and blue indicates the positive amplitude) in the impurity model.

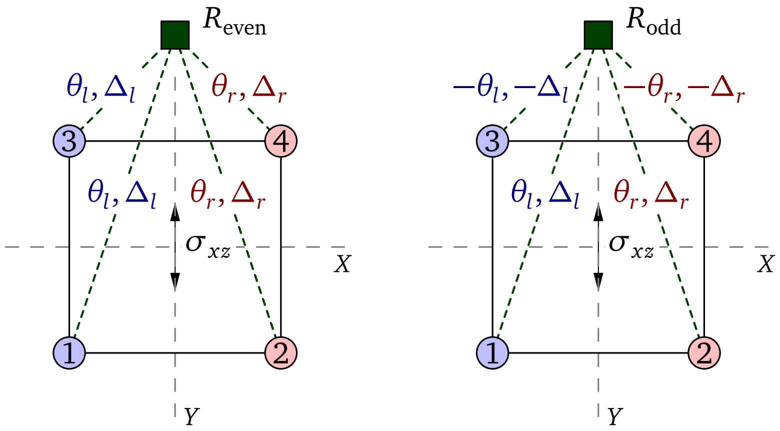

Figure 5.11: Cluster-bath hybridization. Cluster-bath hybridization terms corresponding to the 2 irreducible representations (R_{even} and R_{odd}) of the point group $M_{xz} = \{e, \sigma_{xz}\}$. The elements of $\boldsymbol{\theta}$ are labelled as $\pm\theta_l$, $\pm\theta_r$; for instance, if $\pm\theta_l$ appears on the bond between the cluster site 1 and a bath orbital, say k, then the matrix element (see Eq. (3.60)) $\theta_{1k} = \pm\theta_l$. Similarly, the elements of $\boldsymbol{\Delta}$ are labelled as $\pm\Delta_l$, $\pm\Delta_r$. Note that we have 8 bath orbitals in total; we take the hybridization of the cluster with 4 bath orbitals corresponding to the even irreducible representation R_{even}, and 4 bath orbitals corresponding to the odd irreducible representation R_{odd}.

Thus, there would be two bath hybridization functions

$$\boldsymbol{\Gamma}^{(i)} = \boldsymbol{\Theta}^{(i)} \left(z - \mathbf{E}^{(i)}\right)^{-1} \left(\boldsymbol{\Theta}^{(i)}\right)^{\dagger} \quad, i = 1,\ 2\,, \tag{5.5}$$

for the two clusters, labelled 1 and 2, where

$$\boldsymbol{\Theta}^{(i)} = \begin{pmatrix} \boldsymbol{\theta}^{(i)} & -\left(\boldsymbol{\Delta}^{(i)}\right)^{\dagger} \\ -\left(\boldsymbol{\Delta}^{(i)}\right)^{T} & -\boldsymbol{\theta}^{*} \end{pmatrix}, \ \mathbf{E}^{(i)} = \begin{pmatrix} \boldsymbol{\epsilon}^{(i)} & \mathbf{0} \\ \mathbf{0} & -\boldsymbol{\epsilon}^{(i)} \end{pmatrix}. \tag{5.6}$$

Here $\boldsymbol{\theta}^{(i)}$ is the 4×8 cluster-bath hybridization matrix, $\boldsymbol{\Delta}^{(i)}$ is the 8×4 anomalous hybridization matrix between the cluster and the bath, and $\boldsymbol{\epsilon}^{(i)}$ is the 8×8 bath Hamiltonian matrix, for the ith cluster. Now, we have a total of $2 \times (4 \times 8 + 4 \times 8 + 8) = 144$ bath parameters, i.e., 72 per cluster-bath system. As we discussed in sec. 4.7, we can use point group symmetries of the cluster to reduce the number of independent bath parameters. In this case, we use the point group $M_{xz} = \{e, \sigma_{xz}\}$, where e is the identity operation and σ_{xz} is the reflection across the XZ plane (Eq. (4.17)). Note that the symmetry transformations of the group are compatible with the DW as shown in Fig. 5.10. The basis in which the symmetry operations in M_{xz} are diagonal is the same as $\mathbb{B}_{\text{ir}}$ (Eq. (4.18)). However, there are just two irreducible representations of M_{xz}, known as odd and even irreducible representations, based on whether the sign changes or not respectively, on application of the operation σ_{xz}. The basis elements $|00\rangle$, $|10\rangle$ (Eq. (4.18)) correspond to the even irreducible representation, and elements $|01\rangle, |11\rangle$ (Eq. (4.18)) correspond to the odd irreducible representation. Fig. 5.11 shows the cluster-bath hybridization terms (both normal and anomalous) in terms of the even (R_{even}) and odd (R_{odd}) irreducible representations of M_{xz}. Out of the 8 bath orbitals, we parametrize 4 bath orbitals using the even irreducible representation (R_{even}) and 4 using the odd irreducible representation (R_{odd}), for each cluster-bath system. Hence, the bath hybridization matrices $\boldsymbol{\theta}^{(i)}$ and $\boldsymbol{\Delta}^{(i)}$ take the form

$$\boldsymbol{\theta}^{(i)} = \begin{pmatrix} \theta^{(i)}_{l1} & \theta^{(i)}_{l2} & \theta^{(i)}_{l3} & \theta^{(i)}_{l4} & \theta^{(i)}_{l5} & \theta^{(i)}_{l6} & \theta^{(i)}_{l7} & \theta^{(i)}_{l8} \\ \theta^{(i)}_{r1} & \theta^{(i)}_{r2} & \theta^{(i)}_{r3} & \theta^{(i)}_{r4} & \theta^{(i)}_{r5} & \theta^{(i)}_{r6} & \theta^{(i)}_{r7} & \theta^{(i)}_{r8} \\ \theta^{(i)}_{l1} & \theta^{(i)}_{l2} & \theta^{(i)}_{l3} & \theta^{(i)}_{l4} & -\theta^{(i)}_{l5} & -\theta^{(i)}_{l6} & -\theta^{(i)}_{l7} & -\theta^{(i)}_{l8} \\ \theta^{(i)}_{r1} & \theta^{(i)}_{r2} & \theta^{(i)}_{r3} & \theta^{(i)}_{r4} & -\theta^{(i)}_{r5} & -\theta^{(i)}_{r6} & -\theta^{(i)}_{r7} & -\theta^{(i)}_{r8} \end{pmatrix}, \; i = 1,\, 2 \tag{5.7}$$

$$\boldsymbol{\Delta}^{(i)} = \begin{pmatrix} \Delta^{(i)}_{l1} & \Delta^{(i)}_{l2} & \Delta^{(i)}_{l3} & \Delta^{(i)}_{l4} & \Delta^{(i)}_{l5} & \Delta^{(i)}_{l6} & \Delta^{(i)}_{l7} & \Delta^{(i)}_{l8} \\ \Delta^{(i)}_{r1} & \Delta^{(i)}_{r2} & \Delta^{(i)}_{r3} & \Delta^{(i)}_{r4} & \Delta^{(i)}_{r5} & \Delta^{(i)}_{r6} & \Delta^{(i)}_{r7} & \Delta^{(i)}_{r8} \\ \Delta^{(i)}_{l1} & \Delta^{(i)}_{l2} & \Delta^{(i)}_{l3} & \Delta^{(i)}_{l4} & -\Delta^{(i)}_{l5} & -\Delta^{(i)}_{l6} & -\Delta^{(i)}_{l7} & -\Delta^{(i)}_{l8} \\ \Delta^{(i)}_{r1} & \Delta^{(i)}_{r2} & \Delta^{(i)}_{r3} & \Delta^{(i)}_{r4} & -\Delta^{(i)}_{r5} & -\Delta^{(i)}_{r6} & -\Delta^{(i)}_{r7} & -\Delta^{(i)}_{r8} \end{pmatrix}, \; i = 1,\, 2\,. \tag{5.8}$$

Thus, we have a total of $2 \times (2 \times 8)$ (from $\boldsymbol{\theta}^{(\mathrm{i})}$ and $\boldsymbol{\Delta}^{(\mathrm{i})}$) $+\,8$ (from $\boldsymbol{\epsilon}^{(\mathrm{i})}$) $= 40$ bath parameters per cluster-bath system, i.e., 80 parameters in total w.r.t. which we have to minimize the distance function Eq. (3.59) with $j = 1,\, 2$. In the distance function Eq. (3.59), we use the weight function $W(i\omega_n)$ Eq. (3.57) with $\omega_c = 2t$ and $\beta = 50/t$ [89]. Finally for the *normal* phase, we take the matrices $\boldsymbol{\Delta}^{(i)} = 0$, which leaves us with 48 bath parameters in total. We consider the CDMFT iterations to have converged when $\delta\mathbf{\Gamma} \leq 10^{-5}$, where

$$\delta\mathbf{\Gamma} = \left[\frac{1}{N}\sum_{n=1}^{N} W(i\omega_n)\left[||\mathbf{\Gamma}_j^{(1)}(i\omega_n) - \mathbf{\Gamma}_{j-1}^{(1)}(i\omega_n)||^2 + ||\mathbf{\Gamma}_j^{(2)}(i\omega_n) - \mathbf{\Gamma}_{j-1}^{(2)}(i\omega_n)||^2\right]\right]^{1/2} \tag{5.9}$$

and $\mathbf{\Gamma}_j^{(i)}(i\omega_n)$ is the bath hybridization function of the ith cluster at the jth iteration and $||\mathbf{A}|| = \sqrt{\sum_{i,j}|A_{ij}|^2}$ is the norm of a matrix $\mathbf{A}$.

5.5.1 Are our density-wave orders artefacts of CDMFT?

It is known that CDMFT, by construction, leads to a (partially) broken translational symmetry of the lattice, which appear as modulations in the charge and bond densities (even pair density, in the presence of superconductivity) [168]. These artificial density-waves occur because we take into account the self-energy only within the clusters, and neglect the self-energy between the clusters (see Eq. (3.55)); as a result, the approximation for the quantities between the clusters is different than that for quantities within the clusters. Hence, this difference naturally leads to modulations of charge/bond densities, and the periodicity of such density-waves depends on the shape of the cluster. For instance, CDMFT with a 2×2 cluster leads to artificial period-2 density-waves in the solution [168]. In this section, we address the question whether the period-4 DW orders that we observe are physical or just artefacts of CDMFT.

In this work, we use two 2×2 clusters, each connected to its own bath, to form the impurity model. As we discussed above, we should expect a period-2 density wave because of our 2×2 clusters, and indeed we observe such a DW (measured by the average of Eq. (5.2) with $\mathbf{q} = \pi\hat{\mathbf{x}}$) as shown in Fig. 5.12. Fig. 5.12 shows various period-4 DW orders in the coexistence phase at $U = 16$ along with the BDW order with period 2 (blue triangles). Note that we also observe the period-2 DW for all the phases (normal, superconducting and coexistence) at all values of U. The period-4 DW orders appear with a

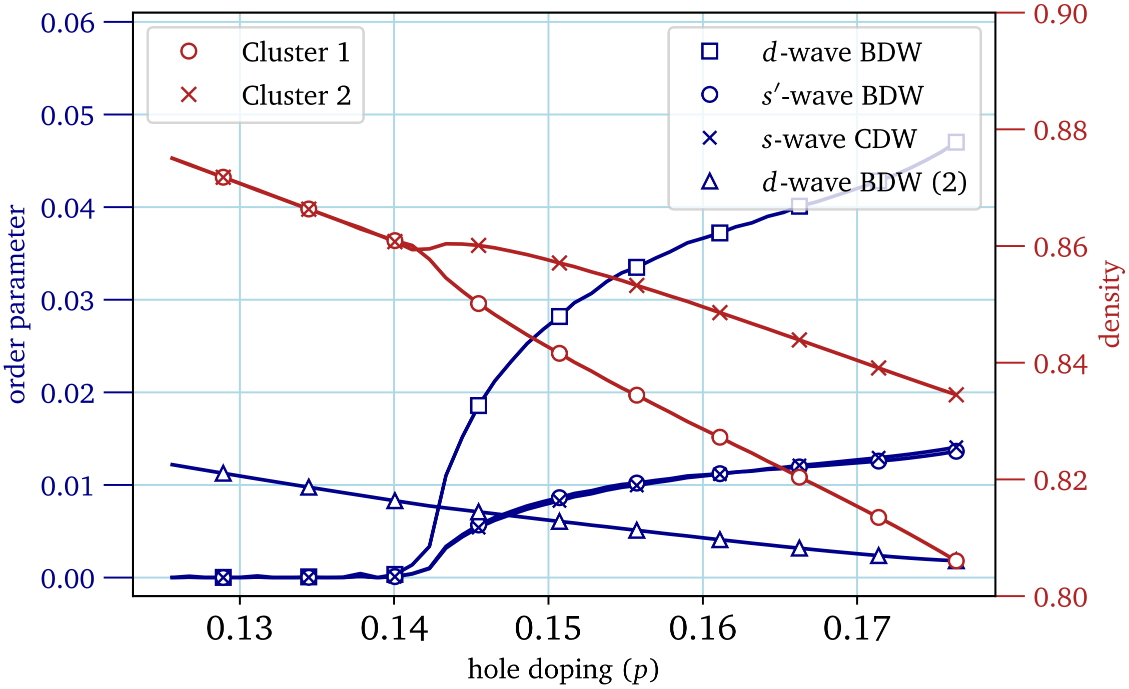

Figure 5.12: The period-2 DW order. DW orders with period 4, along with the BDW order with period 2 (blue triangles) as functions of hole doping in the coexistence phase at $U = 16$. Cluster densities (in red) are also shown as functions of hole doping. The period-4 DW orders appear with the spontaneous breaking of the symmerty between the two clusters, as the cluster densities evolve with doping to be different from each other above $p \approx 0.14$. However, the artificial period-2 BDW order exists in almost the entire doping range, and hence is distinct from the period-4 DW orders. We have shown only 1/5th of the total number of data points that we have, for clarity.

spontaneous breaking of translation symmetry within the super-cell above $p \approx 0.14$; this can be seen from the cluster densities (in red) which start differing from each other as the DW orders grow. However, the period-2 BDW order takes finite values for almost the whole doping range and changes very slowly, as if it were a background. Furthermore, there is no significant change in the period-2 BDW order parameter as the period-4 DW orders start to grow around $p \approx 0.14$, suggesting that it is independent of the period-4 DW orders. Thus, we believe that the density-waves with period 4 are physical effects, which are caused due to a difference in the self-energy of the two clusters, above a critical value of hole doping.

5.6 Perspective

In this work, we use the BDW order within the one-band Hubbard model as a proxy for the CDW order centered on O orbitals in cuprates [52, 54]. A straightforward improvement would be to probe the CDW order centered on O orbitals directly by using CDMFT on the three-band Hubbard model Eq. (2.28). This can be done by choosing a 4×2 super-cell on the CuO_2 lattice (gray box in Fig. 5.13), for a period-4 DW order, with two Cu clusters (each with 4 Cu orbitals as shown by the red box in Fig. 5.13) and two O clusters (each with 8 O orbitals as shown by the blue box in Fig. 5.13). The two Cu clusters would be connected to two sets of bath orbitals, and the O clusters would be taken to be uncorrelated and hence would not be connected to bath orbitals. Thus, the impurity model would be the same as for the one-band Hubbard model (Fig. 5.10). The computation times, in this case, are expected to be of the same order as that of the one-band Hubbard model, since the only additional cost comes from projecting the full lattice Green function onto the Cu orbitals in each CDMFT loop.

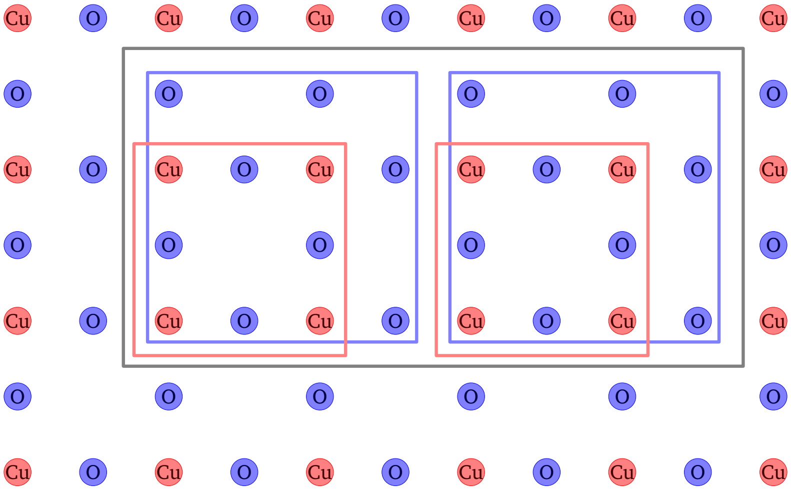

Figure 5.13: Choice of clusters for probing density-waves in the three-band Hubbard model. A 4×2 super-cell (gray box) is chosen to probe a period-4 DW order (Fig. 1.8 (right panel)), with two correlated Cu clusters (red box) and two uncorrelated O clusters (blue box). The two Cu clusters are connected to two sets of bath orbitals, to form the impurity model (same impurity model as used for the one-band Hubbard model).

For some time, the CDW and the pseudogap were thought to be related [54, 55, 60, 77, 78] since they overlap with each other in the temperature-doping phase diagram and both are associated with a destruction of the Fermi surface around the antinodal regions. However, it is now known that they are distinct phenomena [79, 80]. Nevertheless, some recent studies propose that a microscopic theory of the pseudogap might involve a PDW order [81,83,84,185,186]. Although we could probe a period-4 PDW order in our CDMFT computations on the one-band Hubbard model, we could not clearly identify the pseudogap in our results because of two reasons: 1) we always have an intrinsic period-2 density-wave (Fig. 5.12), which is an artefact of the 2 × 2 cluster, and leads to vanishing spectral weights around the antinodal region, which is also a signature of the pseudogap, 2) we have the coexistence phase (where we observe a PDW order) only for a short interval in doping within which the superconducting order parameter and the superconducting gap (in the density of states) behave monotonously, hence it is not possible to identify the pseudogap, although this does not necessarily mean that there is no pseduogap. Thus, we cannot conclude anything regarding the relation between the PDW order and the pseudogap from our present computations. It might be possible to reach a conclusion regarding this from CDMFT computations on the three-band Hubbard model with a suitable choice of clusters for period-4 DW orders, as we proposed above (Fig. 5.13), since the pseudogap appears distinctly as a first-order transition in the presence of superconductivity in the three-band Hubbard model, as we saw in the last chapter (Chapter 4). More specifically, refs. [84, 185, 186] propose that the pseudogap might be caused by a period-8 d-wave PDW order and that this PDW order gives rise to a period-4 d-wave CDW order when it coexists with d-wave superconductivity. It is possible to check this proposal using CDMFT on the three-band Hubbard model as described above, by using a 8 × 2 super-cell containing four correlated Cu clusters and four uncorrelated O clusters; the computation times would scale as twice that of the present one-band model computations.

Summary

In this chapter, we studied various period-4 density-waves related to charge modulations, in the doped Mott insulator, within the one-band Hubbard model using cluster dynamical mean field theory with an exact diagonalization impurity solver at zero temperature. We were able to probe period-4 DW orders by using two 2×2 clusters in the impurity model. We observed that the d-wave BDW order is the dominant density-wave order. In addition, we observed the coexistence of the BDW order with d-wave superconductivity and that they suppress each other when they coexist. Thus we conclude that the BDW order and superconductivity compete with each other. Furthermore, we observed a s'-wave PDW order when both d-wave BDW and d-wave superconductivity coexist. The main results of this chapter are published in *"S. S. Dash and D. Sénéchal. Charge-and pair-density-wave orders in the one-band Hubbard model from dynamical mean field theory.* Physical Review B*, 103(4):045142, 2021. URL:* `https://journals.aps.org/prb/abstract/10.1103/PhysRevB.103.045142`*".*

Conclusion

Let us summarize the important results obtained in this thesis using *cluster dynamical mean field theory* on the one-band and the three-band Hubbard models, with parameters suited for cuprate superconductors, at zero temperature.

First, we observe a discontinuous transition in the superconducting phase, which signals the onset of the pseudogap below a certain value of hole doping, within the three-band Hubbard model for many parameter-sets (variations around the ionic case Eq. (4.1) and the covalent case Eq. (4.2)) at various values of the on-site Coulomb repulsion U_d on Cu orbitals. We observe various changes in the superconducting phase with the first-order transition that lead us to conclude that the superconducting phase in the underdoped region coexists with the pseudogap. The superconducting gap, which appears as a symmetric gap around the Fermi energy in the overdoped region, changes suddenly to a large asymmetric gap across the transition in the underdoped region (Fig. 4.4). Such a large asymmetric gap around the Fermi level is considered the effect of the pseudogap at zero temperature and is observed in STM experiments at very low values of hole doping [1, 188–190]. The other important change that we observe in the superconducting phase across the first-order transition is the growth of a pole in the normal component of the imaginary part of the of anti-nodal self-energy $\text{Im}\left(\Sigma_c^{\text{nor}}\right)((\pi, 0), z)$ near the Fermi level (Fig. 4.8). This pole eventually leads to the formation of the charge-transfer insulator (CTI) at a filling of 5 electrons in the unit cell. Such a pole in the antinodal self-energy has been associated to the pseudogap in various theoretical studies within the one-band Hubbard model [50,90,158,169].

Second, we reproduce the correlation between the maximum T_c and the oxygen hole content at optimal doping seen in experiments [102], with the maximum order parameter as a proxy for the maximum T_c, across various parameter-sets which cover most of the cuprate superconductors [133]. This correlation is also observed theoretically between the actual T_c and the oxygen hole content at optimal doping by our collaborators [177], however for parameter-sets around the ionic case Eq. (4.1), which do not directly correspond to cuprates. Additionally, we observe that the maximum order parameter decreases monotonously with the charge-transfer gap (Fig. 4.12(a)), which is consistent with experiments [86], suggesting that an effective superexchange $J_{\text{eff}} = 4t_{\text{eff}}^2/\Delta_{\text{CT}}$ controls superconductivity in cuprates. We also observe that the maximum order parameter is correlated with the superexchange J (inset of Fig. 4.15), which confirms the role of the antiferromagnetic superexchange in pairing in the three-band Hubbard model, asserting the dominant role of the antiferromagnetic fluctuations in pairing in cuprates. We further find that the charge-transfer gap is perfectly correlated with the oxygen hole content at optimal doping (Fig. 4.13), which ultimately links the correlation between the order parameter and oxygen hole content to the correlation between the order parameter and superexchange. Hence, we conclude that the antiferromagnetic origin (local antiferromagnetic fluctuations) of pairing in cuprates results in the observed correlation between the T_c and oxygen hole content at optimal doping. In other words, the experimental observation of the correlation between the maximum T_c and the oxygen hole content at optimal doping strongly suggests that pairing in cuprate superconductors occurs through short-range antiferromagnetic spin fluctuations. Another very important observation that we make is that the superexchange $J = 4t_{\text{eff}}^2/\Delta_{\text{CT}}$ is higher for variations around the covalent case Eq. (4.2) than for variations around the ionic case Eq. (4.1), for a given value of the charge-transfer gap Δ_{CT}, leading to a higher value of the order parameter for the covalent case. The most important difference between the two cases is ϵ_p, which is significantly lower in the covalent case Eq. (4.2) compared to the ionic case Eq. (4.1). ϵ_p gives a rough estimate of the relative electronegativity of O w.r.t. Cu, which in turn decides the nature of bonding between the two: A larger difference in electronegativity leads to a more ionic nature of the bond and a smaller difference leads to a more covalent nature of the bond. Thus, we can conclude that a more covalent nature of bonding between the cation and the anion (lower ϵ_p) leads to a higher order parameter (hence a higher T_c). This is the reason why, in reality, cuprates have a relatively higher T_c compared to other transition metal oxide superconductors. Thus, combining transition metals to other chalcogens or pnictogens, so that they form a stronger covalent bond, seems to be a promising direction to look for higher temperature superconductors. A measure of the charge-transfer-gap, if possible, could also help to look for higher temperature superconductors. Note that although the charge-transfer gap suppresses superconductivity, a finite gap is required for superconductivity, as seen in Fig. 4.11(a).

Third, we observe various period-4 density-wave orders on doping the Mott insulator beyond a certain critical value, within the one-band Hubbard model. Note that we only take into account the short-range correlations within the two 2×2 clusters in the super-cell. We observe that the d-wave BDW order, which is a proxy for the d-wave CDW modulation centered on O orbitals in cuprates [52, 54], is the dominant DW order consistent with experiments [54, 56]. We also observe that the d-wave BDW order grows as the magnitude of the second-neighbor hopping t' increases (Fig. 5.4), even when the bandwidth remains constant. An increase in the magnitude of t' leads to an increase in the magnetic frustration in the lattice for the case of antiferromagnetic interactions, and hence is detrimental for antiferromagnetic fluctuations. Thus, the d-wave BDW order is favored by the suppression of antiferromagnetic fluctuations on the lattice; in other words, antiferromagnetism is detrimental to the BDW order. Furthermore, we probe a *coexistence* phase where DW orders and superconductivity coexist. By comparing the order parameters in the three phases that we probe: *normal*, *superconducting* and *coexistence* (Figs. 5.5, 5.6, 5.7), we conclude that the d-wave BDW order and superconductivity compete with each other, as observed in experiments [58–60, 62]. This is also consistent with the fact that the d-wave BDW order behaves non-monotonously with U in the coexistence phase (Fig. 5.8), whereas it decreases monotonously with U in the normal phase (Fig. 5.2). We understand this in terms of the competition of superconductivity with BDW order which dominates at lower values of U and becomes less important at higher values of U (Fig. 5.9). Finally, we also observe a period-4 s'-wave PDW order in the coexistence phase when both BDW order and superconductivity coexist, as seen in experiments [81, 82]. However, the PDW order is much weaker compared to both BDW order and superconductivity.

Thus, we were able to describe various experimental observations on the cuprate superconductors using cluster dynamical mean field theory on the Hubbard model, which takes into account the effects of strong correlations only within a cluster. This asserts that: 1) the Hubbard model is an adequate model for describing cuprate superconductors, 2) short-range correlations play an important role in the superconductivity in cuprates.

Now, let us summarize some of the possible future directions to extend the main results of this thesis. The pseudogap transition within the superconducting phase, as observed in this thesis, seems to be related to the Sordi transition in the normal phase which also describes the onset of the pseudogap. It is instructive to check whether the transition in the superconducting phase is a manifestation of the Sordi transition within the superconducting phase. This can be done using CDMFT on the three-band Hubbard model with a finite temperature impurity solver, e.g. CTQMC as done in ref. [179], and the critical temperatures of both these transitions can be compared. Although we could establish that superconductivity is indeed controlled by the superexchange J, in the three-band Hubbard model, which also explains the correlation between the maximum T_c and the oxygen hole content as seen in experiments, our results are based on calculations on a 2×2 cluster. It would be useful to understand how finite-size effects affect our observations by doing the computations with larger clusters. For example, a recent study of superconductivity within the three-band Hubbard model using DCA uses a 4 × 4 cluster [171]. A natural extension of our work on density-waves within the one-band Hubbard model is to use the three-band Hubbard model instead, where the charge-density-waves can be incorporated on the oxygen orbitals as observed in experiments, rather than using bond-density-waves as a proxy for charge-density modulations on oxygen orbitals. This can also help to understand the relation between pair-density-waves and the pseudogap, to check the proposals in refs. [84, 185, 186], since the pseudogap appears with a distinct transition, within the three-band Hubbard model, in the superconducting phase.

Appendix A

Appendices

In these appendices, we discuss various topics that we refer to in the main text.

A.1 Fourier transformation of Green function

We start with the Green function Eq. (2.12) with $t' = 0$, since the Green function only depends on the time difference for an equillibrium system,

$$G^R(\mathbf{r},\mathbf{r}',t) = -i\left[\langle\Omega|c_{\mathbf{r}}(t)c^\dagger_{\mathbf{r}'}(0)|\Omega\rangle + \langle\Omega|c^\dagger_{\mathbf{r}'}(0)c_{\mathbf{r}}(t)|\Omega\rangle\right]\theta(t)\,. \tag{A.1}$$

On writing the time-dependent operators in the Schrödinger picture,

$$\begin{aligned} G^R(\mathbf{r},\mathbf{r}',t) &= -i\left[\langle\Omega|e^{iHt}c_{\mathbf{r}}e^{-iHt}c^\dagger_{\mathbf{r}'}|\Omega\rangle + \langle\Omega|c^\dagger_{\mathbf{r}'}e^{iHt}c_{\mathbf{r}}e^{-iHt}|\Omega\rangle\right]\theta(t) && \text{(A.2)}\\ &= -i\left[\langle\Omega|c_{\mathbf{r}}e^{-i(H-E_0)t}c^\dagger_{\mathbf{r}'}|\Omega\rangle + \langle\Omega|c^\dagger_{\mathbf{r}'}e^{i(H-E_0)t}c_{\mathbf{r}}|\Omega\rangle\right]\theta(t)\,, && \text{(A.3)}\end{aligned}$$

where E_0 is the energy of the many-body ground state $|\Omega\rangle$.

The Green function in the frequency space is given by

$$\begin{aligned} G(\mathbf{r},\mathbf{r}',\omega) &= \int_0^\infty dt\; e^{i\omega t}G(\mathbf{r},\mathbf{r}',t) && \text{(A.4)}\\ \Rightarrow G(\mathbf{r},\mathbf{r}',\omega) &= -i\int_0^\infty dt\;\left[\langle\Omega|c_{\mathbf{r}}e^{i(\omega-H+E_0)t}c^\dagger_{\mathbf{r}'}|\Omega\rangle + \langle\Omega|c^\dagger_{\mathbf{r}'}e^{i(\omega+H-E_0)t}c_{\mathbf{r}}|\Omega\rangle\right] && \text{(A.5)}\\ &= -\left[\langle\Omega|c_{\mathbf{r}}\frac{e^{i(\omega-H+E_0)t}}{\omega-H+E_0}c^\dagger_{\mathbf{r}'}|\Omega\rangle + \langle\Omega|c^\dagger_{\mathbf{r}'}\frac{e^{i(\omega+H-E_0)t}}{\omega+H-E_0}c_{\mathbf{r}}|\Omega\rangle\right]\Bigg|_{t=0}^{t=\infty} && \text{(A.6)}\\ \Rightarrow G(\mathbf{r},\mathbf{r}',\omega) &= \langle\Omega|c_{\mathbf{r}}\frac{1}{\omega-H+E_0}c^\dagger_{\mathbf{r}'}|\Omega\rangle + \langle\Omega|c^\dagger_{\mathbf{r}'}\frac{1}{\omega+H-E_0}c_{\mathbf{r}}|\Omega\rangle\,. && \text{(A.7)}\end{aligned}$$

The retarded Green function in the frequency space becomes

$$G^R(\mathbf{r},\mathbf{r}',\omega) = \langle\Omega|c_{\mathbf{r}}\frac{1}{\omega+i\eta-H+E_0}c^\dagger_{\mathbf{r}'}|\Omega\rangle + \langle\Omega|c^\dagger_{\mathbf{r}'}\frac{1}{\omega+i\eta+H-E_0}c_{\mathbf{r}}|\Omega\rangle \; , \tag{A.8}$$

where $\eta \to 0+$.

A.2 Inversion of a 2×2 block matrix

Let us take a square matrix **A** which is expressed as a 2 × 2 block matrix

$$\mathbf{A} = \begin{bmatrix} \mathbf{A}_{11} & \mathbf{A}_{12} \\ \mathbf{A}_{21} & \mathbf{A}_{22} \end{bmatrix} , \tag{A.9}$$

where $\mathbf{A}_{11}$, $\mathbf{A}_{22}$ are square matrices and $\mathbf{A}_{12}$, $\mathbf{A}_{21}$ are rectangular matrices in general. Let the matrix **B**, also expressed as a 2 × 2 block matrix:

$$\mathbf{B} = \begin{bmatrix} \mathbf{B}_{11} & \mathbf{B}_{12} \\ \mathbf{B}_{21} & \mathbf{B}_{22} \end{bmatrix} \tag{A.10}$$

be the inverse of **A** $\left(\mathbf{B} = \mathbf{A}^{-1}\right)$. Note that the block matrices $\mathbf{A}_{ij}$ and $\mathbf{B}_{ij}$ have the same dimensions. Then, we have

$$\begin{bmatrix} \mathbf{A}_{11} & \mathbf{A}_{12} \\ \mathbf{A}_{21} & \mathbf{A}_{22} \end{bmatrix} \begin{bmatrix} \mathbf{B}_{11} & \mathbf{B}_{12} \\ \mathbf{B}_{21} & \mathbf{B}_{22} \end{bmatrix} = \begin{bmatrix} \mathbb{1} & \mathbf{0} \\ \mathbf{0} & \mathbb{1} \end{bmatrix} . \tag{A.11}$$

Doing the matrix multiplication explicitly, we have, in particular, the equations

$$\mathbf{A}_{21}\mathbf{B}_{11} + \mathbf{A}_{22}\mathbf{B}_{21} = \mathbf{0} \; , \tag{A.12}$$

$$\mathbf{A}_{11}\mathbf{B}_{11} + \mathbf{A}_{12}\mathbf{B}_{21} = \mathbb{1} \; . \tag{A.13}$$

From Eq. (A.12), we have $\mathbf{B}_{21} = -\mathbf{A}_{22}^{-1}\mathbf{A}_{21}\mathbf{B}_{11}$, which in Eq. (A.13) gives

$$\mathbf{A}_{11}\mathbf{B}_{11} - \mathbf{A}_{12}\mathbf{A}_{22}^{-1}\mathbf{A}_{21}\mathbf{B}_{11} = 0 \tag{A.14}$$

$$\Rightarrow \mathbf{B}_{11} = \frac{1}{\mathbf{A}_{11} - \mathbf{A}_{12}\mathbf{A}_{22}^{-1}\mathbf{A}_{21}} \tag{A.15}$$

$$\Rightarrow \boxed{(\mathbf{A}^{-1})_{11} = \frac{1}{\mathbf{A}_{11} - \mathbf{A}_{12}\mathbf{A}_{22}^{-1}\mathbf{A}_{21}}} \; . \tag{A.16}$$

Similarly, using the remaining equations from the matrix multiplication Eq. (A.11), we have

$$\mathbf{B}_{22} = \boxed{(\mathbf{A}^{-1})_{22} = \frac{1}{\mathbf{A}_{22} - \mathbf{A}_{21}\mathbf{A}_{11}^{-1}\mathbf{A}_{12}}} . \tag{A.17}$$

A.3 Path integral formulation of the impurity problem

The action for the one-band Hubbard model Eq. (2.27) [1] is given by

$$S = \int dt \sum_{\mathbf{r},\mathbf{r}',\sigma} \bar{c}_{\mathbf{r}\sigma}(t)(i\delta_{\mathbf{r}\mathbf{r}'}\partial_t - t_{\mathbf{r}\mathbf{r}'})c_{\mathbf{r}'\sigma}(t) - U\sum_{\mathbf{r}}\int dt\, n_{\mathbf{r}\uparrow}(t)n_{\mathbf{r}\downarrow}(t) , \tag{A.18}$$

where $c_{\mathbf{r}\sigma}(t)$, $\bar{c}_{\mathbf{r}\sigma}(t)$ are Grassman variables ($\bar{c}_{\mathbf{r}\sigma}(t)$ is the adjoint of $c_{\mathbf{r}\sigma}(t)$), $n_{\mathbf{r}\sigma}(t) = \bar{c}_{\mathbf{r}\sigma}(t)c_{\mathbf{r}\sigma}(t)$. The action Eq. (A.18) can be expressed in terms of the non-interacting Green function for the lattice:

$$S = \int dt \int dt' \left[\sum_{\mathbf{r},\mathbf{r}',\sigma} \bar{c}_{\mathbf{r}\sigma}(t) G^{-1}_{0,\mathbf{r}\mathbf{r}'}(t-t') c_{\mathbf{r}'\sigma}(t') - U\sum_{\mathbf{r}} n_{\mathbf{r}\uparrow}(t)n_{\mathbf{r}\downarrow}(t')\delta(t-t') \right] , \tag{A.19}$$

with $G^{-1}_{0,\mathbf{r}\mathbf{r}'}(t-t') = i\delta_{\mathbf{r}\mathbf{r}'}\partial_t - t_{\mathbf{r}\mathbf{r}'}\delta(t-t')$.

In CDMFT, a cluster of correlated sites is hybridized to a non-interacting bath which is determined self-consistently. The effective action for a given cluster is taken as

$$S_{c,\mathrm{eff}} = \int dt \int dt' \left[\sum_{\mathbf{r},\mathbf{r}',\sigma} \bar{c}_{\mathbf{r}\sigma}(t) \mathscr{G}^{-1}_{0,\mathbf{r}\mathbf{r}'}(t-t') c_{\mathbf{r}'\sigma}(t') - U\sum_{\mathbf{r}} n_{\mathbf{r}\uparrow}(t)n_{\mathbf{r}\downarrow}(t')\delta(t-t') \right] , \tag{A.20}$$

where $\mathscr{G}_0$ is the *dynamical mean field*. Here $\mathbf{r}$, $\mathbf{r}'$ are restricted to the cluster. The dynamical mean field $\mathscr{G}_0$ is the effective non-interacting Green function for the cluster, which can be expressed in the frequency domain as

$$\mathscr{G}_0(\omega) = \frac{1}{\omega - \mathbf{t}_c - \mathbf{\Gamma}(\omega)} , \tag{A.21}$$

where we do not have the exact expression for the *bath hybridization* $\mathbf{\Gamma}(\omega)$ in this formulation. However, by requiring that the dynamical mean field $\mathscr{G}_0$ is causal [149], i.e., it obeys the physical properties of the Green function, we can express the bath hybridization $\mathbf{\Gamma}(\omega)$ similar to Eq. (3.49).

---

[1] here we take the $-$ sign within the hopping matrix $\mathbf{t}$

A.4 Correlation between the maximum superconducting gap and the hole content in oxygen orbitals

Within mean-field theory, the zero temperature superconducting gap is directly related to the critical temperature T_c. This is also believed to hold approximately for the high-T_c cuprates [4], i.e., for strong coupling superconductivity. The superconducting gap, in a strongly interacting model, can be approximated as $Re\Sigma^{an}(\mathbf{k}, z = 0)$ [47,48], given that the Fermi liquid theory holds in that regime. We plot this gap as a function of the hole content on oxygen orbitals, across various parameter-sets around the ionic case Eq. (4.1) and the covalent case Eq. (4.2), in Fig. A.1, similar to the order parameter plots (Figs. 4.9, 4.10). Although the maxima in the gap does not occur exactly at the same hole content on oxygen as that of the order parameter for a given parameter-set, we observe that the maximum value of the gap increases monotonously with the corresponding oxygen hole content for most of the parameter-sets. This strongly suggests that this monotonous relation is also expected between the T_c and the oxygen hole content at optimal doping, as has also been verified by our collaborators for the ionic case [177]. Note that we do not reach the maxima in the superconducting gap for the covalent case Eq. (4.2) with $t'_{pp} = 0.88$ ($U_d = 12$) and with $U_d = 14$. We also exclude some other parameter-sets around the covalent case Eq. (4.2) at $U = 10$, magenta curves in Fig. 4.10, since they do not lie in the strong coupling regime and hence do not correspond to cuprates. There are also some exceptions to this trend: The parameter-sets with $U_d = 16$ and 18 for the ionic case Eq. (4.1) are outliers, which correspond to the highest values of the CTG among all parameter-sets close to the ionic case. Thus, the deviation from the trend for these parameter-sets might be because we are far away from the Fermi liquid regime, and the approximation for the superconducting gap is no longer valid in this regime.

A.5 Calculation of the superconducting order parameter

We start with the expression for the Gorkov function Eq. (2.47):

$$F_{\mathbf{r}\mathbf{r}'}(z) = \langle\Omega|c_{\mathbf{r}\uparrow}\frac{1}{z - H + E_0}c_{\mathbf{r}'\downarrow}|\Omega\rangle + \langle\Omega|c_{\mathbf{r}'\downarrow}\frac{1}{z + H - E_0}c_{\mathbf{r}\uparrow}|\Omega\rangle \ . \tag{A.22}$$

Introducing a complete basis set in both the terms, we have

$$F_{\mathbf{r}\mathbf{r}'}(z) = \sum_n \frac{\langle\Omega|c_{\mathbf{r}\uparrow}|n\rangle\langle n|c_{\mathbf{r}'\downarrow}|\Omega\rangle}{z - (E_n - E_0)} + \sum_m \frac{\langle\Omega|c_{\mathbf{r}'\downarrow}|m\rangle\langle m|c_{\mathbf{r}\uparrow}|\Omega\rangle}{z + (E_m - E_0)} \ . \tag{A.23}$$

In Eq. (A.23), E_n, $E_m > E_0$ since the states $|n\rangle$ and $|m\rangle$ correspond to excitations from the groundstate $|\Omega\rangle$. Hence the first term of Eq. A.23 has poles on the positive real axis and the second term has poles on the negative real axis. Thus, on integrating $F_{\mathbf{r}\mathbf{r}'}(z)$ over the

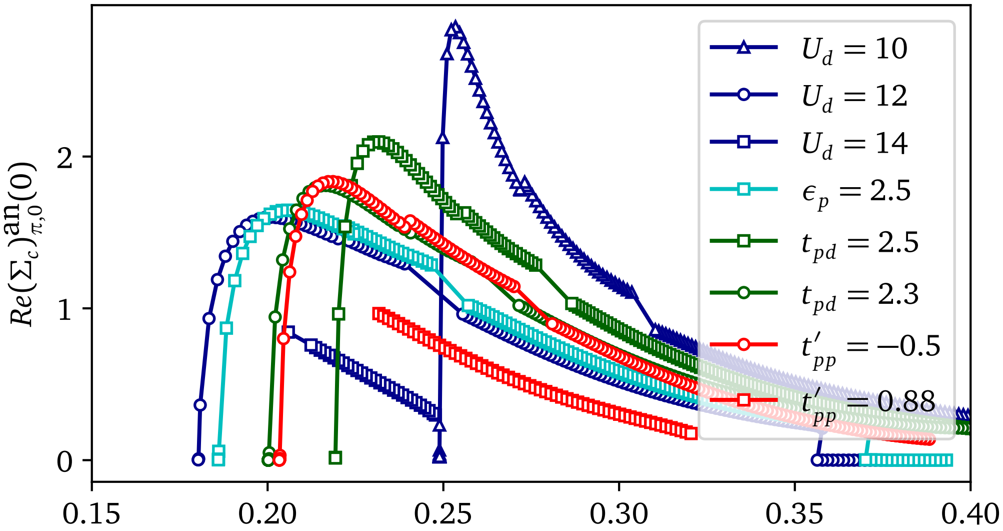
(a) Covalent case (Eq. (4.2)), $U_d = 12.0$

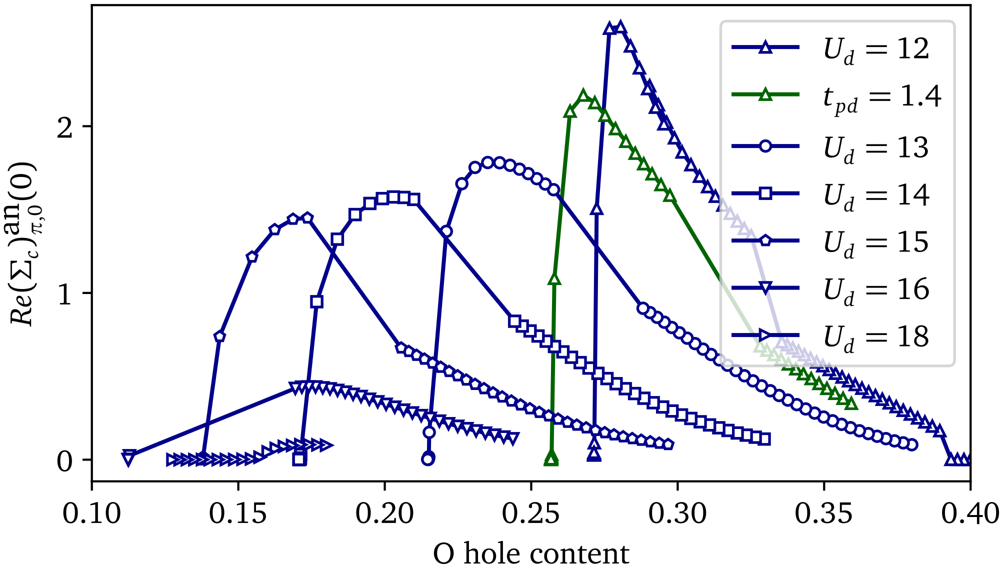
(b) Ionic case (Eq. (4.1)), $U_d = 12.0$

Figure A.1: Correlation between the maximum superconducting gap and the oxygen hole content. We plot the real part of the anomalous self-energy at zero frequency in the antinodal region, which is an approximate measure of the superconducting gap, as a function of the hole content on oxygen orbitals. This is considered as a proxy for T_c.

contour in Fig. 2.1, we get

$$\oint_{C_<} \frac{dz}{2\pi i} F_{\mathbf{r}\mathbf{r}'}(z) = \langle c_{\mathbf{r}'\downarrow} c_{\mathbf{r}\uparrow} \rangle = -\langle c_{\mathbf{r}\uparrow} c_{\mathbf{r}'\downarrow} \rangle \ . \tag{A.24}$$

Hence, the average of the pairing operator $\hat{\Psi} = (1/N)\sum_{\mathbf{r},\mathbf{r}'} g_{\mathbf{r},\mathbf{r}'} c_{\mathbf{r}\uparrow} c_{\mathbf{r}'\downarrow}$ (this is equivalent to the pairing operator defined in Eq. (2.45)[2]), which is the superconducting order parameter, is given by

$$\langle \hat{\Psi} \rangle = -\frac{1}{N} \oint_{C_<} \frac{dz}{2\pi i} \mathrm{tr}\left[\mathbf{gF}\right] \, . \tag{A.25}$$

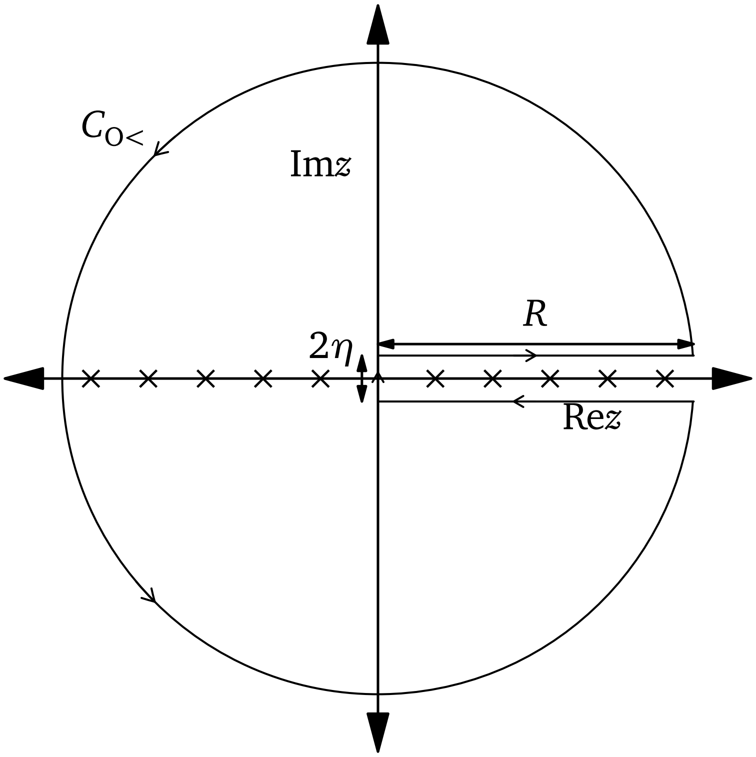

Figure A.2: Deformed version of the contour Fig. 2.1 to express the contour integral in Eqs. (A.24) as an integral over the real frequency. We peform the integral over this contour in the limit $\eta \to 0$ and $R \to \infty$.

We can express the integral (A.25) as an integral over the real axis by going to the contour in Fig. A.2. Let us start with the integral of first term of $F_{\mathbf{rr}'}(z)$ (A.23), $F^{(1)}_{\mathbf{rr}'}(z)$:

$$\oint_{C_{\mathrm{O}<}} \frac{dz}{2\pi i} F^{(1)}_{\mathbf{rr}'}(z) = \oint_{C_{\mathrm{O}<}} \frac{dz}{2\pi i} \sum_n \frac{A_{\mathbf{r}\uparrow,n} B_{\mathbf{r}'\downarrow,n}}{z - E_{n0}} \, , \tag{A.26}$$

---

[2] this holds when $g_{\mathbf{r},\mathbf{r}'} = g_{\mathbf{r}',\mathbf{r}}$, which is true for s-wave, s'-wave and d-wave form factors.

where $A_{\mathbf{r}\uparrow,n} = \langle\Omega|c_{\mathbf{r}\uparrow}|n\rangle$, $B_{\mathbf{r}'\downarrow,n} = \langle n|c_{\mathbf{r}'\downarrow}|\Omega\rangle$ and $E_{n0} = E_n - E_0$. On breaking the integral into integrals over separate sections of the contour $C_{\mathrm{O}<}$, we have

$$\oint_{C_{\mathrm{O}<}} \frac{dz}{2\pi i} \sum_n \frac{A_{\mathbf{r}\uparrow,n} B_{\mathbf{r}'\downarrow,n}}{z - E_{n0}} =$$
$$\int_0^\infty \frac{d\omega}{2\pi i} \sum_n \frac{A_{\mathbf{r}\uparrow,n} B_{\mathbf{r}'\downarrow,n}}{\omega - E_{n0} + i\eta} + \int_\infty^0 \frac{d\omega}{2\pi i} \sum_n \frac{A_{\mathbf{r}\uparrow,n} B_{\mathbf{r}'\downarrow,n}}{\omega - E_{n0} - i\eta} + I^{(1)}_{\text{circular}}\,, \tag{A.27}$$

where ω is the real part of the complex frequency z and $I^{(1)}_{\text{circular}}$ is the contribution of the integral from the circular part of the contour. Note that the integral over the short section along the imaginary axis vanishes in the limit $\eta \to 0$. On simplifying Eq. (A.27), i.e., on making the denominators real and on the inverting the integration limits of the second term, we have

$$\int_0^\infty \frac{d\omega}{2\pi i} \sum_n \frac{A_{\mathbf{r}\uparrow,n} B_{\mathbf{r}'\downarrow,n}\,(\omega - E_{n0} - i\eta)}{(\omega - E_{n0})^2 + \eta^2} - \int_0^\infty \frac{d\omega}{2\pi i} \sum_n \frac{A_{\mathbf{r}\uparrow,n} B_{\mathbf{r}'\downarrow,n}\,(\omega - E_{n0} + i\eta)}{(\omega - E_{n0})^2 + \eta^2} + I^{(1)}_{\text{circular}} \tag{A.28}$$

$$= -\int_0^\infty \frac{d\omega}{\pi} \sum_n \frac{A_{\mathbf{r}\uparrow,n} B_{\mathbf{r}'\downarrow,n}\,(\eta)}{(\omega - E_{n0})^2 + \eta^2} + I^{(1)}_{\text{circular}} \tag{A.29}$$

$$= \int_0^\infty \frac{d\omega}{\pi} \mathrm{Im}\big[F^{(1)}_{\mathbf{r}\mathbf{r}'}(\omega + i\eta)\big] + I^{(1)}_{\text{circular}}\,. \tag{A.30}$$

We can follow exactly the same steps Eq. (A.27)-Eq. (A.30) for the contour integral of the second term of $F_{\mathbf{r}\mathbf{r}'}(z)$ (A.23), $F^{(2)}_{\mathbf{r}\mathbf{r}'}(z)$, and we would finally have

$$\oint_{C_{\mathrm{O}<}} \frac{dz}{2\pi i} F_{\mathbf{r}\mathbf{r}'}(z) = \int_0^\infty \frac{d\omega}{\pi} \mathrm{Im}\big[F^R_{\mathbf{r}\mathbf{r}'}(\omega)\big] + I_{\text{circular}}\,, \tag{A.31}$$

where $F^R_{\mathbf{r}\mathbf{r}'}(\omega) = F_{\mathbf{r}\mathbf{r}'}(\omega + i\eta)$ is the retarded Gorkov function and I_{circular} is the contribution to the contour integral (LHS of Eq. (A.31)) from the circular part of the contour Fig. A.2. Now, the order parameter (Eq. (A.25)) can be written as

$$\boxed{\langle\hat{\Psi}\rangle = -\frac{1}{N} \int_0^\infty \frac{d\omega}{\pi} \mathrm{Im}\big[\mathrm{tr}[\mathbf{g}\mathbf{F}^R(\omega)]\big]}\,, \tag{A.32}$$

where the integral over the circular parts are cancelled upto the leading order in the expansion of $F_{\mathbf{r}\mathbf{r}'}(z)$ in the limit $|z| \to \infty$. Higher order terms do not contribute to the integral in this limit. This can be seen by expanding $F_{\mathbf{rr}'}(z)$ (A.23) in the limit $|z| \to \infty$:

$$\begin{aligned} F_{\mathbf{rr}'}(z) &= \sum_n \frac{\langle\Omega|c_{\mathbf{r}\uparrow}|n\rangle\langle n|c_{\mathbf{r}'\downarrow}|\Omega\rangle}{z}\left[1+\frac{E_{n0}}{z}+\frac{E_{n0}^2}{z^2}+\frac{E_{n0}^3}{z^3}+\cdots\right] \\ &+\sum_m \frac{\langle\Omega|c_{\mathbf{r}'\downarrow}|m\rangle\langle m|c_{\mathbf{r}\uparrow}|\Omega\rangle}{z}\left[1+\frac{E_{m0}}{z}+\frac{E_{m0}^2}{z^2}+\frac{E_{m0}^3}{z^3}+\cdots\right] \qquad \text{(A.33)} \\ &= \sum_n \langle\Omega|c_{\mathbf{r}\uparrow}|n\rangle\langle n|c_{\mathbf{r}'\downarrow}|\Omega\rangle\left[\frac{E_{n0}}{z^2}+\frac{E_{n0}^2}{z^3}+\frac{E_{n0}^3}{z^4}+\cdots\right] \\ &+\sum_m \langle\Omega|c_{\mathbf{r}'\downarrow}|m\rangle\langle m|c_{\mathbf{r}\uparrow}|\Omega\rangle\left[\frac{E_{m0}}{z^2}+\frac{E_{m0}^2}{z^3}+\frac{E_{m0}^3}{z^4}+\cdots\right]. \qquad \text{(A.34)} \end{aligned}$$

Hence, the integral of $F_{\mathbf{rr}'}(z)$ over the circular part of the contour vanishes as $|z| \to \infty$[3].

A.6 Projection of the lattice Green function on Cu orbitals in the three-band Hubbard model

We choose the unitcell of the super-lattice as shown by the gray box in Fig. 4.16(a). The four Cu orbitals within the super-cell form the Cu cluster (red box), which is connected to a bath. The eight uncorrelated O orbitals in the super-cell form the O cluster (blue box); since O orbitals are uncorrelated, the O cluster is not connected to any bath. The lattice Green function in this case can be written following Eq. (3.58) as

$$\mathbf{G}(\tilde{\mathbf{k}}, z) = \begin{bmatrix} z - \mathbf{t}_{\mathrm{Cu}}(\tilde{\mathbf{k}}) - \mathbf{\Sigma}(z) & -\mathbf{t}_{\mathrm{Cu-O}}(\tilde{\mathbf{k}}) \\ -\mathbf{t}_{\mathrm{Cu-O}}(\tilde{\mathbf{k}}) & z - \mathbf{t}_{\mathrm{O}}(\tilde{\mathbf{k}}) \end{bmatrix}^{-1}, \qquad \text{(A.35)}$$

where $\mathbf{t}_{\mathrm{Cu}}(\tilde{\mathbf{k}})$ is the hopping matrix (4×4) of the lattice projected on the Cu orbitals (which is zero, as we do not have hopping between the Cu orbitals (Fig. 2.4)), $\mathbf{t}_{\mathrm{Cu-O}}(\tilde{\mathbf{k}})$ is the inter-cluster hopping matrix (4×8), i.e., between Cu and O orbitals, $\mathbf{t}_{\mathrm{O}}(\tilde{\mathbf{k}})$ is the hopping matrix (8×8) projected on the O orbitals and $\mathbf{\Sigma}$ is the self-energy of the Cu cluster. The O cluster does not have a self-energy because it is uncorrelated. Note that the numbering of orbitals within each cluster is done following the usual convention: from left to right, bottom to top. Since only the Cu cluster is connected to a bath, the lattice Green function that goes into the distance function Eq. (3.56) is the Green function projected on the Cu orbitals $\mathbf{G}_{\mathrm{Cu}}(\tilde{\mathbf{k}}, z)$. This is given by the first 4×4 block of the matrix $\mathbf{G}(\tilde{\mathbf{k}}, z)$. Using Eq. (A.16), this becomes

$$\mathbf{G}_{\mathrm{Cu}}(\tilde{\mathbf{k}}, z) = \left[z - \Sigma(z) - \mathbf{\Gamma}_{\mathrm{O}}(\tilde{\mathbf{k}}, z)\right]^{-1}, \qquad \text{(A.36)}$$

---

[3] $I_{\text{circular}} = \lim_{|z|\to\infty} \int^{\text{circular part}} \frac{dz}{2\pi i} F_{\mathbf{rr}'}(z) < \lim_{R\to\infty} \frac{1}{2\pi i} 2\pi R \max_{|z|=R}[F_{\mathbf{rr}'}(z)] = 0$, since $F_{\mathbf{rr}'}(z) \sim \frac{1}{z^2}$ as $z \to \infty$.

where

$$\boldsymbol{\Gamma}_{\mathrm{O}}(\tilde{\mathbf{k}}, z) = \mathbf{t}_{\mathrm{Cu-O}}(\tilde{\mathbf{k}}) \frac{1}{z - \mathbf{t}_{\mathrm{O}}(\tilde{\mathbf{k}})} \mathbf{t}_{\mathrm{Cu-O}}(\tilde{\mathbf{k}}) \,. \tag{A.37}$$

The exact forms of the matrices $\mathbf{t}_{\mathrm{O}}(\tilde{\mathbf{k}})$ and $\mathbf{t}_{\mathrm{Cu-O}}(\tilde{\mathbf{k}})$ can be deduced easily from Fig. 2.4.

A.7 Susceptibility at zero temperature

As disussed in page 27, the Green function that we have used in this thesis gives the propagation amplitude for a single particle (fermionic) excitation, and is known as the one-particle Green function. It is useful to generalize this to a multi-particle Green function, where we replace the creation and annihilation operators by any operator in general. This object is known as the susceptibility and gives the response of the system to an external field, and hence is also known as the response function [115]. The *retarded* response function (susceptibility) corresponding to an operator A is defined as[4]

$$\chi^R(\mathbf{r}, \mathbf{r}', t, t') = i\langle [A(\mathbf{r}, t), A(\mathbf{r}', t')] \rangle \theta(t - t') \,. \tag{A.38}$$

At zero temperature, it is given by

$$\chi^R(\mathbf{r}, \mathbf{r}', t) = i \left[\langle \Omega | A(\mathbf{r}, t) A(\mathbf{r}') | \Omega \rangle - \langle \Omega | A(\mathbf{r}') A(\mathbf{r}, t) | \Omega \rangle \right] \theta(t) \,, \tag{A.39}$$

where we have set $t' = 0$, since the the function only depends on the time difference for an equillibrium system.

The retarded susceptibility in the frequency space, $\chi^R(\mathbf{r}, \mathbf{r}', \omega)$ becomes

$$\begin{aligned}
\chi^R(\mathbf{r}, \mathbf{r}', \omega) &= i \int_0^\infty dt\; e^{i(\omega + i\eta)t} \left[\langle \Omega | e^{iHt} A(\mathbf{r}) e^{-iHt} A(\mathbf{r}') | \Omega \rangle - \langle \Omega | A(\mathbf{r}') e^{iHt} A(\mathbf{r}) e^{-iHt} | \Omega \rangle \right] && \text{(A.40)} \\
&= i \int_0^\infty dt\; \left[\langle \Omega | A(\mathbf{r}) e^{i(\omega + i\eta - H + E_0)t} A(\mathbf{r}') | \Omega \rangle - \langle \Omega | A(\mathbf{r}') e^{i(\omega + i\eta + H - E_0)t} A(\mathbf{r}) | \Omega \rangle \right] && \text{(A.41)} \\
&= - \left[\langle \Omega | A(\mathbf{r}) \frac{1}{\omega + i\eta - H + E_0} A(\mathbf{r}') | \Omega \rangle - \langle \Omega | A(\mathbf{r}') \frac{1}{\omega + i\eta + H - E_0} A(\mathbf{r}) | \Omega \rangle \right] , && \text{(A.42)}
\end{aligned}$$

---

[4] In general, the susceptibility is defined w.r.t. two operators A and B, where $\chi^R_{BA}(\mathbf{r}, \mathbf{r}', t, t') = i\langle [B(\mathbf{r}, t), A(\mathbf{r}', t')] \rangle \theta(t - t')$ gives the response of the operator B to a perturbation in the Hamiltonian corresponding to the operator A (upto first order in the perturbation). In this thesis, we focus on the case where $A = B$, since we are interested in the inherent fluctuations in a given field, specifically in the antiferromagnetic field.

where E_0 is the energy of the groundstate $|\Omega\rangle$.

The susceptibility function $\chi''(\mathbf{q},\omega)$ plotted in Fig. 4.14 is the imaginary part of the retarded spin susceptibility $\chi^R_{\text{spin}}(\mathbf{q},\omega)$, which is given by

$$\chi^R_{\text{spin}}(\mathbf{q},\omega) = -\left[\langle\Omega|M(\mathbf{q})\frac{1}{\omega + i\eta - H + E_0}M(\mathbf{q})|\Omega\rangle - \langle\Omega|M(\mathbf{q})\frac{1}{\omega + i\eta + H - E_0}M(\mathbf{q})|\Omega\rangle \right] , \tag{A.43}$$

where $|\Omega\rangle$ is the groundstate of the cluster and

$$M(\mathbf{q}) = \sum_{\mathbf{R}} \left(n_{\mathbf{R}\uparrow} - n_{\mathbf{R}\downarrow}\right) e^{i\mathbf{q}\cdot\mathbf{R}} \ , \ \mathbf{R} \in \text{cluster} \ . \tag{A.44}$$

Bibliography

[1] Øystein Fischer, Martin Kugler, Ivan Maggio-Aprile, Christophe Berthod, and Christoph Renner. Scanning tunneling spectroscopy of high-temperature superconductors. *Reviews of Modern Physics*, 79(1):353, 2007. URL: `https://journals.aps.org/rmp/abstract/10.1103/RevModPhys.79.353`.

[2] Dirk Van Delft and Peter Kes. The discovery of superconductivity. *Physics Today*, 63(9):38–43, 2010. URL: `https://snf.ieeecsc.org/sites/ieeecsc.org/files/RN16e.pdf`.

[3] Vitalii L Ginzburg. High-temperature superconductivity (history and general review). *Soviet Physics Uspekhi*, 34(4):283, 1991. URL: `https://iopscience.iop.org/article/10.1070/PU1991v034n04ABEH002361/meta`.

[4] Karl-Heinz Bennemann and John B Ketterson. *Superconductivity: Volume 1: Conventional and Unconventional Superconductors*. Springer Science & Business Media, 2008. URL: `https://link.springer.com/book/10.1007/978-3-540-73253-2`.

[5] Walther Meissner and Robert Ochsenfeld. Ein neuer effekt bei eintritt der supraleitfähigkeit. *Naturwissenschaften*, 21(44):787–788, 1933.

[6] JN Rjabinin and LW Shubnikow. Magnetic properties and critical currents of supra-conducting alloys. *Nature*, 135(3415):581–582, 1935. URL: `https://www.nature.com/articles/135581a0`.

[7] Fritz London and Heinz London. The electromagnetic equations of the supraconductor. *Proceedings of the Royal Society of London. Series A-Mathematical and Physical Sciences*, 149(866):71–88, 1935. URL: `https://royalsocietypublishing.org/doi/abs/10.1098/rspa.1935.0048`.

[8] Vitaly L Ginzburg and Lev D Landau. On the theory of superconductivity. In *On Superconductivity and Superfluidity*, pages 113–137. Springer, 2009. URL: `https://link.springer.com/chapter/10.1007/978-3-540-68008-6_4`.

[9] Alexei A Abrikosov. On the magnetic properties of superconductors of the second group. *Sov. Phys. JETP*, 5:1174–1182, 1957.

[10] Shoji Tanaka. High-temperature superconductivity: History and outlook. *JSAP international*, 4(4):17–22, 2001. URL: `http://www.jsap.or.jp/jsapi/Pdf/Number04/PastPresentFuture.pdf`.

[11] Truong D Thanh, A Koma, and S Tanaka. Superconductivity in the $BaPb_{1-x}Bi_xO_3$ system. In *Ten Years of Superconductivity: 1980–1990*, pages 259–266. Springer, 1980. URL: `https://link.springer.com/chapter/10.1007/978-94-011-1622-0_31`.

[12] J George Bednorz and K Alex Müller. Possible high T_c superconductivity in the Ba-La-Cu-O system. *Zeitschrift für Physik B Condensed Matter*, 64(2):189–193, 1986. URL: `https://link.springer.com/article/10.1007/BF01303701`.

[13] D Jérome, A Mazaud, M Ribault, and K Bechgaard. Superconductivity in a synthetic organic conductor $(TMTSF)_2PF_6$. *Journal de Physique Lettres*, 41(4):95–98, 1980. URL: `https://jphyslet.journaldephysique.org/articles/jphyslet/abs/1980/04/jphyslet_1980__41_4_95_0/jphyslet_1980__41_4_95_0.html`.

[14] Roland Hott, Reinhold Kleiner, Thomas Wolf, and Gertrud Zwicknagl. Superconducting materials—A topical overview. *Frontiers in Superconducting Materials*, pages 1–69, 2005. URL: `https://link.springer.com/chapter/10.1007/3-540-27294-1_1`.

[15] Roland Hott, Reinhold Kleiner, Thomas Wolf, and Gertrud Zwicknagl. Review on superconducting materials. *arXiv preprint arXiv:1306.0429*, 2013. URL: `https://arxiv.org/abs/1306.0429`.

[16] Hiroki Takahashi, Kazumi Igawa, Kazunobu Arii, Yoichi Kamihara, Masahiro Hirano, and Hideo Hosono. Superconductivity at 43k in an iron-based layered compound $LaO_{1-x}F_xFeAs$. *Nature*, 453(7193):376–378, 2008. URL: `https://www.nature.com/articles/nature06972`.

[17] Yuan Cao, Valla Fatemi, Ahmet Demir, Shiang Fang, Spencer L Tomarken, Jason Y Luo, Javier D Sanchez-Yamagishi, Kenji Watanabe, Takashi Taniguchi, Efthimios Kaxiras, et al. Correlated insulator behaviour at half-filling in magic-angle graphene superlattices. *Nature*, 556(7699):80–84, 2018. URL: `https://www.nature.com/articles/nature26154`.

[18] Yinwei Li, Jian Hao, Hanyu Liu, Yanling Li, and Yanming Ma. The metallization and superconductivity of dense hydrogen sulfide. *The Journal of chemical physics*, 140(17):174712, 2014. URL: `https://aip.scitation.org/doi/full/10.1063/1.4874158`.

[19] AP Drozdov, MI Eremets, IA Troyan, Vadim Ksenofontov, and Sergii I Shylin. Conventional superconductivity at 203 Kelvin at high pressures in the sulfur hydride system. *Nature*, 525(7567):73–76, 2015. URL: `https://www.nature.com/articles/nature14964`.

[20] AP Drozdov, PP Kong, VS Minkov, SP Besedin, MA Kuzovnikov, S Mozaffari, L Balicas, FF Balakirev, DE Graf, VB Prakapenka, et al. Superconductivity at 250k in lanthanum hydride under high pressures. *Nature*, 569(7757):528–531, 2019. URL: `https://www.nature.com/articles/s41586-019-1201-8`.

[21] Danfeng Li, Kyuho Lee, Bai Yang Wang, Motoki Osada, Samuel Crossley, Hye Ryoung Lee, Yi Cui, Yasuyuki Hikita, and Harold Y Hwang. Superconductivity in an infinite-layer nickelate. *Nature*, 572(7771):624–627, 2019. URL: `https://www.nature.com/articles/s41586-019-1496-5`.

[22] YJ Yan, MQ Ren, HC Xu, BP Xie, R Tao, HY Choi, N Lee, YJ Choi, T Zhang, and DL Feng. Electron-doped Sr_2IrO_4: An analogue of hole-doped cuprate superconductors demonstrated by scanning tunneling microscopy. *Physical Review X*, 5(4):041018, 2015. URL: `https://www.nature.com/articles/nphys3503.pdf`.

[23] Yeong Kwan Kim, NH Sung, JD Denlinger, and BJ Kim. Observation of a d-wave gap in electron-doped Sr_2IrO_4. *Nature Physics*, 12(1):37–41, 2016. URL: `https://www.nature.com/articles/nphys3503`.

[24] Shoji Tanaka. High-temperature superconductivity. *Japanese journal of applied physics*, 45(12R):9011, 2006. URL: `https://iopscience.iop.org/article/10.1143/JJAP.45.9011/meta`.

[25] Shoji Tanaka. Possibility of two-dimensional superconductivity in $(La, Ba)_2CuO_4$ and $(La, Sr)_2CuO_4$ with high critical temperatures. *Japanese journal of applied physics*, 26(3A):L203, 1987. URL: `https://iopscience.iop.org/article/10.1143/JJAP.26.L203/meta`.

[26] Elbio Dagotto. Correlated electrons in high-temperature superconductors. *Reviews of Modern Physics*, 66(3):763, 1994. URL: `https://journals.aps.org/rmp/abstract/10.1103/RevModPhys.66.763`.

[27] J Orenstein and AJ Millis. Advances in the physics of high-temperature superconductivity. *Science*, 288(5465):468–474, 2000. URL: `https://science.sciencemag.org/content/288/5465/468.abstract`.

[28] Bernhard Keimer, Steven A Kivelson, Michael R Norman, Shinichi Uchida, and J Zaanen. From quantum matter to high-temperature superconductivity in copper oxides. *Nature*, 518(7538):179–186, 2015. URL: `https://www.nature.com/articles/nature14165`.

[29] Warren E Pickett. Electronic structure of the high-temperature oxide superconductors. *Reviews of Modern Physics*, 61(2):433, 1989. URL: `https://journals.aps.org/rmp/abstract/10.1103/RevModPhys.61.433`.

[30] Jan Zaanen. Watching rush hour in the world of electrons. *Science*, 315(5817):1372–1373, 2007. URL: `https://science.sciencemag.org/content/315/5817/1372.summary`.

[31] Philip W Anderson. The resonating valence bond state in La_2CuO_4 and superconductivity. *science*, 235(4793):1196–1198, 1987. URL: `https://science.sciencemag.org/content/235/4793/1196.abstract`.

[32] FC Zhang and TM Rice. Effective hamiltonian for the superconducting Cu oxides. *Physical Review B*, 37(7):3759, 1988. URL: `https://journals.aps.org/prb/abstract/10.1103/PhysRevB.37.3759`.

[33] John Robert Schrieffer and James S Brooks. *Handbook of high-temperature superconductivity: Theory and experiment*. Springer, New York, 2007. URL: `https://link.springer.com/book/10.1007/978-0-387-68734-6`.

[34] DA Wollman, DJ Van Harlingen, WC Lee, DM Ginsberg, and AJ Leggett. Experimental determination of the superconducting pairing state in YBCO from the phase coherence of YBCO-Pb DC SQUIDs. *Physical Review Letters*, 71(13):2134, 1993. URL: `https://journals.aps.org/prl/abstract/10.1103/PhysRevLett.71.2134`.

[35] DA Wollman, Dale J Van Harlingen, John Giapintzakis, and DM Ginsberg. Evidence for $d_{x^2-y^2}$ pairing from the magnetic field modulation of $YBa_2Cu_3O_7$-Pb josephson junctions. *Physical review letters*, 74(5):797, 1995. URL: `https://journals.aps.org/prl/abstract/10.1103/PhysRevLett.74.797`.

[36] HJH Smilde, DHA Blank, GJ Gerritsma, H Hilgenkamp, H Rogalla, et al. d-wave–induced josephson current counterflow in $YBa_2Cu_3O_7$/Nb zigzag junctions. *Physical review letters*, 88(5):057004, 2002. URL: `https://journals.aps.org/prl/abstract/10.1103/PhysRevLett.88.057004`.

[37] MR Norman, H Ding, M Randeria, JC Campuzano, Takayoshi Yokoya, T Takeuchi, T Takahashi, T Mochiku, K Kadowaki, P Guptasarma, et al. Destruction of the Fermi surface in underdoped high-T_c superconductors. *Nature*, 392(6672):157–160, 1998. URL: `https://www.nature.com/articles/32366`.

[38] Tom Timusk and Bryan Statt. The pseudogap in high-temperature superconductors: an experimental survey. *Reports on Progress in Physics*, 62(1):61, 1999. URL: `https://iopscience.iop.org/article/10.1088/0034-4885/62/1/002/meta`.

[39] DS Marshall, DS Dessau, AG Loeser, CH Park, AY Matsuura, JN Eckstein, I Bozovic, P Fournier, A Kapitulnik, WE Spicer, et al. Unconventional electronic structure evolution with hole doping in $Bi_2Sr_2CaCu_2O_{8+\delta}$: Angle-resolved photoemission results. *Physical review letters*, 76(25):4841, 1996. URL: `https://journals.aps.org/prl/abstract/10.1103/PhysRevLett.76.4841`.

[40] Makoto Hashimoto, Inna M Vishik, Rui-Hua He, Thomas P Devereaux, and Zhi-Xun Shen. Energy gaps in high-transition-temperature cuprate superconductors. *Nature Physics*, 10(7):483–495, 2014. URL: `https://www.nature.com/articles/nphys3009`.

[41] C Collignon, S Badoux, SAA Afshar, B Michon, F Laliberté, O Cyr-Choinière, J-S Zhou, S Licciardello, S Wiedmann, N Doiron-Leyraud, et al. Fermi-surface transformation across the pseudogap critical point of the cuprate superconductor $La_{1.6-x}Nd_{0.4}Sr_xCuO_4$. *Physical Review B*, 95(22):224517, 2017. URL: `https://journals.aps.org/prb/abstract/10.1103/PhysRevB.95.224517`.

[42] Michael R Norman, D Pines, and C Kallin. The pseudogap: Friend or foe of high T_c? *Advances in Physics*, 54(8):715–733, 2005. URL: `https://www.tandfonline.com/doi/full/10.1080/00018730500459906`.

[43] Kiyohisa Tanaka, WS Lee, DH Lu, A Fujimori, T Fujii, I Terasaki, DJ Scalapino, TP Devereaux, Z Hussain, Z-X Shen, et al. Distinct Fermi-momentum-dependent energy gaps in deeply underdoped Bi2212. *Science*, 314(5807):1910–1913, 2006. URL: `https://www.science.org/doi/full/10.1126/science.1133411`.

[44] Takeshi Kondo, Rustem Khasanov, Tsunehiro Takeuchi, Jörg Schmalian, and Adam Kaminski. Competition between the pseudogap and superconductivity in the high-T_c copper oxides. *Nature*, 457(7227):296–300, 2009. URL: `https://www.nature.com/articles/nature07644`.

[45] Makoto Hashimoto, Elizabeth A Nowadnick, Rui-Hua He, Inna M Vishik, Brian Moritz, Yu He, Kiyohisa Tanaka, Robert G Moore, Donghui Lu, Yoshiyuki Yoshida, et al. Direct spectroscopic evidence for phase competition between the pseudogap and superconductivity in $Bi_2Sr_2CaCu_2O_{8+\delta}$. *Nature materials*, 14(1):37–42, 2015. URL: `https://www.nature.com/articles/nmat4116`.

[46] IM Vishik, M Hashimoto, Rui-Hua He, Wei-Sheng Lee, Felix Schmitt, Donghui Lu, RG Moore, C Zhang, W Meevasana, T Sasagawa, et al. Phase competition in trisected superconducting dome. *Proceedings of the National Academy of Sciences*, 109(45):18332–18337, 2012. URL: `https://www.pnas.org/content/109/45/18332.short`.

[47] Marcello Civelli, Massimo Capone, A Georges, Kristjan Haule, O Parcollet, TD Stanescu, and G Kotliar. Nodal-antinodal dichotomy and the two gaps of a superconducting doped Mott insulator. *Physical review letters*, 100(4):046402, 2008. URL: `https://journals.aps.org/prl/abstract/10.1103/PhysRevLett.100.046402`.

[48] M Civelli. Doping-driven evolution of the superconducting state from a doped Mott insulator: Cluster dynamical mean-field theory. *Physical Review B*, 79(19):195113, 2009. URL: `https://journals.aps.org/prb/abstract/10.1103/PhysRevB.79.195113`.

[49] Giovanni Sordi, Kristjan Haule, and A-MS Tremblay. Finite doping signatures of the Mott transition in the two-dimensional Hubbard model. *Physical re-*

view letters, 104(22):226402, 2010. URL: `https://journals.aps.org/prl/abstract/10.1103/PhysRevLett.104.226402`.

[50] G Sordi, Kristjan Haule, and A-MS Tremblay. Mott physics and first-order transition between two metals in the normal-state phase diagram of the two-dimensional Hubbard model. *Physical Review B*, 84(7):075161, 2011. URL: `https://journals.aps.org/prb/abstract/10.1103/PhysRevB.84.075161`.

[51] G Sordi, P Sémon, Kristjan Haule, and A-MS Tremblay. Pseudogap temperature as a Widom line in doped Mott insulators. *Scientific reports*, 2(1):1–5, 2012. URL: `https://www.nature.com/articles/srep00547`.

[52] Y Kohsaka, C Taylor, K Fujita, A Schmidt, C Lupien, T Hanaguri, M Azuma, M Takano, H Eisaki, H Takagi, et al. An intrinsic bond-centered electronic glass with unidirectional domains in underdoped cuprates. *Science*, 315(5817):1380–1385, 2007. URL: `https://science.sciencemag.org/content/315/5817/1380`.

[53] G Ghiringhelli, M Le Tacon, Matteo Minola, S Blanco-Canosa, Claudio Mazzoli, NB Brookes, GM De Luca, A Frano, DG Hawthorn, F He, et al. Long-range incommensurate charge fluctuations in (Y, Nd) $Ba_2Cu_3O_{6+x}$. *Science*, 337(6096):821–825, 2012. URL: `https://www.science.org/lookup/doi/10.1126/science.1223532`.

[54] Kazuhiro Fujita, Mohammad H Hamidian, Stephen D Edkins, Chung Koo Kim, Yuhki Kohsaka, Masaki Azuma, Mikio Takano, Hidenori Takagi, Hiroshi Eisaki, Shin-ichi Uchida, et al. Direct phase-sensitive identification of a d-form factor density wave in underdoped cuprates. *Proceedings of the National Academy of Sciences*, 111(30):E3026–E3032, 2014. URL: `https://www.pnas.org/content/111/30/E3026`.

[55] Riccardo Comin and Andrea Damascelli. Resonant X-ray scattering studies of charge order in cuprates. *Annual Review of Condensed Matter Physics*, 7:369–405, 2016. URL: `https://www.annualreviews.org/doi/10.1146/annurev-conmatphys-031115-011401`.

[56] R Comin, R Sutarto, F He, EH da Silva Neto, L Chauviere, A Frano, R Liang, WN Hardy, DA Bonn, Y Yoshida, et al. Symmetry of charge order in cuprates. *Nature materials*, 14(8):796–800, 2015. URL: `https://www.nature.com/articles/nmat4295`.

[57] AJ Achkar, R Sutarto, X Mao, F He, A Frano, S Blanco-Canosa, M Le Tacon, G Ghiringhelli, Lucio Braicovich, Matteo Minola, et al. Distinct charge orders in the planes and chains of ortho-III-ordered $YBa_2Cu_3O_{6+\delta}$ superconductors identified by resonant elastic X-ray scattering. *Physical review letters*, 109(16):167001, 2012. URL: `https://journals.aps.org/prl/abstract/10.1103/PhysRevLett.109.167001`.

[58] E Blackburn, J Chang, M Hücker, AT Holmes, Niels Bech Christensen, Ruixing Liang, DA Bonn, WN Hardy, U Rütt, Olof Gutowski, et al. X-ray diffraction observations of a charge-density-wave order in superconducting ortho-II $YBa_2Cu_3O_{6.54}$ single crystals in zero magnetic field. *Physical review letters*, 110(13):137004, 2013. URL: `https://journals.aps.org/prl/abstract/10.1103/PhysRevLett.110.137004`.

[59] S Blanco-Canosa, A Frano, T Loew, Y Lu, J Porras, G Ghiringhelli, Matteo Minola, C Mazzoli, Lucio Braicovich, E Schierle, et al. Momentum-dependent charge correlations in $YBa_2Cu_3O_{6+\delta}$ superconductors probed by resonant X-ray scattering: Evidence for three competing phases. *Physical review letters*, 110(18):187001, 2013. URL: `https://journals.aps.org/prl/abstract/10.1103/PhysRevLett.110.187001`.

[60] J Chang, Elizabeth Blackburn, AT Holmes, Niels B Christensen, Jacob Larsen, J Mesot, Ruixing Liang, DA Bonn, WN Hardy, A Watenphul, et al. Direct observation of competition between superconductivity and charge density wave order in $YBa_2Cu_3O_{6.67}$. *Nature Physics*, 8(12):871–876, 2012. URL: `https://www.nature.com/articles/nphys2456`.

[61] TP Croft, Christopher Lester, MS Senn, Alessandro Bombardi, and Stephen M Hayden. Charge density wave fluctuations in $La_{2-x}Sr_xCuO_4$ and their competition with superconductivity. *Physical Review B*, 89(22):224513, 2014. URL: `https://journals.aps.org/prb/abstract/10.1103/PhysRevB.89.224513`.

[62] Markus Huecker, Niels Bech Christensen, AT Holmes, Elizabeth Blackburn, Edward M Forgan, Ruixing Liang, DA Bonn, WN Hardy, Olof Gutowski, M v Zimmermann, et al. Competing charge, spin, and superconducting orders in underdoped $YBa_2Cu_3O_y$. *Physical Review B*, 90(5):054514, 2014. URL: `https://journals.aps.org/prb/abstract/10.1103/PhysRevB.90.054514`.

[63] Emmanuele Cappelluti and R Zeyher. Interplay between superconductivity and flux phase in the t-J model. *Physical Review B*, 59(9):6475, 1999. URL: `https://journals.aps.org/prb/abstract/10.1103/PhysRevB.59.6475`.

[64] JPL Faye and D Sénéchal. Interplay between d-wave superconductivity and a bond-density wave in the one-band Hubbard model. *Physical Review B*, 95(11):115127, 2017. URL: `https://journals.aps.org/prb/abstract/10.1103/PhysRevB.95.115127`.

[65] H Meier, C Pépin, M Einenkel, and KB Efetov. Cascade of phase transitions in the vicinity of a quantum critical point. *Physical Review B*, 89(19):195115, 2014. URL: `https://journals.aps.org/prb/abstract/10.1103/PhysRevB.89.195115`.

[66] C Pépin, VS De Carvalho, T Kloss, and X Montiel. Pseudogap, charge order, and pairing density wave at the hot spots in cuprate superconductors. *Physical Review B*,

90(19):195207, 2014. URL: `https://journals.aps.org/prb/abstract/10.1103/PhysRevB.90.195207`.

[67] Jay D Sau and Subir Sachdev. Mean-field theory of competing orders in metals with antiferromagnetic exchange interactions. *Physical Review B*, 89(7):075129, 2014. URL: `https://journals.aps.org/prb/pdf/10.1103/PhysRevB.89.075129`.

[68] Yuxuan Wang and Andrey Chubukov. Charge-density-wave order with momentum $(2Q, 0)$ and $(0, 2Q)$ within the spin-fermion model: Continuous and discrete symmetry breaking, preemptive composite order, and relation to pseudogap in hole-doped cuprates. *Physical Review B*, 90(3):035149, 2014. URL: `https://journals.aps.org/prb/abstract/10.1103/PhysRevB.90.035149`.

[69] Andrea Allais, Johannes Bauer, and Subir Sachdev. Density wave instabilities in a correlated two-dimensional metal. *Physical Review B*, 90(15):155114, 2014. URL: `https://journals.aps.org/prb/pdf/10.1103/PhysRevB.90.155114`.

[70] Matias Bejas, Andrés Greco, and Hiroyuki Yamase. Possible charge instabilities in two-dimensional doped Mott insulators. *Physical Review B*, 86(22):224509, 2012. URL: `https://journals.aps.org/prb/pdf/10.1103/PhysRevB.86.224509`.

[71] JC Séamus Davis and Dung-Hai Lee. Concepts relating magnetic interactions, intertwined electronic orders, and strongly correlated superconductivity. *Proceedings of the National Academy of Sciences*, 110(44):17623–17630, 2013. URL: `https://www.pnas.org/content/pnas/110/44/17623.full.pdf`.

[72] Marcin Raczkowski, Manuela Capello, Didier Poilblanc, Raymond Frésard, and Andrzej M Oleś. Unidirectional d-wave superconducting domains in the two-dimensional t-J model. *Physical Review B*, 76(14):140505, 2007. URL: `https://journals.aps.org/prb/pdf/10.1103/PhysRevB.76.140505`.

[73] Subir Sachdev and Rolando La Placa. Bond order in two-dimensional metals with antiferromagnetic exchange interactions. *Physical review letters*, 111(2):027202, 2013. URL: `https://journals.aps.org/prl/pdf/10.1103/PhysRevLett.111.027202`.

[74] Matthias Vojta, Ying Zhang, and Subir Sachdev. Competing orders and quantum criticality in doped antiferromagnets. *Physical Review B*, 62(10):6721, 2000. URL: `https://journals.aps.org/prb/pdf/10.1103/PhysRevB.62.6721`.

[75] Matthias Vojta. Superconducting charge-ordered states in cuprates. *Physical Review B*, 66(10):104505, 2002. URL: `https://journals.aps.org/prb/pdf/10.1103/PhysRevB.66.104505`.

[76] Steven R White and DJ Scalapino. Competition between stripes and pairing in a t-t'-J model. *Physical Review B*, 60(2):R753, 1999. URL: `https://journals.aps.org/prb/abstract/10.1103/PhysRevB.60.R753`.

[77] R Comin, A Frano, Michael Manchun Yee, Y Yoshida, H Eisaki, E Schierle, E Weschke, R Sutarto, F He, Anjan Soumyanarayanan, et al. Charge order driven by Fermi-arc instability in $Bi_2Sr_{2-x}La_xCuO_{6+\delta}$. *Science*, 343(6169):390–392, 2014. URL: `https://www.science.org/doi/full/10.1126/science.1242996`.

[78] WA Atkinson, Arno P Kampf, and S Bulut. Charge order in the pseudogap phase of cuprate superconductors. *New Journal of Physics*, 17(1):013025, 2015. URL: `https://iopscience.iop.org/article/10.1088/1367-2630/17/1/013025`.

[79] S Badoux, W Tabis, F Laliberté, G Grissonnanche, B Vignolle, D Vignolles, Jerome Béard, DA Bonn, WN Hardy, R Liang, et al. Change of carrier density at the pseudogap critical point of a cuprate superconductor. *Nature*, 531(7593):210–214, 2016. URL: `https://www.nature.com/articles/nature16983`.

[80] S Verret, M Charlebois, D Sénéchal, and A-MS Tremblay. Subgap structures and pseudogap in cuprate superconductors: Role of density waves. *Physical Review B*, 95(5):054518, 2017. URL: `https://journals.aps.org/prb/abstract/10.1103/PhysRevB.95.054518`.

[81] MH Hamidian, SD Edkins, Sang Hyun Joo, A Kostin, H Eisaki, S Uchida, MJ Lawler, E-A Kim, AP Mackenzie, K Fujita, et al. Detection of a Cooper-pair density wave in $Bi_2Sr_2CaCu_2O_{8+x}$. *Nature*, 532(7599):343–347, 2016. URL: `https://www.nature.com/articles/nature17411`.

[82] Wei Ruan, Xintong Li, Cheng Hu, Zhenqi Hao, Haiwei Li, Peng Cai, Xingjiang Zhou, Dung-Hai Lee, and Yayu Wang. Visualization of the periodic modulation of Cooper pairing in a cuprate superconductor. *Nature Physics*, 14(12):1178–1182, 2018. URL: `https://www.nature.com/articles/s41567-018-0276-8`.

[83] Daniel F Agterberg, JC Séamus Davis, Stephen D Edkins, Eduardo Fradkin, Dale J Van Harlingen, Steven A Kivelson, Patrick A Lee, Leo Radzihovsky, John M Tranquada, and Yuxuan Wang. The physics of pair-density waves: cuprate superconductors and beyond. *Annual Review of Condensed Matter Physics*, 11:231–270, 2020. URL: `https://www.annualreviews.org/doi/abs/10.1146/annurev-conmatphys-031119-050711`.

[84] Stephen D Edkins, Andrey Kostin, Kazuhiro Fujita, Andrew P Mackenzie, Hiroshi Eisaki, S Uchida, Subir Sachdev, Michael J Lawler, E-A Kim, JC Séamus Davis, et al. Magnetic field-induced pair density wave state in the cuprate vortex halo. *Science*, 364(6444):976–980, 2019. URL: `https://www.science.org/doi/abs/10.1126/science.aat1773`.

[85] Roberto Casalbuoni and Giuseppe Nardulli. Inhomogeneous superconductivity in condensed matter and QCD. *Reviews of Modern Physics*, 76(1):263, 2004. URL: `https://journals.aps.org/rmp/abstract/10.1103/RevModPhys.76.263`.

[86] Wei Ruan, Cheng Hu, Jianfa Zhao, Peng Cai, Yingying Peng, Cun Ye, Runze Yu, Xintong Li, Zhenqi Hao, Changqing Jin, et al. Relationship between the parent charge transfer gap and maximum transition temperature in cuprates. *Science bulletin*, 61(23):1826–1832, 2016. URL: `https://link.springer.com/article/10.1007/s11434-016-1204-x`.

[87] SS Kancharla, B Kyung, David Sénéchal, M Civelli, Massimo Capone, G Kotliar, and A-MS Tremblay. Anomalous superconductivity and its competition with antiferromagnetism in doped Mott insulators. *Physical Review B*, 77(18):184516, 2008. URL: `https://journals.aps.org/prb/abstract/10.1103/PhysRevB.77.184516`.

[88] L Fratino, P Sémon, Giovanni Sordi, and A-MS Tremblay. An organizing principle for two-dimensional strongly correlated superconductivity. *Scientific reports*, 6(1):1–6, 2016. URL: `https://www.nature.com/articles/srep22715`.

[89] Alexandre Foley, Simon Verret, A-MS Tremblay, and David Senechal. Coexistence of superconductivity and antiferromagnetism in the Hubbard model for cuprates. *Physical Review B*, 99(18):184510, 2019. URL: `https://journals.aps.org/prb/abstract/10.1103/PhysRevB.99.184510`.

[90] B Kyung, SS Kancharla, D Sénéchal, A-MS Tremblay, M Civelli, and G Kotliar. Pseudogap induced by short-range spin correlations in a doped Mott insulator. *Physical Review B*, 73(16):165114, 2006. URL: `https://journals.aps.org/prb/abstract/10.1103/PhysRevB.73.165114`.

[91] Ran Liu, D Salamon, MV Klein, SL Cooper, WC Lee, Sang-Wook Cheong, and DM Ginsberg. Novel Raman-active electronic excitations near the charge-transfer gap in insulating cuprates. *Physical review letters*, 71(22):3709, 1993. URL: `https://journals.aps.org/prl/abstract/10.1103/PhysRevLett.71.3709`.

[92] Ran Liu, MV Klein, D Salamon, S Lance Cooper, WC Lee, S-W Cheong, and DM Ginsberg. Raman studies of charge-transfer insulating cuprates. *Journal of Physics and Chemistry of Solids*, 54(10):1347–1350, 1993. URL: `https://www.sciencedirect.com/science/article/abs/pii/002236979390192T`.

[93] J Zaanen, GA Sawatzky, and JW Allen. Band gaps and electronic structure of transition-metal compounds. *Physical review letters*, 55(4):418, 1985. URL: `https://journals.aps.org/prl/abstract/10.1103/PhysRevLett.55.418`.

[94] VJ Emery. Theory of high-T_c superconductivity in oxides. *Physical Review Letters*, 58(26):2794, 1987. URL: `https://journals.aps.org/prl/abstract/10.1103/PhysRevLett.58.2794`.

[95] CM Varma, S Schmitt-Rink, and Elihu Abrahams. Charge transfer excitations and superconductivity in "ionic" metals. *Solid state communications*, 62(10):681–685, 1987. URL: `https://www.sciencedirect.com/science/article/abs/pii/0038109887904078`.

[96] Gabriel Kotliar and Jialin Liu. Superconducting instabilities in the large-U limit of a generalized Hubbard model. *Physical review letters*, 61(15):1784, 1988. URL: `https://journals.aps.org/prl/abstract/10.1103/PhysRevLett.61.1784`.

[97] D Sénéchal, AGR Day, V Bouliane, and A-MS Tremblay. Resilience of d-wave superconductivity to nearest-neighbor repulsion. *Physical Review B*, 87(7):075123, 2013. URL: `https://journals.aps.org/prb/abstract/10.1103/PhysRevB.87.075123`.

[98] K Miyake, S Schmitt-Rink, and CM Varma. Spin-fluctuation-mediated even-parity pairing in heavy-fermion superconductors. *Physical Review B*, 34(9):6554, 1986. URL: `https://journals.aps.org/prb/abstract/10.1103/PhysRevB.34.6554`.

[99] B Kyung, D Sénéchal, and A-MS Tremblay. Pairing dynamics in strongly correlated superconductivity. *Physical Review B*, 80(20):205109, 2009. URL: `https://journals.aps.org/prb/abstract/10.1103/PhysRevB.80.205109`.

[100] Douglas J Scalapino. A common thread: The pairing interaction for unconventional superconductors. *Reviews of Modern Physics*, 84(4):1383, 2012. URL: `https://journals.aps.org/rmp/abstract/10.1103/RevModPhys.84.1383`.

[101] Lichen Wang, Guanhong He, Zichen Yang, Mirian Garcia-Fernandez, Abhishek Nag, Ke-Jin Zhou, Matteo Minola, Matthieu Le Tacon, Bernhard Keimer, Yingying Peng, et al. Paramagnons and high-temperature superconductivity in mercury-based cuprates. *arXiv preprint arXiv:2011.05029*, 2020. URL: `https://arxiv.org/abs/2011.05029`.

[102] Damian Rybicki, Michael Jurkutat, Steven Reichardt, Czesław Kapusta, and Jürgen Haase. Perspective on the phase diagram of cuprate high-temperature superconductors. *Nature communications*, 7(1):1–6, 2016. URL: `https://www.nature.com/articles/ncomms11413`.

[103] Guo-qing Zheng, Yoshio Kitaoka, Kenji Ishida, and Kunisuke Asayama. Local hole distribution in the CuO_2 plane of high-T_c Cu-oxides studied by Cu and oxygen NQR/NMR. *Journal of the Physical Society of Japan*, 64(7):2524–2532, 1995.

URL: `https://www.jstage.jst.go.jp/article/jpsj/64/7/64_7_2524/_article/-char/ja/`.

[104] Ramamurti Shankar. *Principles of quantum mechanics*. Springer Science & Business Media, 2012.

[105] Dieter W Heermann and Kurt Binder. *Monte Carlo simulation in statistical physics: an introduction*. Springer-Verlag, 1992. URL: `https://aip.scitation.org/doi/pdf/10.1063/1.4823159`.

[106] Richard Blankenbecler, DJ Scalapino, and RL Sugar. Monte Carlo calculations of coupled boson-fermion systems. I. *Physical Review D*, 24(8):2278, 1981. URL: `https://journals.aps.org/prd/abstract/10.1103/PhysRevD.24.2278`.

[107] DJ Scalapino and RL Sugar. Monte Carlo calculations of coupled boson-fermion systems. II. *Physical Review B*, 24(8):4295, 1981. URL: `https://journals.aps.org/prb/abstract/10.1103/PhysRevB.24.4295`.

[108] Mark Jarrell, Th Maier, C Huscroft, and S Moukouri. Quantum Monte Carlo algorithm for nonlocal corrections to the dynamical mean-field approximation. *Physical Review B*, 64(19):195130, 2001. URL: `https://journals.aps.org/prb/abstract/10.1103/PhysRevB.64.195130`.

[109] Emanuel Gull, Andrew J Millis, Alexander I Lichtenstein, Alexey N Rubtsov, Matthias Troyer, and Philipp Werner. Continuous-time Monte Carlo methods for quantum impurity models. *Reviews of Modern Physics*, 83(2):349, 2011. URL: `https://journals.aps.org/rmp/abstract/10.1103/RevModPhys.83.349`.

[110] Alexey N Rubtsov, Vladimir V Savkin, and Alexander I Lichtenstein. Continuous-time quantum Monte Carlo method for fermions. *Physical Review B*, 72(3):035122, 2005. URL: `https://journals.aps.org/prb/abstract/10.1103/PhysRevB.72.035122`.

[111] Nikolai V Prokof'ev and Boris V Svistunov. Polaron problem by diagrammatic quantum Monte Carlo. *Physical review letters*, 81(12):2514, 1998. URL: `https://journals.aps.org/prl/abstract/10.1103/PhysRevLett.81.2514`.

[112] Riccardo Rossi. Determinant diagrammatic Monte Carlo algorithm in the thermodynamic limit. *Physical review letters*, 119(4):045701, 2017. URL: `https://journals.aps.org/prl/abstract/10.1103/PhysRevLett.119.045701`.

[113] Gerald D Mahan. *Many-Particle Systems*. Princeton University Press, 2008.

[114] Alexander L Fetter and John Dirk Walecka. *Quantum theory of many-particle systems*. Courier Corporation, 2012.

[115] John W Negele and Henri Orland. *Quantum many-particle systems*. CRC Press, 2018.

[116] John Hubbard. Electron correlations in narrow energy bands. *Proceedings of the Royal Society of London. Series A. Mathematical and Physical Sciences*, 276(1365):238–257, 1963. URL: `https://royalsocietypublishing.org/doi/abs/10.1098/rspa.1963.0204`.

[117] Junjiro Kanamori. Electron correlation and ferromagnetism of transition metals. *Progress of Theoretical Physics*, 30(3):275–289, 1963. URL: `https://academic.oup.com/ptp/article/30/3/275/1865799?login=true`.

[118] Martin C Gutzwiller. Effect of correlation on the ferromagnetism of transition metals. *Physical Review Letters*, 10(5):159, 1963. URL: `https://journals.aps.org/prl/abstract/10.1103/PhysRevLett.10.159`.

[119] PW Anderson. The theory of superconductivity in the high t. *Tc*, 1998.

[120] Th Maier, Mark Jarrell, Th Pruschke, and Joachim Keller. d-wave superconductivity in the Hubbard model. *Physical review letters*, 85(7):1524, 2000. URL: `https://journals.aps.org/prl/abstract/10.1103/PhysRevLett.85.1524`.

[121] Th A Maier, M Jarrell, TC Schulthess, PRC Kent, and JB White. Systematic study of d-wave superconductivity in the 2D repulsive Hubbard model. *Physical review letters*, 95(23):237001, 2005. URL: `https://journals.aps.org/prl/abstract/10.1103/PhysRevLett.95.237001`.

[122] Massimo Capone and G Kotliar. Competition between d-wave superconductivity and antiferromagnetism in the two-dimensional Hubbard model. *Physical Review B*, 74(5):054513, 2006. URL: `https://journals.aps.org/prb/abstract/10.1103/PhysRevB.74.054513`.

[123] Kristjan Haule and Gabriel Kotliar. Strongly correlated superconductivity: A plaquette dynamical mean-field theory study. *Physical Review B*, 76(10):104509, 2007. URL: `https://journals.aps.org/prb/abstract/10.1103/PhysRevB.76.104509`.

[124] Emanuel Gull, Olivier Parcollet, and Andrew J Millis. Superconductivity and the pseudogap in the two-dimensional Hubbard model. *Physical review letters*, 110(21):216405, 2013. URL: `https://journals.aps.org/prl/abstract/10.1103/PhysRevLett.110.216405`.

[125] Alexis Reymbaut, Simon Bergeron, R Garioud, M Thénault, Maxime Charlebois, P Sémon, and A-MS Tremblay. Pseudogap, Van Hove singularity, maximum in entropy, and specific heat for hole-doped Mott insulators. *Physical Review Research*, 1(2):023015, 2019. URL: `https://journals.aps.org/prresearch/abstract/10.1103/PhysRevResearch.1.023015`.

[126] Claudius Gros, Robert Joynt, and T Maurice Rice. Antiferromagnetic correlations in almost-localized Fermi liquids. *Physical Review B*, 36(1):381, 1987. URL: `https://journals.aps.org/prb/abstract/10.1103/PhysRevB.36.381`.

[127] Philip W Anderson. New approach to the theory of superexchange interactions. *Physical Review*, 115(1):2, 1959. URL: `https://journals.aps.org/pr/abstract/10.1103/PhysRev.115.2`.

[128] Evgeny Mikhailovich Lifshitz, LP Pitaevskii, and VB Berestetskii. Landau and lifshitz course of theoretical physics. *Statistical physics*, 5, 1980.

[129] E Akkermans, G Montambaux, J Pichard, and J Zinn-Justin. Fermi liquids and non-fermi liquids, mesocopic quantum physics. *Proceedings of Les Houches Summer School LXI (Elsevier, Amsterdam, 1995)*.

[130] Gordon Baym and Christopher Pethick. *Landau Fermi-liquid theory: concepts and applications*. John Wiley & Sons, 2008.

[131] AK McMahan, Richard M Martin, and S Satpathy. Calculated effective Hamiltonian for La_2CuO_4 and solution in the impurity Anderson approximation. *Physical Review B*, 38(10):6650, 1988. URL: `https://journals.aps.org/prb/abstract/10.1103/PhysRevB.38.6650`.

[132] Mark S Hybertsen, Michael Schlüter, and Niels E Christensen. Calculation of Coulomb-interaction parameters for La_2CuO_4 using a constrained-density-functional approach. *Physical Review B*, 39(13):9028, 1989. URL: `https://journals.aps.org/prb/abstract/10.1103/PhysRevB.39.9028`.

[133] Cédric Weber, C Yee, Kristjan Haule, and Gabriel Kotliar. Scaling of the transition temperature of hole-doped cuprate superconductors with the charge-transfer energy. *EPL (Europhysics Letters)*, 100(3):37001, 2012. URL: `https://iopscience.iop.org/article/10.1209/0295-5075/100/37001/meta`.

[134] OK Andersen, AI Liechtenstein, O Jepsen, and F Paulsen. LDA energy bands, low-energy hamiltonians, t', t'', $t_\perp(k)$, and $J_\perp$. *Journal of Physics and Chemistry of Solids*, 56(12):1573–1591, 1995. URL: `https://www.sciencedirect.com/science/article/pii/0022369795002693`.

[135] JM Tranquada, SM Heald, and AR Moodenbaugh. X-ray-absorption near-edge-structure study of $La_{2-x}(Ba,Sr)_xCuO_{4-y}$ superconductors. *Physical Review B*, 36(10):5263, 1987. URL: `https://journals.aps.org/prb/pdf/10.1103/PhysRevB.36.5263`.

[136] N Gauquelin, DG Hawthorn, GA Sawatzky, RX Liang, DA Bonn, WN Hardy, and GA Botton. Atomic scale real-space mapping of holes in $YBa_2Cu_3O_{6+\delta}$. *Nature communications*, 5(1):1–7, 2014. URL: `https://www.nature.com/articles/ncomms5275.pdf`.

[137] CT Chen, F Sette, Y Ma, MS Hybertsen, EB Stechel, WMC Foulkes, M Schulter, Sang-Wook Cheong, AS Cooper, LW Rupp Jr, et al. Electronic states in $La_{2-x}Sr_xCuO_{4+\delta}$ probed by soft-x-ray absorption. *Physical review letters*, 66(1):104, 1991. URL: `https://journals.aps.org/prl/pdf/10.1103/PhysRevLett.66.104`.

[138] L Fratino, P Sémon, G Sordi, and A-MS Tremblay. Pseudogap and superconductivity in two-dimensional doped charge-transfer insulators. *Physical Review B*, 93(24):245147, 2016. URL: `https://journals.aps.org/prb/abstract/10.1103/PhysRevB.93.245147`.

[139] James F Annett et al. *Superconductivity, superfluids and condensates*, volume 5. Oxford University Press, 2004.

[140] Michael Tinkham. *Introduction to superconductivity*. Courier Corporation, 2004.

[141] JB Ketterson and SN Song. Superconductivity cambridge university press. *Cambridge, England*, page 215, 1999.

[142] J Robert Schrieffer. Theory of superconductivity, advanced book classics, 1999.

[143] RW Richardson. A restricted class of exact eigenstates of the pairing-force hamiltonian. 1963. URL: `https://deepblue.lib.umich.edu/bitstream/handle/2027.42/32238/0000300.pdf;sequence=1`.

[144] RW Richardson and Noah Sherman. Exact eigenstates of the pairing-force hamiltonian. *Nuclear Physics*, 52:221–238, 1964. URL: `https://www.sciencedirect.com/science/article/abs/pii/002955826490687X`.

[145] Jorge Dukelsky and S Pittel. Exact solutions for pairing interactions. pages 200–211, 2013. URL: `https://www.worldscientific.com/doi/abs/10.1142/9789814412490_0015`.

[146] AB Migdal. Interaction between electrons and lattice vibrations in a normal metal. *Sov. Phys. JETP*, 7(6):996–1001, 1958.

[147] GM Eliashberg. Interactions between electrons and lattice vibrations in a superconductor. *Sov. Phys. JETP*, 11(3):966, 1960. URL: `http://www.jetp.ac.ru/cgi-bin/e/index/e/11/3/p696?a=list`.

[148] Antoine Georges, Gabriel Kotliar, Werner Krauth, and Marcelo J Rozenberg. Dynamical mean-field theory of strongly correlated fermion systems and the limit of infinite dimensions. *Reviews of Modern Physics*, 68(1):13, 1996. URL: `https://journals.aps.org/rmp/abstract/10.1103/RevModPhys.68.13`.

[149] Gabriel Kotliar, Sergej Y Savrasov, Gunnar Pálsson, and Giulio Biroli. Cellular dynamical mean field approach to strongly correlated systems. *Physical review letters*, 87(18):186401, 2001. URL: `https://journals.aps.org/prl/abstract/10.1103/PhysRevLett.87.186401`.

[150] Gabriel Kotliar, Sergej Y Savrasov, Kristjan Haule, Viktor S Oudovenko, O Parcollet, and CA Marianetti. Electronic structure calculations with dynamical mean-field theory. *Reviews of Modern Physics*, 78(3):865, 2006. URL: `https://journals.aps.org/rmp/pdf/10.1103/RevModPhys.78.865`.

[151] A-MS Tremblay, B Kyung, and D Sénéchal. Pseudogap and high-temperature superconductivity from weak to strong coupling. towards a quantitative theory. *Low Temperature Physics*, 32(4):424–451, 2006. URL: `https://aip.scitation.org/doi/abs/10.1063/1.2199446`.

[152] MH Hettler, AN Tahvildar-Zadeh, M Jarrell, Th Pruschke, and HR Krishnamurthy. Nonlocal dynamical correlations of strongly interacting electron systems. *Physical Review B*, 58(12):R7475, 1998. URL: `https://journals.aps.org/prb/abstract/10.1103/PhysRevB.58.R7475`.

[153] Thomas Maier, Mark Jarrell, Thomas Pruschke, and Matthias H Hettler. Quantum cluster theories. *Reviews of Modern Physics*, 77(3):1027, 2005. URL: `https://journals.aps.org/rmp/abstract/10.1103/RevModPhys.77.1027`.

[154] P Sémon, Chuck-Hou Yee, Kristjan Haule, and A-MS Tremblay. Lazy skip-lists: An algorithm for fast hybridization-expansion quantum Monte Carlo. *Physical Review B*, 90(7):075149, 2014. URL: `https://journals.aps.org/prb/abstract/10.1103/PhysRevB.90.075149`.

[155] Claudius Gros and Roser Valenti. Cluster expansion for the self-energy: A simple many-body method for interpreting the photoemission spectra of correlated Fermi systems. *Physical Review B*, 48(1):418, 1993. URL: `https://journals.aps.org/prb/abstract/10.1103/PhysRevB.48.418`.

[156] D Sénéchal, D Perez, and M Pioro-Ladriere. Spectral weight of the Hubbard model through cluster perturbation theory. *Physical review letters*, 84(3):522, 2000. URL: `https://journals.aps.org/prl/abstract/10.1103/PhysRevLett.84.522`.

[157] David Sénéchal, Danny Perez, and Dany Plouffe. Cluster perturbation theory for Hubbard models. *Physical Review B*, 66(7):075129, 2002. URL: `https://journals.aps.org/prb/abstract/10.1103/PhysRevB.66.075129`.

[158] Tudor D Stanescu and Gabriel Kotliar. Fermi arcs and hidden zeros of the Green function in the pseudogap state. *Physical Review B*, 74(12):125110, 2006. URL: `https://journals.aps.org/prb/abstract/10.1103/PhysRevB.74.125110`.

[159] S Verret, A Foley, D Sénéchal, A Tremblay, and M Charlebois. Fermi arcs vs hole pockets: periodization of a cellular two-band model. *arXiv preprint arXiv:2107.01344*, 2021. URL: `https://arxiv.org/abs/2107.01344`.

[160] Cornelius Lanczos. *An iteration method for the solution of the eigenvalue problem of linear differential and integral operators*. United States Governm. Press Office Los Angeles, CA, 1950.

[161] David Sénéchal. An introduction to quantum cluster methods. *arXiv preprint arXiv:0806.2690*, 2008. URL: `https://arxiv.org/abs/0806.2690`.

[162] Zhaojun Bai, James Demmel, Jack Dongarra, Axel Ruhe, and Henk van der Vorst. *Templates for the solution of algebraic eigenvalue problems: a practical guide*. SIAM, 2000.

[163] AI Lichtenstein and MI Katsnelson. Antiferromagnetism and d-wave superconductivity in cuprates: A cluster dynamical mean-field theory. *Physical Review B*, 62(14):R9283, 2000. URL: `https://journals.aps.org/prb/abstract/10.1103/PhysRevB.62.R9283`.

[164] Walter Metzner and Dieter Vollhardt. Correlated lattice fermions in $d = \infty$ dimensions. *Physical review letters*, 62(3):324, 1989. URL: `https://journals.aps.org/prl/abstract/10.1103/PhysRevLett.62.324`.

[165] David Sénéchal. Bath optimization in the cellular dynamical mean-field theory. *Physical Review B*, 81(23):235125, 2010. URL: `https://journals.aps.org/prb/abstract/10.1103/PhysRevB.81.235125`.

[166] Erik Koch, Giorgio Sangiovanni, and Olle Gunnarsson. Sum rules and bath parametrization for quantum cluster theories. *Physical Review B*, 78(11):115102, 2008. URL: `https://journals.aps.org/prb/abstract/10.1103/PhysRevB.78.115102`.

[167] Jeffery L Tallon, C Bernhard, H Shaked, RL Hitterman, and JD Jorgensen. Generic superconducting phase behavior in high-T_c cuprates: T_c variation with hole concentration in $YBa_2Cu_3O_{7-\delta}$. *Physical Review B*, 51(18):12911, 1995. URL: `https://journals.aps.org/prb/abstract/10.1103/PhysRevB.51.12911`.

[168] S Verret, J Roy, A Foley, M Charlebois, D Sénéchal, and A-MS Tremblay. Intrinsic cluster-shaped density waves in cellular dynamical mean-field theory. *Physical Review B*, 100(22):224520, 2019. URL: `https://journals.aps.org/prb/abstract/10.1103/PhysRevB.100.224520`.

[169] Shiro Sakai, Marcello Civelli, and Masatoshi Imada. Hidden fermionic excitation boosting high-temperature superconductivity in cuprates. *Physical review letters*, 116(5):057003, 2016. URL: `https://journals.aps.org/prl/abstract/10.1103/PhysRevLett.116.057003`.

[170] Tudor D Stanescu and Philip Phillips. Pseudogap in doped Mott insulators is the near-neighbor analogue of the Mott gap. *Physical review letters*, 91(1):017002, 2003. URL: `https://journals.aps.org/prl/abstract/10.1103/PhysRevLett.91.017002`.

[171] Peizhi Mai, Giovanni Balduzzi, Steven Johnston, and Thomas A Maier. Pairing correlations in the cuprates: A numerical study of the three-band Hubbard model. *Physical Review B*, 103(14):144514, 2021. URL: `https://journals.aps.org/prb/abstract/10.1103/PhysRevB.103.144514`.

[172] MT Béal-Monod, C Bourbonnais, and VJ Emery. Possible superconductivity in nearly antiferromagnetic itinerant fermion systems. *Physical Review B*, 34(11):7716, 1986. URL: `https://journals.aps.org/prb/abstract/10.1103/PhysRevB.34.7716`.

[173] DJ Scalapino, E Loh Jr, and JE Hirsch. d-wave pairing near a spin-density-wave instability. *Physical Review B*, 34(11):8190, 1986. URL: `https://journals.aps.org/prb/abstract/10.1103/PhysRevB.34.8190`.

[174] Swagata Acharya, Cédric Weber, Evgeny Plekhanov, Dimitar Pashov, A Taraphder, and Mark Van Schilfgaarde. Metal-insulator transition in copper oxides induced by apex displacements. *Physical Review X*, 8(2):021038, 2018. URL: `https://journals.aps.org/prx/abstract/10.1103/PhysRevX.8.021038`.

[175] CM Varma and T Giamarchi. Model for Copper-Oxide metals and superconductors. *Notes for the lectures presented at the Ecole de Physique Theorique des Houches at the session on Strongly Interacting Fermions and High-Tc Superconductivity, August 1990*, 1995.

[176] B Loret, S Sakai, S Benhabib, Y Gallais, M Cazayous, MA Méasson, RD Zhong, J Schneeloch, GD Gu, A Forget, et al. Vertical temperature boundary of the pseudogap under the superconducting dome in the phase diagram of $Bi_2Sr_2CaCu_2O_{8+\delta}$. *Physical Review B*, 96(9):094525, 2017. URL: `https://journals.aps.org/prb/abstract/10.1103/PhysRevB.96.094525`.

[177] Nicolas Kowalski. Dopage, Température critique et étude du modèle de Hubbard à trois bandes. 2020. URL: `https://savoirs.usherbrooke.ca/bitstream/handle/11143/18438/kowalski_nicolas_MSc_2021.pdf?sequence=7`.

[178] S. S. Dash and D. Sénéchal. Pseudogap transition within the superconducting phase in the three-band Hubbard model. *Physical Review B*, 100(21):214509, 2019. URL: `https://journals.aps.org/prb/abstract/10.1103/PhysRevB.100.214509`.

[179] N Kowalski, SS Dash, P Sémon, D Sénéchal, and AMS Tremblay. Oxygen hole content, charge-transfer gap, covalency, and cuprate superconductivity. *Proceedings of the National Academy of Sciences*, 118(40), 2021. URL: `https://www.pnas.org/content/118/40/e2106476118`.

[180] AI Liechtenstein, Olle Gunnarsson, OK Andersen, and RM Martin. Quasiparticle bands and superconductivity in bilayer cuprates. *Physical Review B*, 54(17):12505,

1996. URL: https://journals.aps.org/prb/abstract/10.1103/PhysRevB.54.12505.

[181] Eduardo Fradkin, Steven A Kivelson, and John M Tranquada. Colloquium: Theory of intertwined orders in high temperature superconductors. *Reviews of Modern Physics*, 87(2):457, 2015. URL: https://journals.aps.org/rmp/abstract/10.1103/RevModPhys.87.457.

[182] Erez Berg, Eduardo Fradkin, and Steven A Kivelson. Charge-4 e superconductivity from pair-density-wave order in certain high-temperature superconductors. *Nature Physics*, 5(11):830–833, 2009. URL: https://www.nature.com/articles/nphys1389.

[183] Bumsoo Kyung, G Kotliar, and A-MS Tremblay. Quantum Monte Carlo study of strongly correlated electrons: Cellular dynamical mean-field theory. *Physical Review B*, 73(20):205106, 2006. URL: https://journals.aps.org/prb/abstract/10.1103/PhysRevB.73.205106.

[184] Ansgar Liebsch and Hiroshi Ishida. Temperature and bath size in exact diagonalization dynamical mean field theory. *Journal of Physics: Condensed Matter*, 24(5):053201, 2011. URL: https://iopscience.iop.org/article/10.1088/0953-8984/24/5/053201.

[185] Peayush Choubey, Sang Hyun Joo, K Fujita, Zengyi Du, SD Edkins, MH Hamidian, H Eisaki, S Uchida, AP Mackenzie, Jinho Lee, et al. Atomic-scale electronic structure of the cuprate pair density wave state coexisting with superconductivity. *Proceedings of the National Academy of Sciences*, 117(26):14805–14811, 2020. URL: https://www.pnas.org/content/117/26/14805.short.

[186] MR Norman and JC Séamus Davis. Quantum oscillations in a biaxial pair density wave state. *Proceedings of the National Academy of Sciences*, 115(21):5389–5391, 2018. URL: https://www.pnas.org/content/115/21/5389.short.

[187] S. S. Dash and D. Sénéchal. Charge-and pair-density-wave orders in the one-band Hubbard model from dynamical mean field theory. *Physical Review B*, 103(4):045142, 2021. URL: https://journals.aps.org/prb/abstract/10.1103/PhysRevB.103.045142.

[188] K McElroy, D-H Lee, JE Hoffman, KM Lang, EW Hudson, H Eisaki, S Uchida, J Lee, and JC Davis. Homogenous nodal superconductivity coexisting with inhomogeneous charge order in strongly underdoped Bi-2212. *arXiv preprint cond-mat/0404005*, 2004. URL: https://arxiv.org/abs/cond-mat/0404005.

[189] K McElroy, D-H Lee, JE Hoffman, KM Lang, Jinho Lee, EW Hudson, H Eisaki, S Uchida, and JC Davis. Coincidence of checkerboard charge order and antinodal state decoherence in strongly underdoped superconducting $Bi_2Sr_2CaCu_2O_{8+\delta}$. *Physical Review Letters*, 94(19):197005, 2005. URL: https://journals.aps.org/prl/abstract/10.1103/PhysRevLett.94.197005.

[190] Ch Renner, Bernard Revaz, J-Y Genoud, K Kadowaki, and Ø Fischer. Pseudogap precursor of the superconducting gap in under- and overdoped $Bi_2Sr_2CaCu_2O_{8+\delta}$. *Physical Review Letters*, 80(1):149, 1998. URL: `https://journals.aps.org/prl/abstract/10.1103/PhysRevLett.80.149`.